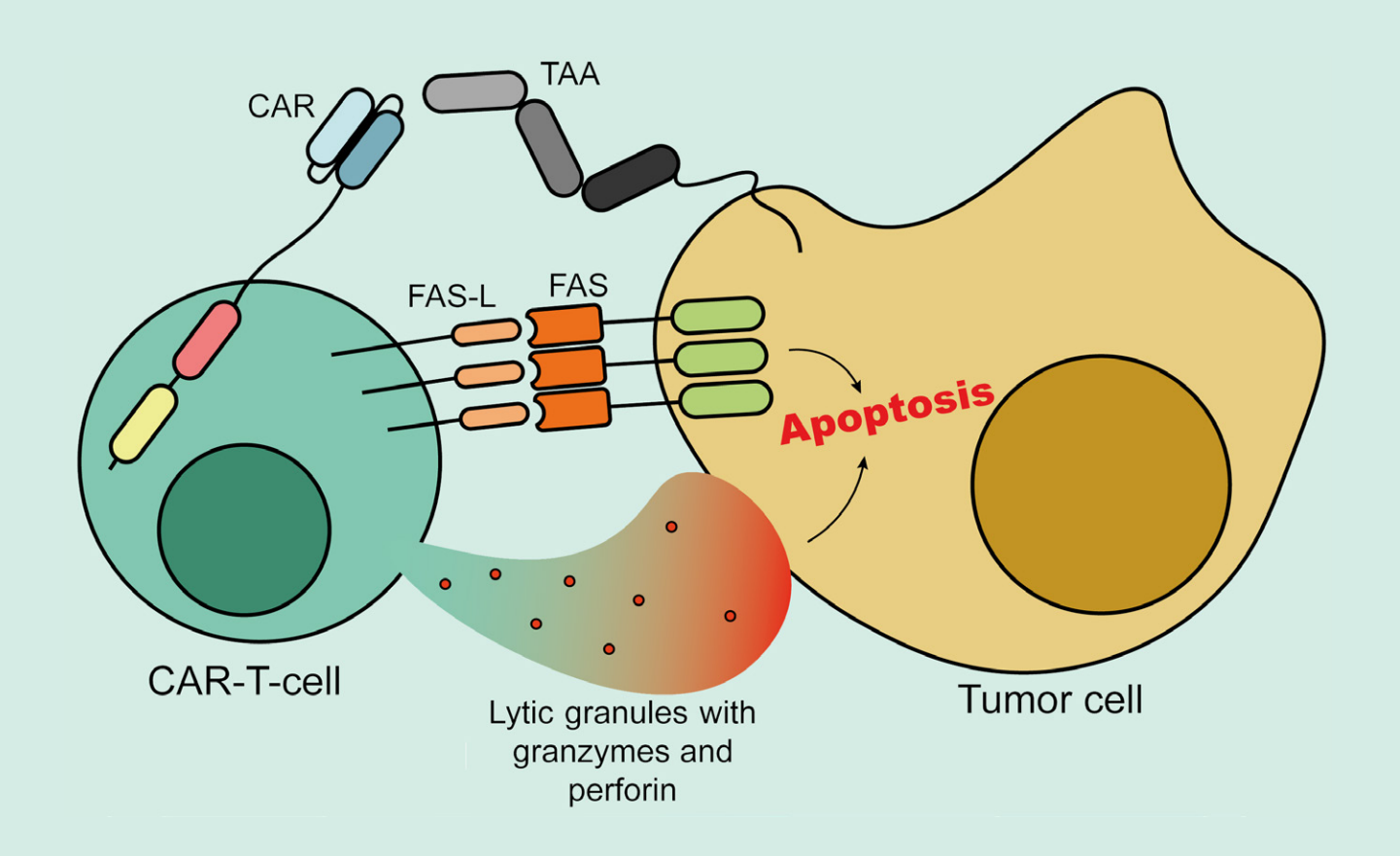
# ActaNaturae

# The Impact of the Intracellular Domains of Chimeric Antigenic Receptors on the Properties of CAR T-cells



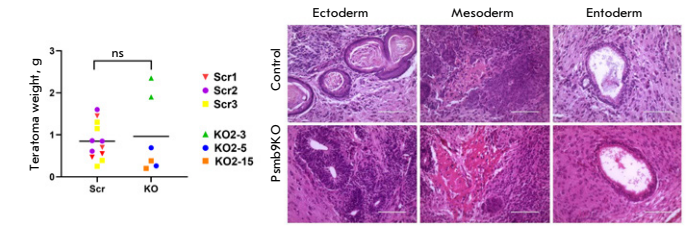
RNA INTERFERENCE
OF THE GENES ASSOCIATED
WITH THE INVASION OF BRAIN
TUMOR CELLS

STORE-OPERATED CALCIUM ENTRY
AS AN IMPORTANT MECHANISM
OF TUMOR ADAPTATION
TO AN AGGRESSIVE MICROENVIRONMENT

## The Generation and Characterization of a Mouse Embryonic Stem Cell Line with *Psmb9* Immunoproteasome Gene Knockout

D. V. Kriger, U. I. Podenkova, A. A. Kuzmin, N. D. Aksenov, A. V. Kropacheva, A. S. Zinovyeva, A. V. Selenina, A. N. Tomilin, A. S. Tsimokha

Using CRISPR/Cas9 technology, a mouse embryonic stem cell (ESC) line with knockout of the Psmb9 gene encoding the immunoproteasome catalytic subunit Lmp2 ( $\beta$ 1i) was generated. It was demonstrated that the absence of Lmp2 does not affect ESC morphology, proliferative activity, or pluripotent status. This cell line represents a promising tool for studying the role of the Psmb9 gene and immunoproteasomes in subsequent stages of  $in\ vitro\ ESC\ differentiation$ .



Evaluation of the pluripotent properties in vivo of Psmb9 knockout ESC lines using a teratoma assay

## PepString Server As a Tool to Search for Short Amino Acid Subsequences: Identification of Potential Amyloid-Beta Targets



Query form to search for protein sequences containing exact matches of short peptides using the PepString server (http://pepstring.eimb.ru)

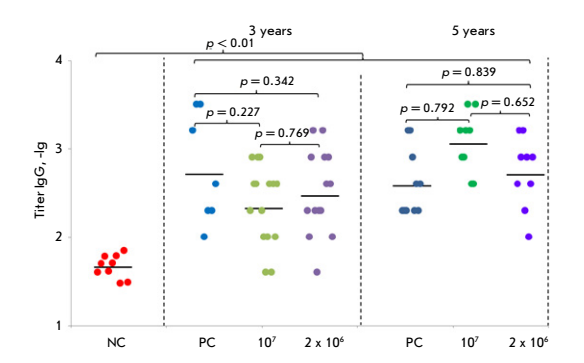
S. A. Kozin, A. A. Anashkina, D. G. Matsuga, B. S. Suvaan, V. G. Tumanyan, V. A. Mitkevich, A. A. Makarov

This paper presents a new bioinformatics tool to meet the needs of researchers in the search for short amino acid subsequences in protein sequences annotated in public databases (UniprotKB, SwissProt) and illustrates its efficacy with the example of a search for the EVHH tetrapeptide in the human proteome, which is a molecular determinant of amyloid beta and is involved in interactions that are crucial in Alzheimer's disease pathogenesis. This tool (PepString server, http://pepstring.eimb.ru/) allows one to use intuitive queries to retrieve information about all the proteins that contain sequences of interest, as well as their combinations.

## The Humoral and Cellular Immune Response to the Administration of OrthopoxVac Vaccine to Volunteers

S. N. Shchelkunov, E. Yu. Prudnikova, A. A. Shestakova, S. N. Yakubitskiy, S. A. Pyankov, A. E. Nesterov, S. V. Usova, M. P. Bogryantseva, E. A. Nechaeva, T. V. Tregubchak, A. P. Agafonov

OrthopoxVac, the world's first fourth-generation smallpox vaccine, has proven to be safe and weakly reactogenic compared to the first-generation live smallpox vaccine, while maintaining the same level of immunogenic properties. This study analyzed the levels of specific humoral and T-cell immune responses following intradermal administration of the OrthopoxVac vaccine to volunteers, either as a single dose of 10<sup>7</sup> PoFU or two doses of 10<sup>6</sup> PoFU, at 1.5, 3, and 5 years after vaccination. Based on the obtained results, it can be concluded that the OrthopoxVac vaccine, when administered intradermally as a single dose of 10<sup>7</sup> PoFU, provides a pronounced specific humoral and T-cell immune response for at least three years.



Logarithms of the ELISA titers of specific IgG to VACV antigens in the blood sera of volunteers from clinical studies of the OrthopoxVac vaccine

## **ActaNaturae**

JULY—SEPTEMBER 2025 VOL. 17 № 3 (66) since april 2009, 4 times a year

#### Founders

Acta Naturae, Ltd, National Research University Higher School of Economics

Editorial Council Editors-in-Chief: A.G. Gabibov, S.N. Kochetkov

V.V. Vlassov, P.G. Georgiev, M.P. Kirpichnikov, A.A. Makarov, A.I. Miroshnikov, V.A. Tkachuk, M.V. Ugryumov

Editorial Board
Managing Editor: V.D. Knorre

K.V. Anokhin (Moscow, Russia)
I. Bezprozvanny (Dallas, Texas, USA)
I.P. Bilenkina (Moscow, Russia)
M. Blackburn (Sheffield, England)
S.M. Deyev (Moscow, Russia)
V.M. Govorun (Moscow, Russia)

O.A. Dontsova (Moscow, Russia)

K. Drauz (Hanau-Wolfgang, Germany)
A. Friboulet (Paris, France)

M. Issagouliants (Stockholm, Sweden)

M. Lukic (Abu Dhabi, United Arab Emirates)

P. Masson (La Tronche, France)

V.O. Popov (Moscow, Russia)

I.A. Tikhonovich (Moscow, Russia)

A. Tramontano (Davis, California, USA)

V.K. Švedas (Moscow, Russia)

J.-R. Wu (Shanghai, China)

N.K. Yankovsky (Moscow, Russia) M. Zouali (Paris, France)

Project Head: N.V. Soboleva
Editor: N.Yu. Deeva
Designer: K.K. Oparin
Art and Layout: K. Shnaider
Copy Chief: Daniel M. Medjo
Web Content Editor: O.B. Semina

Adress: 101000, Moscow, Myasnitskaya Ulitsa, 13, str. 4 Phone/Fax: +7 (495) 727 38 60 E-mail: actanaturae@gmail.com

Reprinting is by permission only.

© ACTA NATURAE, 2025

Номер подписан в печать 30 сентября 2025 г. Тираж 15 экз. Цена свободная. Отпечатано в типографии: НИУ ВШЭ, г. Москва, Измайловское шоссе, 44, стр. 2



Founder and Chairman of the Editorial Board (from 2009 to 2023) of the journal Acta Naturae Academician Grigoriev Anatoly Ivanovich

> Indexed in PubMed, Web of Science, Scopus, and RISC

Impact Factor: 2.0 (WOS); 3.5 (Scopus)

## **CONTENTS**

#### REVIEWS

D. V. Volkov, V. M. Stepanova, I. A. Yaroshevic A. G. Gabibov, Y. P. Rubtsov	:h,
The Impact of the Intracellular Domains of Chimeric Antigenic Receptors on the Properties of CAR T-cells	4
M. A. Dymova, O. A. Kartina, D. V. Drokov, E. V. Kuligina, V. A. Richter	
RNA Interference of the Genes Associated with the Invasion of Brain Tumor Cells	18

A. Yu. Skopin, E. V. Kaznacheyeva	G. M. Proshkina, E. I. Shramova, A. B. Mirkasymov,
Store-Operated Calcium Entry As an Important	I. N. Zavestovskaya, S. M. Deyev
Mechanism of Tumor Adaptation	Targeted Nanoliposomes for the Delivery
to an Aggressive Microenvironment28	of Boronophenylalanine into HER2-Positive Cells 88
	E. A. Tsymbalova, E. A. Chernyavskaya,
RESEARCH ARTICLES	G. N. Bisaga, A. Y. Polushin, E. I. Lopatina, I. N. Abdurasulova, V. I. Lioudyno
	LINE-1 Methylation Status in Multiple Sclerosis Patients
D. O. Egorova, S. V. Gein, N. A. Korolev, N. P. Loginova	Is Associated with Changes in Folate Metabolism 94
_	S. N. Shchelkunov, E. Yu. Prudnikova,
Ortho- and Meta-monochlorinated Biphenyls Suppress Humoral Immunity and Exert Toxic Effects	A. A. Shestakova, S. N. Yakubitskiy, S. A. Pyankov,
on Mouse Liver Cells	A. E. Nesterov, S. V. Usova, M. P. Bogryantseva,
Oil Mouse Liver Cells40	E. A. Nechaeva, T. V. Tregubchak, A. P. Agafonov
T. N. Erokhina, E. V. Ryabukhina, I. S. Lyapina,	The Humoral and Cellular Immune Response
D. Y. Ryazantsev, S. K Zavriev, S. Y. Morozov	to the Administration of OrthopoxVac Vaccine
Cabbage Peptide miPEP156a Enhances	to Volunteers104
the Level of Accumulation of Its mRNA	
in Transgenic Moss Physcomitrium patens44	A. Yu. Rudenko, P. A. Zotova, O. A. Averina,
, ,	A. V. Priymak, M. P. Rubtsova, S. S. Mariasina, R. M. Ozhiganov, O. A. Dontsova, P. V. Sergiev
A. S. Zelentsova, M. V. Pokrovskii,	-
E. A. Patrakhanov, V. S. Shmigerova,	Test System for Studying Biotin Transport upon SLC5A6 Gene Inactivation119
M. Yu. Skorkina, A. V. Deykin	upon 32C3A0 Gene macrivation117
p2rx3 Knockout Mice Have Altered Energy	
Metabolism in Hippocampal Neurons	Guidelines for Authors
A. A. Kleymenova, I. A. Abramov, Ya. V. Tkachev,	
P. S. Galeeva, V. A. Kleymenova, N. F. Zakirova,	
S. N. Kochetkov, M. V. Kozlov	
The Design, Synthesis, and Evaluation of the Biological	
Activity of Hydroxamic Derivatives of Sorafenib 56	TAA
	CAR
S. A. Kozin, A. A. Anashkina, D. G. Matsuga,	
B. S. Suvaan, V. G. Tumanyan, V. A. Mitkevich,	FAS-L FAS
A. A. Makarov	
PepString Server As a Tool to Search	Apoptosis
for Short Amino Acid Subsequences: Identification	
of Potential Amyloid-Beta Targets67	
D. V. Kriger, U. I. Podenkova, A. A. Kuzmin,	CAR-T-cell
N. D. Aksenov, A. V. Kropacheva, A. S. Zinovyeva,	Lytic granules with Tumor cell granzymes and
A. V. Selenina, A. N. Tomilin, A. S. Tsimokha	perforin
The Generation and Characterization	
of a Mouse Embryonic Stem Cell Line with Psmb9	IMAGE ON THE COVER PAGE
Immunoproteasome Gene Knockout 77	(see the article by Volkov et al.)

## The Impact of the Intracellular Domains of Chimeric Antigenic Receptors on the Properties of CAR T-cells

D. V. Volkov<sup>1</sup>\*, V. M. Stepanova<sup>1</sup>, I. A. Yaroshevich<sup>1,2</sup>, A. G. Gabibov<sup>1</sup>, Y. P. Rubtsov<sup>1</sup>

<sup>1</sup>Shemyakin-Ovchinnikov Institute of Bioorganic Chemistry, Russian Academy of Sciences, Moscow, 117997 Russia

<sup>2</sup>Lomonosov Moscow State University, Moscow, 119991 Russia

\*E-mail: ya.wolf.otl@yandex.ru

Received: June 23, 2025; in final form, July 02, 2025

DOI: 10.32607/actanaturae.27728

Copyright © 2025 National Research University Higher School of Economics. This is an open access article distributed under the Creative Commons Attribution License, which permits unrestricted use, distribution, and reproduction in any medium, provided the original work is properly cited.

ABSTRACT The advent of the T-cell engineering technology using chimeric antigen receptors (CARs) has revolutionized the treatment of hematologic malignancies and reoriented the direction of research in the field of immune cell engineering and immunotherapy. Regrettably, the effectiveness of CAR T-cell therapy in specific instances of hematologic malignancies and solid tumors is limited by a number of factors. These include (1) an excessive or insufficient CAR T-cell response, possibly a result of both resistance within the tumor cells or the microenvironment and the suboptimal structural and functional organization of the chimeric receptor; (2) a less-than-optimal functional phenotype of the final CAR T-cell product, which is a direct consequence of the manufacturing and expansion processes used to produce CAR T-cells; and (3) the lack of an adequate CAR T-cell control system post-administration to the patient. Consequently, current research efforts focus on optimizing the CAR structure, improving production technologies, and further developing CAR T-cell modifications. Optimizing the CAR structure to enhance the function of modified cells is a primary strategy in improving the efficacy of CAR T-cell therapy. Since the emergence of the first CAR T-cells, five generations of CARs have been developed, employing both novel combinations of signaling and structural domains within a single molecule and new systems of multiple chimeric molecules presented simultaneously on the T-cell surface. A well thought-out combination of CAR components should ensure high receptor sensitivity to the antigen, the formation of a stable immune synapse (IS), effective costimulation, and productive CAR T-cell activation. Integrating cutting-edge technologies – specifically machine learning that helps predict the structure and properties of a three-dimensional biopolymer, combined with high-throughput sequencing and omics approaches - offers new possibilities for the targeted modification of the CAR structure. Of crucial importance is the selection of specific modifications and combinations of costimulatory and signaling domains to enhance CAR T-cell cytotoxicity, proliferation, and persistence. This review provides insights into recent advancements in CAR optimization, with particular emphasis on modifications designed to enhance the therapeutic functionality of CAR T-cells.

KEYWORDS CAR T-cell, costimulatory molecules, CD3, intracellular signaling, T-cell receptors.

ABBREVIATIONS CAR – chimeric antigen receptor; CAR T-cells – chimeric antigen receptor-modified T-cells; IS – immune synapse; TAA – tumor-associated antigen; FASL – Fas ligand; FAS – Fas receptor; ICD – intracellular domain; scFv – single-chain variable fragment; VHH – variable domain of heavy-chain antibody; CD – cluster of differentiation; BCMA – B-cell maturation antigen; IgSF – immunoglobulin superfamily; TNFRSF – tumor necrosis factor superfamily; APC – antigen-presenting cell; MHC I/II – major histocompatibility complex class I and II; TCR – T-cell receptor; α, β – T-cell receptor recognition chains;  $\xi$ ,  $\gamma$ ,  $\delta$ ,  $\varepsilon$  – CD3 proteins of the T-cell receptor; ITAM – immunoreceptor tyrosine-based activation motif; AA – amino acid; Y – tyrosine; Tn cells – naïve T-cells; ICOSL – inducible T-cell costimulator ligand; IL – interleukin; IFN- $\gamma$  – interferon gamma; TNF- $\alpha$  – tumor necrosis factor alpha; Treg cells – regulatory T-cells; FAP – fibroblast activation protein; Th cells – helper T-cells; Tm cells – memory T-cells; TRAF – TNF receptor-associated factor; Tcm cells – central memory T-cells;

HVEM – herpesvirus entry mediator; Tem cells – effector memory T-cells; GITR – glucocorticoid-induced TNF receptor-related protein; BRS – basic residue-rich sequences (in some CD3 molecules); RK – receptor kinase; PRS – proline-rich sequence of CD3ε; PKC – protein kinase C; bCAR – chimeric antigen receptors with signaling domains represented by parts of various intracellular signaling partners of the TCR; ZAP70KD – kinase domain of ZAP70.

#### INTRODUCTION

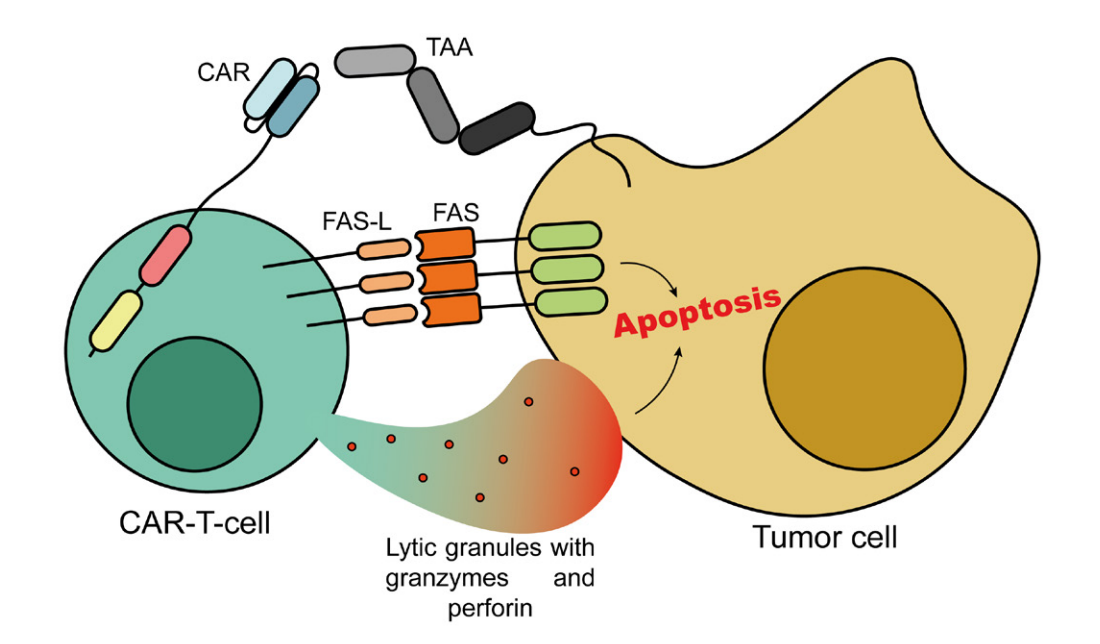
Today, conventional methods of treating tumors chemotherapy and radiation therapy – are frequently integrated with comparatively novel immunotherapeutic approaches. These include therapy with monoclonal antibodies and bispecific T-cell engagers, as well as cell therapy, notably with CAR T-cells, which is the focus of this review. The growing interest in more specific, or so-called targeted, therapies has largely to do with the low effectiveness and severe adverse effects of conventional treatments (e.g., systemic genotoxicity) [1], as well as the growing potential shown by novel methods, as particularly well exemplified by the CAR T-cell technology, in treating hematologic diseases [2]. The mechanism of CAR T-cell therapy is based on the recognition of surface markers on tumor cells by cytotoxic CAR T-cells (Fig. 1).

This capability is made possible by the CAR, which comprises three primary domains: an extracellular domain responsible for antigen recognition and the mobility of the recognition moiety, a transmembrane domain involved in immune synapse (IS) formation, and an intracellular domain containing costimulatory

and signaling domains that determine the entire spectrum of CAR T-cell responses upon specific activation by antigen binding. Furthermore, the off-tumor toxicity of such immunotherapeutic agents is significantly lower compared to conventional therapies [3]. Additionally, successful CAR T-cell therapy can lead to the formation of a specific memory cell population, ensuring long-term remission [4].

Unfortunately, despite individual successes with CAR T-cells, there remain patients for whom current CAR T-cell therapy provides only temporary relief due to insufficient effect duration or cytotoxicity of the highly personalized cell products. Therefore, research is focused on enhancing the efficacy of CAR T-cell therapy. Some of the key factors in this endeavor are enhancing the efficiency of signal transduction from the membrane-bound CAR into the cell, which activates the transcriptional programs responsible for cytotoxicity, and ensuring the survival of activated cells, their proliferation, the secretion of cytokines and lytic granules, the metabolism, and other functions. This signal transduction is controlled by the intracellular domains (ICDs) of the CAR, and the optimization of their structure is the subject of this review.

Fig. 1. The mechanistic basis of CAR T-cell therapy. The interaction between a CAR T-cell and a tumor cell is enabled by the specific recognition of a tumor-associated antigen (TAA) by the chimeric receptor. This leads to the activation of the cytotoxic functions of the CAR T-cell, mediated by the release of lytic granules containing granzymes and perforin, as well as by the interaction between the Fas ligand (FASL) and Fas receptor (FAS). Consequently, apoptosis of the tumor cell is induced



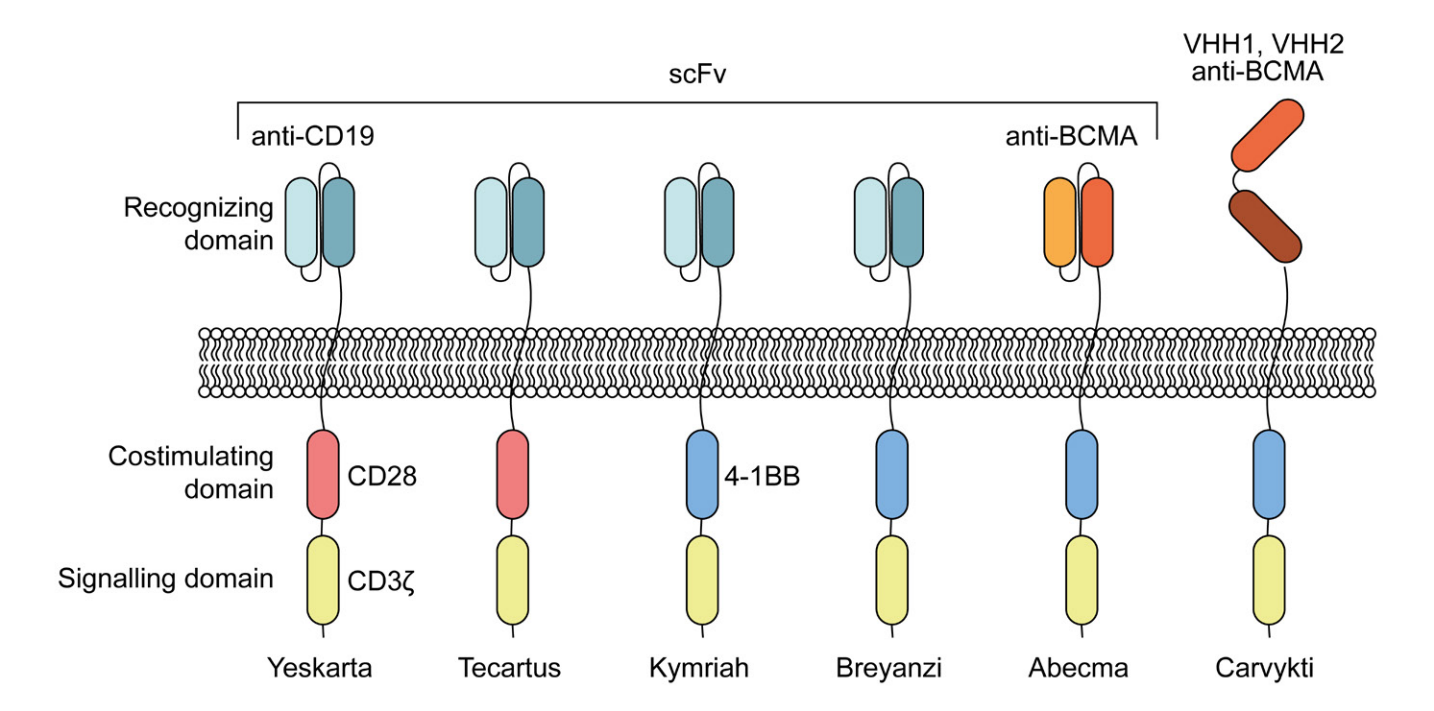


Fig. 2. Approved CAR T-cell preparations. Presented are the key domains that mediate recognition and signal transduction to intracellular partners. scFv – single-chain variable fragment; VHH – heavy chain variable domain (nanobody); CD – cluster of differentiation; BCMA – B-cell maturation antigen

#### **COSTIMULATION DOMAINS**

In clinically approved CAR T-cell preparations, the function of costimulatory domains is executed by the intracellular components of well-characterized costimulatory T-cell membrane molecules: CD28 and 4-1BB [5] (*Fig. 2*).

These membrane proteins are classified into two superfamilies: the immunoglobulin superfamily (IgSF) and the tumor necrosis factor receptor superfamily (TNFRSF). CARs incorporating other costimulatory domains from these same families, such as ICOS, OX40, CD27, and others, are currently at various stages of development (*Fig. 3*).

#### Immunoglobulin superfamily

Among receptors related to the IgSF, CD28 and ICOS serve as T-cell stimulators. This is attributed to a conserved YXXM motif (where X is any amino acid) which contains a tyrosine (Y) residue that undergoes phosphorylation during activation. This phosphorylation encourages interactions with intracellular signaling partners, including various kinases.

CD28. CD28 was the first costimulatory molecule used to generate modified T-cells containing second-generation CARs [6]. These cells demonstrated capability in effect duration and cytokine secretion compared to first-generation cells containing only the CD3ζ signaling domain [7]. CD28 signals are crucial for the activation of naïve T-cells (Tn), since they prevent anergy [8] and promote cytokine secretion, T-cell proliferation, and effector cell differentiation. CD28 is activated by interaction with several ligands, specifically CD80 (B7-1), CD86 (B7-2), and B7-H2 (ICOSL), the latter also an ICOS ligand. Functional motifs within the intracellular part of CD28, proximal (YMNM, PRRP) and distal (PYAP) (Fig. 3), bind kinases with SH2 and/or SH3 domains (YMNM - SHIP1, SLP76, GRAP, CBL, PI3K, GRB2, and GADS; PRRP - ITK; PYAP – PDK1, PKCθ, GRB2, STS1/2, CIN85, CD2AP, LCK, and FLNA). The binding of kinases to the costimulator causes conformational changes, their activation, and subsequent interactions with the downstream elements of signaling cascades. As a result, the transcription factors NFAT, AP-1, and NF-xB

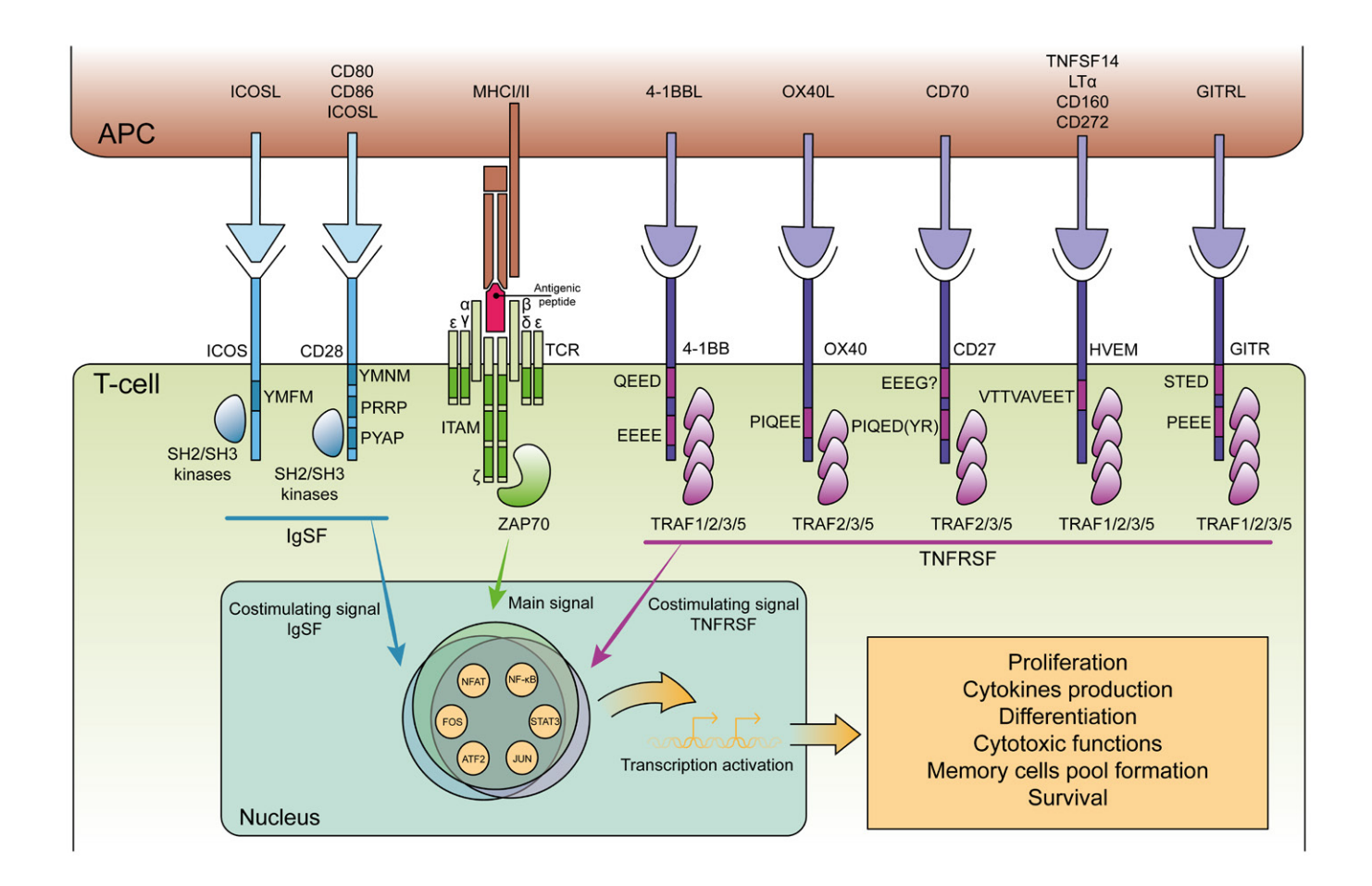


Fig. 3. Key superfamilies of T-cell costimulatory receptors. Presented is a general scheme of T-cell activation requiring both the primary and costimulatory signals, with the latter provided by TCR engagement with the major histocompatibility complex and by activating receptors from the IgSF and TNFRSF superfamilies binding their respective ligands. Amino acid sequences that are labeled in the receptors identify the primary signaling motifs. APC – an antigen-presenting cell; MHC I/II – major histocompatibility complex class I/II; IgSF – immunoglobulin superfamily; TNFRSF – tumor necrosis factor receptor superfamily; TNFSF – tumor necrosis factor superfamily; TCR – T-cell receptor;  $\alpha$ ,  $\beta$  – TCR recognition chains;  $\zeta$ ,  $\gamma$ ,  $\delta$ ,  $\epsilon$  – CD3 proteins of the TCR complex; ITAM – immunoreceptor tyrosine-based activation motif

are activated, and they are associated with interleukin-2 (IL-2) synthesis and the stimulation of Bcl-XL. Simultaneously, this stimulates T-cell metabolism, increasing aerobic glycolysis, nutrient supply, and anabolic processes [8–10].

The CAR construct utilizes ICD CD28, which, upon antigen binding to the chimeric receptor, leads to the activation of the PI3K/AKT pathway, enhancing aerobic glycolysis, which positively affects effector T-cells [11]. At the same time, high levels of glycolysis provoke cell exhaustion and reduce cell persistence [12]. To address these challenges, investigations into the consequences of CD28 functional motif mutations are underway. At the same time, mutations in each mo-

tif can have an impact on the characteristics of the resulting CAR T-cells. For example, in a pancreatic tumor xenograft model, substitution of the YMNM motif with YMFM in SS1 CAR T-cells targeting mesothelin and based on CD28 modulation decreased the level of CD28 interaction with GRB2. This resulted in reduced signaling through VAV1, diminished calcium current, and attenuated NFAT hyperactivation, thereby decreasing T-cell depletion and dysfunction while increasing T-cell persistence and antitumor efficacy [12]. The substitution of ARRA and YFNM for the PRRP and YMNM motifs in CD28, respectively, augments cellular secretion of interferon-gamma (IFN- $\gamma$ ) and tumor necrosis factor-alpha (TNF- $\alpha$ ), reduces

the levels of depletion-associated transcription factor Nur77, and enhances CD19 CAR T-cell cytotoxicity, thereby facilitating persistent inhibition of tumor development in mice [13]. Kofler et al. demonstrated that replacing the PYAPP segment in CD28 with AYAAA disrupts the interaction of the PYAP motif with LCK kinase. This disruption reduces IL-2 secretion and suppresses its dependent signaling while also weakening IL-2-dependent proliferation of intratumoral regulatory T-cells (Tregs), thereby enhancing the antitumor activity of such CAR T-cells against solid tumors with a high Treg infiltration level [14]. Furthermore, this CD28 modification enhances CAR T-cell proliferation, metabolism, activation, and cytotoxicity targeting the fibroblast activation protein (FAP). In combination with immune checkpoint inhibitors, these cells demonstrate efficacy in eliminating tumors and exhibit an ability to persist for a lengthy time in humanized xenograft mice and patients with malignant pleural mesothelioma, suggesting a potentially high safety profile [15]. Given that the CD28 ICD is frequently integrated into CARs, alongside the transmembrane domain, it is important to note that this enables CARs to form heterodimers with native CD28 [16], leading to sustained signaling and augmented effector functions in the associated CAR T-cells.

ICOS. This receptor is expressed at low levels in Tn cells before T-cell receptor (TCR) activation, with increased expression for several hours following activation [17]. The interaction between ICOS and its ligand, ICOSL, promotes T-cell viability through the stimulation of proliferation and differentiation via pathways analogous to CD28. The effects of these receptors on cytokine synthesis and secretion can vary. While CD28 stimulates IL-2 production, ICOS stimulates IL-10, which is more characteristic of Treg cells [18]. In addition to IL-10, ICOS also promotes the release of IFN- $\gamma$ , TNF- $\alpha$ , IL-5, IL-13, and IL-17, thereby enhancing the characteristics of effector T-cells and the development of naïve T helper cells (Th) into effector cells of the Th1, Th2, and Th17 subtypes [18, 19]. Analogous to CD28, ICOS induces Bcl-XL expression, leading to increased T-cell viability [20]. The functional tyrosine-containing ICOS YMFM motif (Fig. 3) interacts with the PI3K regulatory subunit p50 $\alpha$ , which induces a more significant PI3K activation when compared to CD28 [21]. Consequently, the stimulation of ICOS results in the phosphorylation of the AKT, PDK1, ERK1/2, and p38 MAPK kinases, along with the activation of the transcription factors NFAT and NF-αB, which distinguishes ICOS from CD28. The latter also involves JNK kinase in the signaling cascade, and it activates the transcription factor c-Jun [17].

Shen et al. were the first to demonstrate the functional activity of ICOS-based CAR T-cells in a mouse model of glioblastoma [22]. It has been suggested that it is the polarization of CD4+ CAR T-cells towards Th1 and Th17 due to the involvement of PI3K/AKT and p38 MAPK (and other mechanisms) that enhances their persistence [23], which increases the antitumor activity of CD8+ CAR T-cells as well [23]. Before administering CD4+ mesoCAR T-cells (targeting mesothelin) to animals, Wyatt et al. performed low-intensity stimulation of these cells using magnetic beads coated with antibodies against CD3 and ICOS (bead-to-cell ratio = 1:10), simultaneously achieving Th17 polarization using a cytokine cocktail. This treatment (compared to CD3 and CD28 stimulation) yielded less differentiated CD4+ CAR T-cells and shifted their metabolism towards oxidative phosphorylation, which is characteristic of memory T-cells (Tm). These findings emphasize the advantage of ICOS-directed stimulation of CD4+ mesoCAR T-cells. In mesothelioma mice, the combination of CD4+ Th17 mesoCAR T-cells and CD8+ mesoCAR T-cells [24] demonstrated more effective tumor elimination compared to standard activated CAR T-cells. These data underscore the differential involvement of costimulators contingent on the CD4+ or CD8+ status of CAR T-cells. Optimal costimulation can be achieved by modifying CD4+ and CD8+ T-cells with CAR genes with different costimulatory domains, a fact to be taken into account when the most effective CAR T-cell product is needed. Analysis of CAR T-cell costimulation by ICOS revealed that substituting YMFM with FMFM leads to a reduction in CAR T-cell costimulation through ICOS. Consequently, the CAR T-cells exhibit diminished secretion levels of the cytokines in question [25]. To date, modifications to the ICD ICOS that would improve its efficacy have not been documented.

#### Tumor necrosis factor receptor superfamily

This expansive superfamily comprises approximately 30 receptors, classified into three primary groups: (1) tumor necrosis factor receptor-associated factor (TRAF) receptors, (2) death receptors, and (3) molecules with or without a non-functional ICD [26]. To date, only intracellular components from group (1) receptors have been used in the CAR structure, including 4-1BB, OX40, CD27, HVEM, and TNFRSF18. The conserved receptor motifs of this group encompass TRAF-binding (P/A/S/T)X(E/Q)E and PXQQXXD, with X representing any amino acid (AA) [27].

4-1BB. 4-1BB is frequently integrated into CARs during the process of CAR T-cell preparation. Four of the six approved CAR T-cell products have a CAR con-

taining the 4-1BB domain [2]. This is not coincidental, as 4-1BB is a key marker of T-cell activation. Its interaction with the 4-1BBL ligand and recruitment of various TRAF proteins initiates the p38 MAPK, AKT, and ERK signaling pathways. Consequently, transcription is activated from NF-xB-dependent promoters, increasing survivin, Bcl-XL, Bfl-1, and Bcl-2 production while reducing Bim levels [28, 29]. Moreover, 4-1BB signaling elevates the mitochondrial count and transmembrane potential, consequently improving aerobic processes in T-cells and augmenting their effector functions [30]. The 4-1BB TRAF-binding motifs, QEED and EEEE (Fig. 3), are involved in the interaction with TRAF1, TRAF2, TRAF3, and TRAF5 [31].

Incorporating 4-1BB into the CAR design improves the CAR T-cell ability to stay active, resulting in a phenotype closely aligned with central memory T-cells (Tcm). They exhibit low surface expression of PD-1, which is one of the most characteristic markers of T-cell exhaustion [32, 33]. This phenomenon can be partly accounted for by the metabolic shift towards enhanced mitochondrial processes and increased mitochondrial biogenesis induced by 4-1BB costimulation. Additionally, cells with CARs containing 4-1BB show elevated antiapoptotic gene expression and diminished pro-apoptotic factors. However, the activation of CAR T-cells is less pronounced with 4-1BB costimulation relative to CD28 [34]. This is explained by the recruitment of the THEMIS-SHP1 phosphatase tandem, which forms a complex with 4-1BB via a 10-AA motif at its C-terminus. Consequently, the resulting complex inhibits the phosphorylation of the CAR signaling domain: CD3ζ. Mutations in the QEED and EEEE motifs reduce cytokine secretion, the proportion of Tcm cells, and the antitumor activity of CAR T-cells [25, 35]. However, the incorporation of 4-1BB into CARs has been reported to lead to increased aggregation of CAR T-cells, which reduces their viability [36]. It is worth mentioning that deletion of the above-mentioned 10 AAs from the C-terminus of 4-1BB in this case prevents aggregation and restores the function of CAR T-cells. Furthermore, 4-1BB has been observed to elicit tonic signaling, resulting in CAR T-cell apoptosis [37]. Reducing the expression level of such CARs can enable the CAR T-cell activity to return to normal.

OX40. The OX40, a costimulatory receptor, is expressed on the surface of naïve T-cells (Tn) following their activation. The binding of OX40 to its ligand OX40L promotes the recruitment of TRAF2, 3, and 5 through the PIQEE motif (Fig. 3) [38, 39]. TRAF2, 3, and 5 adaptors induce the NF-κB signaling pathway,

which promotes the synthesis of the antiapoptotic factors Bcl-XL and Bfl-1 in cells [40]. Also activated are the PI3K/AKT kinases involved in the synthesis of survivin and Aurora B kinase, inhibiting apoptosis and promoting T-cell proliferation [41, 42].

OX40 costimulation enhances the durability of second-generation CAR T-cells when compared to cells where CD28 and 4-1BB mediate costimulation in CAR constructs. However, the in vivo antitumor activity of CAR T-cells is largely unaffected by the CAR costimulatory domain. CAR T-cells with OX40-mediated costimulation exhibit enhanced target cell elimination in vitro [43]. Transcriptomic analysis of such CAR T-cells revealed upregulated expression of the genes responsible for DNA repair, oxidative phosphorylation, apoptosis inhibition, and memory differentiation and proliferation. According to existing data, the "specialization" of OX40 and 4-1BB implies that 4-1BB mainly enhances the development of CD8+ memory T-cells (Tm), while OX40 is biased towards CD4+ Tm cells [39]. Given that ICOS supports the differentiation of CD4+ T-cells into Th1, Th2, and Th17 effectors, the most effective costimulatory strategy for CD4+ CAR T-cells is likely to involve both ICOS and OX40. At the same time, the combination of CD28 and 4-1BB might be more suitable for the costimulation of CD8+ CAR T-cells.

CD27. CD27 is known to interact with the CD70 ligand, thereby facilitating T-cell proliferation and differentiation through the activation of the NF-xB, PI3K/AKT, and SAPK/JNK signaling pathways [44, 45]. Given that ICOS supports the differentiation of CD4+ T-cells into Th1, Th2, and Th17 effectors, the most effective costimulatory strategy for CD4+ CAR T-cells likely involves both ICOS and OX40. Thus, CD27 promotes the proliferation and viability of effector T-cells, as well as the generation of a Tm cell pool throughout the primary activation of Tn cells, during clonal expansion and at the effector stage (for example, in tumors). CD27 uses the functional motif PIQED(YR) and, possibly, EEEG (Fig. 3) to interact with TRAF2, TRAF3, and TRAF5 [45, 49]. A distinctive characteristic of CD27 compared to other TNFRSF family members is the formation of homodimers through disulfide bonds [49]. It is in this form that CD27 is present on the surface of resting T-cells, while their prolonged activation increases the proportion of the monomeric form, which probably protects T-cells from turning on costimulators during spontaneous activation.

Studies on the costimulatory potential of CD27 have shown that CD27 CAR T-cells can eradicate tumors more effectively than first-generation CAR  $^{\circ}$ 

T-cells, similar to CAR T-cells with CD28 or the 4-1BB costimulatory domain. The duration of CAR T-cell persistence, when costimulated with CD27, was found to be equivalent to that observed with 4-1BB costimulation [50, 51]. However, a direct comparison of the ability of second-generation CAR T-cells with either 4-1BB or CD27 to eliminate solid tumors in mice revealed superior antitumor activity for CD27 CAR T-cells [52]. The most effective configuration was determined to be a combination of three costimulatory domains, CD28, 4-1BB, and CD27, within the CAR. The enhanced proliferation, increased resistance to CAR loss, and reduced exhaustion were observed when compared to costimulation with one or two domains [53, 54].

HVEM. The Herpes Virus Entry Mediator, or HVEM, was first discovered as a receptor for herpes simplex virus-1 [55]. HVEM, an atypical member of its superfamily, exhibits binding capabilities to TNFSF molecules, specifically TNFSF14 and lymphotoxin-α, and to the immunoglobulin-like molecules CD272 and CD160 [56]. HVEM costimulates T-cells via trans-interaction, while cis-interaction inhibits costimulation by forming an isolated complex of HVEM with CD272 or CD160 [57]. Once activated, HVEM interacts with TRAF1, 2, 3, and 5, which triggers signaling via the NF-xB, JNK/AP-1, and PI3K/AKT pathways, thus resulting in heightened synthesis of cytokines and Bcl-2 [58, 59]. Consequently, effector properties, proliferation, and the viability of T-cells are enhanced. It is hypothesized that TRAF molecules interact with HVEM via the VTTVAVEET motif (Fig. 3), which partially aligns with the conserved motif (P/A/S/T/T)X(E/Q)E [58].

It is relatively recently that the potential of HVEMdependent costimulation of CAR T-cells has been evaluated [60, 61]. HVEM has been shown to combine the receptor properties of the IgSF and TNFRSF superfamilies. For instance, while CD28 facilitates the preferential differentiation of modified cells into effector memory T-cells (Tem), and 4-1BB into Tcm cells, HVEM leads to the development of a balanced population with almost identical proportions of both Tcm and Tem cells. Moreover, costimulation through CD28 primarily activates glycolytic metabolism, while 4-1BB activates oxidative phosphorylation. In contrast, HVEM enhances both metabolic pathways, establishing the most effective functional state of CAR T-cells. HVEM costimulation involvement, in comparison to CD28 and 4-1BB, likewise contributes to the minimal depletion of CAR T-cells. The greatest efficacy in solid tumors was achieved in mice treated with CAR T-cells expressing HVEM [61]. Additionally, the concurrent generation of CAR and the HVEM ligand TNFSF14 was found to enhance CAR T-cell infiltration into tumors because of significant chemokine secretion [62].

TNFRSF18. TNFRSF18, also known as GITR (glucocorticoid-induced TNFR-related protein), is constitutively expressed at low levels on the membrane of quiescent T-cells. Upon activation, the level of GITR on the T-cell surface increases significantly. GITR levels are found to be higher in Treg cells than in conventional T-cells, even without stimulation [63]. The interaction of GITR with its ligand GITRL weakens the immunosuppressive actions of Treg cells, and in effector T-cells, it boosts proliferation, cytokine release, and it has an antiapoptotic impact [64, 65]. Intracellular signaling from GITR involves interaction with TRAF1, 2, 3, 5 through the STED and PEEE motifs (Fig. 3) [66]. Stimulation of T-cells with antibodies targeting CD3, CD28, and GITR has been demonstrated to trigger both parallel responses, facilitating signaling synergism during costimulation, and unique effects, such as enhanced IL-27 production following GITR stimulation [67]. Costimulation via GITR primarily involves the NF-xB and MAPK signaling pathways [63].

In terms of tumor-killing efficacy, CAR T-cells costimulated via GITR are comparable to those based on CD28 and 4-1BB [68, 69]. Moreover, increased GITRL production by CAR T-cells improves cytokine secretion, tumor infiltration, and antitumor effects [70].

Some studies have focused on adding new costimulatory receptor parts from TNFRSF members, like BAFF-R, CD30, and CD40, into CARs [35, 71, 72]. CD40-mediated costimulation has been demonstrated to elicit a more robust NF- $\varkappa$ B pathway activation compared to 4-1BB costimulation, potentially promoting enhanced *in vivo* persistence of CD40 CAR T-cells.

#### Other costimulatory domains

The focus on studying signaling pathways in diverse immune cells, such as natural killer cells and macrophages, has raised interest in costimulatory molecules that are not part of the immunoglobulin or TNF receptor superfamilies. Promising signaling molecules include Dap10 [73] and dectin-1 [74]. Contemporary genetic and cellular engineering methods seek to streamline the creation of CAR libraries featuring diverse combinations of costimulatory receptors or their components [71, 75]. Through the integration of high-throughput sequencing, a more detailed evaluation of the effects of diverse costimulators can be achieved, expanding beyond the extensively studied

members of the IgSF and TNFRSF families, including the selection of specific combinations of costimulators for CD4+ or CD8+ T-cell populations.

#### THE CD3°C SIGNALING DOMAIN AND ITS ANALOGS

In the initial stages of development, the CD3ξ intracellular domain was the sole signaling domain incorporated into the CAR structure [76, 77]. This was due to the concept of the receptor itself, which was based on the combination of B- and T-cell receptors to target antigen recognition and subsequent T-cell activation. Early research, for example, revealed that ICD CD3ξ is appropriate for T-cell activation, thus laying the groundwork for CAR development [78]. CD3ξ became firmly "entrenched" in the receptor structure and "migrated" from generation to generation, providing the primary activation signal for CAR T-cells [79]. The inclusion of CD3ξ in all the CAR T-cell drugs approved so far for clinical application (Fig. 1) underscores the significance of this domain for developers, and, until recently, the lack of alternative options [5].

#### Other CD3 group proteins

Over time, interest in this part of CAR has increased significantly. In 2018, Sadelain et al. demonstrated that for full functionality of the CAR, only one active immunoreceptor tyrosine-based activation motif (ITAM) out of the three in CD3 $\xi$  is sufficient [80]. Its location and amino acid composition are both significant factors. The 1XX variant, with 1 indicating the position of the active ITAM relative to the cell membrane and X indicating an inactive ITAM, demonstrated the highest functionality in tumor elimination, whereas XX3 provided moderate support for CAR T-cell persistence. These data highlighted the necessity of reconsidering the role of the seemingly indispensable CD3 $\xi$ .

As a result, investigations were performed on possible analogs of CD3 $\xi$ ; namely, other CD3 group representatives:  $\epsilon$ ,  $\delta$ , and  $\gamma$  [81, 82]. In contrast to CD3 $\xi$ , the molecules within ICDs feature a single ITAM [83]. Although all ITAMs share the conserved YXXL/I-X6-8-YXXL/I sequence (X denotes any amino acid), the unique amino acid composition of each ITAM influences the binding affinity of signaling molecules (*Fig.* 4) [84].

In total, the TKR-CD3 multisubunit complex contains 10 ITAMs. Signal amplification likely results from a high concentration of tyrosine motifs, as a reduced number impairs TKR-CD3 complex function in mice [85]. Additionally, the variation between CD3 and the ITAMs within it is vital for signal transduction and the development of mature T-cells [86].

Beyond the unique amino acid sequences found in ITAM, the intracellular domains of each CD3 subunit exhibit distinctive characteristics (Fig. 4). The CD3ξ and CD3ɛ proteins feature segments rich in positively charged amino acids (basic-rich stretches), enabling their interaction with the inner membrane surface [87, 88]. The interaction of CD3s with LCK kinase is mediated by ionic bonds between the BRS and acidic residues in the unique domain of LCK, and also through a receptor kinase motif (RK) and the SH3 domain of LCK [89, 90]. CD3£ also possesses a prolinerich sequence (PRS) that interacts with the adaptor protein NCK and is crucial for IC maturation and T-cell activation [91]. A proximal serine-dependent dileucine (SDKQTLL) motif within CD3y participates in the decreasing of the number of TCRs on the cell membrane via a protein kinase C (PKC)-dependent mechanism [92]. In addition to ITAM, CD3δ contains a similar motif (ADTQALL), which lacks the serine needed for PKC interaction. Therefore, CD3 $\delta$  is considered less significant in regulating the number of TKRs on the membrane than CD3γ [93].

Distinctive motifs within the structure of each representative CD3 protein are critical in the context of CARs, notwithstanding the fact that each CD3 variant alone may be sufficient for constructing a functional CAR structure. This fact has been illustrated by including CD3 $\epsilon$ ,  $\delta$ , or  $\gamma$  into the CAR structure as a signaling domain instead of CD3 $\xi$  [81, 82]. In vivo, CD3δ, CD3ε, or CD3γ CAR T-cells demonstrated superior tumor elimination efficacy compared to CD3ζ, this attributed to the distinct properties of specific CD3 group members. Thus, the binding of ICD CD3ε to CSK kinase suppresses LCK kinase activation, reducing the depletion of CAR T-cells and enabling their sustained presence. The binding of SHP-1 phosphatase to CD3δ monophosphorylated by a second tyrosine ICD results in a reduction in cytokine signaling and secretion intensity, presumably by mitigating the activation of the NF-xB pathway. The transcriptome analysis data demonstrated the Tm cell phenotype to be characterized by a reduction in glycolytic gene expression and an increase in mitochondrial metabolism gene expression. Additionally, TCF-1, known to be related to memory stem T-cells, is expressed at high levels in CD3δ [94]. Similar to Tn-cells, these cells can self-replicate most effectively and can transform into all kinds of memory cells [95]. Due to its greater proportion of positively charged CARs compared to acidic ones, CD3E may bind more tightly to membrane phospholipids than CD3\(\xi\) does, which would decrease the availability of CARs to intracellular signaling partners, as has been noted with TKR and other proteins [88, 96]. As a

### Intracellular parts of CD3 proteins:



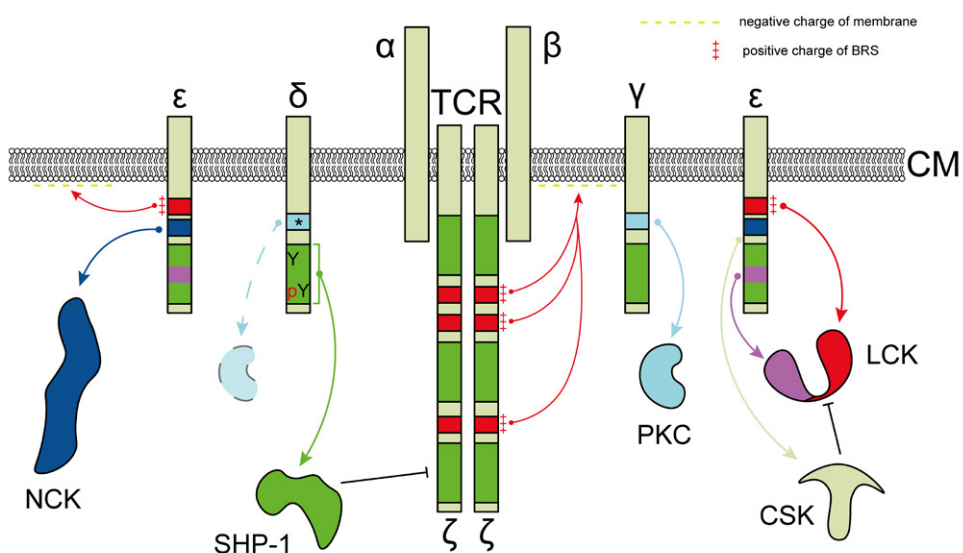


Fig. 4. Structure and functional features of CD3 group proteins. Shown is the arrangement of intracellular CD3 $\epsilon$ ,  $\delta$ ,  $\zeta$ , and  $\gamma$  domains, each possessing specific motifs for interacting with intracellular signaling partners.  $\xi$ ,  $\gamma$ ,  $\delta$ , and  $\varepsilon$  – the representative members of the CD3 T-cell receptor family; ITAM - an immunoreceptor tyrosine-activating motif; BRS - a basic amino acid-rich site: PRS – a proline-rich site: RK – a receptor kinase motif; LL - a serine-dependent dileucine motif (\* indicates the absence of serine upstream of LL, which reduces the involvement of LL in T-cell receptor regulation); TCR – a T-cell receptor;  $\alpha$ ,  $\beta$  – recognizing chains of the T-cell receptor; CM - cell membrane; Y - tyrosine; and pY - phosphorylated tyrosine

result, the probability of both nonspecific and tonic signaling decreases. Incorporating a dimerizing CD8 $\alpha$  hinge domain within the CAR structure revealed that dimeric CD3 $\delta$  and CD3 $\gamma$  amplified cytokine release from CAR T-cells and elevated the surface expression of CD69 and 4-1BB, with the strongest effect observed upon mutation of the dileucine motifs (SDKQTAL and ADTQAAL) [81].

#### TCR signaling partners

A novel CAR format – designated bypassCARs (bCARs) – has been developed by investigating the distinct components of signaling cascades during TCR activation. Segments of the intracellular signaling molecules associated with T-cell receptors were incorporated into the bCAR structure, instead of ITAM-containing domains. The first bCAR-like chimeric molecules were developed at the end of the previous century to determine the key kinases essential for T-cell activation [97]. The structure of

these receptors involved CD16. in combination with LCK, FYN, SYK, or ZAP70. Only within the SYK domain did modified cells exhibit the ability to lyse target cells in response to stimulation. Replacing CD16 with an scFv specific to a target antigen preserved the unique ability of SYK to activate the bCAR T-cell, bypassing the TCR [98].

Next, antitumor bCARs were constructed, which included CSK, FYN, the kinase domain of ZAP70 (ZAP70KD), LAT, SLP76, or PLCγ1, but lacked costimulatory domains [99]. While both ZAP70KD-and PLCγ1-based bCARs activated modified T-cells, the PLCγ1 bCAR showed much weaker expression. ZAP70KD bCAR T-cells proved more efficient at removing solid tumors than CD3ξ CAR T-cells with a 4-1BB costimulatory domain *in vivo*. The ZAP70KD-based bCAR activated T-cells with knocked-out TCR and LCK, but not in the absence of SLP76 or LAT, confirming the preservation of the TCR downstream signaling pathway structure.

The recently developed second-generation bCARs incorporate an adapter domain from LAT or SLP76, which is comparable to the costimulatory domains found in traditional CARs. However, T-cells modified with such constructs exhibited excessively high levels of tonic signaling [100]. In particular, incorporating a CD28 signaling domain upstream of the ZAP70 kinase domain resulted in prolonged remission of B-cell tumors in mice treated with these bCAR T-cells, as opposed to conventional second-generation CAR T-cells with CD3 $\xi$  and a CD28 costimulatory domain.

#### **CONCLUSION**

The investigation of CAR costimulatory and signaling domain combinations is a rapidly evolving field within CAR T-cell research, aiming to broaden the therapeutic application of these cells. The diversity across these domains opens a broad range of possibilities in the design of advanced CAR T-cells with enhanced functional attributes.

The analysis of the collected data suggests that selecting specific costimulatory domains has a significant impact on CAR T-cell activation, cytotoxicity, metabolic activity, *in vivo* persistence, and resistance to functional exhaustion. Consequently, the combination of various domains or the establishment of modular structures may potentially circumvent the critical limitations of existing methodologies in generating therapeutic CAR T-cell products and their applica-

tions, including tumor antigen heterogeneity, the immunosuppressive microenvironment, and the toxicity associated with adoptive transfer.

Furthermore, it is imperative to reduce the size of the CAR while maintaining its functionality and to identify a structure of minimal receptor activity, which should enhance the success of the modification and support increased and stable CAR receptor production by T-cells. Similar investigations are concurrently in progress [101].

Further optimization of CAR T-cell signaling domains requires a deeper understanding of T-lymphocyte activation mechanisms, along with the use of advanced technologies such as CRISPR screening, transcriptomics, proteomics, and computational modeling [75, 102–105]. This will enable the creation of personalized cellular products precisely tailored to the biology of a specific tumor type. Alongside improvements in receptor generation and the development of modular systems [106–108], research in this area could lead to groundbreaking therapeutic solutions, expanding the applications of CAR T-cell technology and enhancing its effectiveness in treating both cancer and, potentially, autoimmune and infectious diseases. •

This work was supported by the Ministry of Science and Higher Education of the Russian Federation (Agreement No. 075-15-2024-536).

#### REFERENCES

- 1. Yazbeck V, Alesi E, Myers J, et al. An overview of chemotoxicity and radiation toxicity in cancer therapy. *Advances in Cancer Research*. Elsevier; 2022:1–27.
- 2. Cappell KM, Kochenderfer JN. Long-term outcomes following CAR T cell therapy: what we know so far. *Nat Rev Clin Oncol*. 2023;20(6):359–371. doi: 10.1038/s41571-023-00754-1
- 3. Li Q, Lei X, Zhu J, et al. Radiotherapy/chemotherapy-immunotherapy for cancer management: From mechanisms to clinical implications. *Oxid Med Cell Longev*. 2023;2023;7530794. doi: 10.1155/2023/7530794
- 4. McLellan AD, Ali Hosseini Rad SM. Chimeric antigen receptor T cell persistence and memory cell forma-

- tion.  $Immunol\ Cell\ Biol.\ 2019;97(7):664-674.\ doi:\ 10.1111/imcb.12254$
- 5. Mitra A, Barua A, Huang L, et al. From bench to bedside: the history and progress of CAR T cell therapy. *Front Immunol.* 2023;14:1188049. doi: 10.3389/fimmu.2023.1188049
- Finney HM, Lawson ADG, Bebbington CR, Weir ANC. Chimeric receptors providing both primary and costimulatory signaling in T cells from a single gene product. J Immunol. 1998;161(6):2791–2797. doi: 10.4049/jimmunol.161.6.2791
- Krause A, Guo HF, Latouche JB, et al. Antigen-dependent CD28 signaling selectively enhances survival and proliferation in genetically modified activated human

- primary T lymphocytes. J Exp Med. 1998;188(4):619–626. doi: 10.1084/jem.188.4.619
- 8. Esensten JH, Helou YA, Chopra G, et al. CD28 costimulation: From mechanism to therapy. *Immunity*. 2016;44(5):973–988. doi: 10.1016/j.immuni.2016.04.020
- 9. Honikel MM, Olejniczak SH. Co-stimulatory receptor signaling in CAR-T cells. *Biomolecules*. 2022;12(9):1303. doi: 10.3390/biom12091303
- 10. Kunkl M, Sambucci M, Ruggieri S, et al. CD28 autonomous signaling up-regulates C-myc expression and promotes glycolysis enabling inflammatory T cell responses in multiple sclerosis. *Cells*. 2019;8(6):575. doi: 10.3390/cells8060575
- 11. Kawalekar OU, O'Connor RS, Fraietta JA, et al. Distinct signaling of coreceptors regulates specific metabolism pathways and impacts memory development in CAR T cells. *Immunity*. 2016;44(2):380–390. doi: 10.1016/j.immuni.2016.01.021
- 12. Guedan S, Madar A, Casado-Medrano V, et al. Single residue in CD28-costimulated CAR-T cells limits long-term persistence and antitumor durability. *J Clin Invest.* 2020;130(6):3087–3097. doi: 10.1172/JCI133215
- 13. Boucher JC, Li G, Kotani H, et al. CD28 costimulatory domain-targeted mutations enhance chimeric antigen receptor T-cell function. *Cancer Immunol Res.* 2021;9(1):62–74. doi: 10.1158/2326-6066.CIR-20-0253
- 14. Kofler DM, Chmielewski M, Rappl G, et al. CD28 costimulation Impairs the efficacy of a redirected t-cell antitumor attack in the presence of regulatory t cells which can be overcome by preventing Lck activation. *Mol Ther.* 2011;19(4):760–767. doi: 10.1038/mt.2011.9
- 15. Gulati P, Rühl J, Kannan A, et al. Aberrant lck signal via CD28 costimulation augments antigen-specific functionality and tumor control by redirected T cells with PD-1 blockade in humanized mice. *Clin Cancer Res.* 2018;24(16):3981-3993, doi: 10.1158/1078-0432.ccr-17-1788
- 16. Ferreira LMR, Muller YD. CAR T-cell therapy: Is CD28-CAR heterodimerization its Achilles' heel? Front Immunol. 2021;12:766220. doi: 10.3389/fimmu.2021.766220
- 17. Yoshinaga SK, Whoriskey JS, Khare SD, et al. T-cell co-stimulation through B7RP-1 and ICOS. *Nature*. 1999;402(6763):827–832. doi: 10.1038/45582
- 18. van Berkel MEAT, Oosterwegel MA. CD28 and ICOS: similar or separate costimulators of T cells? *Immunol Lett.* 2006;105(2):115–122. doi: 10.1016/j.imlet.2006.02.007
- 19. Paulos CM, Carpenito C, Plesa G, et al. The inducible costimulator (ICOS) is critical for the development of human TH17 cells. *Sci Transl Med.* 2010;2(55):55ra78-55ra78. doi: 10.1126/scitranslmed.3000448
- 20. Parry RV, Rumbley CA, Vandenberghe LH, et al. CD28 and inducible costimulatory protein Src homology 2 binding domains show distinct regulation of phosphatidy-linositol 3-kinase, Bcl-xL, and IL-2 expression in primary human CD4 T lymphocytes. *J Immunol.* 2003;171(1):166–174. doi: 10.4049/jimmunol.171.1.166
- 21. Fos C, Salles A, Lang V, et al. ICOS ligation recruits the p50alpha PI3K regulatory subunit to the immunological synapse. *J Immunol.* 2008;181(3):1969-1977. doi: 10.4049/jimmunol.181.3.1969
- 22. Shen C-J, Yang Y-X, Han EQ, et al. Chimeric antigen receptor containing ICOS signaling domain mediates specific and efficient antitumor effect of T cells against EG-FRvIII expressing glioma. *J Hematol Oncol.* 2013;6(1):33. doi: 10.1186/1756-8722-6-33
- 23. Guedan S, Chen X, Madar A, et al. ICOS-based

- chimeric antigen receptors program bipolar TH17/ TH1 cells.  $Blood.\ 2014;124(7):1070-1080.\ doi:\ 10.1182/\ blood-2013-10-535245$
- 24. Wyatt MM, Huff LW, Nelson MH, et al. Augmenting TCR signal strength and ICOS costimulation results in metabolically fit and therapeutically potent human CAR Th17 cells. *Mol Ther.* 2023;31(7):2120–2131. doi: 10.1016/j. ymthe.2023.04.010
- 25. Fujiwara K, Kitaura M, Tsunei A, et al. Structure of the signal transduction domain in second-generation CAR regulates the input efficiency of CAR signals. *Int J Mol Sci.* 2021;22(5):2476. doi: 10.3390/ijms22052476
- 26. Vanamee ÉS, Faustman DL. Structural principles of tumor necrosis factor superfamily signaling. *Sci Signal*. 2018;11(511):eaao4910. doi: 10.1126/scisignal.aao4910
- 27. Ye H, Park YC, Kreishman M, et al. The structural basis for the recognition of diverse receptor sequences by TRAF2. *Mol Cell*. 1999;4(3):321–330. doi: 10.1016/s1097-2765(00)80334-2
- 28. Ward-Kavanagh LK, Lin WW, Šedý JR, Ware CF. The TNF receptor superfamily in co-stimulating and co-inhibitory responses. *Immunity*. 2016;44(5):1005–1019. doi: 10.1016/j.immuni.2016.04.019
- 29. Craxton A, Draves KE, Gruppi A, Clark EA. BAFF regulates B cell survival by downregulating the BH3-only family member Bim via the ERK pathway. *J Exp Med.* 2005;202(10):1363–1374. doi: 10.1084/jem.20051283
- 30. Teijeira A, Labiano S, Garasa S, et al. Mitochondrial morphological and functional reprogramming following CD137 (4-1BB) costimulation. *Cancer Immunol Res.* 2018;6(7):798–811. doi: 10.1158/2326-6066.cir-17-0767
- 31. Glez-Vaz J, Azpilikueta A, Ochoa MC, et al. CD137 (4-1BB) requires physically associated cIAPs for signal transduction and antitumor effects. *Sci Adv*. 2023;9(33):eadf6692. doi: 10.1126/sciadv.adf6692
- 32. Cappell KM, Kochenderfer JN. A comparison of chimeric antigen receptors containing CD28 versus 4-1BB costimulatory domains. *Nat Rev Clin Oncol.* 2021;18(11):715–727. doi: 10.1038/s41571-021-00530-z
- 33. Boroughs AC, Larson RC, Marjanovic ND, et al. A distinct transcriptional program in human CAR T cells bearing the 4-1BB signaling domain revealed by scR-NA-seq. *Mol Ther.* 2020;28(12):2577–2592. doi: 10.1016/j. vmthe.2020.07.023
- 34. Sun C, Shou P, Du H, et al. THEMIS-SHP1 recruitment by 4-1BB tunes LCK-mediated priming of chimeric antigen receptor-redirected T cells. *Cancer Cell*. 2020;37(2):216–225.e6. doi: 10.1016/j.ccell.2019.12.014
- 35. Mamonkin M, Mukherjee M, Srinivasan M, et al. Reversible transgene expression reduces fratricide and permits 4-1BB costimulation of CAR T cells directed to T-cell malignancies. *Cancer Immunol Res.* 2018;6(1):47–58. doi: 10.1158/2326-6066.CIR-17-0126
- 36. Dou Z, Bonacci TR, Shou P, et al. 4-1BB-encoding CAR causes cell death via sequestration of the ubiquitin-modifying enzyme A20. *Cell Mol Immunol.* 2024;21(8):905–917. doi: 10.1038/s41423-024-01198-y
- 37. Gomes-Silva D, Mukherjee M, Srinivasan M, et al. Tonic 4-1BB costimulation in chimeric antigen receptors impedes T cell survival and is vector-dependent. *Cell Rep.* 2017;21(1):17–26. doi: 10.1016/j.celrep.2017.09.015
- 38. Willoughby J, Griffiths J, Tews I, Cragg MS. OX40: Structure and function - What questions remain? *Mol Immunol*. 2017;83:13–22. doi: 10.1016/j.molimm.2017.01.006 39. Croft M. Costimulation of T cells by OX40, 4-1BB, and

- CD27. Cytokine Growth Factor Rev. 2003;14(3-4):265–273. doi: 10.1016/s1359-6101(03)00025-x
- 40. Kawamata S, Hori T, Imura A, et al. Activation of OX40 signal transduction pathways leads to tumor necrosis factor receptor-associated factor (TRAF) 2- and TRAF5-mediated NF-κB activation. J Biol Chem. 1998;273(10):5808–5814. doi: 10.1074/jbc.273.10.5808
- 41. Croft M. Control of immunity by the TNFR-related molecule OX40 (CD134). *Annu Rev Immunol.* 2010;28(1):57–78. doi: 10.1146/annurev-immunol-030409-101243
- 42. Song J, So T, Croft M. Activation of NF-kappaB1 by OX40 contributes to antigen-driven T cell expansion and survival. *J Immunol*. 2008;180(11):7240–7248. doi: 10.4049/jimmunol.180.11.7240
- 43. Tan J, Jia Y, Zhou M, et al. Chimeric antigen receptors containing the OX40 signalling domain enhance the persistence of T cells even under repeated stimulation with multiple myeloma target cells. *J Hematol Oncol*. 2022;15(1):39. doi: 10.1186/s13045-022-01244-0
- 44. Starzer AM, Berghoff AS. New emerging targets in cancer immunotherapy: CD27 (TNFRSF7). ESMO Open. 2020;4(Suppl 3):e000629. doi: 10.1136/esmoopen-2019-000629
- 45. Akiba H, Nakano H, Nishinaka S, et al. CD27, a member of the tumor necrosis factor receptor superfamily, activates NF-kappaB and stress-activated protein kinase/c-Jun N-terminal kinase via TRAF2, TRAF5, and NF-kappaB-inducing kinase. *J Biol Chem.* 1998;273(21):13353–13358. doi: 10.1074/jbc.273.21.13353
- 46. Dolfi DV, Boesteanu AC, Petrovas C, et al. Late signals from CD27 prevent Fas-dependent apoptosis of primary CD8+ T cells. *J Immunol.* 2008;180(5):2912–2921. doi: 10.4049/jimmunol.180.5.2912
- 47. van de Ven K, Borst J. Targeting the T-cell co-stimulatory CD27/CD70 pathway in cancer immunotherapy: rationale and potential. *Immunotherapy*. 2015;7(6):655–667. doi: 10.2217/imt.15.32
- 48. Peperzak V, Veraar EAM, Keller AM, et al. The Pim kinase pathway contributes to survival signaling in primed CD8+ T cells upon CD27 costimulation. *J Immunol.* 2010;185(11):6670–6678. doi: 10.4049/jimmunol.1000159
- 49. Yamamoto H, Kishimoto T, Minamoto S. NF-κB activation in CD27 signaling: Involvement of TNF receptor-associated factors in its signaling and identification of functional region of CD27. *J Immunol*. 1998;161(9):4753–4759. doi: 10.4049/jimmunol.161.9.4753
- 50. Song D-G, Ye Q, Poussin M, et al. CD27 costimulation augments the survival and antitumor activity of redirected human T cells *in vivo*. *Blood*. 2012;119(3):696–706. doi: 10.1182/blood-2011-03-344275
- Song D-G, Powell DJ. Pro-survival signaling via CD27 costimulation drives effective CAR T-cell therapy. Oncoimmunology. 2012;1(4):547–549. doi: 10.4161/onci.19458
- 52. Han Y, Xie W, Song D-G, Powell DJ, Jr. Control of triple-negative breast cancer using ex vivo self-enriched, costimulated NKG2D CAR T cells. *J Hematol Oncol*. 2018;11(1):92. doi: 10.1186/s13045-018-0635-z
- 53. Zhang C, Jia J, Heng G, et al. CD27 agonism coordinates with CD28 and 4-1BB signal to augment the efficacy of CAR-T cells in colorectal tumor. *Med Oncol.* 2023;40(4):123. doi: 10.1007/s12032-023-01959-1
- 54. Supimon K, Sangsuwannukul T, Sujjitjoon J, et al. Anti-mucin 1 chimeric antigen receptor T cells for adoptive T cell therapy of cholangiocarcinoma. *Sci Rep.* 2021;11(1):6276. doi: 10.1038/s41598-021-85747-9

- 55. Montgomery RI, Warner MS, Lum BJ, Spear PG. Herpes simplex virus-1 entry into cells mediated by a novel member of the TNF/NGF receptor family. *Cell*. 1996;87(3):427–436. doi: 10.1016/s0092-8674(00)81363-x
- 56. Šedý JR, Ramezani-Rad P. HVEM network signaling in cancer. Advances in Cancer Research. 2019;142:145–186. doi:10.1016/bs.acr.2019.01.004
- 57. Steinberg MW, Cheung TC, Ware CF. The signaling networks of the herpesvirus entry mediator (TNFRSF14) in immune regulation. *Immunol Rev.* 2011;244(1):169-187. doi: 10.1111/j.1600-065X.2011.01064.x
- 58. Hsu H, Solovyev I, Colombero A, et al. ATAR, a novel tumor necrosis factor receptor family member, signals through TRAF2 and TRAF5. *J Biol Chem.* 1997;272(21):13471–13474. doi: 10.1074/jbc.272.21.13471
- 59. Soroosh P, Doherty TA, So T, et al. Herpesvirus entry mediator (TNFRSF14) regulates the persistence of T helper memory cell populations. *J Exp Med*. 2011;208(4):797–809. doi: 10.1084/jem.20101562
- Nunoya J-I, Masuda M, Ye C, Su L. Chimeric antigen receptor T cell bearing herpes virus entry mediator co-stimulatory signal domain exhibits high functional potency. *Mol Ther Oncolytics*. 2019;14:27–37. doi: 10.1016/j. omto.2019.03.002
- 61. Sun S, Huang C, Lu M, et al. Herpes virus entry mediator costimulation signaling enhances CAR T-cell efficacy against solid tumors through metabolic reprogramming. *Cancer Immunol Res.* 2023;11(4):515–529. doi: 10.1158/2326-6066.CIR-22-0531
- 62. Zhang N, Liu X, Qin J, et al. LIGHT/TNFSF14 promotes CAR-T cell trafficking and cytotoxicity through reversing immunosuppressive tumor microenvironment. *Mol Ther.* 2023;31(9):2575–2590. doi: 10.1016/j.ymthe.2023.06.015
- 63. Azuma M. Co-signal molecules in T-cell activation: Historical Overview and Perspective. *Adv Exp Med Biol.* 2019;1189:3–23. doi: 10.1007/978-981-32-9717-3 1
- 64. Tian J, Zhang B, Rui K, Wang S. The role of GITR/GITRL interaction in autoimmune diseases. Front Immunol. 2020;11:588682. doi: 10.3389/fimmu.2020.588682
- 65. Ronchetti S, Zollo O, Bruscoli S, et al. GITR, a member of the TNF receptor superfamily, is costimulatory to mouse T lymphocyte subpopulations. *Eur J Immunol.* 2004;34(3):613–622. doi: 10.1002/eji.200324804
- 66. So T, Nagashima H, Ishii N. TNF receptor-associated factor (TRAF) signaling network in CD4(+) T-lymphocytes. *Tohoku J Exp Med.* 2015;236(2):139–154. doi: 10.1620/tjem.236.139
- 67. Kanamaru F, Youngnak P, Hashiguchi M, et al. Costimulation via glucocorticoid-induced TNF receptor in both conventional and CD25+ regulatory CD4+ T cells. *J Immunol*. 2004;172(12):7306–7314. doi: 10.4049/jimmunol.172.12.7306
- 68. Xi B, Berahovich R, Zhou H, et al. A real-time potency assay for chimeric antigen receptor T cells targeting solid and hematological cancer cells. *J Vis Exp.* 2019;153. doi: 10.3791/59033
- 69. Golubovskaya VM. GITR domain inside CAR co-stimulates activity of CAR-T cells against cancer. *Front Biosci*. 2018;23(12):2245–2254. doi: 10.2741/4703
- 70. Wang Y, Wang L, Seo N, et al. CAR-modified  $V\gamma 9V\delta 2$  T cells propagated using a novel bisphosphonate prodrug for allogeneic adoptive immunotherapy. *Int J Mol Sci.* 2023;24(13):10873. doi: 10.3390/ijms241310873
- 71. Goodman DB, Azimi CS, Kearns K, et al. Pooled screening of CAR T cells identifies diverse immune

- signaling domains for next-generation immunotherapies. *Sci Transl Med.* 2022;14(670):eabm1463. doi: 10.1126/scitranslmed.abm1463
- 72. Levin-Piaeda O, Levin N, Pozner S, et al. The intracellular domain of CD40 is a potent costimulatory element in chimeric antigen receptors. *J Immunother*. 2021;44(6):209–213. doi: 10.1097/CJI.0000000000000373
- 73. Li S, Zhao R, Zheng D, et al. DAP10 integration in CAR-T cells enhances the killing of heterogeneous tumors by harnessing endogenous NKG2D. *Mol Ther Oncolytics*. 2022;26:15-26. doi: 10.1016/j.omto.2022.06.003
- 74. Liang X, Huang Y, Li D, et al. Distinct functions of CAR-T cells possessing a dectin-1 intracellular signaling domain. *Gene Ther.* 2023/5 2023;30(5):411–420. doi: 10.1038/s41434-021-00257-7
- 75. Daniels KG, Wang S, Simic MS, et al. Decoding CAR T cell phenotype using combinatorial signaling motif libraries and machine learning. *Science*. 2022;378(6625):1194–1200. doi: 10.1126/science.abq0225
- 76. Gross G, Waks T, Eshhar Z. Expression of immunoglobulin-T-cell receptor chimeric molecules as functional receptors with antibody-type specificity. *Proc Natl Acad Sci U S A*. 1989;86(24):10024-10028. doi: 10.1073/pnas.86.24.10024
- 77. Kuwana Y, Asakura Y, Utsunomiya N, et al. Expression of chimeric receptor composed of immunoglobulin-derived V resions and T-cell receptor-derived C regions. *Biochem Biophys Res Commun.* 1987;149(3):960–968. doi: 10.1016/0006-291x(87)90502-x
- 78. Eshhar Z, Waks T, Gross G, Schindler DG. Specific activation and targeting of cytotoxic lymphocytes through chimeric single chains consisting of antibody-binding domains and the gamma or zeta subunits of the immunoglobulin and T-cell receptors. *Proc Natl Acad Sci U S A*. 1993;90(2):720–724. doi: 10.1073/pnas.90.2.720
- 79. Zheng Z, Li S, Liu M, et al. Fine-tuning through generations: Advances in structure and production of CAR-T therapy. *Cancers (Basel).* 2023;15(13):3476. doi: 10.3390/cancers15133476
- 80. Feucht J, Sun J, Eyquem J, et al. Calibrated CAR activation potential directs alternative T cell fates and therapeutic potency. *Blood*. 2018;132(Supplement 1):1412–1412. doi: 10.1182/blood-2018-99-117698
- 81. Velasco Cárdenas RMH, Brandl SM, Meléndez AV, et al. Harnessing CD3 diversity to optimize CAR T cells. *Nat Immunol.* 2023;24(12):2135-2149. doi: 10.1038/s41590-023-01658-z
- 82. Wang P, Wang Y, Zhao X, et al. Chimeric antigen receptor with novel intracellular modules improves antitumor performance of T cells. Signal Transduct Target Ther. 2025;10(1):20. doi: 10.1038/s41392-024-02096-5
- 83. Reth M. Antigen receptor tail clue. *Nature*. 1989;338(6214):383–384. doi: 10.1038/338383b0
- 84. Love PE, Hayes SM. ITAM-mediated signaling by the T-cell antigen receptor. *Cold Spring Harb Perspect Biol.* 2010;2(6):a002485. doi: 10.1101/cshperspect.a002485
- 85. Holst J, Wang H, Eder KD, et al. Scalable signaling mediated by T cell antigen receptor-CD3 ITAMs ensures effective negative selection and prevents autoimmunity. *Nat Immunol.* 2008;9(6):658–666. doi: 10.1038/ni.1611
- 86. Bettini ML, Chou P-C, Guy CS, et al. Cutting edge: CD3 ITAM diversity is required for optimal TCR signaling and thymocyte development. *J Immunol.* 2017;199(5):1555–1560. doi: 10.4049/jimmunol.1700069
- 87. Aivazian D, Stern LJ. Phosphorylation of T cell receptor zeta is regulated by a lipid dependent folding transition.

- Nat Struct Biol. 2000;7(11):1023–1026. doi: 10.1038/80930 88. Xu C, Gagnon E, Call ME, et al. Regulation of T cell receptor activation by dynamic membrane binding of the CD3ɛ cytoplasmic tyrosine-based motif. Cell. 2008;135(4):702–713. doi: 10.1016/j.cell.2008.09.044
- 89. Li L, Guo X, Shi X, et al. Ionic CD3—Lck interaction regulates the initiation of T-cell receptor signaling. *Proc Natl Acad Sci U S A.* 2017;114(29):E5891-E5899. doi: 10.1073/pnas.1701990114
- 90. Hartl FA, Beck-Garcìa E, Woessner NM, et al. Noncanonical binding of Lck to CD3ε promotes TCR signaling and CAR function. *Nat Immunol.* 2020;21(8):902–913. doi: 10.1038/s41590-020-0732-3
- 91. Gil D, Schamel WWA, Montoya Ma, et al. Recruitment of nck by CD3ɛ reveals a ligand-induced conformational change essential for T cell receptor signaling and synapse formation. *Cell.* 2002;109(7):901–912. doi: 10.1016/s0092-8674(02)00799-7
- 92. Dietrich J, Hou X, Wegener AM, Geisler C. CD3 gamma contains a phosphoserine-dependent di-leucine motif involved in down-regulation of the T cell receptor. *EMBO J.* 1994;13(9):2156–2166. doi: 10.1002/j.1460-2075.1994.tb06492.x
- 93. Wegener A-MK, Hou X, Dietrich J, Geisler C. Distinct domains of the CD3-γ chain are involved in surface expression and function of the T cell antigen receptor. *J Biol Chem.* 1995;270(9):4675–4680. doi: 10.1074/jbc.270.9.4675
- 94. Escobar G, Mangani D, Anderson AC. T cell factor 1: A master regulator of the T cell response in disease. *Sci Immunol.* 2020;5(53):eabb9726. doi: 10.1126/sciimmunol. abb9726
- 95. Gattinoni L, Speiser DE, Lichterfeld M, Bonini C. T memory stem cells in health and disease. *Nat Med.* 2017;23(1):18–27. doi: 10.1038/nm.4241
- 96. Yeung T, Gilbert GE, Shi J, et al. Membrane phosphatidylserine regulates surface charge and protein localization. *Science*. 2008;319(5860):210–213. doi: 10.1126/science.1152066
- 97. Kolanus W, Romeo C, Seed B. T cell activation by clustered tyrosine kinases. *Cell.* 1993;74(1):171–183. doi: 10.1016/0092-8674(93)90304-9
- 98. Fitzer-Attas CJ, Schindler DG, Waks T, Eshhar Z. Harnessing Syk family tyrosine kinases as signaling domains for chimeric single chain of the variable domain receptors: optimal design for T cell activation. *J Immunol*. 1998;160(1):145–154. doi: 10.4049/jimmunol.160.1.145
- 99. Tousley AM, Rotiroti MC, Labanieh L, et al. Co-opting signalling molecules enables logic-gated control of CAR T cells. *Nature*. 2023;615(7952):507–516. doi: 10.1038/s41586-023-05778-2
- 100. Balagopalan L, Moreno T, Qin H, et al. Generation of antitumor chimeric antigen receptors incorporating T cell signaling motifs. *Sci Signal*. 2024;17(846):eadp8569. doi: 10.1126/scisignal.adp8569
- 101. Si W, Fan Y-Y, Qiu S-Z, et al. Design of diversified chimeric antigen receptors through rational module recombination. *iScience*. 2023;26(4):106529. doi: 10.1016/j. isci.2023.106529
- 102. Salter AI, Ivey RG, Kennedy JJ, et al. Phosphoproteomic analysis of chimeric antigen receptor signaling reveals kinetic and quantitative differences that affect cell function. *Sci Signal*. 2018;11(544):eaat6753. doi: 10.1126/scisignal.aat6753
- 103. Ramello MC, Benzaïd I, Kuenzi BM, et al. An immunoproteomic approach to characterize the CAR interactome

#### **REVIEWS**

- and signalosome.  $Sci\ Signal.\ 2019;12(568):eaap9777.\ doi: 10.1126/scisignal.aap9777$
- 104. Qiu S, Chen J, Wu T, et al. CAR-Toner: an AI-driven approach for CAR tonic signaling prediction and optimization. *Cell Res.* 2024;34(5):386–388. doi: 10.1038/s41422-024-00936-1
- 105. Rohrs JA, Zheng D, Graham NA, et al. Computational model of chimeric antigen receptors explains site-specific phosphorylation kinetics. *Biophys J.* 2018;115(6):1116–1129. doi: 10.1016/j.bpj.2018.08.018
- 106. Sheykhhasan M, Ahmadieh-Yazdi A, Vicidomini R, et al. CAR T therapies in multiple myeloma: unleashing the

- future. Cancer Gene Ther. 2024;31(5):667–686. doi: 10.1038/s41417-024-00750-2
- 107. Stepanov AV, Xie J, Zhu Q, et al. Control of the antitumour activity and specificity of CAR T cells via organic adapters covalently tethering the CAR to tumour cells. *Nat Biomed Eng.* 2024;8(5):529–543. doi: 10.1038/s41551-023-01102-5
- 108. Stepanov AV, Kalinin RS, Shipunova VO, et al. Switchable targeting of solid tumors by BsCAR T cells. *Proc Natl Acad Sci U S A.* 2022;119(46):e2210562119. doi: 10.1073/pnas.2210562119

## RNA Interference of the Genes Associated with the Invasion of Brain Tumor Cells

M. A. Dymova<sup>\*</sup>, O. A. Kartina, D. V. Drokov, E. V. Kuligina, V. A. Richter

Institute of Chemical Biology and Fundamental Medicine, Siberian Branch of the Russian Academy of Sciences, Novosibirsk, 630090 Russia

\*E-mail: maya.a.rot@gmail.com

Received March 17, 2025; in final form, April 28, 2025

DOI: 10.32607/actanaturae.27657

Copyright © 2025 National Research University Higher School of Economics. This is an open access article distributed under the Creative Commons Attribution License, which permits unrestricted use, distribution, and reproduction in any medium, provided the original work is properly cited.

ABSTRACT High-grade gliomas are among the most aggressive malignant pathologies of the brain. The high invasive potential of tumor cells causes relapses of the disease even after radical resection of the tumor. The signatures of the genes associated with the invasion of glioma cells have now been identified. The expression products of these genes are involved in various signaling pathways, such as cellular protein catabolism, the p53 signaling pathway, transcription dysregulation, and the JAK-STAT signaling pathway. Therefore, they can indirectly modulate the invasive potential of tumor cells. Using RNA interference technology, it is possible to change the expression level of the detected genes and reduce the invasive and proliferative potentials of cancer cells. This review focuses on the use of this technology to influence various links in signaling pathways and, accordingly, the cellular processes associated with the invasion of glioblastoma cells. Furthermore, the review discusses the problems associated with delivering interfering RNAs into cells and ways to solve them. KEYWORDS glioma, invasion, RNA interference, small interfering RNA.

ABBREVIATIONS BBB – blood-brain barrier; EMT – epithelial-mesenchymal transition; CD133 – prominin-1; CENPJ – centromere protein J; CPC – cardiac progenitor cells; CPNE3 – copine 3; EGF – epidermal growth factor; EGFR – epidermal growth factor receptor; EMA – European Medicines Agency; EV – extracellular vesicle; FAK – focal adhesion kinase; FDA – U.S. Food and Drug Administration; HER2 – human epidermal growth factor receptor 2; IDH – isocitrate dehydrogenase; MAGs – metastasis-associated genes; MALAT1 – metastasis-associated lung adenocarcinoma transcript 1; mCSCs – metastatic cancer stem cells; MDK – midkine (cell growth factor); MMPs – matrix metalloproteinases; NAcGal – N-acetylgalactosamine; PDGF – platelet-derived growth factor; RISC – RNA-induced silencing complex; siRNA – small interfering RNA; shRNA – short hairpin RNA; TMZ – temozolomide; VDAC1 – voltage-dependent anion channel 1; VEGF – vascular endothelial growth factor.

#### INTRODUCTION

Glioblastoma (grade IV glioma) is an aggressive malignant pathology of the brain accounting for 49% of primary malignant tumors of the central nervous system [1]. The incidence of this tumor is approximately 10 cases per 100,000 people. The median survival of glioblastoma patients undergoing standard treatment is ~ 14 months; the five-year survival rate is as low as 7.2% [2]. There are several factors contributing to the low survival rate of patients with this cancer: (1) the infiltrative tumor growth pattern complicating its complete resection; (2) the high degree of genetic intratumor and intertumor heterogeneity, which hinders targeted therapy; (3) the blood-brain barrier (BBB) impeding drug delivery to tumor tissue; (4) the im-

munosuppressive tumor microenvironment inhibiting antitumor immunity; and (5) the lack of reliable methods for early disease diagnosis. Today, the standard glioblastoma treatment protocol comprises maximal safe resection of the tumor, temozolomide (TMZ) chemotherapy, and radiation therapy (the so-called Stupp protocol) [2]. Other chemotherapeutic agents are used along with TMZ: vincristine, lomustine, procarbazine [1], methotrexate [3], Gliadel [4], and paclitaxel [5, 6]. The extent of the surgical resection positively correlates with patient survival; however, the infiltrative tumor growth pattern, the blurred boundaries between the tumor and healthy tissue, and the consequential risk of damaging the healthy brain areas during surgery complicate complete tumor resec-

tion [2]. Temozolomide therapy also involves several problems, such as the development of drug resistance by the tumor cells, adverse events associated with myelosuppression, the short half-life of TMZ, and the low effectiveness in crossing the BBB (~ 20%), leading to the need for higher therapeutic doses and, consequently, more severe adverse events [7]. Therefore, searching for novel effective glioblastoma treatments remains one of the most pressing challenges facing practical oncology.

#### Invasion as one of the hallmarks of glioblastoma

A key hallmark of glioblastoma is the active invasion of tumor cells occurring along the existing structures, primarily along blood and lymphatic vessels and the walls of cerebral ventricles, or via direct penetration through the dura mater and bone. The ability of tumor cells to undergo reversible epithelial-mesenchymal transition (EMT) allows a remodeling of their cytoskeleton and amoeboid movement among other cells, thus altering the structure of the extracellular matrix [8, 9]. Metastatic cancer stem cells (mCSCs) stand out among the pool of glioma cells [10]. The epigenetic plasticity of mCSCs enables them to switch between the stationary, slow-proliferative (dormant) state and the migratory mesenchymal-like state. That is how the invasion of tumor cells into the adjacent niches and the formation of metastases, where mCSCs express mesenchymal subtype markers such as CD44 and YK-40, takes place.

Tumor cells are capable of releasing a glutamate neurotransmitter into the extracellular space, thus inducing excitotoxic death of surrounding neurons and making room for amoeboid movement. Microglial and tumor cells also secrete various enzymes (urokinase plasminogen activator, cathepsin B, as well as MMP and ADAM proteases), thereby degrading proteoglycans and hyaluronic acid in the extracellular matrix along blood vessels, making it possible for cells to enter the bloodstream [11]. The formation of dense cellular structures known as pseudopalisades, primarily composed of microglial cells and macrophages, is pathognomonic for glioblastoma [12]. Some tumor cells have lamellipodia; electrical synapses in them ensure intercellular communication and coordination [13].

## Genes associated with glioblastoma invasion processes

Transcriptome analysis and single-cell DNA sequencing of glioma have helped identify the gene signatures (*Table 1*) associated with cancer cell invasion (metastasis-associated genes, MAGs) [14]. The products of these genes are involved in the p53 and JAK-STAT signaling pathways, as well as in cellular processes

such as the catabolism of cellular proteins and regulation of transcription, differentiation, and the proliferation of cells. Suppression of the expression of these genes may contribute to a reduction of both the invasive and the proliferative potential of glioma cells.

Furthermore, Cox regression analysis revealed another three genes (*GNS*, *LBH*, and *SCARA3*) whose expression correlates with the survival time of patients diagnosed with IDH-wildtype glioma [14, 27, 28]. The *GNS* gene encodes glucosamine (N-acetyl)-6-sulfatase, which is involved in the catabolism of heparin, heparan sulfate, and keratan sulfate. The *LBH* gene is highly expressed in gliomas. Under hypoxic conditions, its expression is directly regulated by the transcription factor HIF-1 and promotes tumor angiogenesis. The *SCARA3* gene encodes the scavenger receptor class A member 3 that reduces the level of reactive oxygen species, thereby protecting cells against oxidative stress.

Since tumor cell invasion is considered to be a key prognostic factor of the disease, it is crucial to identify the transcription factors, signaling pathways, and key master regulators of this process both for understanding the molecular mechanisms of oncogenesis and for further developing targeted therapeutics for glioma treatment.

#### RNA interference as a therapeutic approach

RNA interference, a natural evolutionarily conserved cellular defense mechanism against foreign gene invasion, which is commonly found in organisms across various taxa, is one of the gene expression regulation methods [29]. RNA interference is the post-transcriptional suppression of gene expression through degra-

Table 1. The genes associated with an invasion of glioma cells

No.	Signaling pathways and cellular processes	Gene	Reference	
1	Regulation of cellular protein catabolism	CLU, HSP90AB3P, MDM2, OS9, SDCBP, TRIB2	[14-20]	
2	The p53 signaling pathway	CASP3, CCND2, CDK4, IGFBP3, MDM2	[14, 17, 21–24]	
3	Regulation of transcription in cancer cells	CCND2, IGFBP3, MDM2, PLAT, ZEB1	[14, 17, 22, 24–26]	
4	The JAK-STAT signaling pathway	CCND2, FHL1	[14, 22, 26]	

Table 2. FDA-approved siRNA-based therapeutics

Therapeutic	Indications for use	Target	Delivery system	Year of FDA approval
Patisiran	Familial amyloid polyneuropathy	Hepatic transthyretin	Liposomes	2018
Givosiran	Acute hepatic porphyria	porphyria Aminolevulinic acid synthase 1		2019
Lumasiran	Primary hyperoxaluria type 1	Primary hyperoxaluria type 1 Hepatic glyoxylate oxidase		2020
Inclisiran	Hypercholesterolemia	Subtilisin/kexin type 9	NAcGal	2021
Vutrisiran	Hereditary transthyretin amyloidosis with polyneuropathy	Transthyretin	NAcGal	2022
Nedosiran	Primary hyperoxaluria	Hepatic lactate dehydrogenase	NAcGal	2023

dation of their mRNA triggered by small non-coding RNAs complementary to the mRNA sequence. These non-coding RNAs include double-stranded small interfering RNAs (siRNAs) and single-stranded short hairpin RNAs (shRNAs). Eukaryotic cells contain the DICER enzyme that hydrolyzes long endogenous and exogenous double-stranded RNAs into shorter fragments and cleaves the shRNA loop, yielding short siRNAs. siRNA binding to the target mRNA results in the formation of the RNA-induced silencing complex (RISC), which is involved in enzymatic mRNA degradation and suppresses translation [30, 31]. Unlike synthetic siRNAs, which are delivered into cells as short double-stranded RNAs, plasmid DNA or viral vectors are typically utilized in the case of shRNAs. After they have been delivered into the cell, shRNA is transcribed in the cytoplasm and converted to functional siRNA by the DICER enzyme.

RNA interference is a gene therapy method for various diseases. Six siRNA-based therapeutics have been approved for clinical application (*Table 2*). In 2018, the U.S. Food and Drug Administration (FDA) and the European Medicines Agency (EMA) approved patisiran as the first siRNA-based therapeutic for treating polyneuropathy caused by hereditary transthyretin amyloidosis in adult patients. Another six siRNA-based therapeutics have successfully undergone clinical trials. Fitusiran (NCT05662319), teprasiran (NCT03510897), and tivanisiran (NCT05310422) [32] are currently undergoing phase III clinical trials.

## Problems related to the application of siRNA in targeted therapy

Despite the high potential of RNA interference-based therapy, the availability of therapeutics approved for clinical application and several promising clinical trials, the RNA interference technology continues to exhibit a number of fundamental limitations. Significant challenges in the clinical application of interfering RNAs include nuclease degradation of unbound nucleic acids in bodily fluids, rapid renal clearance, interaction with extracellular proteins, and poor cellular internalization efficiency [33]. Along with the biopharmaceutical properties, the physicochemical characteristics of these molecules (their hydrophilicity, negative charge, and instability) also substantially hinder siRNA delivery into cells and reduce their biological activity [34]. Nucleic acids per se are neither tissue- nor cell-specific and poorly penetrate across various biological barriers, thus impeding the development of orally, intranasally, or transdermally administered drugs based on them [33]. Furthermore, off-target effects of RNA interference have been observed [35]. Thus, administration of shRNA targeting HCN1 mRNA into different brain regions of mice induced cytotoxicity mediated by them, including hippocampal cell degeneration even when delivering the control shRNA targeting luciferase mRNA (whose gene is absent from the mouse genome) [36]. These off-target effects of RNA interference may arise from both the binding of siRNA seed regions to the 3'-untranslated regions of non-target mRNAs, leading to their cleavage by the DICER complex, and the fact that the delivery of additional exogeneous RNA into the cell triggers competition with endogenous RNAs at all interference stages (e.g., for binding to DICER and RISC complexes in the cytoplasm). Additionally, synthetic RNA can be mistakenly recognized as viral RNA by endosomal and intracellular receptors of the innate immune system (e.g., the Toll-like receptors TLR-3, TLR-8, and TLR-9; PKR and RIG-I receptors), eliciting an inflammatory antiviral immune response. The off-target effects of RNA interference can be mitigated by chemical modification of RNA nucleotides (e.g., 2'-O-Me, 2'-O-methoxyethyl, 2'-F, phosphorothioate, etc.). Although the entirely non-modified or lightly modified siRNAs can mediate *in vivo* gene suppression, extensive modifications can enhance the chemical stability and siRNA delivery efficiency, reduce the toxicity related to off-target effects, and decrease activation of the innate immune system [37, 38]. The off-target effects can also be minimized by careful selection of siRNA nucleotide sequences using *in silico* algorithms and software for siRNA design [39, 40].

#### Delivery systems for interfering RNAs

siRNA delivery systems that prevent RNA degradation by endogenous nucleases and ensure penetration through the biological barriers, as well as allow regulation of the rate of endosomal escape of siRNA, have been actively developed over the past two decades. Endosomal escape is a critically important step for siRNA activity, limiting both the rate and efficacy of RNA interference, since prolonged residence in endosomes causes RNA degradation [40, 41].

siRNAs can be delivered using lipid, inorganic (Si, Au,  $Ca_3(PO_4)_2$ , and  $Fe_xO_y$ ) and polymeric nanoparticles (chitosan, cyclodextrin, polyethyleneimine, and poly-Llysine), dendrimers (polypropyleneimine and polyamidoamine), carbon nanostructures (carbon nanotubes, quantum dots, and nanodiamonds), as well as peptide carriers and conjugates (antibodies, peptides, NAcGal, and cholesterol) [42–44].

Lipid nanoparticles are structures consisting predominantly of phospholipids. Nanoparticles can be either artificially engineered (liposomes) or obtained from bodily fluids (extracellular vesicles, EVs). These systems for delivering drugs into cells are biocompatible, biodegradable, and have been well-studied [45]. Extracellular vesicles can also be artificially engineered via chemical treatment of cells with actindestabilizing compounds (cytochalasins, latrunculins, etc.) or other agents causing irreversible, chemically induced plasma membrane blebbing (paraformaldehyde, N-ethylmaleimide, etc.) [46, 47].

Lipid nanoparticles having surface modifications that enhance their stability or targeting specificity (e.g., the commercially available ionized amphiphilic lipid nanoparticles for siRNA delivery DLin-DMA, DLin-MC3-DMA, and L319) are of the greatest interest [48]. The nanoparticle surface can be functionalized using various ligands: apolipoproteins, transferrins, folates, integrins, etc. PEGylation of the surface of siRNA-loaded liposomes was shown to ensure prolonged systemic circulation of lipid particles [33]. Additional functionalization of the nanoparticle surface with a peptide aptamer specific to fibronectin,

whose expression on glioma cells is significantly upregulated, ensures targeted delivery of liposomes into tumor cells [49], tumor growth inhibition, and better survival of tumor-bearing animals. In another study, liposomal particles were functionalized with a ligand targeting LRP-1 (low-density lipoprotein receptorrelated protein 1). LRP-1 is expressed by bloodbrain barrier endothelial cells and glioblastoma cells. It was demonstrated that these siRNA-MDK-loaded nanoparticles reduce the resistance of cancer cells to TMZ and inhibit tumor growth in orthotopic glioblastoma mouse models [50]. In the functionalization of lipid particles, ligands specific to  $\alpha v \beta 3$  and  $\alpha v \beta 5$  integrins were used to deliver siRNAs into tumor cells; ανβ6-specific ligands were utilized for siRNA delivery into lung epithelial cells in COVID-19 [51, 52].

siRNAs can be efficiently delivered only provided that the biological barriers impeding the penetration of positively charged particles are overcome [53]. The strategies to overcome the so-called "polycation dilemma" primarily involve designing surface charge-reversible nanoparticles. These ionizable lipid nanoparticles carry a moderately negative or neutral surface charge, which enhances their stability in bodily fluids. However, a shift in pH or the redox potential, or the action of endogenous enzymes and exogenous factors, leads these nanoparticles to change their surface charge to a positive one and be efficiently internalized by target cells [50, 53]. Hence, in order to be able to cross the BBB, liposomes can be shielded with catechol-polyethylene glycol polymers preventing the premature release of the liposomal cargo into the cytoplasm of non-target cells (endothelial cells, pericytes, etc.) [50]. The shielding is removed in a tumor characterized by an elevated level of reactive oxygen species, and these nanoparticles penetrate glioblastoma cells through the action of the targeting ligand.

Hybrid structures composed of liposomes and extracellular vesicles (EVs) have been proposed as an alternative approach to enhancing the targeting specificity of siRNA-loaded lipid nanoparticles. Extracellular vesicles are natural RNA carriers that are superior to liposomes due to their low toxicity and immunogenicity [54]. Extracellular vesicle surface markers can be displayed on the surface of these hybrid structures, making nanoparticles "inherit" their properties. For example, cardiac progenitor cells (CPCs) produce a variety of regulatory growth factors and cytokines. Hence, CPC-derived EVs activate endothelial cell migration and angiogenesis in vivo, which can be further utilized in developing cellular technologies to treat post-infarction conditions. Hybrid liposomal particles produced using CPC-derived EVs are also capable of activating endothelial cell migration [55]. The surface of EVs can be modified with molecules targeting them to specific cells, or EVs can be loaded with biologically active molecules (chemotherapeutics, growth factors, microRNA, or siRNA) [56]. Thus, the therapeutic effect of EV-siBRAF<sup>V600E</sup> was demonstrated in mouse models of colorectal cancer carrying the *BRAF* V600E mutation [57]. When producing, isolating, and characterizing extracellular vesicles, in order to increase the reproducibility and minimize side effects, one must strictly adhere to the "Minimal Information for Studies of Extracellular Vesicles" guidelines developed by the International Society for Extracellular Vesicles [58].

Hence, there is an ongoing effort focusing on the development of lipid systems for optimal intracellular drug delivery. The regulatory approval of patisiran (ONPATTRO, manufactured by Alnylam Pharmaceuticals), which is the PEGylated liposomal nanoparticle loaded with siRNA targeting coagulation factor VII (proconvertin), is one of the successful outcomes of this research [41].

The display of tissue- or organ-specific molecules on the surface of siRNA-loaded nanoparticles is also used in the case of non-lipid nanoparticles. Thus, it has been demonstrated that calcium phosphate nanoparticles "decorated" with apolipoprotein E3 can cross the blood-brain barrier and ensure efficient siRNA delivery, inhibiting the growth of tumor xenografts [59]. siRNA conjugates with N-acetylgalactosamine (NAcGal), a ligand binding to the asialoglycoprotein receptor specifically expressed on the hepatocyte surface, deserve special mention among polymeric nanoparticles. The interaction between these nanoparticles and hepatocytes induces rapid endocytosis and reduces the target mRNA levels in hepatocytes [60, 61]. Five out of the six siRNAbased therapeutics approved for clinical application (Table 2) are siRNA-NAcGal conjugates. However, they are less stable than liposomes and more difficult to manufacture [62, 63]. Compounds such as cholesterol [64], 2'-O-hexadecyl (C16) [65], aptamers [66], antibodies [67], and peptides [68] can be used as siRNA conjugates along with NAcGal.

Delivery using cell-penetrating peptides (CPPs) is a rapidly developing technology for siRNA delivery into cells. CPPs are usually short positively charged peptides capable of entering cells either via endocytosis or by directly crossing the membranes. CPPs were shown to be able to form non-covalent complexes or covalent conjugates with biologically active nucleic acids (including siRNAs) and ensure transfection of various cells [69, 70]. For example, a fragment of human kappa-casein, RL2, is capable of delivering plasmid DNA, small nucleolar RNA, and siRNA into

cells. The most effective transfection was achieved by using the RL2-siRNA complexes; effective suppression of the expression of the target *EGFP* gene was demonstrated in ref. [71]. Despite all their advantages, CPPs also share the shortcomings inherent to protein-based drugs, such as the short half-life, the challenges related to the optimization of the conditions for forming a monodisperse suspension of these particles, and high cost of production. Therefore, CPPs are used as components of hybrid particles (e.g., with PEG) or as antigens displayed on the surface of siRNA-loaded lipid nanoparticles [72, 73].

Hence, first on the list when developing siRNA-based therapeutics is to enhance the stability of the molecule in the internal environment of an organism. This can be achieved both via modification of the siRNA structure and through conjugation of siRNA with other compounds. Further optimization can involve encapsulation of siRNA into nanocarriers such as cationic liposomes or carbon nanostructures and incorporation of a targeting ligand. All these factors protect siRNA against the aggressive biological environment, increase the nanoparticles' tropism towards the target, and, therefore, the effectiveness of RNA interference for a specific target gene.

## RNA interference as a promising approach to glioblastoma therapy

In vitro and in vivo experiments have demonstrated that the RNA interference technology is effective in inhibiting the signaling pathways that facilitate invasion, angiogenesis, and proliferation of glioblastoma cells, as well as their resistance to chemotherapy and radiotherapy. Thus, treatment of human glioblastoma T98G cells with siRNAs targeting the Akt3 and PI3K genes, in combination with temozolomide (TMZ), caused S and G2/M cell cycle arrest, in addition to inducing apoptosis and necrosis in tumor cells [74]. The PI3K/Akt/mTOR signaling pathway regulates apoptosis, proliferation, invasion, metabolism, epithelial-mesenchymal transition, and DNA repair in glioblastoma cells (Fig. 1) [75]. The PI3K/Akt/mTOR pathway is activated upon interaction of the epidermal growth factor (EGF), platelet-derived growth factor (PDGF), and vascular endothelial growth factor (VEGF) with their tyrosine kinase receptors. This signaling pathway was shown to be associated with the development of drug resistance, and its inhibition via RNA interference increased the sensitivity of U251 MG human glioblastoma cells to bortezomib [76].

The CD133 protein is considered to be a marker of cancer stem cells (CSCs), including glioblastoma stem cells [77]. The involvement of CD133 in oncogenesis makes it a crucial therapeutic target for the elimina-

tion of CSCs, which largely contribute to tumor recurrence, as well as for the inhibition of invasion, migration, and epithelial—mesenchymal transition. The activity of CD133–siRNA was shown to reduce the migration rate of U87 MG cells. This can be related to the modulation of the PI3K/Akt/mTOR signaling pathway (Fig. 1). In particular, RNA interference of the CD133 gene downregulated expression of the RAF1, MAP2K1, MAPK3, PIK3CA, AKT3, and mTOR genes [78].

Suppression of the expression of epidermal growth factor receptor (EGFR) and human epidermal growth factor receptor 2 (HER2) is another example of signaling pathway inhibition. These receptors mediate the activation of the MAPK/ERK signaling pathway, which regulates the proliferation and migration of cancer cells (Fig. 1). Thus, ERK activates transcription factors such as c-Myc, which in turn upregulate the expression of cell cycle regulator genes. The target genes of c-Myc include cyclin-dependent kinases, cyclins, and the transcription factor E2F [79]. HER2-siRNA was shown to reduce the migration and proliferation rates of LN-229 and U251 MG cells by approximately 50% [80]. Knockdown of the EGFR gene decreased the proliferation rate of both cell lines by approximately 40%. Expression of the IGFBP3 gene, which belongs to the aforementioned MAG group (Table 1), is also modulated by the MAPK/ERK signaling pathway and positively correlates with cancer grade [24, 81]. The in vivo experiments on an orthotopic mouse model of U87 MG/Luc glioma showed that two siRNAs (siIBP3-1 and siIBP3-2) inhibited tumor growth. The STAT3, cofilin-1, galectin-1, and ELTD1 genes, which are also activated by the MAPK/ERK signaling pathway, are considered promising siRNA targets [82, 83].

A promising target for tumor therapy is the TMEM97 gene, which encodes the transmembrane protein TMEM97 (sigma-2 receptor ( $\sigma$ 2R)) [84] and interacts with the EGF tyrosine kinase receptor (Fig.~1). Suppression of TMEM97 expression via RNA interference in U87 MG and U373 MG cells reduced the proliferation, migration, and invasion of cells, in addition to inducing G1/S cell cycle arrest [85]. Furthermore, RNA interference of the TMEM97 gene led to the modulation of epithelial–mesenchymal transition: the  $\beta$ -catenin and Twist levels declined, while the E-cadherin level increased.

Voltage-dependent anion-selective channel 1 (VDAC1) is a protein involved in non-selective transport of anions and cations across the outer mitochondrial membrane, as well as in the export of ATP into the cytoplasm (Fig.~1). The upregulated expression of the VDAC1 gene is known to play a crucial role in the

reprogramming of metabolic and energy processes in cancer cells [86]. Inhibition of *VDAC1* expression was shown to reduce the migration and invasion rates of human glioblastoma U87 MG cells *in vitro*, as well as slow down the growth of the U87 MG tumor in a mouse model [87, 88]. This is attributed to the dissipation of the mitochondrial membrane potential in tumor cells, reducing the intracellular ATP concentration and causing disruption of the cellular metabolism.

Along with protein-coding genes, the targets for gene-targeted therapy based on RNA interference can also include long non-coding RNAs (e.g., MALAT1 (Fig. 1), whose high expression level is associated with a poor prognosis in glioblastoma patients [89]). The MALAT1 levels were shown to be elevated in TMZ-resistant U251 MG and U87 MG human glioblastoma cells [90]. The cells, transfected with MALAT1-siRNA, were characterized by downregulated expression of the genes mediating drug resistance (MDR1, MRP5, and LRP1), as well as a downregulated expression of the ZEB1 gene, which is involved in the EMT in cancer cells. Tumor progression is accompanied by EMT associated with the degradation of the extracellular matrix and reduction of cancer cell adhesion, thereby intensifying their migration and invasion. Hence, the inhibition of these cellular processes via RNA interference can significantly reduce the metastatic potential of the tumor. Copine 3 (CPNE3), belonging to the CPNE family of Ca2+-dependent phospholipid-binding proteins, plays a crucial role in the EMT of human glioblastoma cells (Fig. 1). CPNE3 induces the EMT by activating the FAK signaling pathway, thus promoting invasion and migration of tumor cells. Suppression of CPNE3 expression using CPNE3-shRNA in U87 MG and U251 MG cells impaired the migratory, invasive, and proliferative potential of glioblastoma cells, which can be associated with inactivation of the FAK and, therefore, the PI3K/Akt/mTOR signaling pathways [91, 92].

The ZEB2 protein is a transcription factor playing an important role in the development of the central nervous system throughout the entire embryonic period. Meanwhile, ZEB2 is also involved in the epithelial–mesenchymal transition of tumor cells; upregulated ZEB2 expression is observed in many cancers, including glioblastoma [63]. An analysis of the migratory potential of U87 MG and U373 MG glioma cells revealed that the migration rate of cells transfected with ZEB2–siRNA was significantly reduced compared to the control cells [93]. ZEB2 overexpression is known to increase the levels of N-cadherin and a number of matrix metalloproteinases (Fig. 1); in turn, it promotes invasion/migration of cancer cells [93–95]. The centromere protein J (CENPJ) controlling the divi-

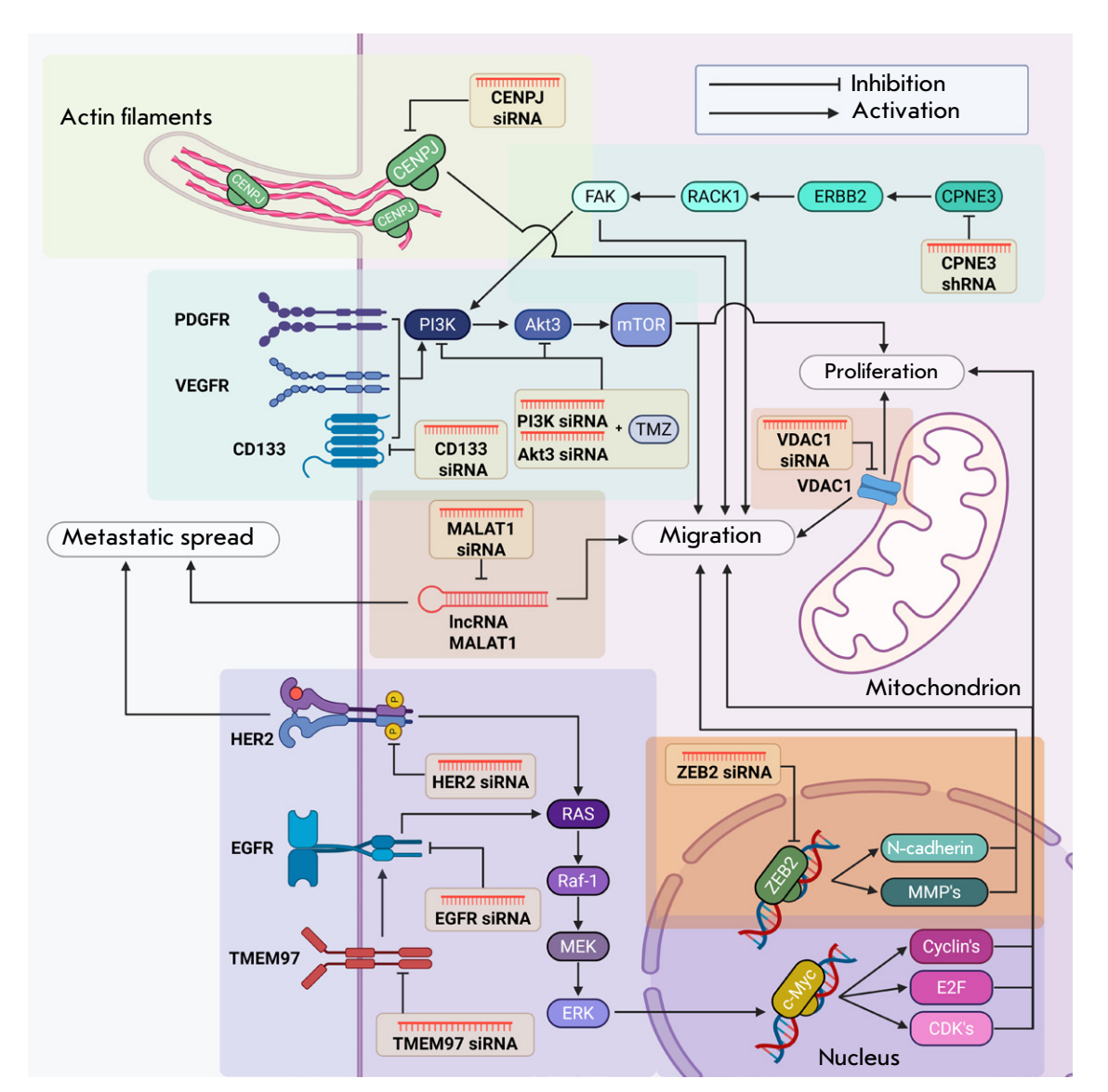


Fig. 1. The use of RNA interference to regulate the expression of genes whose products are involved in the proliferation and migration of glioblastoma cells. siRNA – small interfering RNA; shRNA – short hairpin RNA

sion of neural precursor cells and neuronal migration is also involved in the EMT [96]. *CENPJ* expression was shown to be upregulated in human glioblastoma cell lines compared to healthy brain tissue; this correlates with a poor disease prognosis in glioma patients. Treatment of personalized glioblastoma culture cells (GBM02 and GBM95) with CENPJ-siRNA reduced their migration rate. *CENPJ* knockdown is believed to alter the morphology of glioblastoma cells because of microtubule stabilization and actin microfilament depolymerization, thereby making the cells less prone to epithelial-mesenchymal transition (*Fig.* 1).

NU-0129, a siRNA-based therapeutic designed for glioblastoma treatment, is currently undergoing phase I clinical trials (Clinical trials: NCT03020017).

The therapeutic is a complex of gold nanoparticles and siRNA targeting *Bcl2L12* mRNA. The *Bcl2L12* gene encodes the anti-apoptotic protein Bcl2L12 overexpressed in human glioma cells, which makes them apoptosis-resistant. An analysis of the accumulation of gold particles in patients' tumors demonstrated that NU-0129 penetrates the blood-brain barrier and accumulates in tumor tissue, where it reduces the level of the Bcl2L12 protein [97]. Hence, designing targeted nontoxic nanoparticles carrying siRNAs described above and further research into their effectiveness for glioblastoma treatment is undoubtedly promising; the clinical trials of the developed drugs will broaden the treatment options for neuro-oncological disorders.

#### **CONCLUSIONS**

RNA interference is a promising therapeutic approach to glioblastoma treatment. The currently available promising delivery systems for interfering RNAs lay the groundwork for designing targeted agents that inhibit the proliferation, invasion, migration, and epithelial—mesenchymal transition of tumor cells. The previously described signatures of the MAG genes, as well as the genes encoding the FAK, PI3K/Akt/mTOR, and MAPK/ERK signaling pathways, will facilitate the search for siRNAs with

a potential for developing effective targeted therapies for glioblastoma. When developing siRNA-based therapeutics, our efforts should focus on enhancing their penetration efficiency, stability, and specificity with respect to a selected target.

This study was conducted under the State Assignment for the Institute of Chemical Biology and Fundamental Medicine, Siberian Branch of the Russian Academy of Sciences (No. 125012900932-4).

#### REFERENCES

- 1. Schaff L.R., Mellinghoff I.K. // JAMA. 2023. V. 329. № 7. P. 574. doi: 10.1001/jama.2023.0023.
- Wu W., Klockow J.L., Zhang M., Lafortune F., Chang E., Jin L., Wu Y., Daldrup-Link H.E. // Pharmacol. Res. 2021.
   V. 171. P. 105780. doi: 10.1016/j.phrs.2021.105780.
- 3. Kang X., Chen F., Yang S.-B., Wang Y.-L., Qian Z.-H., Li Y., Lin H., Li P., Peng Y.-C., Wang X.-M., et al. // World J. Clin. Cases. 2022. V. 10. № 17. P. 5595–5605. doi: 10.12998/wjcc.v10.i17.5595.
- 4. Iuchi T., Inoue A., Hirose Y., Morioka M., Horiguchi K., Natsume A., Arakawa Y., Iwasaki K., Fujiki M., Kumabe T., et al. // Neuro-Oncology Adv. 2022. V. 4. № 1. P. vdab189. doi: 10.1093/noajnl/vdab189.
- 5. AbdEl-haq M., Kumar A., Ait Mohand F., Kravchen-ko-Balasha N., Rottenberg Y., Domb A.J. // Int. J. Mol. Sci. 2023. V. 24. № 14. P. 11722. doi: 10.3390/ijms241411722.
- 6. Rodríguez-Camacho A., Flores-Vázquez J.G., Moscardini-Martelli J., Torres-Ríos J.A., Olmos-Guzmán A., Ortiz-Arce C.S., Cid-Sánchez D.R., Pérez S.R., Macías-González M.D.S., Hernández-Sánchez L.C., et al. // Int. J. Mol. Sci. 2022. V. 23. № 13. P. 7207. doi: 10.3390/ijms23137207.
- 7. Tan A.C., Ashley D.M., López G.Y., Malinzak M., Friedman H.S., Khasraw M. // CA. Cancer J. Clin. 2020. V. 70. № 4. P. 299–312. doi: 10.3322/caac.21613.
- 8. Weenink B., French P.J., Sillevis Smitt P.A.E., Debets R., Geurts M. // Cancers (Basel). 2020. V. 12. № 3. P. 751. doi: 10.3390/cancers12030751.
- 9. Krakhmal N.V., Zavyalova M.V., Denisov E.V., Vtorushin S.V., Perelmuter V.M. //Acta Naturae. 2015. V. 7. № 2. P. 17–28. doi: 10.32607/20758251-2015-7-2-17-28.
- Lah T.T., Novak M., Breznik B. // Semin. Cancer Biol. 2020. V. 60. P. 262–273. doi: 10.1016/j.semcancer.2019.10.010.
- Geribaldi-Doldán N., Fernández-Ponce C., Quiroz R.N., Sánchez-Gomar I., Escorcia L.G., Velásquez E.P., Quiroz E.N. // Front. Oncol. 2021. V. 10. P. 603495. doi: 10.3389/ fonc.2020.603495.
- Saavedra-López E., Roig-Martínez M., Cribaro G.P., Casanova P. V., Gallego J.M., Pérez-Vallés A., Barcia C. // Brain Commun. 2020. V. 2. № 1. fcz043. doi: 10.1093/braincomms/fcz043.
- 13. Venkatesh H.S., Morishita W., Geraghty A.C., Silverbush D., Gillespie S.M., Arzt M., Tam L.T., Espenel C., Ponnuswami A., Ni L., et al. // Nature. 2019. V. 573. № 7775. P. 539–545. doi: 10.1038/s41586-019-1563-y.
- 14. Li X., Meng Y. // BMC Cancer. 2020. V. 20. № 1. P. 1114.

- doi: 10.1186/s12885-020-07628-0.
- 15. Ren X., Chang C., Qi T., Yang P., Wang Y., Zhou X., Guan F., Li X. // Int. J. Mol. Sci. 2023. V. 24. № 17. P. 13413. doi: 10.3390/ijms241713413.
- 16. Albakova Z., Siam M.K.S., Sacitharan P.K., Ziganshin R.H., Ryazantsev D.Y., Sapozhnikov A.M. // Transl. Oncol. 2021. V. 14. № 2. P. 100995. doi: 10.1016/j.tranon.2020.100995.
- 17. Pellot Ortiz K.I., Rechberger J.S., Nonnenbroich L.F., Daniels D.J., Sarkaria J.N. // Biomedicines. 2023. V. 11. № 7. P. 1879. doi: 10.3390/biomedicines11071879.
- 18. Zhang P., Meng X., Liu L., Li S., Li Y., Ali S., Li S., Xiong J., Liu X., Li S., et al. // Front. Oncol. 2021. V. 11. P. 633357. doi: 10.3389/fonc.2021.633357.
- 19. Talukdar S., Pradhan A.K., Bhoopathi P., Shen X.N., August L.A., Windle J.J., Sarkar D., Furnari F.B., Cavenee W.K., Das S.K., et al. // Autophagy. 2018. V. 14. № 10. P. 1845–1846. doi: 10.1080/15548627.2018.1502564.
- 20. Wang J., Zuo J., Wahafu A., Wang M. de, Li R.-C., Xie W.-F. // CNS Neurosci. Ther. 2020. V. 26. № 3. P. 297–308. doi: 10.1111/cns.13197.
- 21. Feng X., Zhu F., Dai L., Liu X., Shao L., Hao L., Cang S., Cheng J. // J. Neurooncol. 2023. V. 163. № 2. P. 313–325. doi: 10.1007/s11060-023-04339-x.
- 22. Büschiges R., Weber R.G., Actor B., Lichter P., Collins V.P., Reifenberger G. // Brain Pathol. 1999. V. 9. № 3. P. 435–442. doi: 10.1111/j.1750-3639.1999.tb00532.x.
- 23. Giordano F., D'Amico M., Montalto F.I., Malivindi R., Chimento A., Conforti F.L., Pezzi V., Panno M.L., Andò S., De Amicis F. // Int. J. Mol. Sci. 2023. V. 24. № 12. P. 10094. doi: 10.3390/ijms241210094.
- 24. Chen C.-H., Chen P.-Y., Lin Y.-Y., Feng L.-Y., Chen S.-H., Chen C.-Y., Huang Y.-C., Huang C.-Y., Jung S.-M., Chen L.Y., et al. // J. Neurosurg. 2019. V. 132. № 1. P. 168–179. doi: 10.3171/2018.8.JNS181217.
- 25. Yamashita D., Kondo T., Ohue S., Takahashi H., Ishikawa M., Matoba R., Suehiro S., Kohno S., Harada H., Tanaka J., et al. // Cancer Res. 2015. V. 75. № 6. P. 1123–1133. doi: 10.1158/0008-5472.CAN-14-0938.
- 26. Siebzehnrubl F.A., Silver D.J., Tugertimur B., Deleyrolle L.P., Siebzehnrubl D., Sarkisian M.R., Devers K.G., Yachnis A.T., Kupper M.D., Neal D., et al. // EMBO Mol. Med. 2013. V. 5. № 8. P. 1196–1212. doi: 10.1002/emmm.201302827.
- 27. Liu L., Luo Q., Xu Q., Xiong Y., Deng H. // FEBS Open Bio. 2022. V. 12. № 1. P. 211–220. doi: 10.1002/2211-5463.13325.

- 28. Cao M., Cai J., Yuan Y., Shi Y., Wu H., Liu Q., Yao Y., Chen L., Dang W., Zhang X., et al. // Cancer Biol. Med. 2019. V. 16. № 3. P. 595–605. doi: 10.20892/j.issn.2095-3941.2018.0277.
- 29. Jadhav V., Vaishnaw A., Fitzgerald K., Maier M.A. // Nat. Biotechnol. 2024. V. 42. № 3. P. 394–405. doi: 10.1038/ s41587-023-02105-y.
- 30. Le C.T., Le T.N.Y., Nguyen T.A. // Meth. Enzymol. 2023. V. 692. P. 231–247. doi: 10.1016/bs.mie.2023.02.023.
- 31. Goel K., Ploski J.E. // Front. Mol. Neurosci. 2022. V. 15. P. 914430. doi: 10.3389/fnmol.2022.914430.
- 32. Sehgal I., Eells K., Hudson I. // Pharmacy. 2024. V. 12. № 2. P. 58. doi: 10.3390/pharmacy12020058.
- 33. Shetty K., Yasaswi S., Dutt S., Yadav K.S. // 3 Biotech. 2022. V. 12. № 11. P. 301. doi: 10.1007/s13205-022-03365-2.
- 34. Singh P., Singh A., Shah S., Vataliya J., Mittal A., Chit-kara D. // Mol. Pharm. 2020. V. 17. № 11. P. 4040–4066. doi: 10.1021/acs.molpharmaceut.0c00709.
- 35. Kobayashi Y., Tian S., Ui-Tei K. // Genes (Basel). 2022. V. 13. № 2. P. 319. doi: 10.3390/genes13020319.
- 36. Günther A., Luczak V., Abel T., Baumann A. // J. Exp. Biol. 2017. V. 220. № 8. P. 1400–1404. doi: 10.1242/jeb.154583.
- 37. Friedrich M., Aigner A. // BioDrugs. 2022. V. 36. № 5. P. 549–571. doi: 10.1007/s40259-022-00549-3.
- 38. Chernikov I.V., Ponomareva U.A., Chernolovskaya E.L. // Int. J. Mol. Sci. 2023. V. 24. № 2. P. 956. doi: 10.3390/ijms24020956.
- 39. Lück S., Kreszies T., Strickert M., Schweizer P., Kuhlmann M., Douchkov D. // Front. Plant Sci. 2019. V. 10. P. 1023. doi: 10.3389/fpls.2019.01023.
- 40. Gilleron J., Querbes W., Zeigerer A., Borodovsky A., Marsico G., Schubert U., Manygoats K., Seifert S., Andree C., Stöter M., et al. // Nat. Biotechnol. 2013. V. 31. № 7. P. 638–646. doi: 10.1038/nbt.2612.
- 41. Urits I., Swanson D., Swett M.C., Patel A., Berardino K., Amgalan A., Berger A.A., Kassem H., Kaye A., Viswanath O. // Neurol. Ther. 2020. V. 9. № 2. P. 301–315. doi: 10.1007/s40120-020-00208-1.
- 42. Yazdani S., Mozaffarian M., Pazuki G., Hadidi N., Villate-Beitia I., Zárate J., Puras G., Pedraz J.L. // Pharmaceutics. 2024. V. 16. № 2. P. 288. doi: 10.3390/pharmaceutics16020288.
- 43. Yang C., Lin Z., Zhang X., Xu Z., Xu G., Wang Y., Tsai T., Cheng P., Law W., Yong K., et al. // Macromol. Biosci. 2024. V. 24. № 4. doi: 10.1002/mabi.202300362.
- 44. Rotov A.Yu., Romanov I.S., Tarakanchikova Y.V., Astakhova L.A. // J. Evol. Biochem. Physiol. 2021. V. 57. № 6. P. 1333–1350. doi: 10.1134/S0022093021060132.
- 45. Roostaee M., Derakhshani A., Mirhosseini H., Banaee Mofakham E., Fathi-Karkan S., Mirinejad S., Sargazi S., Barani M. // Nanoscale. 2024. V. 16. № 6. P. 2713–2746. doi: 10.1039/d3nr03495j.
- 46. Oshchepkova A., Chernikov I., Miroshnichenko S., Patutina O., Markov O., Savin I., Staroseletz Y., Meschaninova M., Puchkov P., Zhukov S., et al. // Front. Bioeng. Biotechnol. 2024. V. 12. doi: 10.3389/fbioe.2024.1437817.
- 47. Thone M.N., Kwon Y.J. // Methods. 2020. V. 177. P. 135–145. doi: 10.1016/j.ymeth.2019.11.007.
- 48. Hu B., Zhong L., Weng Y., Peng L., Huang Y., Zhao Y., Liang X.-J. // Signal Transduct. Target. Ther. 2020. V. 5. № 1. P. 101. doi: 10.1038/s41392-020-0207-x.
- 49. Saw P.E., Zhang A., Nie Y., Zhang L., Xu Y., Xu X. // Front. Pharmacol. 2018. V. 9. P. 1194. doi: 10.3389/fphar.2018.01194.

- 50. Zhao Y., Qin J., Yu D., Liu Y., Song D., Tian K., Chen H., Ye Q., Wang X., Xu T., et al. // Nat. Nanotechnol. 2024. V. 19. № 12. P. 1869–1879. doi: 10.1038/s41565-024-01769-0.
- 51. Bugatti K. // ChemBioChem. 2021. V. 22. № 15. P. 2516–2520. doi: 10.1002/cbic.202100209.
- Meecham A., Cutmore L.C., Protopapa P., Rigby L.G., Marshall J.F. // Front. Cell Dev. Biol. 2022. V. 10. P. 920303. doi: 10.3389/fcell.2022.920303.
- 53. Veider F., Sanchez Armengol E., Bernkop-Schnürch A. // Small. 2024. V. 20. № 3. P. 2304713. doi: 10.1002/smll.202304713.
- 54. Herrmann I.K., Wood M.J.A., Fuhrmann G. // Nat. Nanotechnol. 2021. V. 16. № 7. P. 748–759. doi: 10.1038/s41565-021-00931-2.
- 55. Evers M.J.W., van de Wakker S.I., de Groot E.M., de Jong O.G., Gitz-François J.J.J., Seinen C.S., Sluijter J.P.G., Schiffelers R.M., Vader P. // Adv. Healthc. Mater. 2022. V. 11. № 5. P. 2101202. doi: 10.1002/adhm.202101202.
- 56. Velikonivtsev F.S., Golovkin A.S. // Russ. J. Cardiol. 2020. V. 25. № 10. P. 4081. doi: 10.15829/1560-4071-2020-4081.
- 57. Wang D., Wang L., Zhang W., Xu K., Chen L., Guo Z., Wu K., Huang D., Zhao Y., Yao M., et al. // J. Nanobiotechnology. 2025. V. 23. № 1. P. 129. doi: 10.1186/s12951-025-03205-4.
- 58. Welsh J.A., Goberdhan D.C.I., O'Driscoll L., Buzas E.I., Blenkiron C., Bussolati B., Cai H., Di Vizio D., Driedonks T.A.P., Erdbrügger U., et al. // J. Extracell. Vesicles. 2024. V. 13. № 2. P. e12404. doi: 10.1002/jev2.12404.
- 59. Huang J.L., Jiang G., Song Q.X., Gu X., Hu M., Wang X.L., Song H.H., Chen L.P., Lin Y.Y., Jiang D., et al. // Nat. Commun. 2017. V. 8. P. 15144. doi: 10.1038/ncomms15144.
- Zhang M.M., Bahal R., Rasmussen T.P., Manautou J.E., Zhong X. bo. // Biochem. Pharmacol. 2021. V. 189.
   P. 114432. doi: 10.1016/j.bcp.2021.114432.
- 61. Syed Y.Y. // Drugs. 2023. V. 83. № 18. P. 1729–1733. doi: 10.1007/s40265-023-01976-4.
- 62. Adams D., Tournev I.L., Taylor M.S., Coelho T., Planté-Bordeneuve V., Berk J.L., González-Duarte A., Gillmore J.D., Low S.-C., Sekijima Y., et al. // Amyloid. 2023. V. 30. № 1. P. 18–26. doi: 10.1080/13506129.2022.2091985.
- Zhang L., Liang Y., Liang G., Tian Z., Zhang Y., Liu Z., Ji X. // Front. Pharmacol. 2022. V. 13. P. 1090237. doi: 10.3389/fphar.2022.1090237.
- 64. Chernikov I. V., Bachkova I.K., Sen'kova A. V., Meschaninova M.I., Savin I.A., Vlassov V. V., Zenkova M.A., Chernolovskaya E.L. // Cells. 2024. V. 13. № 9. P. 767. doi: 10.3390/cells13090767.
- 65. Brown K.M., Nair J.K., Janas M.M., Anglero-Rodriguez Y.I., Dang L.T.H., Peng H., Theile C.S., Castellanos-Rizaldos E., Brown C., Foster D., et al. // Nat. Biotechnol. 2022. V. 40. № 10. P. 1500–1508. doi: 10.1038/s41587-022-01334-x.
- Wang S., Zhao Y., Yao F., Wei P., Ma L., Zhang S. // Biomed. Pharmacother. 2024. V. 174. P. 116437. doi: 10.1016/j. biopha.2024.116437.
- 67. Rady T., Erb S., Deddouche-Grass S., Morales R., Chaubet G., Cianférani S., Basse N., Wagner A. // iScience. 2024. V. 27. № 3. P. 109068. doi: 10.1016/j.isci.2024.109068.
- 68. Smidt J.M., Lykke L., Stidsen C.E., Pristovšek N., Gothelf K. V. // Nucl. Acids Res. 2024. V. 52. № 1. P. 49– 58. doi: 10.1093/nar/gkad1015.
- 69. Kiisholts K., Kurrikoff K., Arukuusk P., Porosk L., Peters M., Salumets A., Langel Ü. // Pharmaceutics. 2021. V. 13. № 10. P. 1618. doi: 10.3390/pharmaceutics13101618.

- 70. Nai J., Zhang J., Li J., Li H., Yang Y., Yang M., Wang Y., Gong W., Li Z., Li L., et al. // Mol. Ther. Nucl. Acids. 2022. V. 27. P. 349–362. doi: 10.1016/j.omtn.2021.12.016.
- Chinak O., Golubitskaya E., Pyshnaya I., Stepanov G., Zhuravlev E., Richter V., Koval O. // Front. Pharmacol. 2019. V. 10. P. 1043. doi: 10.3389/fphar.2019.01043.
- 72. Boisguérin P., Konate K., Josse E., Vivès E., Deshayes S. // Biomedicines. 2021. V. 9. № 5. P. 583. doi: 10.3390/biomedicines9050583.
- 73. Vysochinskaya V., Zabrodskaya Y., Dovbysh O., Emelyanov A., Klimenko V., Knyazev N., Terterov I., Egorova M., Bogdanov A., Maslov M., et al. // Biochimie. 2024. V. 221. P. 1–12. doi: 10.1016/j.biochi.2024.01.006.
- 74. Paul-Samojedny M., Pudełko A., Kowalczyk M., Fila-Daniłow A., Suchanek-Raif R., Borkowska P., Kowalski J. // BioDrugs. 2016. V. 30. № 2. P. 129–144. doi: 10.1007/s40259-016-0160-v.
- 75. Peng Y., Wang Y., Zhou C., Mei W., Zeng C. // Front. Oncol. 2022. V. 12. P. 819128. doi: 10.3389/fonc.2022.819128.
- 76. Wang J., Ren D., Sun Y., Xu C., Wang C., Cheng R., Wang L., Jia G., Ren J., Ma J., et al. // J. Cell. Mol. Med. 2020. V. 24. № 7. P. 3931–3947. doi: 10.1111/jcmm.14996.
- 77. Joyce T., Jagasia S., Tasci E., Camphausen K., Krauze A.V. // Curr. Oncol. 2023. V. 30. № 9. P. 8278–8293. doi: 10.3390/curroncol30090601.
- 78. Abdoli Shadbad M., Nejadi Orang F., Baradaran B. // Eur. J. Med. Res. 2024. V. 29. № 1. P. 154. doi: 10.1186/s40001-024-01754-2.
- 79. Bretones G., Delgado M.D., León J. // Biochim. Biophys. Acta Gene Regul. Mech. 2015. V. 1849. № 5. P. 506–516. doi: 10.1016/j.bbagrm.2014.03.013.
- 80. Wichmann H., Güttler A., Bache M., Taubert H., Rot S., Kessler J., Eckert A.W., Kappler M., Vordermark D. // Strahlentherapie und Onkol. 2015. V. 191. № 2. P. 180–191. doi: 10.1007/s00066-014-0743-9.
- 81. Zhang X., Wang G., Gong Y., Zhao L., Song P., Zhang H., Zhang Y., Ju H., Wang X., Wang B., et al. // iScience. 2023. V. 26. № 5. P. 106639. doi: 10.1016/j.isci.2023.106639.
- 82. Ahirwar K., Kumar A., Srivastava N., Saraf S.A., Shukla R. // Int. J. Biol. Macromol. 2024. V. 266. Pt 1. P. 131048. doi: 10.1016/j.ijbiomac.2024.131048.
- 83. Shahani A., Slika H., Elbeltagy A., Lee A., Peters C., Dotson T., Raj D., Tyler B. // Cancer Drug Resist. 2025. V. 8. P. 10. doi: 10.20517/cdr.2024.157.

- 84. Zeng C., Riad A., Mach R.H. // Cancers (Basel). 2020. V. 12. № 7. P. 1877. doi: 10.3390/cancers12071877.
- 85. Qiu G., Sun W., Zou Y., Cai Z., Wang P., Lin X., Huang J., Jiang L., Ding X., Hu G. // Tumor Biol. 2015. V. 36. № 10. P. 8231–8238. doi: 10.1007/s13277-015-3552-6.
- 86. Zerbib E., Arif T., Shteinfer-Kuzmine A., Chalifa-Caspi V., Shoshan-Barmatz V. // Cancers (Basel). 2021. V. 13. № 11. P. 2850. doi: 10.3390/cancers13112850.
- 87. Arif T., Vasilkovsky L., Refaely Y., Konson A., Shoshan-Barmatz V. // Mol. Ther. Nucl. Acids. 2014. V. 3. № 4. e159. doi: 10.1038/mtna.2014.9.
- 88. Arif T., Paul A., Krelin Y., Shteinfer-Kuzmine A., Shoshan-Barmatz V. // Cancers (Basel). 2018. V. 10. № 12. P. 499. doi: 10.3390/cancers10120499.
- 89. Argadal O.G., Mutlu M., Ak Aksoy S., Kocaeli H., Tunca B., Civan M.N., Egeli U., Cecener G., Bekar A., Taskapilio-glu M.O., et al. // Bosn. J. Basic Med. Sci. 2020. V. 20. № 1. P. 63–69. doi: 10.17305/bjbms.2019.4297.
- 90. Li H., Yuan X., Yan D., Li D., Guan F., Dong Y., Wang H., Liu X., Yang B. // Cell. Physiol. Biochem. 2017. V. 42. № 3. P. 1192–1201. doi: 10.1159/000478917.
- 91. Shi D., Lin B., Lai J., Li K., Feng Y. // J. Mol. Histol. 2021. V. 52. № 3. P. 589–596. doi: 10.1007/s10735-021-09966-0.
- 92. Paul R., Luo M., Mo X., Lu J., Yeo S.K., Guan J.-L. // Breast Cancer Res. 2020. V. 22. № 1. P. 59. doi: 10.1186/ s13058-020-01298-3.
- 93. Safaee S., Fardi M., Hemmat N., Khosravi N., Derakhshani A., Silvestris N., Baradaran B. // Molecules. 2021. V. 26. № 4. P. 901. doi: 10.3390/molecules26040901.
- 94. Yi X., Shi S., Li X., Zhao L. // Journal of Clinical Otorhinolaryngology Head and Neck Surgery. 2015. V. 29. № 18. P. 1648–1651.
- 95. Dai Y.H., Lv L., Huo J.R., Chu Y., Tang Y.P., Zhou Y.Q., Zhu H.Y. // Dig. Dis. Sci. 2012. V. 57. № 5. P. 1253–1260. doi: 10.1007/s10620-012-2042-6.
- 96. de Freitas G.P.A., Geraldo L.H.M., Faria B.M., Alves-Leon S.V., de Souza J.M., Moura-Neto V., Pontes B., Romão L.F., Garcez P.P. // J. Neurochem. 2022. V. 162. № 6. P. 501–513. doi: 10.1111/jnc.15660.
- 97. Kumthekar P., Ko C.H., Paunesku T., Dixit K., Sonabend A.M., Bloch O., Tate M., Schwartz M., Zuckerman L., Lezon R., et al. // Sci. Transl. Med. 2021. V. 13. № 584. doi: 10.1126/scitranslmed.abb3945.

# Store-Operated Calcium Entry As an Important Mechanism of Tumor Adaptation to an Aggressive Microenvironment

A. Yu. Skopin, E. V. Kaznacheyeva\*

Institute of Cytology, Russian Academy of Sciences, St. Petersburg, 194064 Russia

\*E-mail: evkazn@incras.ru

Received November 29, 2024; in final form, April 22, 2025

DOI: 10.32607/actanaturae.27574

Copyright © 2025 National Research University Higher School of Economics. This is an open access article distributed under the Creative Commons Attribution License, which permits unrestricted use, distribution, and reproduction in any medium, provided the original work is properly cited.

ABSTRACT Calcium signaling ensures efficient cellular functioning; calcium homeostasis disruption leaves behind detrimental sequelae for the cell both under calcium excess and deficiency conditions. Malignant transformation is accompanied by significant alterations in the expression of the proteins critical for store-operated calcium entry, resulting in the dysregulation of calcium signaling. It is plausible that a remodeling of intracellular signal transduction pathways in cancer cells is required in order to accelerate metabolic processes, as well as fuel further tumor growth and invasion. Meanwhile, fine-tuning of calcium signaling is observed under both normal and pathological conditions. In this context, research into the changes accompanying signal transduction within the tumor microenvironment is a key aspect of the investigation of the role of calcium signaling in tumor development. Factors characteristic of the tumor microenvironment were shown to have a significant effect on the function of calcium channels and the proteins that regulate calcium signaling. Major, adverse microenvironmental factors, such as acidification, elevated levels of reactive oxygen species and hypoxia, have a bearing on the store-operated calcium entry. It is crucial to understand whether changes in the expression of the key SOCE components represent an adaptation to the microenvironment or a result of carcinogenesis.

KEYWORDS calcium, store-operated calcium entry, STIM, Orai, malignant transformation, tumor microenvironment, calcium signaling.

**ABBREVIATIONS** SOC – store-operated channels; SOCE – store-operated calcium entry; SERCA – sarcoplasmic/endoplasmic reticulum  $Ca^{2+}$ -ATPase; PMCA – plasma membrane  $Ca^{2+}$ -ATPase; ROS – reactive oxygen species; ER – endoplasmic reticulum; BC – breast cancer.

#### INTRODUCTION

The tumor microenvironment is shaped by various cell types, both cancer and non-cancer ones (e.g., immune cells). Carcinogenesis is under the continuous influence of neighboring cells, soluble factors, and the extracellular matrix. The soluble factors include nutrients, oxygen, reactive oxygen (ROS) and nitrogen species, ATP, cytokines, growth factors, chemokines, various ions (e.g., Ca²+ and H+), metabolic waste products of cancer cells, etc. [1, 2]. Changes in the intracellular calcium concentration affect proliferation, apoptosis, energy metabolism, and the invasiveness of cancer cells, thereby playing a pivotal role in tumor growth and development [3–5]. To date, a significant amount of data has accumulated indicating the presence of alterations in calcium signaling during tumor

transformation. The expression levels of the proteins involved in calcium signaling are known to change during the development of pathological processes. Meanwhile, it remains unclear whether these changes in calcium signaling are driven by adaptation to the tumor microenvironment, where signaling plays a pivotal role, or by changes in the expression levels of specific proteins involved in calcium signal transduction. It seems that both mechanisms — and probably combinations of the two — need consideration.

#### **Store-operated calcium entry**

Store-operated calcium channels (SOC) residing in the plasma membrane are among the major pathways of calcium entry into non-excitable cells and are widely expressed in various cell types (*Fig.* 1) [6]. SOC activ-

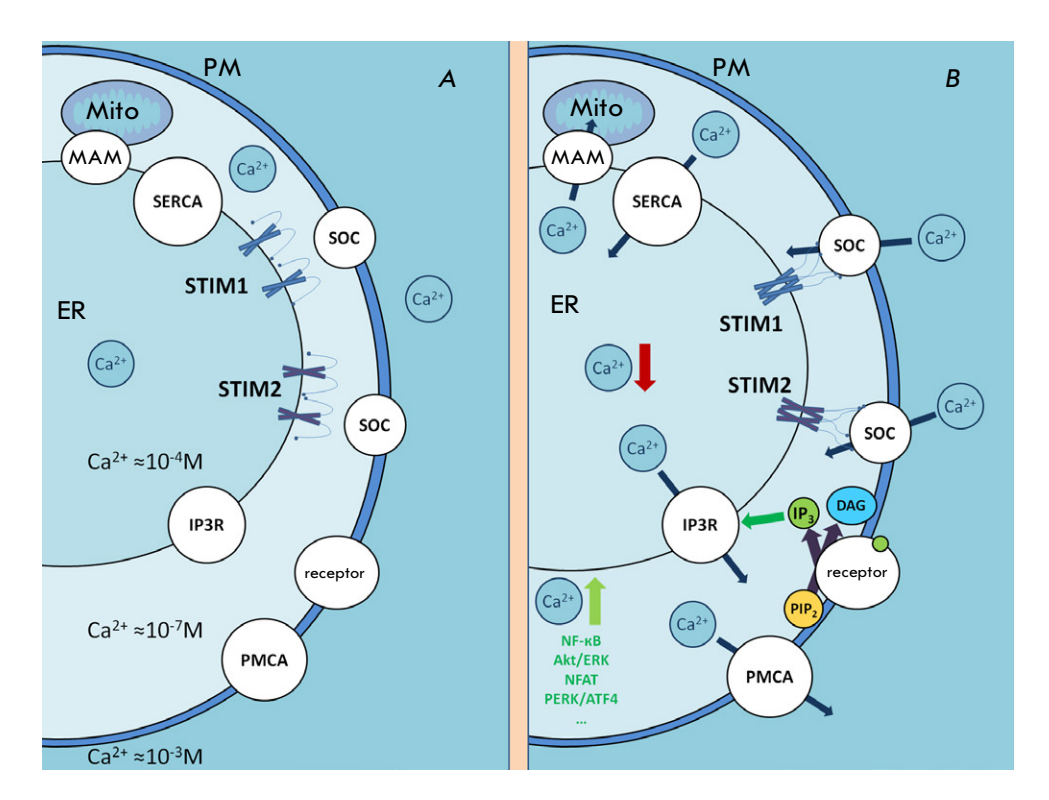


Fig. 1. The schematic of store-operated calcium entry. (A) The region of close contact between the plasma membrane and the ER membrane at rest. (B) Activation of plasma membrane (PM) receptors stimulates IP, production and calcium release from the ER via the IP, receptor. A drop in the calcium concentration within the store causes clustering and conformational changes in STIM proteins, as well as the activation of SOC. Calcium entering the cell can activate signaling pathways, refill the ER calcium store by SERCA pumps, and supply mitochondria (Mito) through membrane contact sites (MAMs). Excess calcium is extruded from the cells primarily by PMCAs

ity is vital for the replenishment of calcium stores in the endoplasmic reticulum (ER) and for the transduction of a multitude of intracellular signals [7]. The entry of extracellular calcium into the cell in response to the depletion of intracellular calcium stores is termed store-operated calcium entry (SOCE). STIM and Orai proteins [8], as well as certain members belonging to the TRPC family, are the key molecular components of SOCE [9-11]. Orai and TRPC form calcium channels in the plasma membrane, while STIM proteins are primarily ER-localized proteins with a single transmembrane domain which function as sensors of the calcium concentration in the ER [12]. A decline in the calcium concentration in the ER is followed by conformational changes, oligomerization, and the clustering of STIM proteins. They were shown to translocate to the area of close contact between the ER membrane and the plasma membrane, where they interact with SOC channels and activate them, thereby mediating the store-operated calcium entry [13].

Two homologs of the STIM protein are expressed in humans: STIM1 and STIM2. Both predominantly reside in the ER membrane, although a small amount of STIM1 is found on the plasma membrane. Both STIM proteins have a similar structure: composed of an N-terminal calcium-binding domain within the ER lumen, a single transmembrane segment, and a C-terminal cytoplasmic domain responsible for pro-

tein-protein interactions [14]. In vertebrates, STIM1 and STIM2 are expressed in all cell types; they function as sensors of the endoplasmic reticulum luminal calcium and activators of SOC. Unlike STIM1, STIM2 is confined exclusively to the ER membrane. STIM2 is known to be a weaker activator of Orai1 than STIM1 but a more sensitive Ca2+ sensor in the ER lumen. The dissociation constant of STIM2 for  $Ca^{2+}$  (500-800  $\mu M$ ) is significantly higher than that of STIM1 (200-600  $\mu$ M) [15]. It is believed that the primary physiological role of STIM2 is to stabilize basal calcium levels in the cytosol and ER [16]. Furthermore, the STIM2 protein mediates various store-dependent and store-independent SOC activation mechanisms and can inhibit SOCE through alternative splicing products [17, 18].

SOCE possess a broad range of regulatory mechanisms. SOC in the plasma membrane is characterized by a set of electrophysiological properties, regulatory mechanisms, and susceptibility to factors such as acidification, hypoxia, and reactive oxygen species. These channels are activated by STIM proteins that differ in their calcium sensitivity and ability to activate Orai channels [19]. Furthermore, SOC can be categorized into groups activated either by STIM1 or STIM2 [20]. Another level of regulation, which is still poorly understood, involves various adapter proteins and lipids residing at the contact sites between

Table 1. SOCE gene expression in breast cancer cell lines and control cells

Cell line	MCF-10A	MCF-7	MDA-MB-231	MDA-MB-468	BT-20	BT-474
Characterization of cells	fibrocystic mastopathy	HER2- ER+	TNBC	TNBC	TNBC	HER2+ ER+
Results of functional studies [29–31]		Orai3 ↑	Orai1 ↑ STIM1 ↑			
Amount of protein normalized with respect to MCF10A [32]	Orai1 Orai2	Orai1↑ Orai2	Orai1↑ Orai2	Orai1 Orai2	Orai1 Orai2↑	
Amount of protein normalized with respect to MCF10A [33]	Orai3 STIM2 TRPC6	Orai3 ↑ STIM2 TRPC6 ↑	Orai3 STIM2↓ TRPC6↑	Orai3 ↑ STIM2 TRPC6 ↑	Orai3 ↑ STIM2 TRPC6	
Amount of protein [34]		STIM1 STIM2	STIM1 ↑ STIM2 ↓			STIM1 ↓ STIM2 ↑
Amount of mRNA [29]		Orai1 ↑ Orai2 Orai3 ↓	Orai1 ↑ Orai2 Orai3 ↓			
Amount of protein normalized with respect to MCF10A [30]	STIM1 Orai1 Orai3	STIM1 ↓ Orai1 ↓ Orai3 ↑	STIM1 Orai1 Orai3 ↓		STIM1 ↑ Orai1 Orai3 ↓	STIM1↓ Orai1↓ Orai3↑
Gene expression [35]	TRPC1 ↑	TRPC1	TRPC1 ↑	TRPC1 ↓	TRPC1 ↑	TRPC1 ↓

Note.  $\uparrow$  – upregulated expression;  $\downarrow$  – downregulated expression. HER2 – HER2/neu receptor; ER – endorphin receptor; TNBC – triple negative breast cancer.

the plasma membrane and the endoplasmic reticulum (e.g., cholesterol,  $IP_3$  receptor, adapter proteins of the Homer family, or cytoskeletal proteins) [14, 21–23].

Importantly, basal calcium concentrations in the cytosol and the ER stores primarily depend on SOCE and significantly affect overall cellular calcium signaling.

Hence, there are several levels of regulation and a broad range of possibilities for fine-tuning the SOCE mechanism to specific conditions. A limited number of reports on alterations in the details of the SOCE mechanism during malignant transformation are available.

## The molecular composition of the mechanism of storage-operated calcium entry in breast cancer

Multiple publications have demonstrated that the expression profile of proteins, as key SOCE components, is altered in cancer (in particular, breast cancer (BC) (*Table 1*), as well as in colon [24], prostate [25], gastric [25], cervical [27], and oral [28] cancers).

*Table 1* lists the data on the expression of the STIM, Orai, and TRPC proteins in the best studied breast cancer cell lines.

The data summarized in *Table 1* attest to significant variations in the protein composition of the store-op-

erated calcium entry (SOCE) across different breast cancer cell lines. Furthermore, the differences in the expression of the key SOCE components result in changes in the functional characteristics of calcium entry in each particular cell line. We define the calcium response amplitude as the maximum change in the intracellular calcium concentration with respect to basal levels. Studies, including our own research, demonstrate that breast cancer lines are characterized by different calcium response amplitudes and basal calcium concentrations (*Fig.* 2), varying sensitivity to specific (CM4620 and BTP2) and non-specific (leflunomide and teriflunomide) SOCE modulators (*Fig.* 3), as well as microenvironmental conditions (ref. [36] and unpublished data).

Currently, there is no clear understanding of whether these functional changes cause the pathology or are a result of SOCE adaptation to new microenvironmental conditions. Both of these scenarios might be possible. For instance, if a cell becomes able to pump slightly more calcium into the cytosol upon initiation of malignant transformation, it promotes active proliferation and invasion. Alternatively, adjustment of a calcium response in cells within a tumor that has already been formed would lead to the accumulation of cells maximally adapted to these specific conditions.

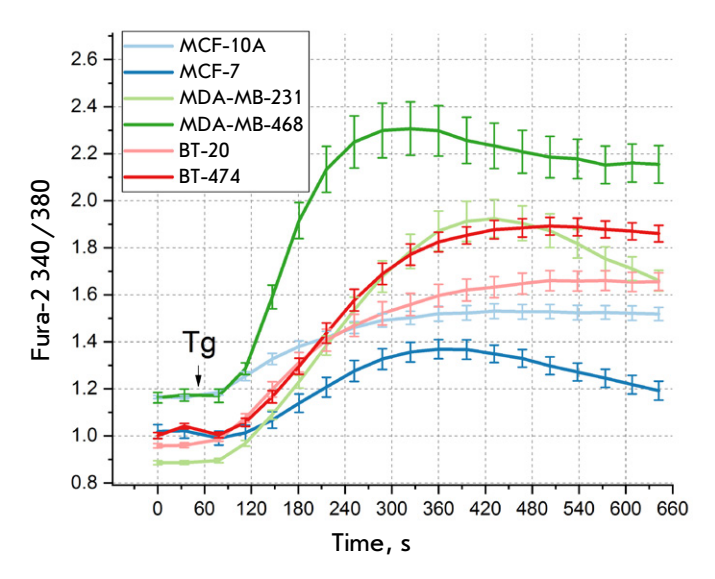


Fig. 2. The Tg-induced responses of different breast cancer cell lines in a medium containing 2 mM Ca<sup>2+</sup>. An arrow indicates the time instant of administering 1  $\mu$ M Tg. The ratio between Fura-2 fluorescence (340 and 380 nm), the mean value, and SEM (n=9-2) are shown

## Physiological functions of store-operated calcium entry upon malignant transformation

Numerous examples demonstrate that the key SOCE proteins are involved in the regulation of proliferation, migration, invasion, the epithelial–mesenchymal transition (EMT), neoangiogenesis, and the metastatic spread of cancer cells [37–39]. Importantly, alterations in protein levels do not trigger a specific transformation pathway common to all cell types. Rather, we observe a degree of disruption of calcium signaling that percolates to various cellular signaling pathways (e.g., the Akt/ERK, NFAT, and PERK/ATF4 pathways), leading to malignant transformation in a manner unique to each tumor type.

In particular, STIM1-mediated calcium entry regulates tumor angiogenesis in Epstein-Barr virus-associated nasopharyngeal carcinoma. The viral-encoded membrane protein LMP1 promotes proliferation, migration, and tubulogenesis by engaging the Akt/ERK pathway. Suppression of STIM1 activity reduces the LMP1 content in exosomes and slows tumor-induced vascular network formation [40]. STIM1 knockout in MDA-MB-231 and other breast cancer cell lines, regardless of their metastatic potential, enhances cell migration, while simultaneously downregulating NFAT1 expression [41]. Orai3 knockout was shown to alter the expression of numerous genes affecting migration and inflammatory/immune responses, includ-

ing hypoxia-induced ones: ID1, TREM-1, and PGF [42]. In colorectal cancer, downregulated STIM2 expression activates the c-Myc and PERK/ATF4 signaling pathways, thus increasing tumor size and promoting invasion and metastatic spread [43]. SOCE was also shown to be implicated in cell cycle disruption. The Orai3-STIM2 complex ensures successful mitosis in prostate cancer cells, preventing mitotic catastrophe. Suppression of Orai3 expression increases SOCE and causes G2/M phase cell cycle arrest, leading to the activation of the Bax/Bcl-2-mediated apoptotic pathway [44]. The Orai1 protein is overexpressed in patients with B-cell chronic lymphocytic leukemia, compared to normal B cells, contributing to the elevation of basal Ca<sup>2+</sup> levels through a constitutive activity of SOC. Selective SOCE inhibitors (GSK-7975A and Synta66) block Ca2+ entry into cells, inducing apoptosis. Furthermore, Orai1 inhibitors exert an additive/synergistic effect when used in combination with therapeutics for B-cell chronic lymphocytic leukemia [45]. In SKBR3 and BT20 breast cancer cell lines characterized by upregulated Orai2 expression, this channel modulates NFAT1 and NFAT4 activation in response to agonists. Orai2 knockdown induces the G0/G1 phase cell cycle arrest and reduces the resistance of cells to apoptosis in patients treated with cisplatin [32].

SOCE-forming proteins have also been found to affect the expression of enzymes that regulate oncogenesis. Tumor samples from patients with oral cancer were characterized by upregulated Orai1 expression and, consequently, an increased rate of Ca<sup>2+</sup> entry into these cells. mRNA analysis revealed that Orai1 regulates many genes encoding oral cancer markers, including metalloproteinases regulated by NFAT4 [46].

Furthermore, there are carcinogenic mechanisms that boost the activity of the SOCE machinery. For instance, upregulated expression of the EHD2 and CAV1/2 proteins is observed in various subtypes of breast cancer. These proteins possibly stabilize plasma membrane caveolae and ensure high cell-surface expression of Orai1, thus leading to increased SOCE that stimulates oncogenesis [47]. In prostate cancer patients, the TSPAN18 protein protects STIM1 against TRIM32-mediated ubiquitination; consequently, STIM1-mediated calcium entry increases, thus intensifying the metastatic spread [48]. Transcriptome analysis data have indicated that NSUN2 expression is significantly upregulated in gastric cancer patients. The NSUN2 gene regulates the stability of Orai2 mRNA through the 5-methylcytosine modification, thereby promoting Orai2 expression and further development of peritoneal metastasis in gastric cancer patients [49].

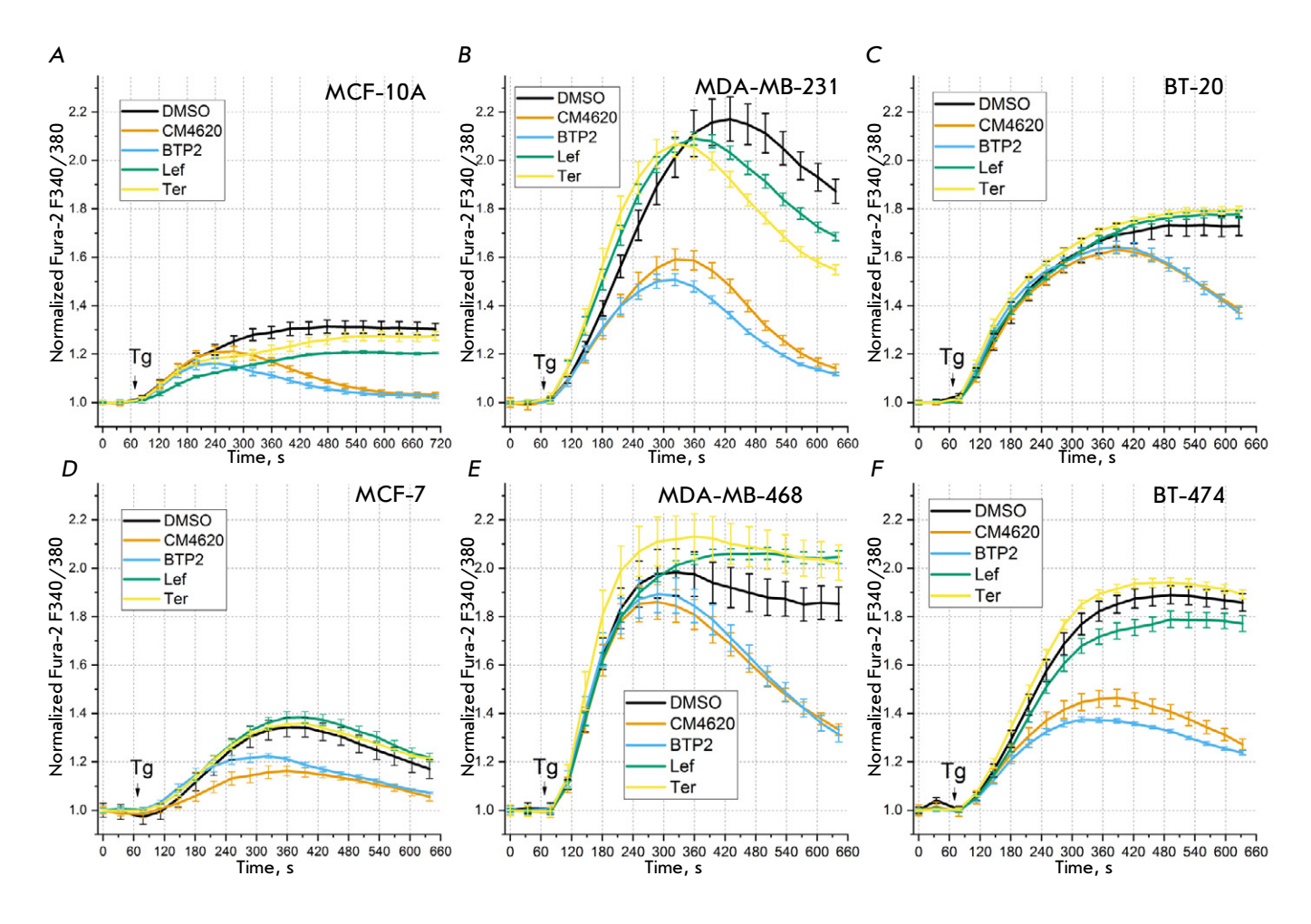


Fig. 3. Measurements of the amplitude of the Tg-induced response in the medium containing 2 mM Ca<sup>2+</sup> after 25-min incubation in the presence of 0.5% DMSO (control),  $5 \mu$ M CM4620 and BTP2,  $50 \mu$ M leflunomide (Lef) and teriflunomide (Ter) in cell lines: (A) MCF-10A; (B) MDA-MB-231; (C) BT-20; (D) MCF-7; (E) MDA-MB-468, and (F) BT-474. An arrow indicates the time instant of administering 1  $\mu$ M Tg. The ratio between Fura-2 fluorescence (340 and 380 nm) normalized with respect to the basal level, the mean value, and SEM (n=9-2) as a function of time are shown. Adapted from ref. [36]

This partial list showing the involvement of SOCE in malignant transformation underscores the critical importance of selecting the proper therapeutic target. Along with impairment of SOCE protein expression, there are certain malignant transformations that directly affect the function of SOCE without altering the expression levels of these proteins. Therefore, effective treatment requires agents that can precisely target the function of specific SOCE proteins in a particular situation. For example, while suppression of STIM1 protein activity is beneficial in nasopharyngeal carcinoma, this approach is forbidden in certain types of breast cancer. Reduction of Orai2 activity is a justified strategy for treating specific breast cancer subtypes, as well as gastric cancer.

## The interplay between store-operated calcium entry and mitochondria

The regulation of mitochondrial activity in cancer cells is one of the fundamental functions of calcium, which is critical for carcinogenesis. The ER is the primary source of calcium for mitochondria, and the structural relationship between these organelles is modulated by various proteins, including calcium channels [50].

By stimulating Ca<sup>2+</sup>-dependent dehydrogenases of the tricarboxylic acid (TCA) cycle, Ca<sup>2+</sup> enhances ATP production and stabilizes the mitochondrial membrane potential [51]. However, a critical increase in Ca<sup>2+</sup> concentration is accompanied by an abrupt rise in the permeability of the inner mitochondrial membrane due to the opening of non-selective pores [50], resulting in the disruption of the respiratory chain, ATP hydrolysis, and osmotic swelling, eventually causing the release of apoptogenic molecules and cell death [52].

Hence, ATP production, biosynthesis of phospholipids and steroid hormones, calcium signal transduction, and oxidation of various metabolites in cancer cells all depend on mitochondrial activity, which is regulated, among other factors, by calcium. Upon carcinogenesis, the amount of calcium entering the cell depends on both internal factors (e.g., the expression of the genes encoding the SOCE proteins) and tumor microenvironment factors. If the amount of incoming calcium is insufficient, cancer cells will not receive the energy required to ensure their viability. Conversely, an excessive influx of calcium will lead to the death of cancer cells. This compels the cell to regulate the calcium influx in a constantly changing microenvironment. Next, we will examine how SOCE is affected by tumor microenvironment factors such as reactive oxygen species, acidification, and hypoxia.

## THE EFFECT OF REACTIVE OXYGEN SPECIES ON STORE-OPERATED CALCIUM ENTRY

Reactive oxygen species are a group of molecules formed via partial reduction of  $\mathrm{O}_2$  and that exhibit high reactivity [53]. Mitochondria generating ROS during ATP synthesis are their intracellular source [54]. Thus, elevated ROS levels were observed in triple-negative breast cancer cells, made possible by mitochondrial activity; ROS have been shown to be important for the survival of these cells, since treatment with antioxidants induced their death [55].

ROS have long been considered harmful to cells, believed to cause oxidative damage to various molecules such as proteins, lipids, and DNA. However, we know that moderate ROS levels are essential for physiological cellular functions, including intracellular signaling, proliferation, and immune responses [56]. The cell employs a number of defense mechanisms to strike a balance between intracellular ROS production and elimination [57].

A large number of ROS sources have been found within tumors and their microenvironment. It has been demonstrated that cancer cells can induce a pathological elevation of ROS levels [58]. Oncogene activation, loss of tumor suppressor genes, hypoxia, as well as mitochondrial DNA mutations, can increase the ROS levels in cancer cells [59]. The tumor microenvironment comprises various types of cells recruited upon tumor formation: neutrophils, T cells, macrophages, and fibroblasts. Exposure to cytokines such as interferon- $\gamma$  (IFN $\gamma$ ), tumor necrosis factor- $\alpha$  (TNF $\alpha$ ),

and interleukin-1 (IL-1) was shown to enhance ROS production by various types of cancer cells [60].

Overall, low ROS levels appear to be beneficial for cancer cells as they can support their proliferative and invasive properties. However, beyond a certain threshold, ROS can become toxic to them. It seems that cancer cells can deploy an adaptive behavior to cope with different stages of ROS elevation (i.e., induce either pro-oxidant or antioxidant mechanisms) [53].

## The effect of reactive oxygen species on the components of store-operated calcium entry

SOCE adaptation is a plausible mechanism of cellular adaptation to altered ROS levels. In particular, ROS modulate the function of Orai channels, thus regulating the calcium response, which is crucial for tumor growth. It has been demonstrated that endogenous and overexpressed Orai1 channels are inhibited by  $\rm H_2O_2$  with  $\rm IC_{50}=34~\mu M$  [61]. The same inhibitory effect was observed for Orai2 channels. In contrast, Orai3 channels were not inhibited by  $\rm H_2O_2$ , indicating that Orai1 and Orai2 are sensitive to ROS, while Orai3 is not [61].

Cysteine residues are the primary targets for ROS in Orai1 and Orai2 [62]. In an Orai3 molecule, cysteine-195 is replaced with glycine, which confers partial resistance to  $\rm H_2O_2$ . Taking into account the differences in sensitivity to ROS among Orai1, Orai2, and Orai3, the ratio between these isoforms in the cell can be a factor that helps calcium signaling adapt to elevated ROS levels.

Similar processes are observed in immune cells. For example, an elevated Orai3/Orai1 ratio was revealed in monocytes, killing bacteria due to rapid  $\rm H_2O_2$  secretion; therefore, switching to the less ROS-sensitive Orai3 channels is an effective adaptation mechanism used by monocytes to withstand their own ROS production [63]. In primary human CD4+ T cells, naïve cells upregulate the Orai3/Orai1 expression ratio upon differentiation into effector cells residing within areas of the inflammation characterized by an elevated ROS concentration [61].

The ratio of expressed Orai proteins – and consequently the dependence of store-operated calcium entry on ROS – is altered not only in immune but also cancer cells (*Table 1*). Thus, reduced Orai3/Orai1 ratios have been observed in prostate cancer [64] and basal-like breast cancer cells [42]. However, elevated Orai3/Orai1 ratios have been reported in prostate cancer [65], as well as estrogen receptor-positive breast cancer [30, 42, 66] and non-basal-like breast cancer [42] as well. The differently directed changes in Orai channel expression in cancer cells are presumably

driven by ROS, as well as other intrinsic and extrinsic factors within the tumor microenvironment.

As discussed above, STIM1 and STIM2 differ in terms of their sensitivity to the calcium level in the stores and ability to activate Orai channels. Furthermore, their sequences carry different oxidation-sensitive cysteine residues. STIM1 carries cysteine residues at positions 49 and 56, which can form a disulfide bond between each other in the presence of ROS [67]. Since cysteine 56 resides next to the Ca<sup>2+</sup>binding domain of STIM1, it probably helps the protein to acquire a constitutively active form that activates SOCE, regardless of ER calcium levels [68]. Interestingly, the situation is diametrically opposite when these cysteine residues are oxidized by reactive nitrogen species. S-nitrosylation of cysteine residues C49 and C56 in STIM1 enhances the thermodynamic stability of its calcium-binding domain, thereby reducing its sensitivity to calcium and suppressing SOCE [69].

In contrast to STIM1, the STIM2 protein carries ten additional cysteine residues within its cytosolic domain. One of these STIM2-specific cysteine residues plays a crucial role in the context of the redox regulation of SOCE. Oxidation of cysteine C313 inhibits SOCE primarily by impeding STIM2 clustering, without affecting the STIM2-Orai1 interplay [70].

Therefore, both STIM proteins are sensitive to ROS-induced oxidation but via different mechanisms: STIM1 is modulated by ROS in the ER lumen, whereas STIM2 is inhibited by ROS in the cytosol.

## Adaptation of store-operated calcium entry to oxidative stress

The mechanisms that alter the expression of SOCE proteins under oxidative stress have been identified. Simulation of 24-h oxidative stress in rat astroglioma cells led to a downregulated expression of STIM2, Orai1, and Orai3, and it also reduced the agonist-induced calcium response. However, the amplitude of SOCE and the degree of filling of the calcium stores remained virtually unchanged [71].

SOCE is highly susceptible to ROS. Sufficiently high ROS concentrations significantly, and nonselectively, affect the fundamental mechanisms maintaining cellular calcium homeostasis. In the case of adaptation to low ROS concentrations, the cell appears to have room for maneuver via the expression of different Orai channel isoforms.

## SUSCEPTIBILITY OF STORE-OPERATED CALCIUM ENTRY TO pH CHANGES

Compromised pH regulation is a shared characteristic of solid tumor cells. In most cases, these cells

have an elevated intracellular pH (7.3–7.6 vs. normal pH 7.2) and reduced extracellular pH (6.8–7.0 vs. normal pH 7.4) compared to nontransformed cells [72]. The increased glycolytic activity in solid tumor cells leads to higher levels of lactate, protons, and carbonic acid in the extracellular environment, resulting in acidification of the tumor microenvironment [73]. Like hypoxia, acidification contributes to drug resistance from the tumor and immunosuppression within its microenvironment [74].

## The effect of pH changes on the components of store-operated calcium entry

Fluctuations in pH levels significantly affect the functioning of numerous ion channels in the cell [75]. The influence of changes in extracellular and intracellular pH on the activity of Orai isoforms has been investigated rather well. Electrophysiological studies have demonstrated that changes in pH modulate both the endogenous SOCE and SOCE in HEK293 cells expressing exogenous STIM1/2 and Orai1/2/3 proteins. It turns out that extracellular acidification inhibits SOCE, while alkalinization potentiates it. Similarly, intracellular acidification reduces SOCE activation. whereas alkalinization accelerates the SOCE activation kinetics without altering the overall current amplitude [76]. Detailed studies demonstrated that the amplitude and kinetics of Orai1-mediated current are strongly dependent on the intracellular pH. The dependence of the current through Orai2 on intracellular pH manifests itself only as changes in amplitude. The Orai3 channel is totally independent of variations in intracellular pH [77]. It is most likely that intra- and extracellular pH regulate the activity of Orai channels through different mechanisms. Extracellular pH appears to modulate SOCE by affecting the Orai channel pore, while intracellular pH can affect aggregation and binding of STIM to Orai at several pH-sensitive sites. Thus, the H155F mutation in Orai noticeably reduces responsiveness to both acidic and alkaline intracellular pH values [78].

Since the amino acids E106, E190, and H115 are conserved in all three Orai isoforms, it is reasonable to assume that they act as common external sensors for acidic pH in all the Orai isoforms. Upon extracellular alkalinization, the amplitude of the current through all Orai channels increases (for Orai2, it rises to a larger extent compared to Orai1 and to a lesser extent compared to Orai3). It is possible that additional mechanisms governing the sensitivity of these channels to elevated pH levels exist [76, 78].

Interestingly, the STIM1-independent Orai1 mutant exhibits a reduced sensitivity to both intracellular alkalinization and acidification [77]. This fact can imply that, under conditions of changing intracellular pH, SOCE is regulated at the level of STIM proteins.

The effect of extracellular pH on other components of the calcium response remains insufficiently explored. The TRPC6 channel, which can be involved in SOCE, is known to be inhibited in acidic pH [79]. Intensification of research into the pH-dependent functioning of the proteins involved in calcium signaling can be anticipated in the coming years.

## Adaptation of store-operated calcium entry to changes in pH

It still remains unclear whether changes in pH affect the expression of SOCE proteins in cancer cells; however, we know that pH has been shown to influence their clustering. Specialized clusters of SOCE proteins, known as calcium entry units (CEUs), are formed in muscle cells. The assembly of functional CEUs - including STIM and Orai proteins - is more intensive at elevated temperatures and reduced pH (i.e., upon intense muscle activity) [80]. Cluster assembly can perfectly be an additional mechanism of SOCE adaptation to a changing microenvironment of a higher order than the STIM-Orai interplay is. This mechanism enables the maintenance of the extracellular calcium influx essential for muscle function during transient acidification, thus preventing its reduction.

Hence, Orai channels, and possibly TRPC6, impede calcium overload of cancer cells under acidic tumor microenvironment conditions, which is caused by their sensitivity to extracellular acidification and reduced conductivity at low pH values. Acidification of the intracellular medium is accompanied by the involvement of additional mechanisms of SOCE regulation at the level of the interplay between the STIM and Orai proteins and the possibility to choose among the Orai isoforms.

## THE EFFECT OF HYPOXIA ON STORE-OPERATED CALCIUM ENTRY

Hypoxia is an essential factor within the tumor microenvironment closely related to cell proliferation, metabolism, angiogenesis, and the immune response. These processes frequently contribute to tumor progression and enhance its metastatic potential, including through the effect of hypoxia on the components of cellular calcium signaling [81].

## The effect of hypoxia on store-operated calcium entry components

With respect to SOCE, hypoxic conditions contribute to the emptying of the ER calcium stores and elevation of the calcium concentration in the cytosol via two interrelated mechanisms: reduction of the cellular ATP level and production of low ROS levels.

Hypoxia may trigger STIM1 activation possibly by reducing the ATP level and pumping Ca<sup>2+</sup> into the cellular store [82]. Hypoxia can also cause the depletion of intracellular calcium stores via the production of low ROS levels, rather than the reduction of the ATP level [83]. Emptying of calcium stores leads to the activation of SOCE, which is further weakened by hypoxia-induced acidification.

Hypoxia is known to cause rapid acidification of many cell types, including smooth muscle, cardiac, cancer, and neuronal cells [84, 85]. Under long-term hypoxia conditions, the cells of most tumor types become characterized by a high glycolysis rate and increased production of metabolic acids [86].

We have demonstrated the existence of a substantial inhibition of the calcium response under short-term hypoxia in MCF-7 and BT-474 BC cells characterized by an elevated Orai3 level (*Table 1*) [36]. Contrariwise, an increased calcium response level under short-term hypoxia is observed in MDA-MB-231 and BT-20 cells characterized by a reduced Orai3 level [30, 36]. Hence, the resistance of cells to calcium overload under hypoxic conditions is dependent on the Orai3 level in the overall SOCE structure. On the other hand, hypoxia upregulates Orai3 expression [42]. Based on the aforementioned data, a conclusion can be drawn that expression of Orai proteins under long-term hypoxia in BC cells can be altered, with the Orai3 level increasing.

## Adaptation of store-operated calcium entry to hypoxia

The Orai3 expression is upregulated under hypoxic conditions in many cancer cells: HCC1569, MDA-MB-231, MCF-7, and PMC42LA breast cancer cells, HT29 colon cancer cells, and Du145 prostate cancer cells. Furthermore, it has been demonstrated for the BC cell lines that changes in the expression levels of Orai3 are a response to long-term hypoxic conditions rather than the reason for the fluctuations in intracellular signaling [42].

The TRPC1 channel is another potential participant in the response to hypoxia in cancer cells [11]. TRPC1 expression is upregulated under hypoxic conditions in MDA-MB-231, MDA-MB-468, and HCC1569 breast cancer cell lines, but the expression levels of the homologous protein TRPC3 remain substantially unaltered [35]. Interestingly, suppression of TRPC1 expression in MDA-MB-231 and MDA-MB-468 cells increases the SOCE amplitude. This fact indirectly indicates that upregulated TRPC1 expression reduces the SOCE amplitude [35, 87]. In this case, similar to

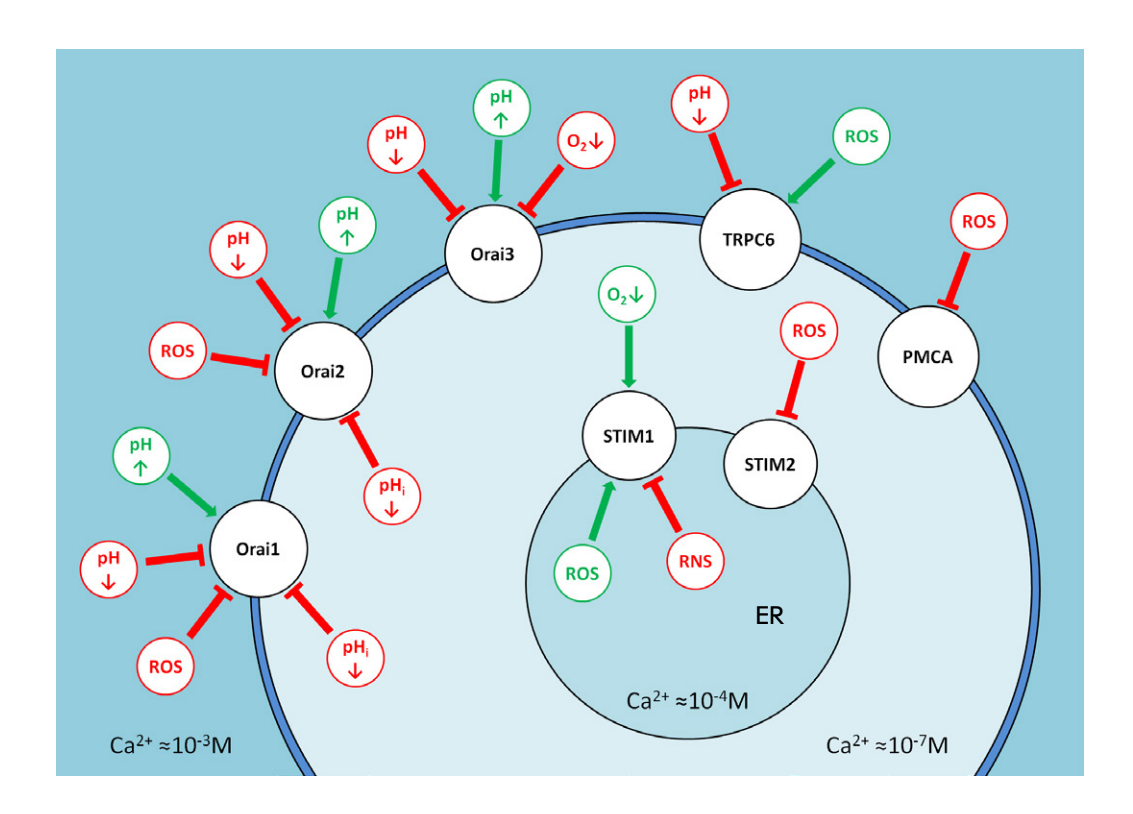


Fig. 4. A schematic showing the effects of tumor microenvironment components on the store-operated calcium entry. The approximate concentrations of calcium in the cell, ER, and the extracellular matrix are specified. The major SOCE proteins are shown in black; the green and red colors denote the activating and inhibitory effects of the respective microenvironmental factors

the Orai3 channel, the TRPC1 channel is involved in the cellular defense mechanism under hypoxic conditions.

Hence, the synergistic effect of several factors causing intracellular calcium imbalance, including acidification and ROS production, is witnessed under hypoxic conditions. The TRPC1 and Orai3 channels can confront these detrimental factors to a certain extent.

# **CONCLUSIONS**

Calcium plays an important role in oncogenesis processes due to its signaling function, as well as by ensuring the functioning of mitochondria [38, 39]. Various calcium signaling mechanisms are involved in the adaptation of cancer cells to the complex land-scape of the tumor microenvironment (*Fig.* 4).

At an increasing ROS concentration, Orai3 ensures the functioning of SOCE, while inhibition of STIM2 prevents calcium overload in the cell. At acidic intercellular and intracellular pH values, conductivity of all the Orai channels suffers, except for Orai3, which is independent of the intracellular pH.

Along with the properties of SOCE proteins *per se*, their expression is also altered in response to stress conditions. Expression of the STIM2, Orai1, and Orai3 proteins is downregulated under oxidative stress; hypoxia upregulates the expression of the TRPC1 and

Orai3 proteins. The reason behind the changes in the expression levels of channels is individual in each particular case (adaptation or a sequela of carcinogenesis); however, these alterations normalize the current tumor microenvironment rather than destabilize calcium signaling in the tumor. Therefore, the lower adaptative potential for cancer cells enhances the effectiveness of antitumor therapy and exerts an independent curative effect.

Many SOCE components are viewed as targets for antitumor therapy [26, 88]. There are certain challenges related to the narrow choice of selective SOCE modulators. Currently, the number of potential targets substantially surpasses the number of available modulators. Unfortunately, there are no selective modulators for most proteins involved in SOCE. For example, the Orai3 channel plays a crucial role in the adaptation of cancer cells to changes in microenvironmental pH, hypoxia, and an elevated ROS level. However, selective modulators for this channel remain to be identified. Meanwhile, both of the activators of this channel, which would lead to calcium overload in cancer cells characterized by upregulated Orai3 expression, and inhibitors that disrupt the overall calcium homeostasis in these cells, are of interest for therapeutic purposes. The existing selective SOCE inhibitors target the main calcium entry pathway through STIM1-Orai1 proteins, making these inhibitors highly

## **REVIEWS**

toxic to the body [89]. They can be used only provided that the targeted delivery problem is solved; otherwise, the systemic harm from their administration outweighs the potential therapeutic benefit. The situation is somewhat better in the therapy of autoimmune diseases, where Auxora (also known as CM4620), a selective Orai1 inhibitor, exhibits a therapeutic effect, although this is accompanied by severe side effects [90]. Minor SOCE components, such as the proteins STIM2, TRPC1, and numerous adapter proteins (SARAF,  $\alpha$ -SNAP, STIMATE, Junctate, IRE1, etc.), should be selected as targets to reduce the chances of systemic toxic effects on the body [23]. Previously, we have identified a modulator of the STIM2-dependent signaling pathway: the low-molecular-weight com-

pound 4-MPTC that exerts an inhibitory effect on SOCE via the STIM2-dependent calcium entry pathway but does not suppress calcium entry through the STIM1-dependent pathway. The target of this compound is still to be identified [91].

A larger number of available selective modulators would enable fine-tuning of SOCE, enhance therapeutic versatility, reduce the adverse effects of therapy, and facilitate the transition toward personalized medicine.

This work was supported by the Ministry of Science and Higher Education of the Russian Federation (Agreement No. 075-15-2021-1075) and the Russian Science Foundation (grant No. 23-44-00054).

### REFERENCES

- 1. Califano A., Alvarez M.J. // Nat. Rev. Cancer. 2017. V. 17. № 2. P. 116–130. doi: 10.1038/nrc.2016.124.
- 2. Xing Y., Zhao S., Zhou B.P., Mi J. // FEBS J. 2015. V. 282.  $\mathbb{N}_2$  20. P. 3892–3898. doi: 10.1111/febs.13402.
- 3. Patergnani S., Danese A., Bouhamida E., Aguiari G., Previati M., Pinton P., Giorgi C. // Int. J. Mol. Sci. 2020. V. 21. № 21. P. 1–27. doi: 10.3390/ijms21218323.
- 4. Nieto-Felipe J., Macias-Diaz A., Sanchez-Collado J., Berna-Erro A., Jardin I., Salido G.M., Lopez J.J., Rosado J.A. // J. Cell. Physiol. 2023. V. 238. № 4. P. 714–726. doi: 10.1002/jcp.30971.
- Benson J.C., Trebak M. // Cell Calcium. 2023. V. 111.
   P. 102716. doi: 10.1016/j.ceca.2023.102716.
- 6. Soboloff J., Rothberg B.S., Madesh M., Gill D.L. // Nat. Rev. Mol. Cell Biol. 2012. V. 13. № 9. P. 549–565. doi: 10.1038/nrm3414.
- 7. Smyth J.T., Hwang S.Y., Tomita T., DeHaven W.I., Mercer J.C., Putney J.W. // J. Cell. Mol. Med. 2010. V. 14. № 10. P. 2337–2349. doi: 10.1111/j.1582-4934.2010.01168.x.
- 8. Prakriya M. // Curr. Top. Membr. 2013. V. 71. P. 1–32. doi: 10.1016/b978-0-12-407870-3.00001-9.
- 9. Kaznacheyeva E., Glushankova L., Bugaj V., Zimina O., Skopin A., Alexeenko V., Tsiokas L., Bezprozvanny I., Mozhayeva G.N. // J. Biol. Chem. 2007. V. 282. № 32. P. 23655–23662. doi: 10.1074/jbc.m608378200.
- 10. Bugaj V., Alexeenko V., Zubov A., Glushankova L., Nikolaev A., Wang Z., Kaznacheyeva E., Bezprozvanny I., Mozhayeva G.N. // J. Biol. Chem. 2005. V. 280. № 17. P. 16790–16797. doi: 10.1074/jbc.m500192200.
- 11. Skopin A., Shalygin A., Vigont V., Zimina O., Glushankova L., Mozhayeva G.N., Kaznacheyeva E. // Biochimie. 2013. V. 95. № 2. P. 347–353. doi: 10.1016/j.biochi.2012.10.004.
- 12. Liou J., Kim M.L., Heo W.Do, Jones J.T., Myers J.W., Ferrell J.E., Meyer T. // Curr. Biol. 2005. V. 15. № 13. P. 1235–1241. doi: 10.1016/j.cub.2005.05.055.
- 13. Prakriya M., Feske S., Gwack Y., Srikanth S., Rao A., Hogan P.G. // Nature. 2006. V. 443. № 7108. P. 230–233. doi: 10.1038/nature05122.
- Sallinger M., Grabmayr H., Humer C., Bonhenry D., Romanin C., Schindl R., Derler I. // J. Physiol. 2024. V. 602.
   P. 1475–1507. doi: 10.1113/jp283828.

- 15. Enomoto M., Nishikawa T., Back S.I., Ishiyama N., Zheng L., Stathopulos P.B., Ikura M. // J. Mol. Biol. 2020. V. 432. № 2. P. 367–383. doi: 10.1016/j.jmb.2019.10.003.
- Brandman O., Liou J., Park W.S., Meyer T. // Cell. 2007.
   V. 131. № 7. P. 1327–1339. doi: 10.1016/j.cell.2007.11.039.
- 17. Ong H.L., De Souza L.B., Zheng C., Cheng K.T., Liu X., Goldsmith C.M., Feske S., Ambudkar I.S. // Sci. Signal. 2015. V. 8. № 359. P. ra3. doi: 10.1126/scisignal.2005748.
- 18. Rana A., Yen M., Sadaghiani A.M., Malmersjö S., Park C.Y., Dolmetsch R.E., Lewis R.S. // J. Cell Biol. 2015. V. 209. № 5. P. 653–670. doi: 10.1083/jcb.201412060.
- Lunz V., Romanin C., Frischauf I. // Cell Calcium. 2019.
   V. 77. P. 29–38. doi: 10.1016/j.ceca.2018.11.009.
- 20. Shalygin A., Skopin A., Kalinina V., Zimina O., Glushankova L., Mozhayeva G.N., Kaznacheyeva E. // J. Biol. Chem. 2015. V. 290. № 8. P. 4717–4727. doi: 10.1074/jbc.m114.601856.
- 21. Ahmad M., Narayanasamy S., Ong H.L., Ambudkar I. // Biomolecules. 2022. V. 12. № 8. P. 1152. doi: 10.3390/biom12081152.
- Nikolaev A.V., Skopin A.Y., Kaznacheyeva E.V. // Biol. Membr. 2004. V. 21. № 6. P. 451–457.
- 23. Berlansky S., Humer C., Sallinger M., Frischauf I. // Int. J. Mol. Sci. 2021. V. 22. № 1. P. 1–29. doi: 10.3390/ijms22010471.
- 24. Kang Q., Peng X., Li X., Hu D., Wen G., Wei Z., Yuan B. // Front. Oncol. 2021. V. 11. P. 649476. doi: 10.3389/fonc.2021.649476.
- 25. Perrouin Verbe M.A., Bruyere F., Rozet F., Vandier C., Fromont G. // Hum. Pathol. 2016. V. 49. P. 77–82. doi: 10.1016/j.humpath.2015.09.042.
- Chang Y., Roy S., Pan Z. // Front. Pharmacol. 2021.
   V. 12. P. 668730. doi: 10.3389/fphar.2021.668730.
- 27. Pan Y., Huang J., Liu K., Xie C., Chen H., Guo Z., Guo S., Chen Y. // Front. Mol. Biosci. 2022. V. 9. P. 1041674. doi: 10.3389/fmolb.2022.1041674.
- 28. Nguyen A., Sung Y., Lee S.H., Martin C.E., Srikanth S., Chen W., Kang M.K., Kim R.H., Park N.H., Gwack Y., et al. // Cells. 2023. V. 12. № 18. P. 2225. doi: 10.3390/cells12182225.
- 29. McAndrew D., Grice D.M., Peters A.A., Davis F.M., Stewart T., Rice M., Smart C.E., Brown M.A., Kenny P.A., Roberts-Thomson S.J., et al. // Mol. Cancer Ther. 2011.

- V. 10. № 3. P. 448–460. doi: 10.1158/1535-7163.mct-10-0923. 30. Motiani R.K., Abdullaev I.F., Trebak M. // J. Biol. Chem. 2010. V. 285. № 25. P. 19173–19183. doi: 10.1074/jbc. M110.102582.
- 31. Yang S., Zhang J.J., Huang X.Y. // Cancer Cell. 2009. V. 15. № 2. P. 124–134. doi: 10.1016/j.ccr.2008.12.019.
- 32. Sanchez-Collado J., Lopez J.J., Cantonero C., Jardin I., Regodón S., Redondo P.C., Gordillo J., Smani T., Salido G.M., Rosado J.A. // Cancers (Basel). 2021. V. 14. № 1. P. 114. doi: 10.3390/cancers14010114.
- 33. Sanchez-Collado J., Lopez J.J., Gonzalez-Gutierrez L., Cantonero C., Jardin I., Salido G.M., Rosado J.A. // Biochem. J. 2020. V. 477. № 17. P. 3183–3197. doi: 10.1042/bcj20200560.
- 34. Miao Y., Shen Q., Zhang S., Huang H., Meng X., Zheng X., Yao Z., He Z., Lu S., Cai C., et al. // Breast Cancer Res. 2019. V. 21. № 1. P. 99. doi: 10.1186/s13058-019-1185-1.
- 35. Azimi I., Milevskiy M.J.G., Kaemmerer E., Turner D., Yapa K.T.D.S., Brown M.A., Thompson E.W., Roberts-Thomson S.J., Monteith G.R. // J. Cell Sci. 2017. V. 130. № 14. P. 2292–2305. doi: 10.1242/jcs.196659.
- 36. Skopin A.Y., Glushankova L.N., Gusev K.O., Kaznacheyeva E.V. // Life (Basel, Switzerland). 2024. V. 14. № 3. P. 357. doi: 10.3390/life14030357.
- 37. Umemura M., Nakakaji R., Ishikawa Y. // J. Physiol. Sci. 2023. V. 73. № 1. P. 21. doi: 10.1186/s12576-023-00878-0.
- 38. Panda S., Chatterjee O., Roy L., Chatterjee S. // Drug Discov. Today. 2022. V. 27. № 3. P. 923–934. doi: 10.1016/j. drudis.2021.11.012.
- 39. Gross S., Mallu P., Joshi H., Schultz B., Go C., Soboloff J. // Advances Cancer Res. 2020. V. 148. P. 233–317. doi: 10.1016/bs.acr.2020.05.003.
- 40. Deng Y., Liu X., Huang Y., Ye J., He Q., Luo Y., Chen Y., Li Q., Lin Y., Liang R., et al. // Cell. Oncol. (Dordr). 2023. V. 46. № 4. P. 987–1000. doi: 10.1007/s13402-023-00790-0.
- 41. Hammad A.S., Yu F., Al-Hamaq J., Horgen F.D., Machaca K. // Cell Calcium. 2023. V. 114. P. 102779. doi: 10.1016/j. ceca.2023.102779.
- 42. Azimi I., Milevskiy M.J.G., Chalmers S.B., Yapa K.T.D.S., Robitaille M., Henry C., Baillie G.J., Thompson E.W., Roberts-Thomson S.J., Monteith G.R. // Cancers. 2019. V. 11. № 2. P. 208. doi: 10.3390/cancers11020208.
- 43. Pathak T., Benson J.C., Johnson M.T., Xin P., Abdelnaby A.E., Walter V., Koltun W.A., Yochum G.S., Hempel N., Trebak M. // bioRxiv Prepr. Serv. Biol. 2023. V. 10. № 02. P. 560521. doi: 10.1101/2023.10.02.560521.
- 44. Kouba S., Buscaglia P., Guéguinou M., Ibrahim S., Félix R., Guibon R., Fromont G., Pigat N., Capiod T., Vandier C., et al. // Cell Calcium. 2023. V. 115. P. 102794. doi: 10.1016/j. ceca.2023.102794.
- Scaviner J., Bagacean C., Christian B., Renaudineau Y., Mignen O., Abdoul-Azize S. // Eur. J. Pharmacol. 2024.
   V. 971. P. 176515. doi: 10.1016/j.ejphar.2024.176515.
- 46. Son G.Y., Tu N.H., Santi M.D., Lopez S.L., Souza Bomfim G.H., Vinu M., Zhou F., Chaloemtoem A., Alhariri R., Idaghdour Y., et al. // Sci. Signal. 2023. V. 16. № 801. P. eadf9535. doi: 10.1126/scisignal.adf9535.
- 47. Luan H., Bielecki T.A., Mohapatra B.C., Islam N., Mushtaq I., Bhat A.M., Mirza S., Chakraborty S., Raza M., Storck M.D., et al. // Elife. 2023. V. 12. P. e81288. doi: 10.7554/elife.81288.
- 48. Zhou Q., Chen X., Yao K., Zhang Y., He H., Huang H., Chen H., Peng S., Huang M., Cheng L., et al. // J. Exp. Clin. Cancer Res. 2023. V. 42. № 1. P. 195. doi: 10.1186/s13046-023-02764-4.

- 49. Liu K., Xu P., Lv J., Ge H., Yan Z., Huang S., Li B., Xu H., Yang L., Xu Z., et al. // Oncogene. 2023. V. 42. № 24. P. 1980–1993. doi: 10.1038/s41388-023-02707-5.
- 50. Garbincius J.F., Elrod J.W. // Physiol. Rev. 2022. V. 102. № 2. P. 893–992. doi: 10.1152/physrev.00041.2020.
- 51. Wescott A.P., Kao J.P.Y., Lederer W.J., Boyman L. // Nat. Metab. 2019. V. 1. № 10. P. 975–984. doi: 10.1038/s42255-019-0126-8.
- 52. Madreiter-Sokolowski C.T., Sokolowski A.A., Graier W.F. // Nutrients. 2017. V. 9. № 10. P. 1117. doi: 10.3390/nu9101117.
- Helfinger V., Schröder K. // Mol. Aspects Med. 2018.
   V. 63. P. 88–98. doi: 10.1016/j.mam.2018.02.003.
- 54. Brand M.D. // Free Radic. Biol. Med. 2016. V. 100. P. 14–31. doi: 10.1016/j.freeradbiomed.2016.04.001.
- 55. Sarmiento-Salinas F.L., Delgado-Magallón A., Montes-Alvarado J.B., Ramírez-Ramírez D., Flores-Alonso J.C., Cortés-Hernández P., Reyes-Leyva J., Herrera-Camacho I., Anaya-Ruiz M., Pelayo R., et al. // Front. Oncol. 2019. V. 9. P. 480. doi: 10.3389/fonc.2019.00480.
- 56. Martínez-Reyes I., Diebold L.P., Kong H., Schieber M., Huang H., Hensley C.T., Mehta M.M., Wang T., Santos J.H., Woychik R., et al. // Mol. Cell. 2016. V. 61. № 2. P. 199–209. doi: 10.1016/j.molcel.2015.12.002.
- 57. Ray P.D., Huang B.W., Tsuji Y. // Cell. Signal. 2012. V. 24. № 5. P. 981–990. doi: 10.1016/j.cellsig.2012.01.008.
- 58. Schumacker P.T. // Cancer Cell. 2006. V. 10. № 3. P. 175–176. doi: 10.1016/j.ccr.2006.08.015.
- 59. Sullivan L.B., Chandel N.S. // Cancer Metab. 2014. V. 2. № 17. doi: 10.1186/2049-3002-2-17.
- 60. Liou G.Y., Storz P. // Free Radical Research. 2010. V.44. №5. P. 479–496. doi: 10.3109/10715761003667554.
- 61. Bogeski I., Kummerow C., Al-Ansary D., Schwarz E.C., Koehler R., Kozai D., Takahashi N., Peinelt C., Griesemer D., Bozem M., et al. // Sci. Signal. 2010. V. 3. № 115. P. ra24. doi: 10.1126/scisignal.2000672.
- 62. Veal E.A., Day A.M., Morgan B.A. // Mol. Cell. 2007. V. 26. No 1. P. 1–14. doi: 10.1016/j.molcel.2007.03.016.
- 63. Saul S., Gibhardt C.S., Schmidt B., Lis A., Pasieka B., Conrad D., Jung P., Gaupp R., Wonnenberg B., Diler E., et al. // Sci. Signal. 2016. V. 9. № 418. P. ra26. doi: 10.1126/scisignal.aaf1639.
- 64. Holzmann C., Kilch T., Kappel S., Dörr K., Jung V., Stöckle M., Bogeski I., Peinelt C. // Biophys. J. 2015. V. 109. № 7. P. 1410–1419. doi: 10.1016/j.bpj.2015.08.006.
- 65. Dubois C., Vanden Abeele F., Lehen'kyi V., Gkika D., Guarmit B., Lepage G., Slomianny C., Borowiec A.S., Bidaux G., Benahmed M., et al. // Cancer Cell. 2014. V. 26. № 1. P. 19–32. doi: 10.1016/j.ccr.2014.04.025.
- 66. Motiani R.K., Zhang X., Harmon K.E., Keller R.S., Matrougui K., Bennett J.A., Trebak M. // FASEB J. 2013. V. 27. № 1. P. 63–75. doi: 10.1096/fj.12-213801.
- 67. Prins D., Groenendyk J., Touret N., Michalak M. // EMBO Rep. 2011. V. 12. № 11. P. 1182–1188. doi: 10.1038/ embor.2011.173.
- 68. Hawkins B.J., Irrinki K.M., Mallilankaraman K., Lien Y.C., Wang Y., Bhanumathy C.D., Subbiah R., Ritchie M.F., Soboloff J., Baba Y., et al. // J. Cell Biol. 2010. V. 190. № 3. P. 391–405. doi: 10.1083/jcb.201004152.
- 69. Gui L., Zhu J., Lu X., Sims S.M., Lu W.Y., Stathopulos P.B., Feng Q. // J. Mol. Biol. 2018. V. 430. № 12. P. 1773–1785. doi: 10.1016/j.jmb.2018.04.028.
- Gibhardt C.S., Cappello S., Bhardwaj R., Schober R., Kirsch S.A., Bonilla del Rio Z., Gahbauer S., Bochicchio A., Sumanska M., Ickes C., et al. // Cell Rep. 2020. V. 33.

- № 3. P. 108292. doi: 10.1016/j.celrep.2020.108292.
- 71. Mokrane N., Snabi Y., Cens T., Guiramand J., Charnet P., Bertaud A., Menard C., Rousset M., de Jesus Ferreira M.C., Thibaud J.B., et al. // Front. Aging Neurosci. 2021. V. 13. P. 785727. doi: 10.3389/fnagi.2021.785727.
- 72. White K.A., Grillo-Hill B.K., Barber D.L. // J. Cell Sci. 2017. V. 130. № 4. P. 663–669. doi: 10.1242/jcs.195297.
- 73. Chiche J., Brahimi-Horn M.C., Pouysségur J. // J. Cell. Mol. Med. 2010. V. 14. № 4. P. 771–794. doi: 10.1111/j.1582-4934.2009.00994.x.
- 74. Arnaiz E., Harris A.L. // Front. Immunol. 2022. V. 13. P. 821816. doi: 10.3389/fimmu.2022.821816.
- 75. Pethő Z., Najder K., Carvalho T., McMorrow R., Todesca L.M., Rugi M., Bulk E., Chan A., Löwik C.W.G.M., Reshkin S.J., et al. // Cancers (Basel). 2020. V. 12. № 9. P. 1–37. doi: 10.3390/cancers12092484.
- 76. Beck A., Fleig A., Penner R., Peinelt C. // Cell Calcium. 2014. V. 56. № 3. P. 235–243. doi: 10.1016/j.ceca.2014.07.011.
- 77. Rychkov G.Y., Zhou F.H., Adams M.K., Brierley S.M., Ma L., Barritt G.J. // J. Physiol. 2022. V. 600. № 3. P. 623–643. doi: 10.1113/JP282502.
- 78. Tsujikawa H., Yu A.S., Xie J., Yue Z., Yang W., He Y., Yue L. // Sci. Rep. 2015. V. 5. P. 16747. doi: 10.1038/srep16747.
- 79. Semtner M., Schaefer M., Pinkenburg O., Plant T.D. // J. Biol. Chem. 2007. V. 282. № 46. P. 33868–33878. doi: 10.1074/jbc.m702577200.
- 80. Girolami B., Serano M., Di Fonso A., Paolini C., Pietrangelo L., Protasi F. // Int. J. Mol. Sci. 2023. V. 24. № 6. P. 5328. doi: 10.3390/ijms24065328.
- 81. Audero M.M., Prevarskaya N., Pla A.F. // Int. J. Mol. Sci. 2022. V. 23. № 13. P. 7377. doi: 10.3390/ijms23137377.
- 82. Mancarella S., Wang Y., Deng X., Landesberg G., Scalia R., Panettieri R.A., Mallilankaraman K., Tang X.D.,

- Madesh M., Gill D.L. // J. Biol. Chem. 2011. V. 286. № 52. P. 44788–44798. doi: 10.1074/jbc.m111.303081.
- 83. Gusarova G.A., Trejo H.E., Dada L.A., Briva A., Welch L.C., Hamanaka R.B., Mutlu G.M., Chandel N.S., Prakriya M., Sznajder J.I. // Mol. Cell. Biol. 2011. V. 31. № 17. P. 3546–3556. doi: 10.1128/mcb.05114-11.
- 84. Chiche J., Ilc K., Laferrière J., Trottier E., Dayan F., Mazure N.M., Brahimi-Horn M.C., Pouysségur J. // Cancer Res. 2009. V. 69. № 1. P. 358–368. doi: 10.1158/0008-5472. CAN-08-2470.
- 85. Kandilci H.B., Richards M.A., Fournier M., Şimşek G., Chung Y.J., Lakhal-Littleton S., Swietach P. // Front. Cardiovasc. Med. 2021. V. 7. P. 617038. doi: 10.3389/fcvm.2020.617038.
- 86. Li Y., Zhao L., Li X.F. // Technol. Cancer Res. Treat. 2021. V. 20. P. 15330338211036304. doi: 10.1177/15330338211036304.
- 87. Davis F.M., Peters A.A., Grice D.M., Cabot P.J., Parat M.O., Roberts-Thomson S.J., Monteith G.R. // PLoS One. 2012. V. 7. № 5. P. e36923. doi: 10.1371/journal. pone.0036923.
- 88. Rubaiy H.N. // Pharmaceuticals (Basel). 2023. V. 16. № 2. P. 162. doi: 10.3390/ph16020162.
- 89. Norman K., Hemmings K.E., Shawer H., Appleby H.L., Burnett A.J., Hamzah N., Gosain R., Woodhouse E.M., Beech D.J., Foster R., et al. // PLoS One. 2024. V. 19. № 1. P. e0296065. doi: 10.1371/journal.pone.0296065.
- 90. Miller J., Bruen C., Schnaus M., Zhang J., Ali S., Lind A., Stoecker Z., Stauderman K., Hebbar S. // Crit. Care. 2020. V. 24. № 1. P.502. doi: 10.1186/s13054-020-03220-x.
- 91. Skopin A.Y., Grigoryev A.D., Glushankova L.N., Shalygin A. V., Wang G., Kartzev V.G., Kaznacheyeva E.V. // Acta Naturae. 2021. V. 13. № 1. P. 140–146. doi: 10.32607/actanaturae.11269.

# Ortho- and Meta-monochlorinated Biphenyls Suppress Humoral Immunity and Exert Toxic Effects on Mouse Liver Cells

D. O. Egorova<sup>1\*</sup>, S. V. Gein<sup>1</sup>, N. A. Korolev<sup>1</sup>, N. P. Loginova<sup>2</sup>

<sup>1</sup>Perm Federal Research Center, Ural Branch of the Russian Academy of Sciences (PFRC UB RAS), Perm, 614990 Russia

<sup>2</sup>E.A. Vagner Perm State Medical University, Perm, 614990 Russia

\*E-mail: daryao@rambler.ru

Received: December 16, 2024; in final form, May 13, 2025

DOI: 10.32607/actanaturae.27596

Copyright © 2025 National Research University Higher School of Economics. This is an open access article distributed under the Creative Commons Attribution License, which permits unrestricted use, distribution, and reproduction in any medium, provided the original work is properly cited.

ABSTRACT Widespread environmental contamination with polychlorinated biphenyls (PCBs) leads to serious health problems for humans and animals. Our main focus should be on studying the negative effects of exposure to medium- and highly chlorinated PCBs in the human body. There is limited information on the impact of low-chlorinated biphenyls containing 1–2 substituents per molecule on the functions of mammalian organs and systems. Under natural conditions, PCBs can undergo bacterial degradation; the resulting compounds belong to a group of secondary pollutants and are considered hazardous to the environment. Because of limited research, the question regarding the impact of mono-substituted chlorobiphenyl congeners, as well as the products of their biotransformation, remains open. In the presented work, the effects of ortho- and meta-substituted monochlorinated biphenyls on the functions of immune system cells and the morphofunctional state of the liver of mammals in vivo are revealed for the first time. PCB 1 and PCB 2 were found to suppress humoral immunity and induce a productive inflammatory response, as well as widespread protein dystrophy with necrotic foci in the liver. The products of a aerobic bacterial transformation of PCB 1 and PCB 2 were shown to not have a negative effect on the mammalian immune system but proved toxic to hepatocytes, although to a lesser extent than the original chlorobiphenyls.

**KEYWORDS** monochlorinated biphenyls, humoral immunity, hepatocytes, biodegradation, leukocytes. **ABBREVIATIONS** PCBs – polychlorinated biphenyls; PCB 1 - ortho-monochlorobiphenyl; PCB 2 - meta-monochlorobiphenyl; PFCs – plaque-forming cells; GC-MS – gas chromatography-mass spectrometry; HPLC – high-performance liquid chromatography.

# **INTRODUCTION**

One of the pressing issues of our time is the impact of polychlorinated biphenyls (PCBs) and their derivatives, formed in the environment under the influence of natural factors, on the human and animal organisms. Even though the Stockholm Convention prohibits the production and use of PCBs, they continue to remain in the environment and to pose a direct threat to public health [1]. The PCB group consists of 209 compounds that are different in their number of substituents and positions in the molecule. PCBs enter the human body via accumulation in food chains [2]. PCBs lead to disruption in the development of animal fetuses, are one of the causes of diabetes, cause diseases of the skin and nervous system, and provoke

the emergence of cancers and genetic disorders [3, 4]. The negative effect of individual medium- and highly chlorinated PCB congeners containing more than three substituents per molecule, as well as commercial mixtures, on immunity has been demonstrated [5–7]. However, the question of the impact of low-chlorinated biphenyls on animal and human health remains open.

The main path to preventing the insertion of PCBs into food chains is by biodegrading them in the environment via the activity of the enzymatic systems of aerobic bacteria. This results in the formation of hydroxylated chlorobiphenyl derivatives and chlorobenzoic acids, which can also have negative effects when ingested by mammals [8].

In this work, the effects of *ortho*- and *meta*-substituted monochlorinated biphenyls and the products of their bacterial degradation on the parameters of adaptive immunity and the morphofunctional state of the mouse liver were investigated for the first time *in vivo*.

### **EXPERIMENTAL PART**

White Swiss mice of either sex weighing 18–23 g were used in this study. The animals were kept under vivarium conditions with a 12-h lighting cycle, twice-daily feeding with natural feed in an amount corresponding to daily norms, with unlimited access to water. Experiments were conducted in accordance with the recommendations and ethical standards specified in the European Convention for the Protection of Vertebrate Animals Used for Experimental and Other Scientific Purposes. Permission No. IRB00010009 was obtained from the Local Ethics Committee of the Institute of Ecology and Genetics of Microorganisms, UB RAS (Perm, Russian Federation) (Protocol No. 29 dated October 8, 2024).

Ortho-monochlorobiphenyl (PCB 1) and metamonochlorobiphenyl (PCB 2) were administered to mice orally, in corn oil, sequentially, every other day, at a dosage of 100 mg/kg. This dosage choice is based on literature sources [9]. The biodegradation products of PCB 1 and PCB 2 were administered to mice orally as an aqueous solution, every other day, at a dosage corresponding to 100 mg/kg of the initial substrate. The control groups were given corn oil and a mineral culture medium free of bacterial cells; each group contained 7–11 individuals.

The duration of the experiment was 25 days. Humoral immunity was induced on day 19 of the experiment by immunization with sheep red blood cells into the abdominal cavity, at a concentration of 108 cells in 200 µL of physiological saline. Induction of delayedtype hypersensitivity (DTH) reaction was achieved on day 24 of the experiment by inserting a resolving dose of sheep red blood cells under the skin of the left foot and an identical volume of a 0.9% NaCl solution under the skin of the right foot. On day 25, the animals were relieved from the experiment by decapitation under ether anesthesia. The humoral immune response was assessed according to the number of plaque-forming cells using localized hemolysis in a gel (Jerne plaque assay). The severity of the DTH reaction was assessed by measuring paw edema using the mass index, which was calculated using the following formula:

$$(R_{\rm exp}-R_{\rm c})/R_{\rm c}$$
  $\times$  100%,

where  $R_{\rm exp}$  is the mass of the limb under experiment and  $R_{\rm c}$  is the mass of the control limb.

Liver tissues were fixed in 10% neutral formalin in a phosphate buffer (pH 7.2), followed by embedding in Histomix paraffin. Histological specimens were prepared using standard histological methods. To assess the overall morphological picture in the experiment, sections were stained with hematoxylin and eosin. Evaluation and photographing were performed using an Olympus microscope (Japan) with the Imeg prosoftware package (free version).

The biodegradation products of PCB 1 and PCB 2 were obtained in experiments with washed cells of the aerobic strain *Rhodococcus* sp. FG1 (VKM Ac-3030), according to the procedure described in ref. [11]. Cultivation lasted 24 h. Quantitative analysis of chlorobiphenyls and their hydroxy derivatives was performed under GC-MS conditions [11]. The content of substances in each test sample was calculated using the internal normalization method. Qualitative analysis was performed using the NIST17 database. The contents of benzoic and chlorobenzoic acid were determined by HPLC in a culture medium freed from bacterial cells by centrifugation (9,660 g, 3 min, mini-Spin centrifuge (Eppendorf, Germany)) according to ref. [10].

Statistical analysis of the results was performed using the unpaired Student's t-test in Microsoft Excel. The data in the tables are presented as a mean and standard error (M  $\pm$  m).

## **RESULTS AND DISCUSSION**

As previously reported, medium- and high-chlorinated biphenyls have a suppressive effect on both humoral and cell-mediated immunity in vertebrates [5–7]. The present study demonstrated in an *in vivo* experiment that PCB 1 and PCB 2 significantly reduced the number of plaque-forming cells (PFCs) in the spleen, both in terms of relative and absolute values. However, these compounds did not have a significant effect on delayed-type hypersensitivity (DTH) (*Table 1*).

Hence, administration of PCB 1 and PCB 2 resulted in the suppression of humoral immunity, while not affecting cell-mediated immunity parameters.

It was discovered that, after microbial transformation, the products of PCB 1 and PCB 2 had no statistically significant effect on the number of plaque-forming cells in the spleen or on the intensity of the DTH response compared to the control animals that were receiving a mineral medium (Cs) used for cultivation of the microorganisms utilized for pollutant degradation (*Table 2*).

The GC-MS and HPLC data, as well the data in the NIST17 and KEGG databases (http://kegg.jp), appear to suggest that the strain *Rhodococcus* sp. FG1 de-

Table 1. The effect of *ortho*-monochlorobiphenyl (PCB 1) and *meta*-monochlorobiphenyl (PCB 2) on the number of PFCs in the spleen and the intensity of the DTH response

Substance	lgPFC/million	lgPFC/organ	DTH index,
Corn oil (Cm)	$2.25 \pm 0.11$	$4.66 \pm 0.09$	$20.06 \pm 1.78$
PCB 1	$1.70 \pm 0.19^*$	$4.11 \pm 0.20^*$	$21.73 \pm 2.37$
PCB 2	$1.69 \pm 0.22^*$	$4.07 \pm 0.22*$	$25.59 \pm 3.62$

Note: \* $p \le 0.05$  vs. control.

Table 2. The Effect of biodegradation products of *ortho*-monochlorobiphenyl (PCB 1) and *meta*-monochlorobiphenyl (PCB 2) on the number of PFCs in the spleen and the intensity of the DTH response

Substance	lgPFC/million	lgPFC/organ	DTH index,
Mineral medium (Cs)	$2.04 \pm 0.15$	$4.29 \pm 0.19$	$30.97 \pm 4.56$
PCB 1 biodegradation products	$2.00 \pm 0.07$	4.48 ± 0.11	$24.63 \pm 5.38$
PCB 2 biodegradation products	$2.02 \pm 0.17$	$4.43 \pm 0.19$	$19.59 \pm 2.68$

grades PCB 1 through the classical aerobic oxidative pathway, giving rise to 2-chlorobenzoic acid as the main compound. PCB 2 degradation results in the formation of two congeners of hydroxylated chlorobiphenyl derivatives, as well as benzoic and 3-chlorobenzoic acids (*Fig. 1*). However, in contrast to the 2,4,4'-trichlorobiphenyl metabolites [8], they do not exert a negative effect on the immune system of mice.

Histological examination of the liver revealed that the control groups presented a standard organ structure, with all the structures showing signs of functional activity (Fig. 2A,D). Oral administration of PCB 1 and PCB 2, as compared to the control group, resulted in a significant increase in the number of binucleated hepatocytes, as well as in that of cells with nuclei of different sizes, small foci of hepatocyte necrosis, and in a pronounced productive inflammatory reaction with signs of widespread protein dystrophy (Fig. 2B,C). According to ref. [11], the reaction severity was estimated at 3 points. Lugewig and Robertson [12] have noted that intraperitoneal administration of low-chlorinated biphenyls results in extensive cellular changes in liver tissues, while they found no dependence be-

Fig. 1. The scheme of PCB 2 oxidation by the enzymatic system of the strain *Rhodococcus* sp. FG1 and the main degradation products: (A) the metabolic pathway begins with oxidation of 2 and 3 carbon atoms in the unsubstituted ring of the biphenyl molecule; (B) the metabolic pathway begins with oxidation of 2 and 3 carbon atoms in the substituted ring of the biphenyl molecule

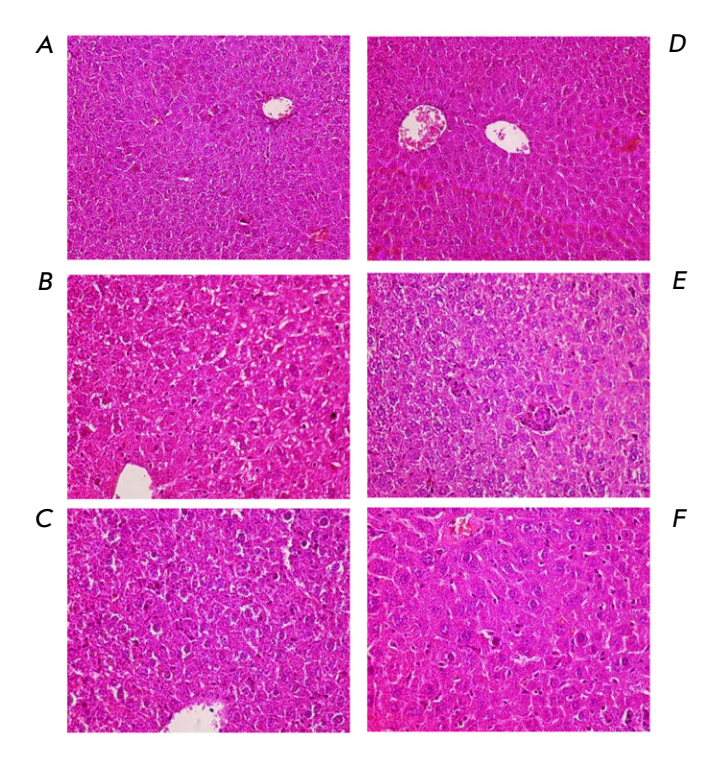


Fig. 2. The structure of the liver of the mice in the control groups ((A) corn oil; (D) bacterial culture medium), under the influence of PCB 1 (B), PCB 2 (C), PCB 1 biodegradation products (E), and PCB 2 biodegradation products (F) by the strain Rhodococcus sp. FG1. Magnification:  $\times 400$ . Hematoxylin and eosin staining

# RESEARCH ARTICLES

tween the administered PCB congener and the severity of the resulting effect. Signs of moderate protein dystrophy of hepatocytes, moderate anisokaryosis, an increased number of binucleated hepatocytes in the central regions of the hepatic lobules, and a moderately productive inflammatory reaction were all observed in the liver of the animals that received bacterial degradation products of PCB 1 and PCB 2, (Fig. 2E,F). According to ref. [11], the reaction severity was estimated at 1.5 points. In light of all this, it appears safe to assume that the hydroxy derivatives of PCB 1 and PCB 2, and (chloro)benzoic acids, are less toxic to hepatocytes than the parent monochlorobiphenyls.

### CONCLUSION

This study has revealed for the first time that *ortho*-and *meta*-monochlorinated biphenyls suppress humoral immunity and cause a productive inflammatory reaction in the liver, accompanied by signs of cellular dystrophy with necrotic foci. The products of bacterial degradation of the chlorobiphenyls under consideration do not exhibit an immunosuppressive effect; however, they continue to have a toxic effect on liver cells, albeit to a lesser extent. •

This work was supported by the Russian Science Foundation (grant No. 24-24-00498).

## REFERENCES

- Zhu M., Yuan Y., Yin H., Guo Z., Wei X., Qi X., Liu H., Dang Z. // Sci. Total Environ. 2022 V. 805. Article 150270. doi: 10.1016/j.scitotenv.2021.150270.
- 2. Frossard V., Vagnon C., Cottin N., Pin M., Santoul F., Naffrechoux E. // Sci. Total. Environ. 2023. V. 902. Article 166037. doi: 10.1016/j.scitotenv.2023.166037.
- 3. Lan T., Liu B., Bao W., Thorne P.S. // Sci. Rep. 2023. V. 13. № 1. Article 18322. doi: 10.1038/s41598-023-45301-1.
- 4. Miletić M., Kmetič I., Kovač V., Šimić B., Petković T., Štrac D.Š., Pleadin J., Murati T. // Env. Sci. Pollut. Res. 2023. V. 30. №. 31. P. 77318–77327. doi: 10.1007/s11356-023-27812-6.
- 5. Gao Y., Huang W., Jiang N., Fang J.K.H., Hu M., Shang Y., Wang Y. // Mar. Environ. Res. 2023. V. 192. Article 106214. doi: 10.1016/j.marenvres.2023.106214.
- 6. Duffy J.E., Carlson E., Li Y., Prophete C., Zelikoff J.T. // Mar. Environ. Res. 2002. V. 54.  $\mathbb{N}_2$  3–5. P. 559–563. doi: 10.1016/s0141-1136(02)00176-9.

- 7. Hammond J.A., Hall A.J., Dyrynda E.A. // Aquat. Toxicol. 2005. V. 74. № 2. P. 126–138. doi: 10.1016/j.aquatox.2005.05.006.
- 8. Rengelshausen J., Randerath I., Schettgen T., Esser A., Kaifie A., Lang J., Kraus T., Ziegler P. // Arch. Toxicol. 2023. V. 97. № 10. P. 2609–2623. doi: 10.1007/s00204-023-03578-1.
- 9. Guidelines for Preclinical Studies of Medicinal Products. Part 1. M.: Grif & K. 2012. 944 p.
- Egorova D.O., Gorbunova T.I., Pervova M.G., Kir'yanova T.D., Demakov V.A., Saloutin V.I., Chupakhin O.N. // J. Haz. Mat. 2020. V. 400. Article 123328. doi: 10.1016/j. jhazmat.2020.123328.
- 11. Senkova A.V., Savin I.A., Chernopovskaya E.L., Davydova A.S., Meshchaninova M.I., Bishani A., Vorobyeva M.A., Zenkova M.A. // Acta Naturae. 2024. V. 16. № 2 (61). P. 61–71. doi: 10.32607/actanaturae.27393.
- 12. Ludewig G., Robertson L.W. // Cancer Lett. 2013. V. 334. P. 46–55. doi: 10.1016/j.canlet.2012.11.041.

# Cabbage Peptide miPEP156a Enhances the Level of Accumulation of Its mRNA in Transgenic Moss *Physcomitrium patens*

T. N. Erokhina<sup>1\*</sup>, E. V. Ryabukhina<sup>1</sup>, I. S. Lyapina<sup>1</sup>, D. Y. Ryazantsev<sup>1</sup>, S. K Zavriev<sup>1</sup>, S. Y. Morozov<sup>2</sup>

<sup>1</sup>Shemyakin-Ovchinnikov Institute of Bioorganic Chemistry, Russian Academy of Sciences,

Moscow, 117997 Russia

<sup>2</sup>Lomonosov Moscow State University, Moscow, 119991 Russia

\*E-mail: tne@mx.ibch.ru

Received April 07, 2025; in final form, May 13, 2025

DOI: 10.32607/actanaturae.27668

Copyright © 2025 National Research University Higher School of Economics. This is an open access article distributed under the Creative Commons Attribution License, which permits unrestricted use, distribution, and reproduction in any medium, provided the original work is properly cited.

ABSTRACT MicroRNAs are endogenous, small non-coding RNAs that regulate gene expression at the post-transcriptional level by cleaving target mRNAs. Mature microRNAs are products of the processing of their primary transcripts (pri-miRNAs). Now, it has been discovered that the products of the translation of some plant pri-miRNAs are peptide molecules (miPEP). These peptides have the capacity to physically interact with their open reading frames (ORFs) in the transcribed pri-miRNAs and, thus, positively regulate the accumulation of these RNAs and the corresponding mature microRNAs. Most conserved microRNAs play an important role in plants development and their response to stress. In this work, we obtained transgenic Physcomitrium patens moss plants containing Brassica oleracea miPEP156a ORF in the genome under the control of a strong 35S cauliflower mosaic virus promoter and analyzed the effect of the exogenous peptide on the transcription of this ORF in the protonemata of two transgenic moss lines. It turned out that the chemically synthesized peptide miPEP156a increases the accumulation of its own mRNA during moss culture growth, as was previously shown in studies by foreign researchers and in our own work for a number of peptides in monocotyledonous and dicotyledonous plants. These findings confirm that pri-miRNA regions that are located outside the coding region of the peptide are not required for transcriptional activation. Moreover, we have also succeeded in showing that the presence of a specific promoter of the microRNA gene does not affect the phenomenon of transcription activation; this phenomenon per se is not species-specific and is observed in transgenic plants, regardless of the origin of the miPEP.

KEYWORDS microRNA, peptides, miPEP, pri-miRNA, transgenic plants, PCR analysis.

ABBREVIATIONS pri-miRNA – primary transcripts of microRNA genes; miPEP – peptide encoded by primary transcript of microRNA genes; OTF – open translation frame; PCR – polymerase chain reaction.

# **INTRODUCTION**

MicroRNA genes are known to be transcribed in the form of large primary transcripts (pri-miRNA) and to become mature miRNAs only after several maturation stages [1]. Like any protein-coding gene, microRNA genes are transcribed by RNA polymerase II, yielding the primary transcript pri-miRNA, which consists of several hundreds or thousands of nucleotides. The internal domain of this primary transcript contains a characteristic hairpin structure consisting of a partially double-stranded microRNA sequence which is cleaved into its mature form under the action of the DCL1 protein encoded by the *Dicer* gene [1]. First, this enzyme cleaves the 5'- and 3' terminal regions of the primary transcript to convert the transcript into a

hairpin-like miRNA precursor (pre-miRNA) and, then, cleaves pre-miRNA to release the miRNA-miRNA\* duplex. This duplex is then translocated into the cytoplasm, where one of the strands (corresponding to microRNA) is incorporated into the ribonucleoprotein particle formed by Argonaute nuclease, giving rise to the RISC complex, which further ensures microRNA-mediated gene silencing [1].

Ten years ago, a number of pri-miRNAs were found to contain small open reading frames which can encode regulatory peptides known as microRNA-encoded peptides (miPEPs) [2]. In plants, miPEPs potentiate the transcription and accumulation of the respective pri-miRNA, being an example of positive feedback. This enhances the accumulation of mature

microRNAs and suppression of the target genes for microRNAs [3, 4]. Overexpression of miPEP in the treatment of leaves and roots with chemically synthesized exogenic peptides may significantly alter the development of roots, as well as enhance anthocyanin accumulation and resistance to biotic and abiotic stress [4–7]. Importantly, a number of these phenomena can be successfully used to improve the commercially significant properties of plants [4, 5, 7, 8].

Previously, we employed the bioinformatic approach to perform a comparative analysis of ORF sequences within pri-miRNA genes in plant genomes and identified a novel group of miPEPs (miPEP156a peptides) encoded by pri-miR156a across several dozen species belonging to the Brassicaceae family [9]. Chemically synthesized exogenous miPEP156a peptides can efficiently penetrate plant seedlings through their root system and systemically migrate to leaves. The peptides exhibit an explicit morphological effect that accelerates primary root growth. Simultaneously, miPEP156a peptides upregulate the expression of their own pri-miR156a [9]. Importantly, this peptide is able to rapidly enter the cell nucleus and bind to chromatin. In this study, we have identified the general properties of the secondary miPEP156a structure and detected its alterations that are induced by the formation of a peptide complex with nucleic acids [9].

It has been proved recently that the Mt-miPEP171b peptide expressed in legumes interacts with transcribed (mostly incomplete) pri-miR171b molecules within the complex with the chromosomal DNA template strand. A hypothesis has been put forward that this is a novel type of protein-RNA binding that is entirely dependent on the presence of a specific linear codon set in the template encoding this miPEP, and that these peptides can perform specific regulatory functions only with respect to their pri-miRNAs [10]. Based on the features of the interaction between miPEPs and their pri-miRNA, the following sequence for the activation of pri-miRNA transcription by encoded peptides has been proposed: (1) in the cytoplasm, miPEP is translated from full-length pri-miRNA or its fragment comprising the ORF encoding the miPEP; (2) this peptide then migrates to the nucleus, where it binds to the synthesized pri-miRNA within its coding sequence; and (3) this interaction boosts microRNA accumulation at the transcriptional level [4, 10]. Existing experimental evidence precludes drawing any conclusion as to whether miPEP binds to the ribonucleotide strands of pri-miRNA (or RNA, forming an RNP) or to RNA-DNA hybrids. Clearly, it cannot be ruled out that miPEPs can interact not only with RNA, but also, as demonstrated previously [3], with DNA (and/or chromatin) in microRNA gene regions. Hence, miPEPs can regulate the activity of RNA polymerase II and/or the mediator complex during the transcription initiation and/or elongation stage [8].

Our study, employing the model of miPEP156a expressed in cabbage (Brassica oleracea), aimed to elucidate the following: (1) the significance of the primiRNA regions outside the peptide-coding domain for transcriptional activation; (2) the role of the specific microRNA gene promoter in the transcriptional activation phenomenon; and (3) whether the transcriptional activation phenomenon is species-specific: i.e., whether the miPEP peptide from one plant species can function in other taxonomically distant species. For this purpose, we engineered transgenic moss (Physcomitrium patens) plants harboring the ORF for broccoli miPEP156a in their genome, under the control of the strong cauliflower mosaic virus (CaMV) 35S promoter, and analyzed the effect of the exogenous peptide on the transcription of this ORF in moss protonemata.

### **EXPERIMENTAL PART**

The coding region of the miPEP156a ORF, including the initiation and termination codons, was amplified by polymerase chain reaction (PCR) using the chromosomal DNA from *B. oleracea* as a template. A pair of DNA primers was used for this purpose: mir156r (5'-CTTTCTTTATGGCTCTTGTCGCTT) and mir156f (5'-AAATGTTCTGTTCAATTCAATGC) [9]. The resulting amplification product was cloned into the pPLV27 vector using ligation-independent cloning (LIC) [11]. Following cloning, the pPLV27-miPEP156a plasmid (*Fig. 1*) was propagated in *Escherichia coli* cells, purified using the Qiagen Plasmid Maxi Kit (Qiagen, Germany), and sequenced.

To engineer transgenes, protonemata of the P. patens moss (Gransden 2004 strain) were cultivated on 9-cm Petri dishes containing a solid Knop medium supplemented with 1.5% agar (Helicon, Russia) and 500 mg/L ammonium tartrate (Helicon) under white light illumination from fluorescent lamps (MLR-352H Sanyo Plant Growth Incubator, Panasonic, Japan), with a photon flux density of 61 µmol/m<sup>2</sup> under a 16-h photoperiod at 24°C and 50% relative humidity. Protoplasts were isolated from five-day-old protonemal tissue. The protonemata were collected from the agar surface using a spatula, gently pressed, and placed into a 0.5% Driselase solution (Sigma-Aldrich, USA) in 0.48 M mannitol for 45 min under continuous rocking in the dark. The resulting suspension was filtered through a 100-µm metal sieve. The protoplasts were pelleted in 50-mL plastic tubes by 5-min centrifugation at 150 g and washed twice with 0.48 M mannitol, followed by centrifugation under identi-

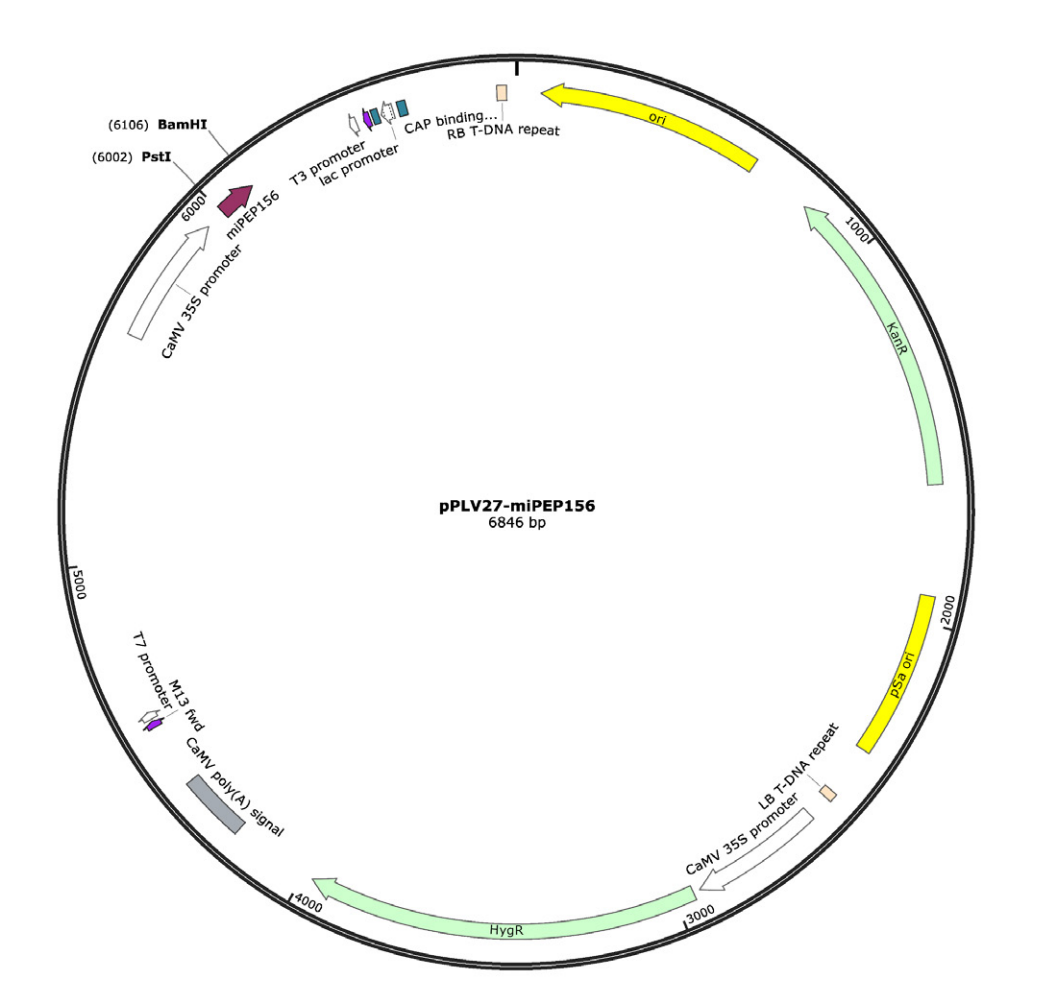


Fig. 1. Scheme of plasmid pPLV27-miPEP156a bearing the coding region of miPEP156a (shown with a violet arrow) for expression in transgenic plants

cal conditions. After removing the supernatant, the protoplasts were transformed according to the PEG-mediated transformation protocol in [11]. The protoplasts (1.5  $\times$  106/mL) were resuspended in a MMg solution (0.48 M mannitol, 15 mM MgCl $_{\!_{2}}$ , 0.1% MES, pH 5.6) and incubated for 20 min. Next, 10 µg of the pPLV27-miPEP156a plasmid (Fig. 1) and 33% PEG solution were added, followed by an additional 30 min of incubation. After washing, the protoplasts were plated in top agar in Petri dishes containing a film-coated solid medium. The plates were kept in the dark for 24 h and then transferred to standard cultivation conditions to allow protoplast regeneration.

To select the clones carrying the target gene insertion, the regenerated protoplasts were cultivated on a selective medium containing hygromycin. Five stable transgenic lines of *P. patens* moss were identified: 2450, 2451, 2453, 2456, and 2483. Total DNA was extracted from the plant tissues of these lines using a DNeasy Plant Kit according to the manufacturer's protocol (Qiagen). The PCR analysis shows that specific reaction products carrying a 700-bp miR156a ORF insertion, obtained using the primers p35Sf (5'-AACAAAGGATAATTTCGGGGAAAC) and tNOSr

(5'-TCGCGTATTAAATGTATAATTGC) complementary to the pPLV27 plasmid regions carrying the 35S promoter and transcription terminator, respectively (Fig. 1), formed only in lines 2450 and 2483 (Fig. 2). Insertion specificity was confirmed by sequencing the PCR products. Interestingly, the colonies of these moss lines were characterized by substantially different growth rates. Whereas the growth rate of line 2483 was similar to that of wild-type plants, slower colony development was observed for line 2450. Therefore, it is important to mention that transgenic P. patens plants overexpressing a number of endogenous peptides also tend to exhibit a reduced colony growth rate [11].

To investigate the effect of the miPEP156a peptide on mRNA expression in transgenic plants by quantitative PCR, protonemata of lines P patens 2450 and 2483 were cultured in 100 mL of a liquid Knop medium supplemented with 500 mg/L ammonium tartrate (Helicon, Russia) on rocking shakers under white light illumination from fluorescent lamps in a Sanyo Plant Growth Incubator MLR-352H (Panasonic, Japan), with a photosynthetic photon flux density of 61  $\mu$ mol/m², under a 16-h photoperiod at 24°C and 50% relative

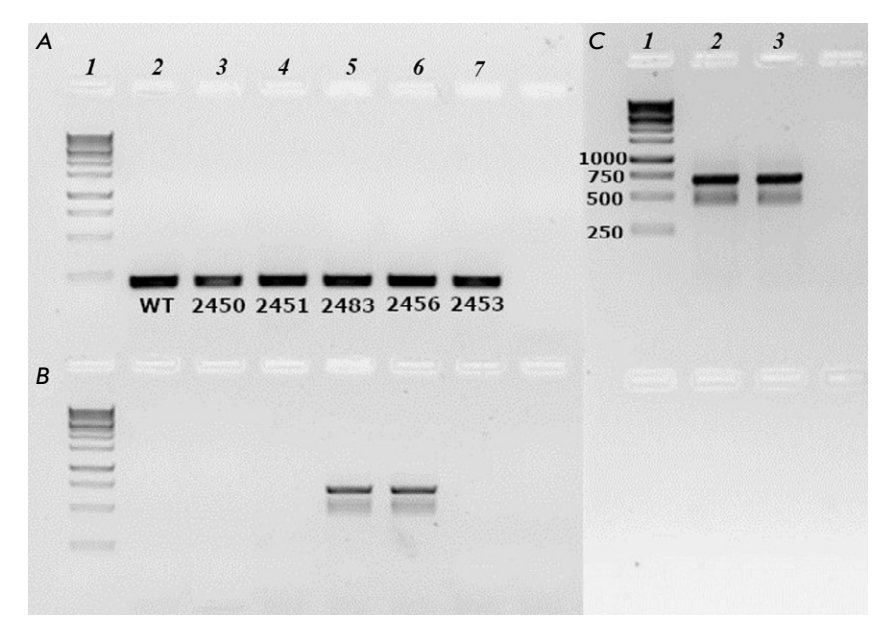


Fig. 2. Results of PCR for detection of the desired inserts in the selected hygromycin-resistant lines of P. patens (lines 2450, 2451, 2483, 2456, and 2453). Genomic DNA from the non-transformed moss line (WT) was used as the control. (A) – control PCR for reference moss gene EF1-alpha (translation elongation factor 1a). Lane 1 - DNA size markers; 2 - WT; 3 - line 2450; 4 - line 2452; 5 - line 2483; 6 - line 2456; and 7 - line 2453. (B) - PCR of moss genomic DNA with the primers p35Sf and tNOSr. Lanes are arranged identically to panel (A). (C) – second PCR experiment with slow-growing moss line 2450. Lane 1 - DNA size markers; 2 - line 2550; and 3 - DNA of plasmid pPLV27-miPEP156a

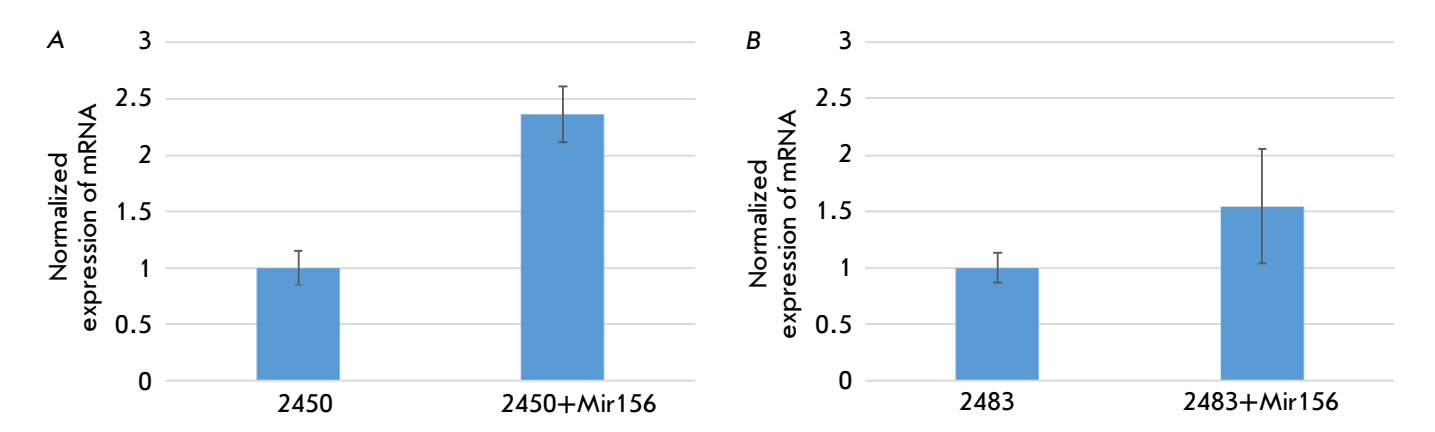


Fig. 3. PCR for measuring the expression level for mRNA of miPEP156a in the transgenic moss P. patens lines. (A) line 2450 and (B) line 2483. RNA was isolated from five independent moss cultures for each line. The figure shows the average statistical values as a bar chart and standard deviations. The statistical significance of the differences in the sum of values in the control experiments (without incubation with the peptide) and experimental experiments (with miPEP156a peptide added) was p < 0.05 for these two samples according to the Student's t test (GraphPad Prism 7.0, https://graphpad\_prism.software.informer.com/7.0/)

humidity. For the analysis, seven-day-old protone-mata were treated with an aqueous solution of the peptide (5  $\mu$ g/mL) in a final volume of 50 mL. The samples were incubated overnight. Next, the protone-mal filaments were separated from the medium, blotted using filter paper to remove excess moisture, and flash-frozen in liquid nitrogen. Total RNA was extracted from the frozen tissues using the TRIzol<sup>TM</sup> reagent (Invitrogen, USA) according to the manufacturer's protocol. After concentration quantification, 2  $\mu$ g of RNA was treated with DNase I (Thermo Fisher Scientific, USA). Reverse transcription with a random hexamer primer using a Mini kit (Eurogen, Russia)

was then performed. The resulting cDNA was added to the qPCR reaction mixture using the reagents and protocols provided by the manufacturer (Eurogen). Quantitative PCR was carried out using the premixed qPCRmix HS (Eurogen) on a DTprime amplification system (DNA-Technology, Russia). The reaction mixture (25  $\mu$ L) contained 10 pmol of each primer and 1× Eva Green intercalating dye. The following amplification program was used: 95°C – 5 min; 95°C – 15 s, 60°C – 15 s\*; 72°C – 15 s; 45 cycles (\* – fluorescence detection in the FAM channel). After data processing, the Cq values were used to calculate normalized expression using the QGene software [12] (*Fig. 3*).

### **RESULTS AND DISCUSSION**

Quantitative PCR (Fig.~3) revealed that treatment of the moss culture with chemically synthesized exogenous peptide miPEP156a in the nutrient solution enhanced the accumulation level of its own mRNA in the transgenic moss culture. In line 2483, accumulation of the RNA template for the miPEP156a peptide increased by  $\sim 60\%$ . This effect was even more pronounced for line 2450: accumulation of the RNA template for the cabbage peptide increased by 240%, exceeding the effect observed for treated cabbage seedlings [9].

In this study, we generated transgenic moss *P. patens* plants harboring the ORF for broccoli miPEP156a in their genome under the control of the strong Cauliflower Mosaic Virus 35S promoter and analyzed the effect of the exogenous peptide on the transcription of this ORF in the protonemata of two transgenic moss lines. The chemically synthesized exogenous miPEP156a peptide was found to enhance the accumulation of its own mRNA in the

moss culture, as was demonstrated previously for a range of peptides in monocotyledonous and dicotyledonous plants [3–5]. Our findings here indicate that pri-miRNA regions outside the peptide-coding domain are not required for transcriptional activation. Furthermore, the specific microRNA gene promoter is not involved in the transcriptional activation phenomenon, and activation per se is not species-specific. In other words, the miPEP156a peptide expressed in Brassica plants can function in other taxonomically distant plant species such as moss. Hence, our findings are consistent with the proposed mechanism of miPEP action, where the peptide binds to its own transcribed pri-miRNA template, thereby activating the synthesis of these RNAs [10]. ●

The authors declare no conflict of interest.

This study was supported by the Russian Science Foundation (grant No. 24-24-00016, https://rscf.ru/project/24-24-00016/).

#### REFERENCES

- 1. Axtell M.J. // Annu. Rev. Plant Biol. 2013. V. 64. № 1. P. 137–159. doi: 10.1146/annurev-arplant-050312-120043.
- 2. Lauressergues D., Couzigou J.M., Clemente H.S., Martinez Y., Dunand C., Bécard G., Combier J.P. // Nature. 2015. V. 520. № 7545. P. 90–93. doi: 10.1038/nature14346.
- 3. Erokhina T.N., Ryazantsev D.Y., Zavriev S.K., Morozov S.Y. // Int. J. Mol. Sci. 2023. V. 24. № 3. P. 2114. doi: 10.3390/ijms24032114.
- Thuleau P., Ormancey M., Plaza S., Combier J.P. // J. Exp. Bot. 2024. P. erae501. doi: 10.1093/jxb/erae501.
- 5. Erokhina T.N., Ryazantsev D.Y., Zavriev S.K., Morozov S.Y. // Plants. 2024. V. 13. № 8. P. 1137. doi: 10.3390/plants13081137.
- 6. Ormancey M., Guillotin B., Ribeyre C., Medina C., Jariais N., San Clemente H., Thuleau P., Plaza S., Beck M., Combier J.P. // Plant Biotechnol. J. 2024. V. 22. № 8. P. 13–15. doi: 10.1111/pbi.14187.
- 7. Zhou J., Zhang R., Han Q., Yang H., Wang W., Wang Y.,

- Zheng X., Luo F., Cai G., Zhang Y. // Plant Cell Rep. 2024. V. 44. N<sub>2</sub> 1. P. 9. doi: 10.1007/s00299-024-03380-y.
- 8. Ormancey M., Thuleau P., Combier J.P., Plaza S. // Biomolecules. 2023. V. 13. № 2. P. 206. doi: 10.3390/biom13020206.
- 9. Erokhina T.N., Ryazantsev D.Y., Samokhvalova L.V., Mozhaev A.A., Orsa A.N., Zavriev S.K., Morozov S.Y. // Biochemistry (Moscow). 2021. V. 86. № 5. P. 551–562. doi: 10.1134/S0006297921050047.
- Lauressergues D., Ormancey M., Guillotin B., Gervais V., Plaza S., Combier J.P. // Cell Rep. 2022. V. 38. № 6.
   P. 110339. doi: 10.1016/j.celrep.2022.110339.
- 11. Fesenko I., Kirov I., Kniazev A., Khazigaleeva R., Lazarev V., Kharlampieva D., Grafskaia E., Zgoda V., Butenko I., et al. // Genome Res. 2019. V. 29. № 9. P. 1464–1477. doi: 10.1101/gr.253302.119.
- 12. Simon P. // Bioinformatics. 2003. V. 19. № 11. P. 1439–1440. doi: 10.1093/bioinformatics/btg157.

# p2rx3 Knockout Mice Have Altered Energy Metabolism in Hippocampal Neurons

A. S. Zelentsova, M. V. Pokrovskii, E. A. Patrakhanov, V. S. Shmigerova, M. Yu. Skorkina, A. V. Deykin

Belgorod State National Research University, Belgorod, 308015 Russia

\*E-mail: marinaskorkina0077@gmail.com

Received: November 02, 2024; in final form, February 18, 2025

DOI: 10.32607/actanaturae.27551

Copyright © 2025 National Research University Higher School of Economics. This is an open access article distributed under the Creative Commons Attribution License, which permits unrestricted use, distribution, and reproduction in any medium, provided the original work is properly cited.

ABSTRACT The hippocampus is a key component of the brain that is associated with the formation of longterm memory, the energy metabolism of neurons playing a pivotal role in its mechanisms. The P2X3 receptor in the hippocampus is considered an attractive target when searching for novel biologically active substances that could work to reduce anxiety, epileptic conditions, and improve cognitive functions. In this work, the intensity of mitochondrial respiration, the glycolytic capacity, and the energy phenotype of hippocampal neurons were studied in p2rx3 knockout mice. The p2rx3 knockout mice were engineered by genome editing using the CRISPR/Cas9 system. The primary mixed culture of hippocampal neurons was derived from two-day-old newborn mice with the  $p2rx3^{+/-}$  and  $p2rx3^{+/-}$  genotypes. Mitochondrial respiration was measured on a Seahorse Bioscience HS mini Cell Metabolism Analyzer (Agilent, USA) using the appropriate kits for the Mitostress test, glycotest, and energy phenotype assessment test. The transgenic mice with the  $p2rx3^{-1}$ genotype were characterized by an aerobic type of mitochondrial respiration, an increase in ATP production by 84.4% (p < 0.05), an increase in maximum respiration by 72.3% (p < 0.05), and a 36% (p < 0.05) increase in the respiratory reserve. Meanwhile, the spare respiratory capacity of mitochondria, the rate of glycolysis, and the glycolytic capacity in these mice were reduced by 36.6, 75.7 and 78.6% (p < 0.05), respectively. Our findings indicate that mitochondria work at close to maximum energy capacity. The p2rx3 knockout animals are a unique model for the search for pharmacological targets that can help correct the energy metabolism of brain cells and eliminate cognitive dysfunctions.

KEYWORDS p2rx3 gene, hippocampus, primary mixed neuronal culture, mitochondrial respiration.

ABBREVIATIONS ROS – reactive oxygen species; CNS – central nervous system; EDTA – ethylenediamine-tetraacetic acid; AMPA – alpha-amino-3-hydroxy-5-methyl-4-isoxazolepropionic acid; ATP – adenosine triphosphate; CAMK II – calcium calmodulin-dependent protein kinase; CRISPR/Cas9 – clustered regularly interspaced short palindromic repeats; ECAR – extracellular acidification rate; FCCP – carbonyl cyanide-4 (trifluoromethoxy) phenylhydrazone; NMDA – ionotropic glutamate receptor selectively binding N-methyl-D-aspartate; OCR – oxygen consumption rate; PBS – phosphate buffered saline; P2X3KO – mice lacking the P2X3 receptor.

# **INTRODUCTION**

Energy metabolism of hippocampal neurons is closely related to cognitive functions, memory, and learning processes [1]. The mechanisms of synaptic signal transmission in the hippocampus involve the ATP molecule and purine receptors [2]. The functional attribute of the P2X receptor family is to generate intracellular Ca<sup>2+</sup> signals when the membrane potential is close to its physiological resting level [3]. The P2X3 receptor in the hippocampus is an attractive

target for the study of anxiety and motivation processes [4], as well as that of the pathogenesis of epileptic states [5]. Abnormalities in hippocampal synaptic plasticity, as well as impaired long-term depression in the CA1 and CA3 synapses and the dentate gyrus of the hippocampus, were observed in mice lacking the P2X3 receptor (P2X3KO). Yet P2X3KO mice still performed adequately on spatial learning tests in a water maze, suggesting that knocking out the p2rx3 gene improved learning. In addition, P2X3KO mice

performed better in a task that involved visually locating and swimming to a platform compared to wild-type mice [5]. Despite the numerous studies that have been devoted to various aspects of how the P2X3 receptor functions [6], the question of the relationship between the receptor and mitochondrial function that determines the activity of cellular metabolism, calcium homeostasis, and, as a consequence, the regulation of the synaptic plasticity of the hippocampus in the central nervous system remains poorly studied. Our study focuses on the intensity of mitochondrial respiration and glycolytic capacity. It also assesses the energy phenotype of hippocampal neurons in p2rx3 knockout mice.

# **EXPERIMENTAL PART**

# Work with laboratory animals

The animals were kept in a conventional vivarium of the Belgorod State National Research University, with artificially regulated daylight hours (12 h dark and 12 h light), under a temperature regime of 22–26°C. They had free access to food and water. The work was guided by the ethical principles that regulate the handling of laboratory animals in accordance with the

European Convention for the Protection of Vertebrate Animals Used for Experimental and other Scientific Purposes (ETS No. 170). All painful manipulations with the animals were performed in accordance with regulatory standards: Directive 2010/63/EU of the European Parliament and of the Council of the European Union of September 22, 2010 on the protection of animals used for scientific purposes and approved by the Committee for the Control of the Care and Use of Laboratory Animals of Belgorod National Research University (expert opinion No. 01i/23 dated January 23, 2023).

The animals with an edited genome were obtained by microinjection of the genetic construct into the pronucleus of the donor mouse zygote, followed by transplantation of the reproductive material into the recipient's female (Fig. 1B) [7–9]. A single guide RNA (sgRNA) recognizing the sequence of the second exon of the p2rx3 gene was selected using the CHOPCHOP online search tool. The selected sgRNA 5'-GGCCTACCAAGTGCGGGACACGG(CCA)-3' (PAM, shown in parentheses) (Fig. 1A), which had no off-target sites with fewer than three mismatches, was tested in a series of control experiments on blastocysts and used to generate p2rx3 knockout mice.

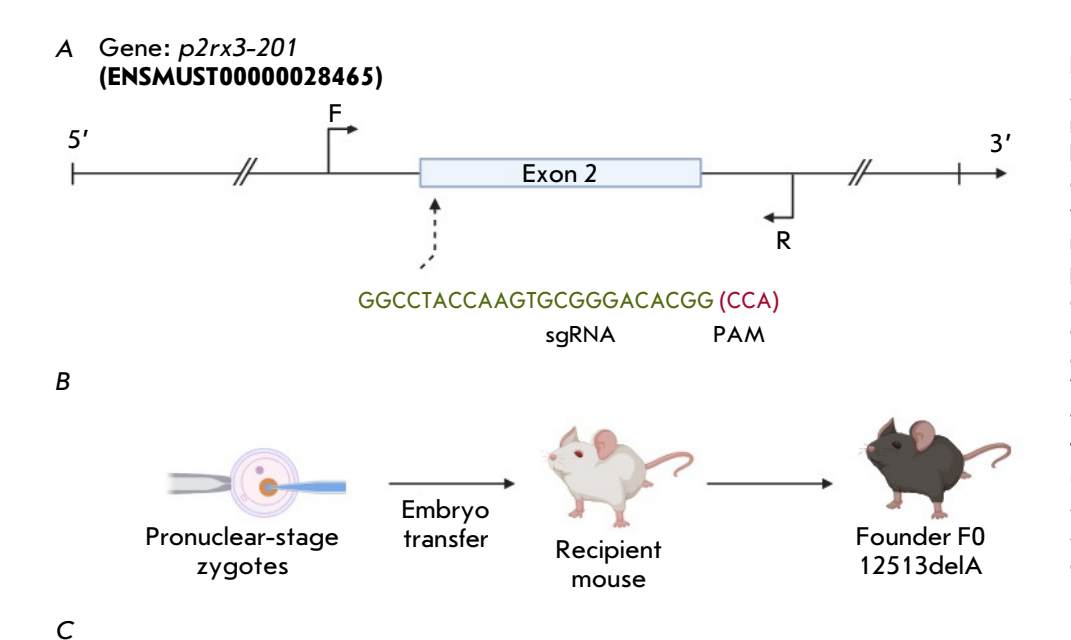
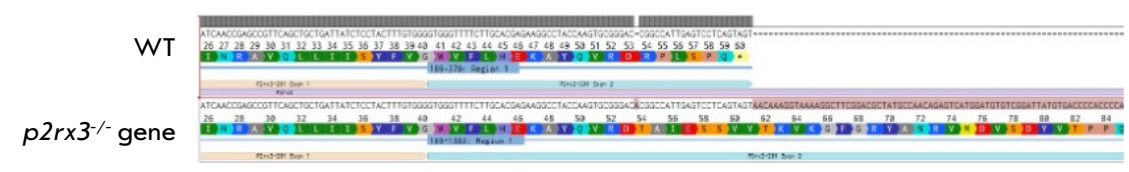


Fig. 1. Creating a p2rx3 knockout mouse. (A) Guide RNA selected for gene editing using the CRISPR / Cas9 method. (B) The process of pronuclear injection and creation of the F0 generation. (C) The transcript of the *p2rx3* gene from a wild-type (WT) mouse and a mouse with a knockout of this gene

ENSMUSG00000028456-12513delA



# Genetic analysis of the offspring

Genotyping of mice was performed by Sanger sequencing of the PCR product containing the recognition zone of the selected sgRNA (forward and reverse primers 5'-ACTAAGCAGGAACTCATCCCAA-3' and 5'-CATAATCCGACACATCCATGAC-3') (Eurogen, Russia), Fig. 1A, in the Genome Collective Use Center according to the recommended protocol. The results were analyzed using the Decodr Internet resource.

Animals with a frameshift in the p2rx3 gene by one nucleotide in exon 2 were obtained, leading to the replacement of six codons and formation of a stop codon (Fig. 1C). The mutation was successfully fixed in the first generation. Mice with homo and heterozygous mutation are viable. The animals were transferred to the C57Bl/6 genetic background.

# Isolation, seeding, and cultivation of a primary mixed culture of the hippocampus of newborn mice

For the purpose of performing metabolic tests, two groups of animals, with the  $p2rx3^{-/-}$  (experimental) and  $p2rx3^{+/-}$  (control) genotypes, were formed, each group containing 30 animals. The primary mixed culture of hippocampal neurons was obtained from 2-day-old newborn mice. Mice were euthanized by cervical dislocation. The skin was cut with scissors along the line of the skull base. The head was separated and placed in a tray with crushed ice. The brain was removed and placed in a Petri dish with chilled phosphate-buffered saline (PBS, pH 7.4). The cerebral hemispheres were separated under a binocular microscope (Leica, Germany). The hippocampus was placed on a glass slide with a "well" in a drop of cooled phosphate-buffered saline (PBS, pH 7.4), divided into six to eight pieces, and transferred into a test tube with 0.25% trypsin-EDTA. The tissue was trypsinized in a 0.25% trypsin-EDTA solution (Gibco, 25200056) in a Binder incubator (Germany) at an atmosphere of 5% CO, for 20 min at 37°C. After trypsinization, the cell suspension was washed three times in PBS (pH 7.4). A total of 2 mL of a neurobasal medium (Gibco, 21103049) containing a 2% B-27 protein supplement (Gibco, 17504044), 0.5 mM L-glutamax (Gibco, 25030081), and 1% PenStrep (PanEco, Russia) was added to the resulting suspension [10].

The primary mixed culture of hippocampal neurons was grown in eight-well plates for the Seahorse HS mini Cell Metabolism Analyzer (Agilent, USA). Sterile distilled water (400  $\mu$ L) was added to the grooves around the wells. The culture wells B–G were coated with 10  $\mu$ L of 0.01 mg/mL poly-D-lysine, and 180  $\mu$ L of distilled water was added into the background correction wells A and H. The plates were left for 1 h in a laminar flow hood under a

UV lamp. The plates were then washed three times with distilled water and dried in a laminar flow hood. A cell suspension containing  $2 \times 10^4$  hippocampal cells (80 µL) was added into each well of the Cell Culture Miniplates (Agilent). The primary mixed culture of  $p2rx3^{-/-}$  mouse hippocampal neurons was added into three wells of an eight-well plate, and the culture of  $p2rx3^{-/+}$  mouse hippocampal cells was added into the other three wells. The number of cells for seeding and the selection of the optimal FCCP concentration for performing the Mitostress test were determined by pre-calibrating the device to optimize the number of cells and determine the FCCP concentration for a given cell type according to the manufacturer's instructions. The cells in the plates were grown for three days, with ½ of the medium replaced daily.

# **Metabolic tests**

Two groups of animals (30 per group) with the  $p2rx3^{-/-}$  (experimental) and  $p2rx3^{+/-}$  (control) genotypes were formed to conduct metabolic tests.

Evaluation of mitochondrial respiration parameters. Mitochondrial respiration was measured on a Seahorse Bioscience HS mini Cell Metabolism Analyzer (Agilent). A sensor cartridge (Agilent) was hydrated 24 h prior to analysis by filling it with a calibration standard solution (Seahorse XF Calibrant) (200 µL in each well). The cartridge was placed in an incubator without CO, at 37°C for 24 h. The assay medium was prepared using Seahorse XF DMEM Media containing glucose at a final concentration of 10 mM, pyruvate 1 mM, and L-glutamine 2 mM, according to the manufacturer's recommendations. The MitostressTest kit was used to assess the function of mitochondria. Stock solutions were prepared according to the manufacturer's instructions. The kit includes oligomycin, FCCP, and a mixture of rotenone and antimycin A. In the experiment, working solutions were prepared to the following final concentrations per well: oligomycin, 1 µM; FCCP, 2.5 µM; and rotenone/antimycin A, 0.5 µM. Mitostressors were injected into the cell cultures through the ports of the Agilent Seahorse XFp sensor cartridge (Agilent, USA). The cartridge was calibrated; the calibration plate was then replaced with a plate with the cells, and measurements of the rate of oxygen consumption (OCR) indicating the degree of mitochondrial respiration in a cell were conducted. Three technical measurements were performed in each experimental and control cell. Data were normalized by the number of cells. The basal respiration, proton leak, maximum respiration, spare respiratory capacity, non-mitochondrial respiration, ATP production, and the respiratory coupling coefficient were calculated using the Multi-File Seahorse XF Mitostress test software product (USA). Non-mitochondrial respiration was taken as the minimum measured OCR value after injection of the rotenone/antimycin A mixture. Basal respiration was calculated as the last measured OCR value before the first injection minus nonmitochondrial respiration. Maximum respiration was evaluated as the difference between the maximum OCR values after FCCP injection and non mitochondrial respiration. Proton loss was calculated as the minimum OCR value after oligomycin injection minus nonmitochondrial respiration. ATP production was counted after oligomycin addition as the difference between the last OCR value measured before oligomycin injection and the minimum OCR value after oligomycin injection. The spare respiratory capacity of mitochondria was determined as the difference between maximal respiration and basal respiration. The respiratory efficiency coefficient was measured as the ratio between ATP production and basal respiration.

Studying the cellular bioenergetic balance. The energy phenotype of neurons was assessed using a Cell Energy Phenotype kit (Kit 103325-100, Agilent). The kit contained oligomycin (ATP synthase inhibitor) at a final concentration of 100  $\mu M$  and FCCP (mitochondrial uncoupler) at a final concentration of 100  $\mu M$ . The concentration of the oligomycin/FCCP stress solution added to the cartridge port was 1.0/1.0  $\mu M$ . Based on the results of measurements using the Multi-File Seahorse XF Cell Energy Phenotype software (USA), stress OCR and ECAR were calculated according to the formulas:

Stressed OCR = 
$$\frac{Stressed\ OCR}{Baseline\ OCR} \times 100$$
, (1)

$$Stressed\ ECAR = \frac{Stressed\ ECAR}{Baseline\ ECAR} \times 100, \tag{2}$$

where *Stressed OCR* is the stress phenotype by the rate of oxygen uptake, %;

Stressed ECAR is the stress phenotype by the rate of medium acidification, %;

Stressed OCR/ECAR is the rate of oxygen uptake / rate of medium acidification after the addition of mitostressors (a mixture of oligomycin and FCCP) to the medium;

Baseline OCR/ECAR is the rate of oxygen uptake / rate of medium acidification before the addition of stressors.

*Glycotest stress*. The analysis was performed using the Glycolysis Stress Test kit.

The kit used glucose at a final concentration of 10 mM, oligomycin (1 µM), and 2-deoxyglucose (500 mM), which were injected into cell cultures through the ports of the Agilent sensor cartridge Cartridge (Seahorse XFp). The cartridge was calibrated, the calibration plate was then replaced with a plate with cells, and the extracellular acidification rate of the medium (ECAR) was measured. The data were normalized by the number of cells. The glycolysis rate, glycolytic capacity of neurons, glycolytic reserve, and non-glycolytic population were calculated using the Multi-File Seahorse XF Glycotest software (USA). The glycolysis rate was calculated as the difference between the maximum ECAR value before oligomycin injection and the last ECAR measurement before glucose injection. The glycolytic capacity was calculated as the difference between the maximum measured ECAR after oligomycin injection and the last ECAR measurement before glucose injection. The glycolytic reserve was estimated as the glycolytic capacity divided by the glycolysis rate (mpH/pmol/min/cell) and multiplied by 100%. Nonglycolytic acidification was taken into account as the last ECAR measurement before glucose injection. All metabolic tests were performed in quadruplicates with three technical measurements each.

# Statistical analysis

The experimental data were processed using the Wave 2.6 software (USA) and the Excel 10.0 descriptive statistics package. The experimental data are presented as the median and standard deviation (M  $\pm$  SD). Considering that all the obtained numerical data do not obey the normal distribution hypothesis, the statistical significance of the results was assessed using the Mann–Whitney U test for samples with the number of measurements  $n \leq 20$ . The critical level of significance was considered at p = 0.05.

# **RESULTS**

The energy phenotype of a primary mixed culture of hippocampal neurons was studied in transgenic animals. In tests of this type, the rate of extracellular acidification (ECAR) is a reliable indicator of the glycolysis rate. However, when highly aerobic cells are exposed to stress, carbon dioxide production by mitochondria can provoke a rise in ECAR [11] and increase the contribution of glycolysis to the metabolic potential. The susceptibility of the hippocampal cells of the engineered transgenic mice to this effect was assessed using this test. The hippocampal neurons of both the homozygous and heterozygous transgenic animals were not susceptible to this effect. The energy phenotype of mitochondrial respiration of the primary

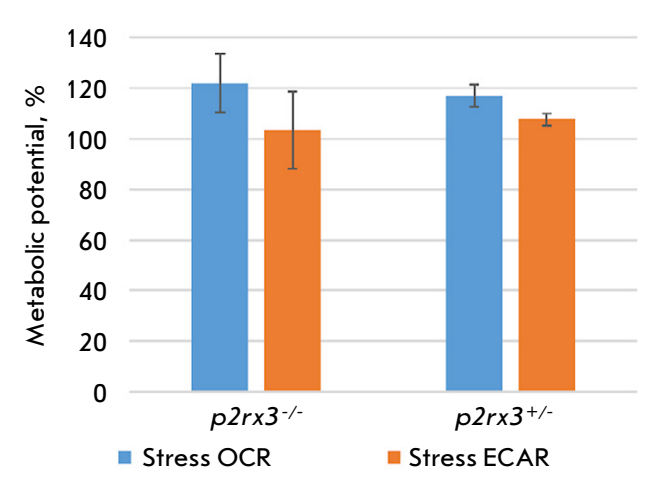


Fig. 2. The metabolic potential of the primary mixed culture of hippocampal neurons of transgenic p2rx3 knockout mice

mixed culture of hippocampal neurons of transgenic animals is aerobic respiration relying on oxidative phosphorylation. In the primary mixed culture of hippocampal neurons obtained from  $p2rx3^{-/-}$  mice, the ratio of the oxygen consumption rate (OCR) to the extracellular acidification rate (ECAR) was 1:2; in mice with the  $p2rx3^{+/-}$  genotype, OCR/ECAR=1.1. No clearly expressed differences in the metabolic phenotype of hippocampal neurons were revealed between the studied groups of animals (Fig.~2).

When studying the features of mitochondrial respiration, the real-time curves of the oxygen uptake rate were recorded (*Supplementary Fig. S1A*). An increase in almost all the parameters of mitochondrial respiration was denoted, except for the spare respiratory capacity obtained from  $p2rx3^{-/-}$  homozygotes (*Table 1*).

According to the data in Table 1, non mitochondrial, basal and maximal respiration, as well as the respiratory reserve, significantly increased in the culture of neurons obtained from  $p2rx3^{-/-}$  mice by 52.4% (p < 0.05), 72.3% (p < 0.05), and 61.3% (p < 0.05), respectively, compared to the control. The culture of hippocampal neurons collected from mice was characterized by an increase in the ATP production by 84.4% (p < 0.05); respiratory reserve, by 36% (p < 0.05); and respiratory efficiency coefficient, by 43% (p < 0.05) compared to the control. Due to the high intensity of mitochondrial respiration, the reserve respiratory capacity of the primary mixed culture of the hippocampus of  $p2rx3^{-/-}$  mice was down by 36.6% (p < 0.05) compared to the control.

In the primary mixed culture of hippocampal neurons from  $p2rx3^{-/-}$  mice, the glycolysis rate and glycolytic capacity were significantly reduced, by 75.7% (p < 0.05) and 78.6% (p < 0.05) compared to similar indicators in mice with the  $p2rx3^{+/-}$  genotype (Fig. 3).

The glycolytic reserve of hippocampal neurons of  $p2rx3^{-/-}$  mice increased almost two-fold and amounted to  $351.3 \pm 158.2\%$  compared to that of the hippocampal culture of  $p2rx3^{+/-}$  mice ( $163.2 \pm 60.5\%$ ). The real-time glycolytic curves are presented in *Supplementary Fig. S1B*.

# **DISSCUSSION**

The primary mixed culture of hippocampal neurons obtained from animals of both the  $p2rx3^{+/-}$  and  $p2rx3^{+/-}$  genotypes is characterized by aerobic respiration when the cell uses predominantly oxidative phosphorylation. The experimentally determined aerobic type of metabolism of hippocampal neurons and the absence of any switch of the energy phenotype in re-

Table 1. Parameters of the mitochondrial respiration of hippocampal neuron cultures from transgenic p2rx3 knockout mice

Parameters	$p2rx3^+/^-$ (control)	$p2rx3^{-}/^{-}$ (experiment)	P U test ≤ 17
Nonmitochondrial respiration, pmol/min/cell	$27.1 \pm 5.3$	$56.9 \pm 18.0^*$	0
Basal respiration, pmol/min/cell	$65.9 \pm 12.2$	238.1 ± 7.9*	0
Maximal respiration, pmol/min/cell	$124.3 \pm 8.9$	$320.9 \pm 18.5^*$	0
Proton (H <sup>+</sup> ) loss, pmol/min/cell	$14.5 \pm 8.1$	$40.4 \pm 16.4$	19
ATP production, pmol/min/cell	$36.1 \pm 12.8$	$231.5 \pm 9.9*$	0
Respiratory reserve, pmol/min/cell	$56.0 \pm 16.4$	87.4 ± 14.3*	0
Spare respiratory capacity, %	$188.3 \pm 45.20$	137.8 ± 7.2*	0
Respiratory efficiency coefficient, %	$58.8 \pm 21.6$	103.4 ± 10.4*	1

<sup>\*</sup>Significance of differences at p < 0.05 compared to the control according to the Mann–Whitney U test.

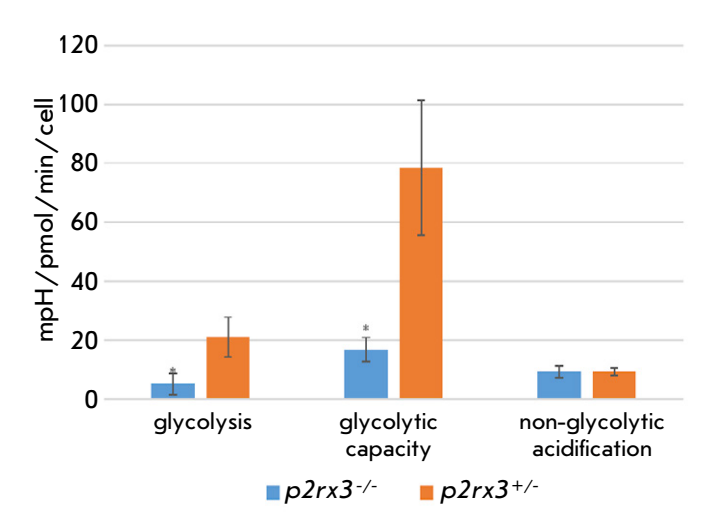


Fig. 3. Glycolytic function indices of the primary mixed culture of hippocampal neurons from p2rx3 knockout mice. \* – significance of differences at p < 0.05 compared to heterozygotes according to the Mann–Whitney U test

sponse to the introduction of mitochondrial respiration stressors are indicative of the enhanced bioenergetic function of mitochondria.

We found that hippocampal neurons from p2rx3-/knockout mice have increased basal and nonmitochondrial respiration compared to hippocampal neurons derived from  $p2rx3^{+/-}$  mice. Our findings also show that  $p2rx3^{-/-}$  hippocampal neurons exhibit high ATP production and a reduced glycolysis rate and glycolytic capacity, which essentially characterizes maximal capacity to generate ATP during glycolysis. These findings indicate that  $p2rx3^{-/-}$  knockout hippocampal neurons in the basal state already operate close to the peak of their mitochondrial energy capacity. The combination of intense mitochondrial respiration, together with the leak of protons, which further produce reactive oxygen species (ROS), and together with reduced spare respiratory capacity, may cause difficulties for such neurons to cope with significant fluctuations in bioenergetic needs during various cellular stresses, as well as during aging. Increased oxidative phosphorylation in neurons is the main cause of elevated ROS levels [12]. The main question is why p2rx3 knockout neurons have such high energy requirements. According to the published data, the dopamine neurons of mice with Alzheimer's disease have higher energy requirements [13]. Such energy expenditure is associated with large axonal arborization, which requires highly efficient production of mitochondrial ATP because of the increased mitochondrial density that characterizes these terminals [13]. In our study, we did not determine the degree of neuronal branching in the engineered transgenic mice and can only hypothesize about the role played by ionotropic receptors in enhancing the bioenergetics of hippocampal neurons based on the data available in the literature.

The p2rx3 gene encodes the P2X3 receptor, which is expressed in various brain regions, including pyramidal neurons, dentate granule cells, and hippocampal interneurons [14]. Considering that the hippocampus is a key structure of the brain associated with the formation of long-term memory, changes in the activity of ionotropic receptors - purinergic (P2X) and glutamatergic (NMDA) — can modulate plasticity and hippocampus-dependent learning, as well as memory. This plasticity is based on the activation of hippocampal kinases and changes in the intracellular calcium levels [15]. There are publications that describe cross-interactions of P2X receptors with NMDA. It has been proved that activation of P2X receptors inhibits Ca<sup>2+</sup> currents through NMDA receptors. The functional significance of such interaction is related to the fact that P2X receptors act as low-frequency filters of the calcium signal under physiological rest conditions when membrane depolarization is not required for calcium entry as is the case with NMDA receptors [3]. The p2rx3 knockout mice demonstrated impaired long-term depression in the hippocampal CA1, CA3, and dentate granule cell synapses, as well as improved learning and spatial orientation [5]. Inhibition of P2X family receptors (P2X3, P2X4, and P2X6 families) enhances the induction of long-term memory [3]. It is known that during the long-term potentiation underlying memory and learning, mitochondrial energy production is altered [16], the activity of the mitochondrial calcium pump increases [17], and the expression of mitochondrial genes is enhanced [18]. Blocking mitochondrial oxidative phosphorylation results in significant impairment of long-term potentiation [19]. Mitochondrial energy production is critical for transmitter release via vesicle exocytosis, mobilization of synaptic reserve pool vesicles, and regulation of synaptic strength [20]. The increased bioenergetic needs of neurons may be associated with excessive activation of NMDA receptors. According to researchers, activation of NMDA receptors increases the volume of spines in cultured hippocampal neurons and increases the surface expression of AMPA receptors [21]. Regulation of dendritic division of mitochondria, accompanied by an increase in the Ca2+ content in the mitochondrial matrix, and mediation by activation of Ca<sup>2+</sup> and calmodulin-dependent protein kinase II (CAMK II) has been described [22]. One of the most recent studies has shown the localization of an NMDA-like receptor on the mitochondrial mem-

## RESEARCH ARTICLES

brane, which enhances the activity of ATP synthase and ATP production by neurons [23].

### CONCLUSION

Our findings indicate that p2rx3 gene knockout mice have mitochondria with increased bioenergetic function. Transgenic mice with the p2rx3-/- genotype are characterized by an aerobic type of mitochondrial respiration, high ATP production, increased basal and non mitochondrial respiration, increased neuron loss, a fairly high level of the respiratory efficiency coefficient, while the spare respiratory capacity of mitochondria, the glycolysis rate, and glycolytic capacity are reduced. The data obtained indicate that mitochondria work close to the peak of their energy capacity. It is possible that such activation of the cellular energy metabolism is associated with reciprocal interactions between ionotropic purinergic and glu-

tamatergic receptors. An important and open question remains: how will the bioenergetic balance of hippocampal neurons change in p2rx3 knockout animals in response to blockade of the NMDA receptor? Understanding the interactions between purinergic and glutamatergic receptors is important, since these receptors are involved in certain types of hippocampus-dependent memories. The p2rx3 knockout animals in this study are a unique model for searching for pharmacological targets in efforts to correct the energy metabolism of brain cells and eliminate cognitive dysfunctions.  $\bullet$ 

This research was supported by the Russian Science Foundation (grant No. 23-24-00600).

Supplementaries are available online at https://doi.org/10.32607/actanaturae.27551.

## REFERENCES

- Rubin R.D., Watson P.D., Duff M.C., Cohen N.J. // Front. Hum. Neurosci. 2014. V. 8. P. 742. doi: 10.3389/ fnhum.2014.00742.
- Lalo U., Pankratov Y. // Neuropharmacology. 2023. V. 229.
   P. 109477. doi: 10.1016/j.neuropharm.2023.109477.
- 3. Pankratov Y.V., Lalo U.V., Krishtal O.A. // J. Neurosci. 2002. V. 22. № 19. P. 8363–8369. doi: 10.1523/JNEUROSCI.22-19-08363.2002.
- 4. Wang Y., Mackes J., Chan S., Haughey N.J., Guo Z., Ouyang X., Furukawa K., Ingram D.K., Mattson M.P. // J. Neurochem. 2006. V. 99. № 5. P. 1425–1434. doi: 10.1111/j.1471-4159.2006.04198.x.
- 5. Zhou X., Ma L.M., Xiong Y., Huang H., Yuan J.X., Li R.H., Li J.N., Chen Y.M. // Neurochem. Res. 2016. V. 41. № 6. P. 1263–1273. doi: 10.1007/s11064-015-1820-x.
- 6. Oparin P., Khokhlova O., Cherkashin A., Nadezhdin K., Palikov V., Palikova Y., Korolkova Y., Mosharova I., Rogachevskaja O., Baranov M., et al. // Mol. Ther. 2025. V. 33. № 2. P. 771–785. doi: 10.1016/j.ymthe.2024.12.036.
- 7. Gurskiy Y.G., Garbuz D.G., Soshnikova N.V., Krasnov A.N., Deikin A., Lazarev V.F., Sverchinskyi D., Margulis B.A., Zatsepina O.G., Karpov V.L., et al. // Cell Stress Chaperones. 2016. V. 21. № 6. P. 1055–1064. doi: 10.1007/s12192-016-0729-x.
- 8. Silaeva Y.Y., Kirikovich Y.K., Skuratovskaya L.N., Deikin A.V. // Russ. J. Develop. Biol. 2018. V. 49. № 6. P. 356–361. doi: 10.1134/S106236041806005X.
- Kalmykov V.A., Kusov P.A., Yablonskaia M.I., Korshunov E.N., Korshunova D.S., Kubekina M.V., Silaeva Y.Yu., Deykin A.V., Lukyanov N.E. // Research Results in Pharmacology. 2018. V. 4. № 4. P. 115–122. doi: 10.3897/rrpharmacology.4.32209.
- Zelentsova A.S., Borisova A.Y., Shmigerova V.S., Skorkina M.Y., Deykin A.V. // Genes and Cells. 2024. V. 19. № 1.
   P. 201–210. doi: 10.17816/gc529662.

- 11. Vohwinkel C.U., Lecuona E., Sun H., Sommer N., Vadász I., Chandel N.S., Sznajder J.I. // J. Biol. Chem. 2011. V. 286. № 43. P. 37067–37076. doi: 10.1074/jbc.M111.290056.
- 12. Hill B.G., Benavides G.A., Lancaster J.R. Jr., Ballinger S., Dell'Italia L., Jianhua Z., Darley-Usmar V.M. // Biol. Chem. 2012. V. 393. № 12. P. 1485–1512. doi: 10.1515/hsz-2012-0198.
- 13. Pacelli C., Giguère N., Bourque M.J., Lévesque M., Slack R.S., Trudeau L.É. // Curr. Biol. 2015. V. 25. № 18. P. 2349–2360. doi: 10.1016/j.cub.2015.07.050.
- Jang I.S., Rhee J.S., Kubota H., Akaike N., Akaike N.
   J. Physiol. 2001. V. 536. P. 505-519. doi: 10.1111/j.1469-7793.2001.0505c.xd.
- Medina J.H., Viola H. // Front. Mol. Neurosci. 2018. V. 11.
   P. 361. doi: 10.3389/fnmol.2018.00361.
- 16. Wieraszko A. // Brain Res. 1982. V. 237.  $\mathbb{N}_2$  2. P. 449–457. 17. Stanton P.K., Schanne F.A. // Brain Res. 1986. V. 382.  $\mathbb{N}_2$  1. P. 185–188. doi: 10.1016/0006-8993(86)90130-7.
- 18. Williams J.M., Thompson V.L., Mason-Parker S.E., Abraham W.C., Tate W.P. // Brain Res. Mol. Brain Res. 1998. V. 60. № 1. P. 50–56. doi: 10.1016/s0169-328x(98)00165-x.
- 19. Cunha R.A., Vizi E.S., Ribeiro J.A., Sebastião A.M. // J. Neurochem. 1996. V. 67.  $\mathbb{N}_2$  5. P. 2180–2187. doi: 10.1046/j.1471-4159.1996.67052180.x.
- 20. Ivannikov M.V., Sugimori M., Llinás R.R. // J. Mol. Neurosci. 2013. V. 49. № 1. P. 223–230. doi: 10.1007/s12031-012-9848-8.
- 21. Divakaruni S.S., van Dyke A.M., Chandra R., LeGates T.A., Contreras M., Dharmasri P.A., Higgs H.N., Lobo M.K., Thompson S.M., Blanpied T.A. // Neuron. 2018. V. 100. № 4. P. 860–875.e7. doi: 10.1016/j.neuron.2018.09.025.
- 22. Duarte F.V., Ciampi D., Duarte C.B. // Cell Mol. Life Sci. 2023. V. 80.  $\mathbb{N}_2$  6. P. 173. doi: 10.1007/s00018-023-04814-8.
- 23. Korde A.S., Maragos W.F. // Mitochondrion. 2021. V. 59. P. 76–82. doi: 10.1016/j.mito.2021.04.011.

# The Design, Synthesis, and Evaluation of the Biological Activity of Hydroxamic Derivatives of Sorafenib

A. A. Kleymenova<sup>1</sup>, I. A. Abramov<sup>1</sup>, Ya. V. Tkachev<sup>1</sup>, P. S. Galeeva<sup>1</sup>, V. A. Kleymenova<sup>2</sup>, N. F. Zakirova<sup>1</sup>, S. N. Kochetkov<sup>1</sup>, M. V. Kozlov<sup>1</sup>

<sup>1</sup>Engelhardt Institute of Molecular Biology, Russian Academy of Sciences, Moscow, 119991 Russia <sup>2</sup>Sechenov First Moscow State Medical University (Sechenov University), Moscow, 119991 Russia <sup>\*</sup>E-mail: kozlovmavi@gmail.com

Received: November 26, 2024; in final form, May 13, 2025

DOI: 10.32607/actanaturae.27566

Copyright © 2025 National Research University Higher School of Economics. This is an open access article distributed under the Creative Commons Attribution License, which permits unrestricted use, distribution, and reproduction in any medium, provided the original work is properly cited.

ABSTRACT Sorafenib is a multiple tyrosine kinase inhibitor that is used in the treatment of liver and renal cancers. We synthesized the hydroxamic derivatives of sorafenib bearing the pharmacophore elements of zinc-dependent histone deacetylase inhibitors. We uncovered that suppression of cancer cell proliferation by the synthesized hybrid inhibitors critically depends on the structure of the "deacetylase" element.

**KEYWORDS** sorafenib, vorinostat, protein tyrosine kinases, zinc-dependent histone deacetylases, antiproliferative activity, hybrid inhibitors.

ABBREVIATIONS PTKs – protein tyrosine kinases; HDACs – zinc-dependent histone deacetylases; B-RAF – signaling tyrosine kinase; SRF – sorafenib; DMSO-d $^6$  – deuterated dimethyl sulfoxide; IC $_{50}$  – half maximal inhibitory concentration; AMC – 7-amino-4-methylcoumarin.

## **INTRODUCTION**

Hepatocellular carcinoma (HCC) is one of the most heterogeneous, intractable type of cancer [1]. Sorafenib (SRF, Fig. 1), a multipotent inhibitor of protein tyrosine kinases (PTKs) – e.g. signaling RAF kinase, VEGFR and PDGFR tyrosine kinases, and others – has proven to be a first-line drug for the treatment of advanced HCC stages [2]. However, long-term use of sorafenib becomes ineffective due to acquired or inherited resistance in some transformed hepatocytes [3].

The combined use of sorafenib with multipotent zinc-dependent histone deacetylase (HDAC) inhibitors is a promising strategy in the treatment of HCC, because many HDAC inhibitors demonstrate not only antiproliferative activity on their own, but also a synergistic effect in combination with sorafenib [4]. For example, the combination of sorafenib with vorinostat (SAHA, Fig. 1) effectively initiates apoptosis in hepatoma cells [5] and the combination with valproic acid (VPA) significantly delays the development of resistance [6]. In contrast to the combined use of two drugs, monomolecular hybrids boast more predictable pharmacokinetic and pharmacodynamic parameters, including metabolism and bioavailability. In addition, their use ensures the simultaneous activation of sev-

eral antitumor mechanisms in the tumor site and in the required optimal ratio [7]. Thus, the development of PTK/HDAC hybrid inhibitors seems to be a very promising and justified area of research.

The pharmacophore of histone deacetylase inhibitors (HDACi) comprises four elements: (i) a zinc-binding group (ZBG), (ii) a linker occupying the active site 'lysine channel' that leads to the catalytic zinc ion, (iii) a connecting unit (CU), and (iv) an aromatic/heterocyclic fragment (cap) responsible for recognizing the surface of the enzyme's active site at the entrance to the 'lysine channel' [8]. We synthesized new hybrid inhibitors – hydroxamic derivatives of sorafenib – bearing the pharmacophore elements of zinc-dependent histone deacetylase inhibitors. We investigated the antiproliferative activity of the produced compounds and the class selectivity of HDAC inhibition.

# **EXPERIMENTAL PART**

In this study, we used the following compounds: aminocaproic acid, 4-(aminomethyl)-benzoic acid, diazabicycloundecene (DBU), 1,1'-carbonyldiimidazole (CDI), hydroxylamine hydrochloride, a 50% aqueous hydroxylamine solution, and hydrazine hydrate (Sigma-Aldrich, USA); ethyl ester of 4-aminobenzoic acid (Acros Organics, USA), bis(2-oxo-3-oxazolidinyl)

Fig. 1. The structures of sorafenib (SRF) and vorinostat (SAHA) with highlighted pharmacophore elements: cap (blue), connecting unit (CU, brown), linker (green), and zinc-binding group (ZBG, red)

phosphinic chloride (BOP-Cl) (LEAPChem, China); 4-formyl-N-hydroxybenzamide was synthesized according to [9]. Column chromatography was performed using the Kieselgel silica gel, 0.060-0.200 mm, (Acros Organics); elution systems are provided in the text. TLC was performed on Kieselgel 60 F254 plates (Supelco, USA). NMR spectra ( $\delta$ , ppm; J, Hz) were acquired on an Avance III spectrometer (Bruker, Germany) with an operating frequency of 300 MHz for <sup>1</sup>H-NMR (internal standard: Me<sub>4</sub>Si; solvent: DMSO- $d_s$ ), 100.6 MHz for <sup>13</sup>C NMR (with suppression of carbon-proton interaction; solvent: DMSO- $d_s$ ), and 282 MHz for  $^{19}$ F NMR (solvent: DMSO- $d_c$ ). Chemical shifts are provided in parts per million, and spin-spin coupling constants (SSCCs) are expressed in Hz. <sup>1</sup>H NMR NOESY and ROESY spectra were measured in dry DMSO- $d_{\epsilon}$ . The mixing time used for NOESY spectra was specifically selected to maximize the intensity of dipole cross peaks (0.25 s).

# Synthesis of the hydroxamic derivatives of sorafenib SRF-CHA, SRF-BHA, SRF-THA, and SRF-H-BHA

CI 
$$\frac{3}{4}$$
  $\frac{4}{5}$   $\frac{5}{6}$   $\frac{10}{8}$   $\frac{11}{13}$   $\frac{12}{19}$   $\frac{16}{18}$   $\frac{7}{12}$   $\frac{7}{12}$   $\frac{3}{4}$   $\frac{5}{5}$  OH  $\frac{7}{2}$   $\frac{7}{4}$   $\frac{7}{4}$ 

# 6-(4-(4-(4-(4-chloro-3-(trifluoromethyl)phenyl)ureido)phenoxy)picolinamide)hexanoic acid (SRF-CA).

A mixture of 466 mg (1 mmol) of a sorafenib carboxylic acid methyl ester (*SRF-ME*) [10], 262 mg (2 mmol) of aminocaproic acid, and 383 mg (2.5 mmol) of DBU in 10 mL of MeOH was stirred under boiling conditions for 6 h. The mixture was cooled to room temperature, diluted with 10 mL of H<sub>2</sub>O, neutralized with HCl (1:1) to pH 5–6, and cooled at 10°C for 18 h. The precipitate formed was triturated, filtered, washed with H<sub>2</sub>O, and air-dried. The product was isolated by chromatography on a silica gel using a CHCl<sub>3</sub>/EtOH (10:1) mixture as an eluent. The collected fractions were evaporated, and the residue was dissolved in 3 mL of CHCl<sub>3</sub> and cooled at 10°C for

18 h. The resulting precipitate was filtered, washed with CHCl<sub>a</sub> and air-dried, finally yielding 400 mg (71%) of SRF-CA. <sup>1</sup>H NMR (DMSO- $d_s$ ):  $\delta$  11.94 (1H, s, OH), 9.20 (1H, s, NH $^{\alpha}$ ), 8.97 (1H, s, NH $^{b}$ ), 8.76 (1H, t, J 6.0, NH $^{\gamma}$ ), 8.51 (1H, d, J 5.6, H18), 8.12 (1H, d, J 2.1, H16), 7.73-7.53 (4H, m, H4, H10, and H14, H19), 7.40 (1H, d, J 2.5, H1), 7.24–7.08 (3H, m, H5, H11, and H13), 3.26 (2H, q, J 6.5, H1'), 2.19 (2H, t, J 7.3, H5'), 1.65-1.43 (4H, m, H2' and H4'), 1.36-1.20 (2H, m, H3'). <sup>13</sup>C NMR (DMSO- $d_c$ ):  $\delta$  174.87 (C6'), 166.46 (C15), 163.60 (C20), 152.96 (C8 or C17), 152.94 (C8 or C17), 150.77 (C18), 148.35 (C12), 139.80 (C9), 137.51 (C6), 132.44 (C4 or C5), 127.21 (q, J 30.3, C2), 123.57 (C4 or C5), 123.29 (q, J 273, C7), 122.85 (C3), 121.89 (C10 and C14), 121.00 (C11 and C13), 117.33 (q, J 5.5, C1), 114.53 (C19), 109.24 (C16), 39.17 (C1'), 34.04 (C5'), 29.30 (C2'), 26.41 (C3'), 24.68 (C4'). <sup>19</sup>F NMR (DMSO- $d_e$ ):  $\delta$  -61.47 (CF<sub>2</sub>).

# (ii) SRF-CHA

4-(4-(3-(4-chloro-3-(trifluoromethyl)phenyl)ureido)phenoxy)-N-(6-(hydroxyamino)-6-oxohexyl)picolinamide (SRF-CHA). A solution of 363 mg (0.643 mmol) of SRF-CA in 0.7 mL of DMF was combined with 115 mg (0.71 mmol) of CDI. After 1 h 40 min, 70 mg (1.00 mmol) of hydroxylamine hydrochloride was added, stirred until dissolved for 10 min, and left for 2 h. The reaction mixture was diluted with 3.5 mL of H<sub>2</sub>O and cooled at 10°C for 18 h. The supernatant was decanted, and the precipitated oil was triturated in 7 mL of cold water until the formation of a loose sediment, filtered, and dried in air. The product was isolated by chromatography on a silica gel using a CHCl<sub>2</sub>-EtOH (first 7.5:1 and then 5:1) mixture as an eluent. The collected fractions were evaporated to yield 262 mg (70%) of SRF-CHA. <sup>1</sup>H NMR (DMSO- $d_c$ ):  $\delta$  10.30 (1H, s, NH<sup>d</sup>), 9.23 (1H, s, NH<sup> $\alpha$ </sup>), 9.01 (1H, s, NH<sup>b</sup>), 8.75 (1H, t, J 5.9, NH<sup>γ</sup>), 8.63 (1H, s, OH), 8.51 (1H, d, J 5.5, H18), 8.13 (1H, s, H16), 7.74-7.54 (4H, m, H4, H10 and H14, H19), 7.39 (1H, d, J 2.3, H1), 7.22–7.12 (3H, m, H5, H11,

and H13), 3.25 (2H, q, J 6.6, H1′), 1.94 (2H, t, J 7.3, H5′), 1.61–1.41 (4H, m, H2′ and H4′), 1.34–1.17 (2H, m, H3′). <sup>13</sup>C NMR (DMSO- $d_6$ ):  $\delta$  169.57 (C6′), 166.47 (C15), 163.60 (C20), 152.95 (C8 and C17), 150.77 (C18), 148.35 (C12), 139.79 (C9), 137.51 (C6), 132.44 (C4 or C5), 127.21 (q, J 30.7, C2), 123.58 (C4 or C5), 123.29 (q, J 273, C7), 122.85 (C3), 121.89 (C10 and C14), 121.00 (C11 and C13), 117.33 (q, J 5.5, C1), 114.54 (C19), 109.24 (C16), 39.21 (C1′), 32.67 (C5′), 29.34 (C2′), 26.49 (C3′), 25.33 (C4′). <sup>19</sup>F NMR (DMSO- $d_6$ ):  $\delta$  -61.47 (CF<sub>3</sub>).

$$F_{3}C_{7}$$
  $C_{1}$   $C_{1}$ 

# (iii) SRF-A

4-(4-(3-(4-chloro-3-(trifluoromethyl)phenyl)ureido)phenoxy)picolinic acid (SRF-A). 0.67 g (12 mmol) of KOH was dissolved in 12 mL of a THF-MeOH-H<sub>9</sub>O (1:1:1) mixture, and 2.32 g (5 mmol) of SRF-ME was added with stirring in two equal parts over 10 min, and, after dissolution of the starting compound, the mixture was left to rest at room temperature for 1 h. The reaction mixture was diluted with 12 mL of H<sub>2</sub>O and neutralized with HCl (1:1) to pH  $\approx$  1.5. The precipitate was triturated, another 12 mL of H<sub>2</sub>O was added, and the mixture was cooled at 10°C for 1 h. The precipitate was filtered, washed with H<sub>o</sub>O, and air-dried to yield 2.20 g (97%) of SRF-A. <sup>1</sup>H NMR (DMSO- $d_s$ ):  $\delta$  9.29 (1H, s, NH $^{\alpha}$ ), 9.06 (1H, s, NHb), 8.58 (1H, d, J 5.7, H18), 8.13 (1H, d, J 2.4, H16), 7.70–7.56 (4H, m, H4, H10 and H14, H19), 7.44 (1H, d, J 2.5 H1), 7.24-7.13 (3H, m, H5, H11 and H13). <sup>13</sup>C NMR (DMSO- $d_6$ ):  $\delta$  166.47 (C20), 165.85 (C15), 152.96 (C8), 151.19 (C18), 150.86 (C17), 148.20 (C12), 139.81 (C9), 137.65 (C6), 132.44 (C4 or C5), 127.21 (q, J 30.5, C2), 123.54 (C4 or C5), 123.28 (q, J 273, C7), 122.83 (C3), 121.84 (C10 and C14), 120.99 (C11 and C13), 117.30 (q, J 5.5, C1), 115.12 (C19), 112.32 (C16). <sup>19</sup>F NMR (DMSO- $d_{\epsilon}$ ):  $\delta$  -61.46 (CF<sub>2</sub>).

# (iv) SRF-BEE

Ethyl 4-(4-(4-(3-(4-chloro-3-(trifluoromethyl)phenyl) ureido)phenoxy)picolinamide)benzoate (SRF-BEE). A suspension of 452 mg (1 mmol) of SRF-A in 10 mL of a 1:1 pyridine—THF mixture was combined with

300 mg (1.18 mmol) of BOP-Cl, stirred for 10 min, and then combined with 230 mg (1.39 mmol) of a p-aminobenzoic acid ethyl ester (ABEE). The reaction mixture was stirred at room temperature for 1.5 h, before another 300 mg (1.18 mmol) of BOP-Cl was added. After 10 min, 230 mg (1.39 mmol) of ABEE was added and stirring was continued at room temperature for 1.5 h. Water (30 ml) was added and stirred for 1-1.5 h to form a homogeneous precipitate. The precipitate was filtered and washed with water (thrice, 20 mL each). After air drying, the precipitate was suspended in 10 mL of methanol, filtered, washed with 5 mL of methanol, filtered, and air-dried to yield 442 mg (74%) of SRF-BEE. <sup>1</sup>H NMR (DMSO- $d_s$ ):  $\delta$  10.93 (1H, s, NH $^{\gamma}$ ),  $\delta$  9.22 (1H, s, NH<sup> $\alpha$ </sup>), 9.01 (1H, s, NH<sup> $\beta$ </sup>), 8.64 (1H, d, J 5.6, H18), 8.13 (1H, d, J 1.9, H16), 8.05 (2H, d, J 8.8, H3' and H5'), 7.95 (2H, d, J 8.7, H2' and H6'), 7.71-7.59 (4H, m, H4, H10 and H14, H19), 7.54 (1H, d, J 2.5 H1), 7.29-7.16 (3H, m, H5, H11 and H13), 4.30 (2H, q, J 7.1, H8'), 1.32 (3H, t, J 7.1, H9'). <sup>13</sup>C NMR (DMSO- $d_s$ ):  $\delta$  166.70 (C7'), 165.75 (C15), 162.86 (C20), 152.94 (C8), 152.29 (C17), 150.94 (C18), 148.25 (C12), 142.97 (C1'), 139.78 (C9), 137.62 (C6), 132.43 (C4 or C5), 130.46 (C3' and C5'), 127.20 (q, J 30.5, C2), 125.48 (C4'), 123.57 (C4 or C5), 123.28 (q, J 273, C7), 122.85 (C3), 121.88 (C10 and C14), 121.02 (C11 and C13), 120.20 (C2' and C6'), 117.31 (q, J 5.4, C1), 115.19 (C19), 110.02 (C16), 60.93 (C8'), 14.63 (C9'). <sup>19</sup>F NMR (DMSO- $d_s$ ):  $\delta$  -61.44 (CF<sub>2</sub>).

# (v) SRF-BHA

4-(4-(3-(4-chloro-3-(trifluoromethyl)phenyl)ureido)phenoxy)-N-(4-(hydroxycarbamoyl)phenyl)picolinamide (SRF-BHA). A solution of 300 mg (0.50 mmol) of SRF-BEE in 7.5 mL of a 1:2 MeOH-THF mixture was supplemented with 500 mg (7.58 mmol) of NH<sub>2</sub>OH (50%), the mixture was cooled to 0°C, and 56 mg (1.00 mmol) of KOH dissolved in 1 mL of MeOH was added. After 30 min, cooling was ceased and the reaction mixture was left for 18 h. The reaction mixture was cooled to 0°C, and 28 mg (0.5 mmol) of KOH dissolved in 0.5 mL of MeOH was added. After 30 min, cooling was ceased and the mixture was left to rest for 3 h, after which 0.5 mL (8.75 mmol) of AcOH was added, and the mixture was evaporated to half the original volume, before 4 mL of MeOH was added, and the mixture was again evaporated to half its volume. The residue was supplemented with 5 mL of MeOH. The resulting precipitate was triturated, filtered, dried on the filter, successively washed twice with 3 mL of a 2% solution of triethylamine in MeCN. 3 mL of MeCN, and 3 mL of CH<sub>2</sub>Cl<sub>2</sub>, then air-dried to yield 230 mg (71%) of SRF-BHA. <sup>1</sup>H NMR (DMSO- $d_e$ ): δ 11.13 (1H, s, NH $^{\delta}$ ), δ 10.82 (1H, s, NH $^{\gamma}$ ), δ 9.28 (1H, s,  $NH_{a}$ ),  $\delta$  9.07 (1H, s,  $NH^{b}$ ),  $\delta$  8.96 (1H, s, OH), 8.63 (1H, d, J 5.6, H18), 8.13 (1H, d, J 2.0, H16), 7.96 (2H, d, J 8.7, H3' and H5'), 7.75 (2H, d, J 8.7, H2' and H6'), 7.71-7.58 (4H, m, H4, H10 and H14, H19), 7.53 (1H, d, J 2.5, H1), 7.29-7.16 (3H, m, H5, H11 and H13). <sup>13</sup>C NMR (DMSO- $d_{\epsilon}$ ):  $\delta$  166.73 (C7'), 164.35 (C15), 162.86 (C20), 152.97 (C8), 152.43 (C17), 150.94 (C18), 148.26 (C12), 141.18 (C1'), 139.82 (C9), 137.65 (C6), 132.45 (C4 or C5), 128.51 (C4'), 128.03 (C3' and C5'), 127.21 (q, J 30.8, C2), 123.59 (C4 or C5), 123.29 (q, J 273, C7), 122.84 (d, J 1.5, C3), 121.91 (C10 and C14), 121.03 (C11 and C13), 120.16 (C2' and C6'), 117.33 (q, J 5.4, C1), 115.16 (C19), 109.93 (C16). <sup>19</sup>F NMR (DMSO- $d_c$ ):  $\delta$  -61.44 (CF<sub>2</sub>).

# (vi) SRF-TA

4-(4-(4-(4-(4-chloro-3-(trifluoromethyl)phenyl)ureido))phenoxy)picolinamide)methylbenzoic acid (SRF-TA). A mixture of 466 mg (1 mmol) of SRF-ME, 302 mg (2 mmol) of 4-(aminomethyl)benzoic acid, and 383 mg (2.5 mmol) of DBU in 6 mL of MeOH was stirred under boiling for 14 h. The reaction mixture was cooled to room temperature, diluted with 15 mL of H<sub>2</sub>O, and neutralized with AcOH to pH  $\approx 5-6$ . The resulting precipitate was triturated and cooled at 10°C for 4 h. The precipitate was filtered, washed with H<sub>2</sub>O, and dried in air. The product was isolated by chromatography on a silica gel using a 5:1 CHCl<sub>3</sub>-EtOH mixture supplemented with AcOH (1% of the total volume) as an eluent. The collected fractions were evaporated; the residue was triturated in 10 mL MeOH, filtered, washed with 4 mL of MeOH, and air-dried to yield 269 mg (46%) of SRF-TA. <sup>1</sup>H NMR (DMSO- $d_s$ ):  $\delta$  12.82  $(1H, s, OH), 9.44 (1H, t, J 6.4, NH^{\gamma}), 9.20 (1H, s, NH^{\alpha}),$ 8.98 (1H, s, NHb), 8.54 (1H, d, J 5.6, H18), 8.12 (1H, d, J 2.4, H16), 7.89 (2H, d, J 8.3, H4' and H6'), 7.70-7.57 (4H, m, H4, H10 and H14, H19), 7.45-7.37 (3H, m, H1, H3' and H7'), 7.24-7.13 (3H, m, H5, H11 and H13), 4.54 (2H, d, J 6.3, H1').  $^{13}$ C NMR (DMSO- $d_s$ ):  $\delta$  167.64 (C8'), 166.51 (C15), 164.06 (C20), 152.94 (C8 or C17), 152.67 (C8 or C17), 150.93 (C18), 148.31 (C12), 145.00 (C2'), 139.79 (C9), 137.55 (C6), 132.44 (C4 or C5), 129.83 (C4' and C6'), 129.78 (C5'),127.75 (C3' and C7'), 127.21 (q, J 30.6, C2), 123.58 (C4 or C5), 123.29 (q, J 273, C7), 122.83 (C3), 121.91 (C10 and C14), 121.01 (C11 and C13), 117.33 (q, J 5.6, C1), 114.78 (C19), 109.46 (C16), 42.78 (C1'). <sup>19</sup>F-NMR (DMSO- $d_c$ ): δ -61.45 (CF $_c$ ).

(vii) SRF-THA

4-(4-(3-(4-chloro-3-(trifluoromethyl)phenyl)ureido)phenoxy)N-(4-(hydroxycarbamoyl)benzyl)picolinamide (SRF-THA). A solution of 275 mg (0.47 mmol) of SRF-TA in 0.55 mL of DMF was supplemented with 120 mg (0.74 mmol) of CDI. After 1 h 30 min, 120 mg (1.73 mmol) of hydroxylamine hydrochloride was added, the mixture was stirred until dissolution for 10 min and left to rest for 18 h. The reaction mixture was diluted with 7 mL of H<sub>2</sub>O; the precipitate was thoroughly triturated, filtered after 30 min, washed on a filter with 7 mL of H<sub>2</sub>O, and dried in air. The product was isolated by chromatography on a silica gel using a 7:1 CHCl<sub>3</sub>-EtOH mixture as an eluent. The collected fractions were evaporated to yield 125 mg (44%) of SRF-THA. <sup>1</sup>H NMR (DMSO- $d_s$ ):  $\delta$  11.14 (1H, s,  $NH^{\delta}$ ), 9.41 (1H, t, J 6.3,  $NH^{\gamma}$ ), 9.23 (1H, s, OH), 9.01 (1H, s, NH $^{\alpha}$ ), 8.96 (1H, s, NH $^{b}$ ), 8.54 (1H, d, J 5.6, H18), 8.12 (1H, d, J 1.8, H16), 7.76–7.55 (6H, m, H4, H10 and H14, H19, H4' and H6'), 7.41 (1H, d, J 2.5, H1), 7.36 (2H, d, J 8.2, H3' and H7'), 7.26–7.12 (3H, m, H5, H11 and H13), 4.50 (2H, d, J 6.3, H1').  $^{13}$ C NMR (DMSO- $d_e$ ):  $\delta$  166.50 (C15), 164.63 (C8'), 164.01 (C20), 152.94 (C8 or C17), 152.70 (C8 or C17), 150.93 (C18), 148.32 (C12), 143.12 (C2'), 139.79 (C9), 137.54 (C6), 132.45 (C4 or C5), 131.81 (C5'), 127.66 (C2, C4' and C6'), 127.37 (C2, C3' and C7'), 127.01 (C2), 123.58 (C4 or C5), 123.29 (q, J 273, C7), 122.84 (C3), 121.91 (C10 and C14), 121.01 (C11 and C13), 117.33 (q, J 5.4, C1), 114.77 (C19), 109.44 (C16), 42.72 (C1'). <sup>19</sup>F NMR (DMSO- $d_6$ ): δ -61.44 (CF<sub>2</sub>).

# (viii) SRF-H

 $1\text{-}(4\text{-}chloro\text{-}3\text{-}(trifluoromethyl)phenyl)\text{-}3\text{-}(4\text{-}((2\text{-}(hydra-zinecarbonyl)pyridin-}4\text{-}yl)oxy)phenyl)urea (SRF-H). A suspension of 466 mg (1 mmol) of SRF-ME in 3 mL of a 2:1 MeOH-CH<math display="inline">_2$ Cl $_2$  mixture was combined with 250 mg (5 mmol) of hydrazine hydrate and stirred for

10 min until the dissolution of the starting compound. After 2 h, 2 mL of MeOH was added and the mixture was evaporated to a thick syrup. After addition of 10 mL of H<sub>2</sub>O, the mixture was triturated until a homogeneous precipitate formed, cooled at 0°C for 1.5 h, filtered, washed with water (twice, 3 mL each), and air-dried to yield 404 mg (87%) of SRF-H. 1H-NMR (DMSO- $d_c$ ):  $\delta$  9.86 (1H, s, NH $^{\gamma}$ ), 9.19 (1H, s, NH $^{\alpha}$ ), 8.97 (1H, s, NHb), 8.48 (1H, d, J 5.6, H18), 8.12 (1H, d, J 2.3, H16), 7.72-7.55 (4H, m, H4, H10 and H14, H19), 7.38 (1H, d, J 2.5 H1), 7.17 (2H, d, J 8.9, H11 and H13), 7.12 (1H, dd, J 5.6 and 2.6, H5), 4.56 (2H, s, NH<sup>d</sup>). <sup>13</sup>C NMR (DMSO- $d_c$ ):  $\delta$  166.31 (C15), 162.45 (C20), 152.94 (C8), 152.60 (C17), 150.96 (C18), 148.36 (C12), 139.79 (C9), 137.51 (C6), 132.43 (C4 or C5), 127.22 (q, J 30.8, C2), 123.58 (C4 or C5), 123.29 (q, J 273, C7), 122.86 (d, J 1.7, C3), 121.86 (C10 and C14), 121.01 (C11 and C13), 117.34 (q, J 5.7, C1), 114.33 (C19), 109.25 (C16). <sup>19</sup>F NMR (DMSO- $d_e$ ):  $\delta$  -61.45 (CF<sub>2</sub>).

# (ix) SRF-H-BHA

(E)-4-((2-(4-(4-(3-(4-chloro-3-(trifluoromethyl)phe*nyl*)*ureido*)*phenoxy*)*picolinoyl*)*hydrazinoylidene*) methyl)-N-hydroxybenzamide (SRF-H-BHA). A solution of 85 mg (0.515 mmol) of 4-formyl-N-hydroxybenzamide [9] in 3.5 mL of MeOH-CH<sub>2</sub>Cl<sub>2</sub>, 5:2, and 30 µL of AcOHcat was added to a suspension of 233 mg (0.50 mmol) of SRF-H in 3 mL of a 2:1 MeOH-CH<sub>2</sub>Cl<sub>2</sub> mixture, and the mixture was stirred for 5 min until the starting compound had dissolved. After 4 h, the resulting precipitate was filtered, washed successively on a filter with 10 mL of EtOH and 5 mL MeOH, and air-dried to yield 258 mg (84%) of SRF-H-BHA. <sup>1</sup>H NMR (DMSO- $d_{\rm s}$ ):  $\delta$  12.23 (1H, s, NH $^{\gamma}$ ), 11.27 (1H, s, NH<sup>d</sup>), 9.25 (1H, s, NH $^{\alpha}$ ), 9.08 (1H, s, OH), 9.04 (1H, s, NHb), 8.69 (1H, s, H1'), 8.60 (1H, d, J 5.6, H18), 8.13 (1H, d, J 2.2, H16), 7.84 (2H, d, J 8.4, H3' and H7'), 7.71 (2H, d, J 8.4, H4' and H6'), 7.71-7.59 (4H, m, H4, H10 and H14, H19), 7.50 (1H, d, J 2.5, H1), 7.25-7.18 (3H, m, H5, H11 and H13).  ${}^{13}$ C NMR (DMSO- $d_ε$ ): δ 166.56 (C15), 164.14 (C8'), 160.49 (C20), 152.96 (C8), 152.23 (C17), 151.04 (C18), 148.98 (C1'), 148.27 (C12), 139.80 (C9), 137.62 (C6), 137.23 (C2'), 134.46 (C5'), 132.48 (C4 or C5), 127.93 (C3' and C7'), 127.47 (C4' and C6'), 127.21 (q, J 30.7, C2), 123.63 (C4 or C5), 123.30 (q, J 273, C7), 122.86 (d, J 1.3, C3), 121.94 (C10 and C14), 121.05 (C11 and C13), 117.35 (q, J 5.7, C1), 115.16 (C19), 110.14 (C16). <sup>19</sup>F NMR (DMSO- $d_s$ ):  $\delta$  -61.43 (CF<sub>3</sub>).

# Cells, media, and reagents

In the study, we used the following cell lines: Huh7, Huh7.5, HepG2, and PLC/PRF/5 hepatocellular carcinomas, HCT116 colorectal cancer, SH-SY5Y neuroblastoma, HL60 promyelocytic leukemia, and K562 chronic myeloid leukemia. Differentiated HepaRG cells were produced according to [11]. Sorafenib and vorinostat were purchased from Selleck Chemicals; the fluorogenic substrates Boc-Lys(Acyl)-AMC were prepared as described previously [12].

# Assessment of adherent cell viability

Adherent cell lines were passaged into 96-well culture plates so that the cell confluence stood at 50–60% 24 h after seeding. The cells were incubated with the investigated inhibitors, at different concentrations, for 48 h, and cell viability was assessed using the Cell Proliferation Kit I (MTT assay) according to the manufacturer's instructions (Sigma-Aldrich, USA). The optical density of the reduction product, formazan, was measured using a Spark multifunctional plate reader (Tecan Trading, Switzerland) at 544 nm. Each inhibitor concentration was tested at least six times.

# Assessment of differentiated HepaRG cell viability

Undifferentiated HepaRG cells were passaged into 96-well culture plates ( $^{5} \times 10^{4}$  cells per well) and incubated as described previously [11]. After achieving 100% confluency, the cells were subjected to differentiation. For this purpose, the plates with the cells were kept for 14 days, with the medium changed once every 7 days, then kept in a medium containing 1.8% DMSO (Sigma) for 14 days, with the medium changed once every 7 days. Upon completion of differentiation (28 days), the medium was replaced with a medium containing 1.8% DMSO and the test compounds at the desired concentrations and incubated for 72 h. Cell viability was assessed using the MTT test as described above. Each inhibitor concentration was tested at least eight times.

# Assessment of cell viability in suspension culture

A cell suspension was passaged into 96-well culture plates (~1.5  $\times$   $10^4$  cells per well). After 24 h of seeding, the cells were incubated with the investigated inhibitors in different concentrations for 48 h. Then, 10  $\mu L$  of a resazurin solution in PBS (2 mg/mL) was added and the cells were kept in a CO $_2$  incubator for 4 h. Fluorescence of the reduction product, resafurin, was measured using a Spark multifunctional plate reader (Tecan Trading, Switzerland) at wavelengths of  $571_{\rm ex}/584_{\rm em}$  nm. Each inhibitor concentration was tested at least six times.

# Cell-based system for testing the potency and selectivity of HDAC inhibition

HCT116 cells were passaged into 96-well culture plates so that the cells became 70-80% confluent 24 h after seeding. These cells were incubated with the investigated inhibitors at different concentrations for 24 h. Then, three-quarters of the volume was removed from each well and replaced with the same volume of a cell medium containing both the inhibitor at the same concentration and one of the three substrates; i.e., Sub<sup>Ac/Pro/Tfa</sup>, at a concentration of 30  $\mu$ M. After an additional 4-h incubation, aliquots of the culture fluid were transferred to a fluorescence assay plate (SPL Life Sciences, Republic of Korea), diluted 2-fold with a trypsin solution (2 mg/mL in Tris-HCl buffer, pH 8.0), and incubated at 37°C for 60 min. Fluorescence was measured using a Spark multi-plate reader (Tecan Trading) at  $360_{\rm ex}/470_{\rm em}$  nm. The fluorescence intensity in each well was normalized to the cytotoxicity values obtained for the same well. The fluorescence signal value (in RFU) for each concentration of the test compound was calculated using the following formula:

$$RFU = \frac{\sum_{n} (\frac{F_{i} - F_{0}}{C_{v}})}{\sum_{n} F_{i}};$$

where  $F_i$  is the fluorescence intensity of the sample in the well,  $F_0$  is the fluorescence intensity in the well with the substrate dissolved in the medium without cells. Cv is the cell viability, and n is the number of replicates.

# **RESULTS AND DISCUSSION**

# The structural design of hydroxamic derivatives of sorafenib

Upon designing hybrid inhibitors (HIs), we were guided by the desire to maximally preserve the structure of sorafenib as a known strong 'kinase' component and to use hydroxamic acid moieties, *n*-hexanoic and benzoic acids, characteristic of highly effective HDACi in the 'deacetylase' component (*Fig. 2*). In order to meet both requirements, we chose the picolinamide moiety of sorafenib as the docking site for the 'kinase' and 'deacetylase' components. According to crystallography data [13], this moiety is exposed to the exit from the binding site of sorafenib with the B-RAF kinase active center. We presumed that the 'deacetylase' fragment of the hybrid inhibitor, a linker–ZBG, would not create steric hindrances in the interaction with B-RAF.

# Synthesis of the hydroxamic derivatives of sorafenib

According to the synthesis scheme (Fig. 2), the starting compound for the production of all HIs was the

sorafenib carboxylic acid methyl ester (SRF-ME), whose preparation was described previously [10]. This picoline ester was found to be substantially activated, to the point that the formation of an amide bond with the amino group of  $\varepsilon$ -aminocaproic and 4-(aminomethyl)benzoic acids was achieved by boiling in methanol in the presence of a strong base (DBU). The resulting carboxylic acids, SRF-CA and SRF-TA, were converted into the corresponding hydroxamates, SRF-CHA and SRF-THA, by treatment with CDI and hydroxylamine hydrochloride as described previously [14].

The high reactivity of *SRF-ME* enabled the production of sorafenib carboxylic acid *SRF-A* via mild alkaline hydrolysis in a virtually quantitative yield, similar to [15]. But we had significantly simplified the isolation procedure. Amidation of *SRF-A* with ethyl *p*-aminobenzoate in the presence of the condensation agent BOP-Cl yielded the intermediate ester *SRF-BEE* that was used to prepare the target hydroxamate *SRF-BHA* by hydroxyaminolysis (*Fig. 2*).

Hydrazinolysis of *SRF-ME* proceeded as smoothly as in [10], but somewhat faster. The resulting sorafenib carboxylic acid hydrazide *SRF-H* was used in a click reaction with 4-formyl-N-hydroxybenzamide [9] to yield the required *SRF-H-BHA* as the (*E*)-isomer of picolinoylhydrazone (*Figs. 2* and 3). It should be noted that all the synthesized hybrid inhibitors retained the N-monosubstituted picolinate amide moiety of sorafenib (PyCONHR) that, according to crystallographic data, interacts with the main chain carbonyl of Cys531 of B-RAF kinase as part of the complex [13].

# Determination of the picolinoylhydrazone configuration

To confirm that the produced SRF-H-BHA is an (E)isomer, we measured two-dimensional NOESY correlation spectra [16] (Fig. 3A), which revealed an intense positive cross-peak at (12.23, 8.69), which corresponds to the interaction of H1' and NH $^{\gamma}$  protons. Since the molecular weight of the substance occurs in the range between 0.5 and 1.0 kDa, where the nuclear Overhauser effect (NOE) changes its sign ( $\omega\tau_{_{c}}$  ~ 1), and the observed dipole-dipole cross peaks cannot generally be distinguished from the exchange peaks by their sign, we measured the ROESY spectrum [17] (NOE in a rotating coordinate system, Fig. 3B), where an intense negative cross peak at (12.23, 8.69) was also observed, which clearly confirmed its dipole-dipole nature. The molecular models of SRF-H-BHA (data not shown) demonstrate that the distance between H1' and  $NH^{\gamma}$  protons in the (E)-isomer is approximately 0.25 nm, which corresponds to the strong NOE

Fig. 2. The scheme for the synthesis of the hydroxamic derivatives of sorafenib: SRF-CHA, SRF-BHA, SRF-THA, and SRF-H-BHA: cap (blue), connecting unit (CU, brown), linker (green), and zinc-binding group (ZBG, red). Reagents, conditions, and yield (%): (i) NH<sub>2</sub>(CH<sub>2</sub>)<sub>5</sub>CO<sub>2</sub>H, DBU, MeOH, D, 6 h, (71%); (ii) CDI, DMF, 2 h, then NH<sub>2</sub>OH·HCI, 18 h, (70%); (iii) KOH, THF/MeOH/H<sub>2</sub>O, 1 h, (97%); (iv) p-NH<sub>2</sub>PhCO<sub>2</sub>Et, BOP-CI, THF/Py, 3 h, (74%); (v) NH<sub>2</sub>OH, MeOH/THF, 0°C, 0.5 h, then 18 h, (71%); (vi) p-NH<sub>2</sub>CH<sub>2</sub>PhCO<sub>2</sub>H, DBU, MeOH, D, 14 h, (46%); (vii) CDI, DMF, 1.5 h, then NH<sub>2</sub>OH·HCI, 18 h, (44%); (viii) NH<sub>2</sub>NH<sub>2</sub>·H<sub>2</sub>O, MeOH/CH<sub>2</sub>CI<sub>2</sub>, 2 h, (87%); (ix) p-(CHO)-PhCONHOH, AcOH<sub>cat</sub>, MeOH/CH<sub>2</sub>CI<sub>2</sub>, 4 h, (84%)

observed in the two-dimensional correlation spectra. At the same time, in the (Z)-isomer, it is 0.37 nm and occurs near the experimental detection limit of NEO. Therefore, the probability of detecting intense crosspeaks is negligible.

# Evaluation of the cytotoxicity of sorafenib hydroxamic derivatives

The cytotoxic effect of the produced inhibitors was first tested on a panel of four human hepatoma cell lines: Huh7, Huh7.5, HepG2, and PLC/PRF/5 (*Table 1*).

For the same purpose, differentiated HepaRG cells were used, which, as a surrogate for primary human hepatocytes, are widely used to study the cytotoxic effect of xenobiotics [11]. Sorafenib (*SRF*) and vorinostat (*SAHA*), a class I/IIb HDAC inhibitor, were used as reference compounds (*Fig.* 1).

As seen from the data in *Table 1*, the antiproliferative activity of HIs against hepatoma cell lines significantly depended on the structure of the 'deacetylase' component linker. Compared with sorafenib, the extended alkyl linker in the *SRF-CHA* molecule

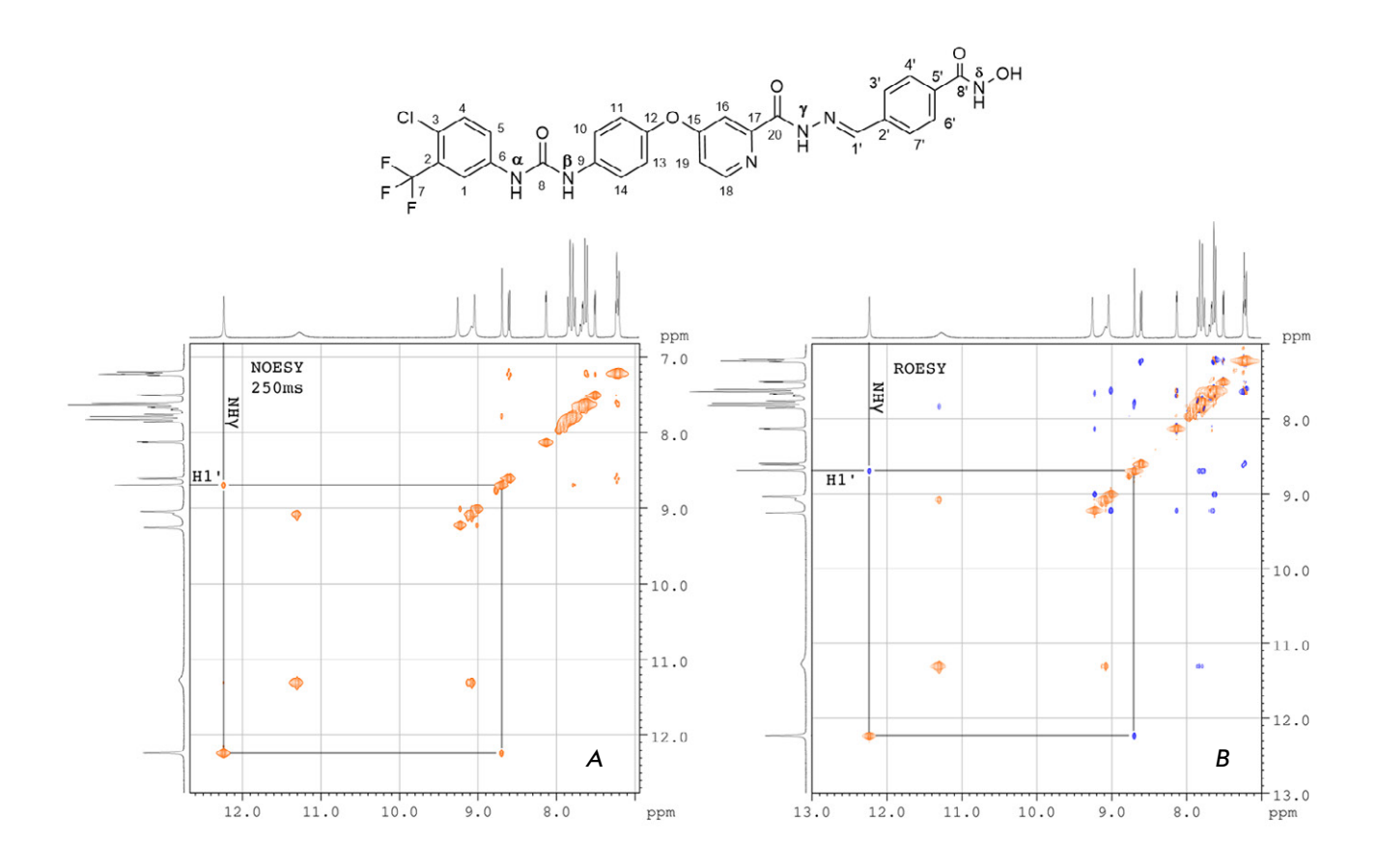


Fig. 3. The molecular structure of the (E)-isomer of SRF-H-BHA with atomic numbering as well as two-dimensional <sup>1</sup>H spectra (A) NOESY at the mixing time of 0.25 s and (B) ROESY, 8 mg of SRF-H-BHA in DMSO-d<sup>6</sup>. Cross-peaks between the picolinoylhydrazone proton NH<sup>7</sup> and proton H1<sup>1</sup> at a double bond are shown. NOESY – Nuclear Overhauser Effect Spectroscopy, ROESY – Rotating frame Overhauser Effect Spectroscopy

was linked to a 3- to 4-fold decrease in the antiproliferative activity. Conversely, SRF-BHA and SRF-H-BHA carrying a phenyl linker were 1.5- to 2-fold more active. The IC $_{50}$  values of the SRF-THA inhibitor, which comprises a benzyl linker, were close to those of sorafenib, with an upward and downward bias of less than 50%.

Because differentiated HepaRG cells do not proliferate, the decrease in the MTT signal in this case was obviously due to the cytotoxic effect of the inhibitors. The hydroxamic derivatives, SRF-BHA, SRF-THA, and SRF-H-BHA, and the reference compounds, SRF and SAHA, had approximately equal cytotoxicity in a narrow range of  $IC_{50}$  values = 11.3– $14.3~\mu M$ , and the SRF-CHA inhibitor was approximately 5-fold less toxic. Interestingly, the profile of  $IC_{50}$  values for the entire set of compounds was largely similar to the test results in proliferating PLC/PRF/5 cells, which suggests similar inhibition mechanisms in both cases.

The cytotoxic activity of the produced inhibitors was further investigated on the SH-SY5Y neuroblastoma cell line and two suspension leukemia cell lines: HL60 and K562 (*Table 1*). The *SRF-CHA* derivative was shown to be much less active than sorafenib against both neuroblastoma and leukemia, whereas the activity of *SRF-BHA*, *SRF-THA*, and *SRF-H-BHA* was approximately identical to that of sorafenib. Thus, the dependence of HI antiproliferative activity on the structure of the 'deacetylase' component in neuroblastoma and leukemia cell lines was identical to that in hepatoma cell lines.

# Testing the potency and selectivity of histone deacetylase inhibition

The histone deacetylase inhibitor *SAHA*, which was used as a control, exerted a strong cytotoxic effect on most of the investigated cell lines (*Table 1*). To assess the relationship between the antitumor activity

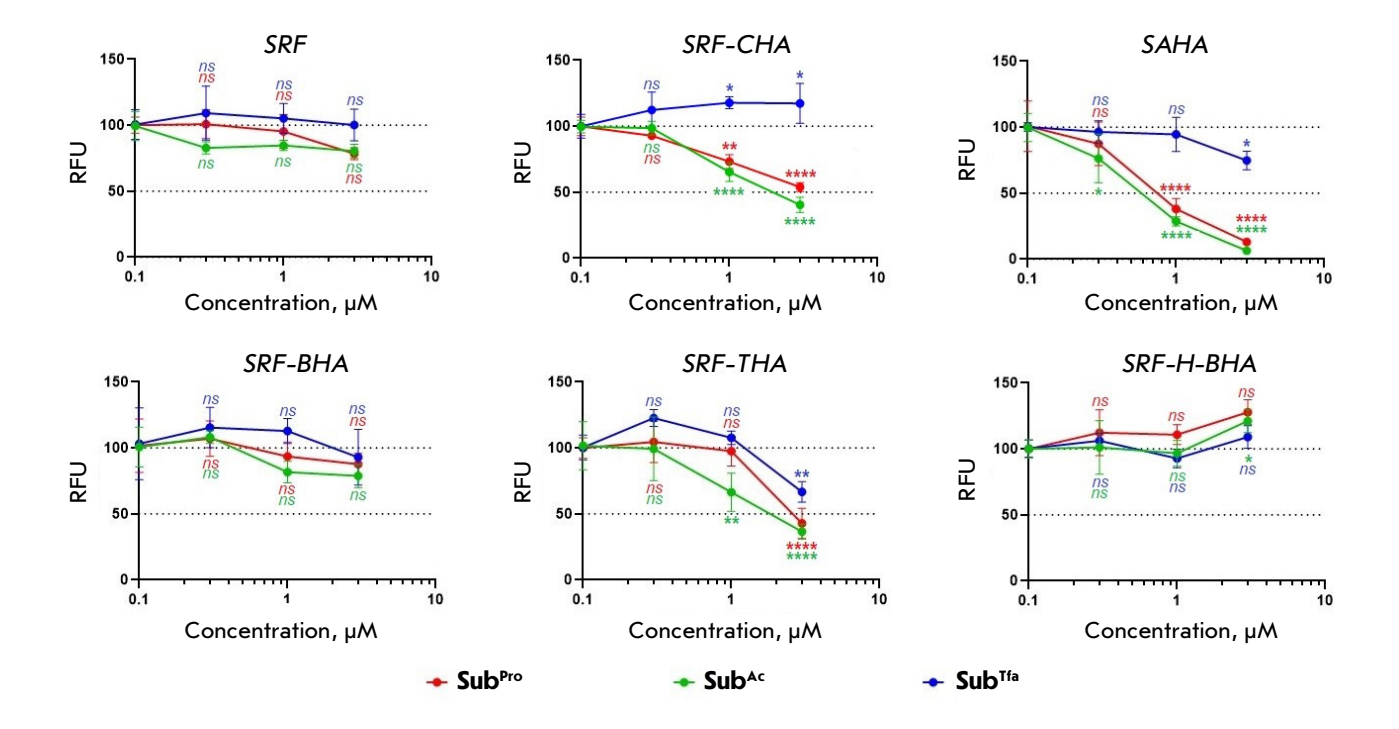


Fig. 4. The results of in-cell testing of the selectivity and potency of HDAC inhibition in the presence of sorafenib (*SRF*), hybrid inhibitors (*SRF-CHA*, *SRF-BHA*, *SRF-THA*, and *SRF-H-BHA*), and vorinostat (*SAHA*). Fluorogenic substrates of histone deacetylases: **Sub**<sup>Pro</sup> (HDACs class I), **Sub**<sup>Ac</sup> (HDACs class I and IIb), and **Sub**<sup>Tfa</sup> (HDACs class IIa); RFU is the relative fluorescence units. The statistical significance was calculated using the ANOVA test (GraphPad Prizm 8): \*\*\*\*\*p < 0.001, \*\*\*0.001 , \*\*0.01 <math>, \*0.05 <math>, and ns – not significant

of the hydroxamic derivatives of sorafenib and the suppression of histone deacetylase activity *in cell*, we assessed residual HDAC activity in the presence of HIs using the s³CTS cellular test system as described previously [12]. The s³CTS signal reflected the level of *in-cell* deacylation of three class-selective fluorogenic histone deacetylase substrates of the general structure Boc-Lys(Acyl)-AMC, where Acyl = propionyl (Sub<sup>Pro</sup>, HDACs class I), acetyl (Sub<sup>Ac</sup>, HDACs class I and IIb), and trifluoroacetyl (Sub<sup>Tfa</sup>, HDACs class IIa). Sorafenib and vorinostat were used as negative and positive controls, respectively, for the test system activity.

SRF, SRF-BHA, and SRF-H-BHA were found not to inhibit *in-cell* histone deacetylase activity up to a concentration of 3  $\mu$ M (Fig. 4). However, SRF-CHA and SAHA, with the latter a stronger inhibitor, demonstrated the same selectivity as class I and IIb HDAC inhibition. Finally, pan-inhibition of histone deacetylase activity was observed in the presence of SRF-THA. However, the simultaneous decrease in three fluorescent signals observed in this case might point to a malfunction of the s³CTS test system due

to additional inhibition of zinc-dependent palmitoyl-CoA thioesterase MBLAC2. It is worth noting that this effect is often observed precisely in the case of selective toluylhydroxamic inhibitors of HDAC6 class IIb, including tubastatin A and nexturastat A [12, 18].

Thus, based on the testing results, only SRF-CHA and SRF-THA of the produced four hydroxamic derivatives of sorafenib proved to be histone deacetylase inhibitors (Fig. 4). Given the data on antiproliferative activity (Table 1), we concluded that the alkyl linker in SRF-CHA blocked the inhibition of tyrosine protein kinases, and that this effect was only partially compensated by the inhibition of histone deacetylases. A strong negative effect on the activity of sorafenib derivatives with extended alkyl substituents in the picolinamide moiety was noted earlier [10, 19]. The fact that the potency of the antitumor activity of SRF-THA and sorafenib in all the cell lines under study was approximately identical does not contradict previously reported data on the similar values of antiproliferative activity for sorafenib and its N-benzyl derivative [20]. Given these facts, we believe that

# RESEARCH ARTICLES

Table 1. The antiproliferative/cytotoxic effect of hybrid inhibitors on the cell cultures of hepatoma [■], neuroblastoma [■], promyelocytic, and chronic myeloid leukemia [□]; the incubation time was 48 h; in the case of HepaRG cells, the incubation time was 72 h

Cells	Huh7	Huh7.5	HepG2	PLC/PRF/5	HepaRG	SH-SY5Y	HL60	K562
	ΙC <sub>50</sub> , μΜ							
SRF Sorafenib	3.87±1.14	4.54±0.59	16.6±2.4	18.0±0.9	13.7±2.6	9.19±2.61	6.34±0.21	9.33±0.02
SRF-BHA	3.63±1.42	2.86±1.09	12.9±6.1	7.69±0.81	12.4±4.8	4.00±0.21	5.08±1.50	4.17±0.27
SRF-THA	5.60±0.40	5.27±0.46	8.80±2.21	12.4±3.4	11.3±3.1	7.15±0.27	8.45±3.15	13.1±1.9
SRF-H-BHA	1.80±0.10	2.47±0.82	9.87±1.34	8.33±2.82	$12.4\pm3.9$	3.41±0.85	$6.97 \pm 2.31$	9.08±1.23
SRF-CHA	18.1±2.2	14.6±3.5	$77.9 \pm 4.1$	61.3±2.5	$69.5 \pm 4.8$	39.5±9.9	54.5±1.7	51.6±4.6
SAHA Vorinostat	1.73±0.18	1.89±0.22	1.88±0.19	11.4±2.6	14.3±0.6	1.90±0.08	9.43±2.98	8.74±3.06

1-3 μΜ 3-10 μΜ 10-30 μΜ 30-100 μΜ

**SRF-THA** may be used to design derivatives that carry a more effective 'deacetylase' component.

It is interesting that the antiproliferative activity of both SRF-BHA and SRF-H-BHA in most cases significantly exceeded that of sorafenib, although these compounds are not histone deacetylase inhibitors (Table 1 and Fig. 4), which is indirect indication of the enhancement of the 'kinase' component in these compounds. As we noted, sorafenib interacts with the main chain carbonyl of Cys531 of B-RAF kinase at the exit from the binding site; in this case, the picolinamide moiety of the inhibitor and the indole ring of Trp530 are parallel to each other and the distance between them is about 4.3 Å [10, 13]. Given this, we suggest the presence of a stacking interaction between the indole ring of Trp530 and the phenyl linker of SRF-BHA or SRF-H-BHA because of the mutual coplanarity of both ring systems and their spatial proximity.

# CONCLUSION

In this study, by modifying the picolinamide moiety of the inhibitor, we designed and synthesized four hydroxamic derivatives of sorafenib. The structure of all the produced compounds was confirmed by NMR methods. Using *in cell* testing, we showed that only two derivatives, *SRF-CHA* and *SRF-THA*, were able to inhibit HDACs at low micromolar concentrations. Testing the antiproliferative activity of the target compounds in a panel of hepatoma, neuroblastoma, and leukemia cells revealed elevated activity of three compounds: *SRF-BHA*, *SRF-THA*, and *SRF-H-BHA*, comparable or superior to that of sorafenib. *SRF-THA* may be used as a parent molecule to develop new hybrid PTK/HDAC inhibitors with high toxicity against tumor cells. ●

This study was supported by the Russian Science Foundation (grant No. 23-24-00542).

# REFERENCES

- 1. Fan G., Wei X., Xu X. // Ther. Adv. Med. Oncol. 2020. V. 12. P. 1–21. doi: 10.1177/175835920927602.
- 2. Wilhelm S.M., Adnane L., Newell P., Villanueva A., Llovet J.M., Lynch M. // Mol. Cancer Ther. 2008. V. 7. № 10. P. 3129–3140. doi: 10.1158/1535-7163.MCT-08-0013.
- 3. Cabral L.K.D., Tiribelli C., Sukowati C.H.C. // Cancers. 2020. V. 12. P. 1576. doi: 10.3390/cancers12061576.
- Chang Y., Lee Y.B., Cho E.J., Lee J.-H., Yu S.J., Kim Y.J., Yoon J.-H. // BMC Cancer. 2020. V. 20. P. 1001. doi: 10.1186/ s12885-020-07471-3.
- 5. Hsu F.-T., Liu Y.-C., Chiang I.-T., Liu R.-S., Wang H.-E., Lin W.-J., Hwang J.-J. // Int. J. Oncol. 2014. V. 45. P. 177–188. doi: 10.3892/ijo.2014.2423.
- Liu J., Yang X., Liang Q., Yu Y., Shen X., Sun G. // Int. J. Biochem. Cell Biol. 2020. V. 126. P. 105820. doi: 10.1016/j. biocel.2020.105820.
- 7. Bass A.K.A., El-Zoghbi M.S., Nageeb E.M., Mohamed M.F.A., Badr M., Abuo-Rahma G.E.A. // Eur. J.

- Med. Chem. 2021. V. 209. P. 112904. doi: 10.1016/j.ej-mech.2020.112904.
- Melesina J., Simoben C.V., Praetorius L., Bülbül E.F., Robaa D., Sippl W. // ChemMedChem. 2021. V. 16. P. 1336– 1359. doi: 10.1002/cmdc.202000934.
- 9. Rodrigues D.A., Ferreira-Silva G.À., Ferreira A.C.S., Fernandes R.A., Kwee J.K., Sant'Anna C.M.R., Ionta M., Fraga C.A.M. // J. Med. Chem. 2016. V. 59. № 2. P. 655–670. doi: 10.1021/acs.jmedchem.5b01525.
- Wang K., Kuerbana K., Wan Q., Yu Z., Ye L., Chen Y. // Molecules. 2020. V. 25. P. 573. doi: 10.3390/molecules25030573.
- Gutmann M., Stimpfl E., Langmann G., Koudelka H., Mir-Karner B., Grasl-Kraupp B. // Toxicol. Lett. 2023.
   V. 390. P. 15–24. doi: 10.1016/j.toxlet.2023.10.014.
- Kleymenova A., Zemskaya A., Kochetkov S., Kozlov M. // Biomedicines. 2024. V. 12. P. 1203. doi: 10.3390/biomedicines12061203.
- 13. Wan P.T., Garnett M.J., Roe S.M., Lee S., Niculescu-Du-

## RESEARCH ARTICLES

- vaz D., Good V.M., Jones C.M., Marshall C.J., Springer C.J., Barford D., et al. // Cell. 2004. V. 116. P. 855–867. doi: 10.1016/s0092-8674(04)00215-6.
- 14. Kozlov M.V., Konduktorov K.A., Malikova A.Z., Kamarova K.A., Shcherbakova A.S., Solyev P.N., Kochetkov S.N. // Eur. J. Med. Chem. 2019. V. 183. P. 111723. doi: 10.1016/j.ejmech.2019.111723.
- 15. Le P., Kunold E., Macsics R., Rox K., Jennings M.C., Ugur I., Reinecke M., Chaves-Moreno D., Hackl M.W., Fetzer C., et al. // Nat. Chem. 2019. V. 12. P. 145–158. doi: 10.1038/s41557-019-0378-7.
- Jeener J., Meier B.H., Bachmann P., Ernst R.R.
   J. Chem. Phys. 1979. V. 71. P. 4546–4553. doi: 10.1063/1.438208.

- 17. Bax A., Davis D.G. // J. Magn. Reson. 1985. V. 63. P. 207–213. doi: 10.1016/0022-2364(85)90171-4.
- 18. Lechner S., Malgapo M.I.P., Grätz C., Steimbach R.R., Baron A., Rüther P., Nadal S., Stumpf C., Loos C., Ku X., et al. // Nat. Chem. Biol. 2022. V. 18. P. 812–820. doi: 10.1038/s41589-022-01015-5.
- 19. Khire U.R., Bankston D., Barbosa J., Brittelli D.R., Caringal Y., Carlson R., Dumas J., Gane T., Heald S.L., Hibner B., et al. // Bioorg. Med. Chem. Lett. 2004. V. 14. P. 783–786. doi: 10.1016/j.bmcl.2003.11.041.
- 20. Babić Ž., Crkvenčić M., Rajić Z., Mikecin A.-M., Kralj M., Balzarini J., Petrova M., Vanderleyden J., Zorc B. // Molecules. 2012. V. 17. P. 1124–1137. doi: 10.3390/molecules17011124.

# PepString Server As a Tool to Search for Short Amino Acid Subsequences: Identification of Potential Amyloid-Beta Targets

S. A. Kozin<sup>1</sup>, A. A. Anashkina<sup>1\*</sup>, D. G. Matsuga<sup>2,3</sup>, B. S. Suvaan<sup>3</sup>, V. G. Tumanyan<sup>1</sup>, V. A. Mitkevich<sup>1</sup>, A. A. Makarov<sup>1</sup>

<sup>1</sup>Engelhardt Institute of Molecular Biology, Moscow, 119991 Russia

<sup>2</sup>Biological Chemistry and Clinical laboratory diagnostics department, Astrakhan State Medical University, Astrakhan, 414000 Russia

<sup>3</sup>Sechenov First Moscow State Medical University (Sechenov University), Moscow, 119991 Russia

E-mail: anastasia.a.anashkina@mail.ru

Received: February 09, 2025; in final form, April 22, 2025

DOI: 10.32607/actanaturae.27630

Copyright © 2025 National Research University Higher School of Economics. This is an open access article distributed under the Creative Commons Attribution License, which permits unrestricted use, distribution, and reproduction in any medium, provided the original work is properly cited.

ABSTRACT This paper presents a new bioinformatics tool to meet the needs of researchers in the search for short ( $\geqslant$  3) amino acid subsequences in protein sequences annotated in public databases (UniprotKB, SwissProt) and illustrates its efficacy with the example of a search for the EVHH tetrapeptide in the human proteome, which is a molecular determinant of amyloid beta and is involved in interactions that are crucial in Alzheimer's disease pathogenesis. The topicality of developing such a tool is, on the one hand, supported by experimental data on the role of short tetrapeptide motifs in the architecture of intermolecular interfaces. On the other hand, there are currently no software products for efficient search for short ( $\geqslant$  3) amino acid sequences in public databases, which drastically limits researchers' ability to identify proteins with exact matches of short subsequences. This tool (PepString server, http://pepstring.eimb.ru/) allows one to use intuitive queries to retrieve information about all the proteins that contain sequences of interest, as well as their combinations.

KEYWORDS Alzheimer's disease, amyloid-beta, short amino acid sequences, PepString, drug target, peptide, EVHH, HAEE.

# **INTRODUCTION**

Protein-protein interactions play a fundamental role in virtually all cellular processes. Of particular interest to biomedicine and pharmaceuticals are protein-protein interfaces involving molecules associated with the development of pathological conditions. Neurodegenerative diseases are associated with aggregation of certain proteins into ordered supramolecular structures. In this case, the initiation of pathological aggregation occurs via a seeding mechanism. The key role in this mechanism is played by repetitive protein-protein interactions with identical intermolecular interfaces. One of the leading strategies for the development of disease-modifying drugs for the treatment of neurodegenerative diseases is the use of agents of various natures (e.g., antibodies, peptides, peptidomimetics) capable of specifically disrupting the formation of disease-associated intermolecular interfaces and thereby preventing unwanted aggregation [1]. Therefore, the identification of the amino acid residues that form these interfaces is crucially important.

Alzheimer's disease (AD) is the most common neurodegenerative disease and the leading cause of dementia in the world [2]. AD is characterized by the conformational transformation of endogenous amyloid- $\beta$  (A $\beta$ ) molecules from the monomeric state to soluble oligomers and insoluble aggregates [3] that initiate neuroinflammation and other pathological processes associated with AD development [4]. Insoluble A $\beta$  aggregates are present in the brain both as diffuse aggregates on the walls of blood vessels and as fibrillar aggregates (amyloid plaques) on the surface of neurons [5]. A $\beta$  aggregates and soluble oligomers are in dynamic equilibrium [6].

 $A\beta$  is a small polypeptide molecule consisting of 38-43 amino acid residues (aa) [7].  $A\beta$  is produced by proteolysis of the amyloid precursor protein (APP) [8]. The amino acid sequence of the most abundant

A $\beta$  isoform in amyloid plaques, A $\beta$ 42, contains 42 aa [9, 10]. The A $\beta$  peptide is present in both brain tissue and peripheral organs [11]. In the blood, A $\beta$  exists mainly in platelets [12] and crosses the blood–brain barrier [11]. A $\beta$  is found in the picomolar concentration range in the blood of both healthy individuals and sporadic AD patients [13]. The physiological functions of A $\beta$  include suppression of microbial infections, regulation of synaptic plasticity, promotion of recovery after brain injury, sealing of the blood–brain barrier, and presumably suppression of tumor cell proliferation [14, 15].

Aggregation of Aβ molecules *in vivo* is initiated by intermolecular interactions. Zinc ions and the metalbinding domain (Aβ16) located in the 1-16 region of Aβ play a crucial role in these interactions. Therefore, data on the three-dimensional structure of  $A\beta16$  and the molecular mechanism of zinc-dependent Aβ oligomerization are used for the rational search and design of candidate molecules on the basis of the anti-amyloid strategy [16]. The spatial structure of A $\beta$ 16 from several natural AB variants, in free and zinc-bound states, has been determined [17-21]. There are also experimental data on the structure of Aβ16 in amyloid fibrils isolated from the brain of AD patients [22]. According to these data, the 11-EVHH-14 region of human Aβ has a polypeptide backbone structure that remains almost unchanged both in the free A\u00e316 molecule and in the complex of  $A\beta16$  with the zinc ion, as well as in the N-terminal fragment of Aβ fibrils isolated from the brain tissue of AD patients.

Taken together, these properties characterize the 11-EVHH-14 site of A $\beta$  as a structural invariant and suggest that this site plays an important role in the interaction of  $A\beta$  with other biological molecules. Indeed, the 11-EVHH-14 site of Aβ has been found (1) to be the main center for the recognition and binding of zinc ions, (2) to be located at the intermolecular interface in complexes between  $A\beta$  and the  $\alpha 4\beta 2$  subtype nicotinic acetylcholine receptor [23, 24], (3) to form a symmetric zinc-dependent interface in both A $\beta$  dimers [25, 26] and A $\beta$  oligomers [17], (4) to participate in zinc-dependent binding of nucleic acids [27]. The amino acid sequence of the Aß metalbinding domain (Aβ16) is located in the extracellular membrane-spanning portion of the amyloid precursor protein (APP), it constitutes the C-terminal fragment of the soluble  $\alpha$ -form of APP (sAPP $\alpha$ ) [28], and both APP and sAPPa play vital physiological functions [29]. Furthermore, in both APP and sAPPa, the 11-EVHH-14 region of the Aβ metal-binding domain is sterically accessible for interactions with both zinc ions and other biomolecules, including A\u03c3. Thus, both of these proteins may act as potential binding partners for  $A\beta$  through zinc-dependent interactions via the symmetrical 11-EVHH-14 regions of the metal-binding domains in appropriate molecules.

In AD pathogenesis, the interaction of A $\beta$  with zinc ions, mediated by the 11-EVHH-14 site of A $\beta$ , is a key factor in the formation and spread of amyloid plaques. Therefore, this site is a promising drug target [16]. It is important to note that most of the monoclonal antibodies used to neutralize A $\beta$  oligomers in AD therapy block the 11-EVHH-14 site [30]. However, monoclonal antibodies have many side effects [31]; so, the search for and development of low-molecular weight agents of various chemical classes [32], e.g., peptidomimetics and natural or artificial peptides [33], seems topical.

Recently, the use of a synthetic analogue of the 35-HAEE-38 site of the  $\alpha 4$  subunit of the  $\alpha 4\beta 2$  subtype nicotinic acetylcholine receptor has been substantiated as an effective agent to inhibit the aggregation of endogenous Aß molecules in AD pathogenesis [23]. This analogue (hereinafter HAEE) specifically binds to the 11-EVHH-14 site of  $A\beta$  both in the absence and in the presence of zinc ions, leading to the formation of stable complexes that, in turn, block the formation and propagation of Aβ aggregates [34]. However, it is unknown whether HAEE can bind to EVHH sites in other proteins, and how this may affect patients if HAEE is used as a drug. Given the key role of the EVHH tetrapeptide region in the formation of intermolecular interfaces involving  $A\beta$ , it is important to identify all proteins of the human proteome that contain this site because these proteins may be potential partners for Aβ. However, at the time of this study, there were no effective bioinformatics tools to search for short (≥ 3 aa) subsequences in known proteins. In this paper, we describe an original PepString server that could be used to search for exact matching of short protein sequence fragments. The use of the PepString server resources is illustrated with the example of the EVHH sequence of amyloid-beta, which is a promising target for the development of pathogenetic anti-amyloid drugs for AD treatment.

# **EXPERIMENTAL PART**

# PepString server

The PepString server (http://pepstring.eimb.ru) is developed based on the PostgreSQL version of the popular UniprotKB and SwissProt databases. This server allows the user to search for exact matches of short peptides in protein sequences. The query can be limited to a specific taxon, such as Mammalia, Bacteria, or Vertebrata, or to all species. The query can also be based on the presence of multiple fragments in a single sequence ( $\leq$  5) or on the presence of at least one

## **Peptide Search** Here you can search peptide sequences with small size starting with 3 amino acids and greater. For sequences greater than 6 amino acids you may use this site or move to <u>UniProt peptide search</u> section. To apply some kind of sorting - use settings below. Type your peptide sequence here, min length - 3 You may type several sequences like this: ALC, RADGG / ALC, RADGG / ALC RADGG. Or you may put every peptide on a separate line. Use only uppercase letters. Max amount of sequences in one guery is 5 OPTIONS: AND: find sequences with several peptides inside one sequence. Example: ALC, RADGG Result: ALCCCCCRADGGVIM O AND OR: find sequences which contain at least one of the peptides from a list. OR (only Swiss-Prot) Example: ALC, RADGG Result: MGLKALCIGITCVLEV WDMDGLRADGGGAGGAP Type NCBI ID or Taxon Name and choose from the list Lineage taxon: find peptide sequences in organisms that contain particular taxon inside taxon lineage. Example: Homo Sapiens as well as Mus musculus contain taxon Vertebrata 'vertabrates' Database inside its lineage so when you choose Vertebrata 'vertebrates' in lineage taxon option - both of Swiss-Prot & Isoforms these organisms will be used in peptide search. Search Reset Database: find peptide sequence in particular database. UniProtKB (Swiss-Prot + TrEMBL)

Fig. 1. Query form to search for protein sequences containing exact matches of short peptides using the PepString server (http://pepstring.eimb.ru)

fragment from the list in a sequence. A screenshot of the home page is provided in Fig. 1. Multiple sequences can be entered using a comma and/or space as a separator, e.g., "ALC, RADGG", "ALC, RADGG", or "ALC RADGG". Each of the multiple sequences can be placed on a separate line. One query can contain up to five sequences. Two operators, AND and OR, can be used for a search. The AND operator finds protein sequences that include all peptides from the query. The OR operator finds protein sequences that include at least one peptide from the query list. The search can be limited by selecting a taxon of any level, e.g., either Vertebrata, or Archaea, or Mammalia, or Homo sapiens.

Figure 2 shows an example of the results. The results are sorted by organism name. The user can save the query result in the FASTA or CSV format. Searching for a 3-amino acid fragment in the SwissProt database takes a few seconds, whereas in the UniprotKB database it takes from 10 minutes to several hours.

Python and PostgreSQL were used to create a protein sequence database based on UniprotKB (SwissProt+TrEMBL). The database structure diagram is shown in Supplementary Fig. S1. The database is updated automatically almost at the same time as the official UniProtKB database; i.e., approximately once every 8 weeks. The web interface is written using the Django framework.

The taxonomy in our database is identical to the NCBI taxonomy. Please note that NCBI identifiers and organism names may not match the data in the UniProt database. The reason is that UniProt also updates its taxonomy once every 8 weeks. However, our database uses the NCBI Taxonomy database that receives new updates daily, so the version we have used for the update may be different from the UniProt version.

The user's query result is stored in the django celery results taskresult table for 24 h and then deleted.

# **BLAST-based conservation calculations**

EVHH site conservation was calculated using the homologous protein sequences of other species from gnathostome vertebrates via the BLAST program [35]. Thousands of homologous sequences were found for each Uniprot protein identifier from Table 1. The number of sequences containing the EVHH site (the first number in the Conservation column in Table 1) was divided by the number of sequences with all variants of this site (the second number in the Conservation column in Table 1) and multiplied by 100 to obtain the Conservation value in %.

# **EVHH** site variants

A short C++ program was written to parse the fasta sequence files and count all EVHH site variants. The program text is available upon request.

# RESEARCH ARTICLES



Fig. 2. Search result for two ALC RADGG peptides among proteins from the *Mammalia* species using the PepString server

Table 1. Conservation of the EVHH fragment in human proteins determined by BLAST\*

Conservation	Uniprot ID	Protein name	EVHH location
885/985 (89.8%)	P05067	Amyloid-beta precursor protein	682-685, YEVHHQ
683/800 (85.4%)	Q13634	Cadherin-18	46-49, TEVHHR
667/930 (71.7%)	P78310	Coxsackievirus and adenovirus receptor	272–275, KEVHHD
437/995 (43.9%)	Q06124	Tyrosine-protein phosphatase non-receptor type 11	441-444, EEVHHK
405/950 (42.6%)	Q9H8M1	Coenzyme Q-binding protein COQ10 homolog B	234-237, HEVHHT
276/965 (28.6%)	Q9Y2E6	E3 ubiquitin-protein ligase DTX4	575-578, NEVHHK
168/779 (21.6%)	Q03001-11	Neural isoform of dystonin	101-104, VEVHHQ
154/844 (18.2%)	Q58FF7	Putative heat shock protein HSP 90-beta-3	4-7, EEVHHG
133/859 (15.5%)	P08238	Heat shock protein HSP 90-beta	4-7, EEVHHG
134/990 (13.5%)	Q6ZSZ5	Rho guanine nucleotide exchange factor 18	459-462, TEVHHV
105/1000 (10.5%)	O75676	Ribosomal protein S6 kinase alpha-4	471–474, HEVHHD
100/991 (10.1%)	Q86SQ4	Adhesion G-protein coupled receptor G6	797-800, QEVHHP
81/872 (9.6%)	Q7Z3D6	D-glutamate cyclase, mitochondrial	273-276, PEVHHI
47/522 (9.0%)	Q9Y4G2	Pleckstrin homology domain-containing family M member 1	233-236, IEVHHS
87/974 (8.9%)	Q53F39	Metallophosphoesterase 1	309-312, CEVHHG
60/1000 (6.0%)	P54296	Myomesin-2	751-754, REVHHK
48/959 (5.0%)	O76064	E3 ubiquitin-protein ligase RNF8	229-232, TEVHHE
48/1000 (4.8%)	Q5TG30	Rho GTPase-activating protein 40	392-395, DEVHHN
43/998 (4.3%)	Q2M3C7	A-kinase anchor protein SPHKAP	682–685, DEVHHK
25/960 (2.7%)	P10912	Growth hormone receptor	71-74, DEVHHG
26/999 (2.6%)	Q8NH48	Olfactory receptor 5B3	171-174, NEVHHF
4/262 (1.5%)	Q9H0D2	Zinc finger protein 541	218-221, YEVHHG
9/949 (0.9%)	Q5VT97	Rho GTPase-activating protein SYDE2	567-570, REVHHT
4/998 (0.4%)	P41226	Ubiquitin-like modifier-activating enzyme 7	283-286, QEVHHA

<sup>\*</sup>The entries are listed in descending order of conservation.

Table 2. EVHH site variants found in homologues of human APP (P05067) from different species

Motif	Number of sequences	Species
EVHH	885	All birds, reptiles, amphibians, eels and bonefish <i>Albula goreensis</i> , <i>Aldrovandia affinis</i> (Hilbert's halosaur), <i>Latimeria chalumnae</i> (Coelacanth), <i>Megalops atlanticus</i> (Tarpon) (Clupea gigantea), fish such as Salmonidae and others, and almost all mammals
EVRH	64	Balaenoptera acutorostrata scammoni (North Pacific minke whale), Balaenoptera musculus (Blue whale), Castor canadensis (American beaver), Chinchilla lanigera (Long-tailed chinchilla), Dipodomys ordii (Ord's kangaroo rat), Fukomys damarensis (Damaraland mole rat), Haplochromis burtoni (Burton's mouthbrooder), Heterocephalus glaber (Naked mole rat), Ictidomys tridecemlineatus (Thirteen-lined ground squirrel), Jaculus jaculus (Lesser Egyptian jerboa), Marmota marmota marmota (Alpine marmot), Mesocricetus auratus (Golden hamster), Microtus ochrogaster (Prairie vole), Mus musculus (Mouse), Mus spicilegus (Steppe mouse), Nannospalax galili (Northern Israeli blind subterranean mole rat), Octodon degus (Degu), Peromyscus maniculatus bairdii (Prairie deer mouse), Rattus norvegicus (Rat), Sciurus vulgaris (Eurasian red squirrel), Urocitellus parryii (Arctic ground squirrel), Pundamilia nyererei, Maylandia zebra (Zebra mbuna), Atractosteus spatula (Alligator gar), Lepisosteus oculatus (Spotted gar), Oreochromis aureus (Israeli tilapia), Oreochromis niloticus (Nile tilapia)
EVYH	24	Cyprinus carpio carpio, Cirrhinus molitorella (Mud carp), Onychostoma macrolepis, Sinocyclocheilus rhinocerous, Sinocyclocheilus anshuiensis, Danio rerio (Zebrafish), Sinocyclocheilus grahami (Dianchi golden-line fish), Triplophysa rosa (Cave loach)
AVHH	7	Oryzias javanicus (Javanese ricefish), Oryzias latipes (Japanese rice fish), Oryzias melastigma (Marine medaka), Oryzias sinensis (Chinese medaka)
-VHH	1	Clupea harengus (Atlantic herring)
EVHP	1	Denticeps clupeoides (Denticle herring)
EV-H	1	Astyanax mexicanus (Blind cave fish)
EVYP	1	Triplophysa tibetana
RGGW	1	Puma concolor (Mountain lion)

# **RESULTS AND DISCUSSION**

The PepString server found 63 sequences of 24 protein isoforms containing the EVHH fragment in the human proteome. If we take 1,000 homologous proteins from the Uniprot database and count how many of them contain a fragment homologous to EVHH, and in how many cases this fragment is exactly EVHH, we can form some idea of the conservation of this fragment in proteins in different species. In Table 1, we collected information on the EVHH fragment conservation in protein sequences and the position of this fragment in the sequence. A longer version of the table which lists all isoforms containing the EVHH fragment and structural information is presented in Supplementary Table S1. The EVHH fragment in the APP protein is the most conserved (89.8%) (Table 1). EVHH sites in the cadherin-18 and coxsackie virus and adenovirus receptor sequences are somewhat less conserved, 85.4 and 71.7%, respectively. The neuronal isoform of dystonin also deserves attention, because, in addition to the conserved form of EVHH found in 168 out of 779 sequences (21.6%), 315 out of 779 sequences (40.4%) of homologous proteins from different species contain a sequence of this EAHH site that is very similar in physicochemical properties.

In the human amyloid precursor protein (APP) sequence, EVHH is located in the Aß peptide and is able to bind with the Zn2+ ion and form dimers and oligomers [17, 21, 25]. Analysis of APP protein sequences from other gnathostome vertebrate species revealed that APP sequences in all birds, reptiles, amphibians, fishes, and almost all mammals contain a highly conserved variant of EVHH, with a few exceptions (Table 2). For example, both APP isoforms from blue and fin whales contain the EVRH sequence, although the conserved EVHH variant is present in other marine mammals. The same EVRH variant is found in some rodents, including mice, rats, moles, ground squirrels, degus, and naked mole rats (see Table 2 for a complete list). The substitution is not found in all rodents. For example, we found the conserved EVHH variant in APP sequences from Oryctolagus cuniculus (rabbit) and Chrysochloris asiatica (Cape golden mole). Another exception is Puma concolor (mountain lion) that has a single APP isoform comprising a completely different RGGW site at this location.

Further, we will consider the functions of each identified protein. Cadherin-18 is annotated in Uniprot as a protein involved in calcium-dependent cell-cell adhesion, cell migration, and morphogenesis. In the

cadherin-18 sequence, the EVHH fragment is located in the 25–53 propeptide that is cleaved from the protein during maturation. In the AlphaFold model of the structure of this protein, the EVHH site is located in a disordered loop, on the protein surface (Supplementary, Table S1). The function of this propeptide is not yet known. According to Uniprot, asparagine residue 36 can be glycosylated, which makes the propeptide sensitive to blood glucose levels. Cadherin-18 is known to be associated with AD. Cadherin was experimentally shown to interact with presenilin-1 that is involved in AD [36].

The coxsackievirus and adenovirus receptor is a component of the epithelial apical junction complex, which can function as a homophilic cell adhesion molecule and is required for maintaining tight junctions [37]. It is also involved in transepithelial leukocyte migration through adhesive interactions with JAML, a transmembrane protein of the plasma membrane of leukocytes. After binding to the epithelial coxsackievirus adenovirus receptor (CXADR), JAML induces subsequent signaling events in gamma-delta T cells through PI3-kinase and MAP-kinase. This leads to T cell proliferation and production of cytokines and growth factors that, in turn, stimulate epithelial tissue repair [38]. The EVHH fragment is located in the 269-285 domain of this receptor that is annotated as a domain rich in charged amino acids. This means that this fragment is very flexible and can change its conformation depending on the structure of the interaction partner. The coxsackievirus and adenovirus receptor is associated with AD. Coxsackievirus [39] or adenovirus [40] infection has been shown to be capable of triggering the onset of AD in the elderly, because it provokes prion protein expression.

The next protein with high conservation of the EVHH fragment is tyrosine phosphatase non-receptor type 11 that is involved in cascades of various receptor and cytoplasmic tyrosine kinases and participates in signal transmission from the cell surface to the nucleus. Kinase activation suppresses the function of integrins and causes dephosphorylation of focal adhesion kinase [41]. It is one of the important negative regulators of the nuclear export of telomerase reverse transcriptase [42]. Mutations in this protein are associated with a number of diseases, e.g., LEOPARD syndrome [43] or Noonan syndrome [44], that develop due to downregulation of the intracellular RAS/MAPK signaling pathway. There are currently no data on any association with AD.

The mitochondrial coenzyme Q-binding protein COQ10 homologue B (Q9H8M1) is necessary for the function of coenzyme Q10 in the respiratory chain and may serve as a chaperone or may partici-

pate in the transport of Q10 from its site of synthesis to the catalytic sites of the respiratory complexes. According to the AlphaFold model, the EVHH site is a part of the  $\beta$ -strand on the protein surface (see Supplementary, Table S1). There is an opinion in the scientific community that the introduction of coenzyme Q10 increases the concentration of mitochondria in the brain and provides a neuroprotective capability [45, 46]. However, this was not convincingly shown in phase II clinical trials, and it was decided not to conduct phase III clinical trials [47].

E3 ubiquitin-protein ligase DTX4 (Q9Y2E6) is involved in the negative regulation of type I interferon signaling through NLRP4 by targeting the kinase TBK1 for degradation [48]. In addition to 276/965 (28.6%) identified conserved EVHH sequences, an EIHH fragment with very similar physicochemical properties was found in 687/965 (71.2%) sequences. A homologous ubiquitin ligase DTX2 is associated with small vessel damage in the early stages of AD [49].

A neuronal isoform of dystonin (Q03001-11), apart from an EVHH site variant found in 168 out of 779 sequences (21.6%), also occurs as a very physicochemically similar EAHH site variant in 315 out of 779 sequences (40.4%). Mutations in the gene for this protein lead to progressive degeneration of sensory neurons in mice. These mice suffer from sensory ataxia and die by weaning age [50]. They develop a severe movement disorder due to sensory neuron degeneration [51].

We analyzed EVHH site locations and conformations in protein structures. In human proteins, EVHH site conformations form four clusters (Fig.~3). The conformation of the EVHH site in myomesin is the closest to that of the zinc-binding domain in A $\beta$ . An association of myomesin-2 with AD was also found. Investigation of cardiomyopathy in transgenic mice showed that small heat shock protein  $\alpha$ -B-crystallin (CryAB) aggregates found in diseased hearts contained an amyloid oligomer that may be the main toxic species in AD and other amyloid-associated degenerative diseases [52].  $\alpha$ -B-crystallin is known to interact with myomesin-2 [53].

In 21 out of 24 structures, the EVHH site is located on the protein surface. There is no AlphaFold model for the dystonin sequence (Q03001-11). In the Rho guanine nucleotide exchange factor 18 (Q6ZSZ5) model, the EVHH site is located inside the protein globule. In the A-kinase anchor protein SPHKAP (Q2M3C7) model, the EVHH site is surrounded by unstructured loops.

In summary, the 11-EVHH-14 site in the  $A\beta$  sequence is highly conserved in all gnathostome ver-

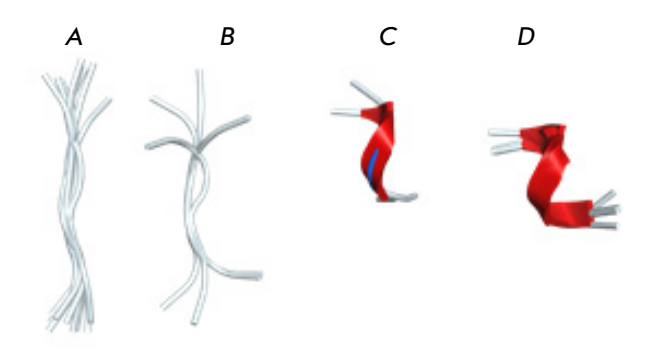


Fig. 3. EVHH site conformations in human protein structures form four clusters. (A) Unfolded conformation (O76064, Q9H8M1, Q5VT97, Q13634, Q7Z3D6, Q9Y4G2, P08238, Q58FF7, P10912, O75676, Q53F39). (B) Unstructured conformation (Q9Y2E6, Q5TG30, Q8NH48, Q86SQ4). (C) Convoluted conformation (P54296, 1ze9). (D) α-Helix (Q2M3C7 (EVHH site within the globule), Q9H0D2, 3B7O, P78310, Q6ZSZ5 (EVHH site within the globule), P41226). Only EVHH sites in Q6ZSZ5 and Q2M3C7 are buried in the protein globule and are inaccessible

tebrates. Gnanthostomes amount to more than 99% of all living vertebrate species, including humans. Previously, the H13R substitution was shown to protect rats from AD [18]. In Balaenoptera acutorostrata scammoni (North Pacific minke whale) and Balaenoptera musculus (blue whale), as well as in some rodents, such as Heterocephalus glaber (naked mole rat) or Nannospalax galili (Northern Israeli blind subterranean mole rat) (Table 2), exactly this substitution that converts EVHH into EVRH exists, which apparently renders these species protected against pathological Aβ aggregation and thus not susceptible to AD. The explanation for this follows from the molecular mechanism of Zn-dependent oligomerization of Aβ [17], which indicates a key role for the EVHH site in the pathological process.

We found that the EVHH site was present in 63 isoforms of 24 proteins. Each of these proteins may be a potential molecular partner of zinc-dependent interaction with the amyloid-beta molecule. Some of them are known to be associated with AD pathogenesis, but there is no data on the mechanisms of their action. Six of the 24 identified proteins, namely APP, cadherin-18, coxsackievirus and adenovirus receptor, adhesion G protein-coupled receptor G6, growth hormone receptor, and olfactory receptor 5B3, reside in the cell membrane, are receptors, and probably transmit a signal into the cell.

The identified proteins are both potential targets for HAEE and possible partners of A $\beta$ . As shown previously [17, 25], residues of site 11–14 of the A $\beta$  peptide (EVHH) form a zinc-mediated interface with a similar region of another A $\beta$  molecule. It is logical to assume that such interactions can occur not only between identical molecules of amyloid-beta, but also with other proteins that have a similar region available for interaction.

Let us make several suggestions. First, APP functions as a cell surface receptor and performs physiological functions on the surface of neurons, which are related to neurite outgrowth, neuronal adhesion, and axonogenesis [54]. Interactions between APP molecules on neighboring cells are known to promote synaptogenesis [54]. Since zinc ions are involved in synaptogenesis, we venture to suggest that the interaction between APP molecules occurs through the Zn-dependent interface of EVHH sites. This bold suggestion requires further experimental evidence.

EVHH sites have been found in mitochondrial proteins, D-glutamate cyclase, and coenzyme Q-binding protein Q9H8M1. Since A $\beta$  peptide is known to induce the AGER-dependent pathway that involves activation of p38 MAPK, resulting in internalization of the A $\beta$  peptide and mitochondrial dysfunction in cultured cortical neurons [55], the second suggestion is that the A $\beta$  peptide is able to penetrate the mitochondrial membrane and form zinc-dependent complexes with one or both proteins.

Notably, another of the identified EVHH site-containing proteins, namely tyrosine-protein phosphatase non-receptor type 11, positively regulates the MAPK signaling pathway [44]. A third suggestion is that A $\beta$  regulates the MAPK signal transduction pathway through the zinc-dependent interface with tyrosine-protein phosphatase non-receptor type 11. Another protein from this list, namely the coxsackievirus and adenovirus receptor, also triggers one of the MAPK activation pathways.

Another group of proteins, which we found to be involved in the regulation of neuronal activity, includes cadherin-18, coxsackievirus and adenovirus receptor, and adhesion G-protein-coupled receptor G6 that interacts with laminin-2, Rho guanine nucleotide exchange factor 18, and dystonin. Cadherins are calcium-dependent cell adhesion proteins. They preferentially interact amongst themselves in a homophilic manner in connecting cells; thus, cadherins may facilitate the sorting of heterogeneous cell types. The coxsackievirus and adenovirus receptor, in addition to its negative role in virus entry, is a component of the epithelial apical—junctional complex, which can function as a homophilic cell ad-

hesion molecule and is essential to the integrity of tight junctions. The adhesion G-protein-coupled receptor G6 is a major component of the basal membrane. It couples with G(i) and G(s) proteins and is required for normal differentiation of promyelinating Schwann cells and for normal axonal myelination [56]. Rho factor 18 acts as a guanine nucleotide exchange factor (GEF) for the GTPase RhoA, inducing the formation of actin stress fibers and the production of reactive oxygen species (ROS). It can be activated by the beta-gamma subunits of G proteins [57]. The neuronal isoform of dystonin is poorly understood. Mutations in the gene for this protein in mice are known to result in progressive degeneration of sensory neurons. These mice suffer from sensory ataxia and die by weaning age [50]. The fourth suggestion is that these proteins are partners of the G protein, and the interaction with them through the zinc-dependent interface affects the function of the G protein and G protein-associated processes in the cell. However, the structural model of Rho guanine nucleotide exchange factor 18 suggests that the EVHH site is located inside the protein globule and is inaccessible to a solvent.

The fifth suggestion is that the A $\beta$  peptide can form complexes with two heat shock proteins, HSP 90-beta (P08238) and 90-beta-3 (Q58FF7), through the zinc-dependent interface and affects maturation, maintenance of the structure, and proper regulation of specific target proteins. Apart from chaperone activity, it also plays a role in the regulation of the transcription mechanism. HSP90 and its co-chaperones modulate transcription at least on three different levels. First, they alter the steady-state levels of certain transcription factors in response to various physiological signals. Second, they modulate the activity of some epigenetic modifiers, such as histone deacetylases or DNA methyltransferases, and respond to changes in the environment. Third, they are involved

in the migration of histones from the promoter region of certain genes and, thereby, switch on gene expression [58].

Gene expression can also be influenced by zinc finger protein 541 (Q9H0D2). This transcriptional regulator is essential for male fertility and meiotic prophase completion in spermatocytes. The aforementioned tyrosine-protein phosphatase non-receptor type 11 (Q06124) is also involved in a cascade of various receptor and cytoplasmic protein tyrosine kinases, participating in signal transmission from the cell surface to the nucleus. Zinc finger proteins [59] and tyrosine phosphatases [60] are known to be associated with AD, but the exact mechanism of the interaction remains unknown.

#### **CONCLUSION**

This paper introduces an original PepString server for the search for short amino acid sequences in the UniprotKB and SwissProt databases. Using the PepString server, we demonstrated for the first time that the tetrapeptide EVHH site, which is a structural and functional determinant of human amyloid-beta both in health and in AD, is present in 63 isoforms of 24 proteins. On the basis of an analysis of data on the association between these proteins and AD, we proposed a potential role for cadherin-18, coxsackievirus and adenovirus receptor, E3-ubiquitin ligase DTX4, the neuronal isoform of dystonin, and myomesin-2 in AD pathogenesis. •

This work was supported by the Russian Science Foundation (grant No. 19-74-30007).

The authors express their gratitude to Yu.V. Kravatsky for his help and valuable advice.

The Supplementary Materials are available at https://doi.org/10.32607/actanaturae.27630.

#### REFERENCES

- Baig M.H., Ahmad K., Saeed M., Alharbi A.M., Barreto G.E., Ashraf G.M., Choi I. // Biomed. Pharmacother. 2018.
   V. 103. P. 574–581. doi: 10.1016/j.biopha.2018.04.025.
- 2. Livingston G., Huntley J., Sommerlad A., Ames D., Ballard C., Banerjee S., Brayne C., Burns A., Cohen-Mansfield J., Cooper C., et al. // Lancet Lond. Engl. 2020. V. 396. № 10248. P. 413–446. doi: 10.1016/S0140-6736(20)30367-6.
- 3. Walker L.C. // Free Neuropathol. 2020. V. 1. P. 1–31. doi: 10.17879/freeneuropathology-2020-3025.
- 4. Long J.M., Holtzman D.M. // Cell. 2019. V. 179.  $\mathbb{N}_{2}$  2. P. 312–339. doi: 10.1016/j.cell.2019.09.001.
- Querfurth H.W., LaFerla F.M. // N. Engl. J. Med. 2010.
   V. 362. № 4. P. 329–344. doi: 10.1056/NEJMra0909142.

- Cohen S.I.A., Linse S., Luheshi L.M., Hellstrand E., White D.A., Rajah L., Otzen D.E., Vendruscolo M., Dobson C.M., Knowles T.P.J. // Proc. Natl. Acad. Sci. USA. 2013. V. 110. № 24. P. 9758–9763. doi: 10.1073/pnas.1218402110.
- 7. Surguchov A., Emamzadeh F.N., Titova M., Surguchev A.A. // Biomedicines. 2023. V. 11. № 4. P. 1215. doi: 10.3390/biomedicines11041215.
- 8. Golde T.E., DeKosky S.T., Galasko D. // Science. 2018. V. 362. № 6420. P. 1250–1251. doi: 10.1126/science.aau0437.
- 9. Masters C.L., Selkoe D.J. // Cold Spring Harb. Perspect. Med. 2012. V. 2. № 6. P. a006262. doi: 10.1101/cshperspect. a006262.
- 10. Kepp K.P. // Chem. Rev. 2012. V. 112.  $\mathbb{N}_{2}$  10. P. 5193–5239. doi: 10.1021/cr300009x.

- 11. Wang J., Gu B.J., Masters C.L., Wang Y.-J. // Nat. Rev. Neurol. 2017. V. 13. № 10. P. 612–623. doi: 10.1038/nrneurol.2017.111.
- 12. Cadoni M.P.L., Coradduzza D., Congiargiu A., Sedda S., Zinellu A., Medici S., Nivoli A.M., Carru C. // J. Clin. Med. 2024. V. 13. № 7. P. 2102. doi: 10.3390/jcm13072102.
- 13. Roher A.E., Esh C.L., Kokjohn T.A., Castaño E.M., van Vickle G.D., Kalback W.M., Patton R.L., Luehrs D.C., Daugs I.D., Kuo Y.-M., et al. // Alzheimers Dement. J. Alzheimers Assoc. 2009. V. 5. № 1. P. 18–29. doi: 10.1016/j. jalz.2008.10.004.
- Brothers H.M., Gosztyla M.L., Robinson S.R. // Front. Aging Neurosci. 2018. V. 10. P. 118. doi: 10.3389/fnagi.2018.00118.
- 15. Jeong H., Shin H., Hong S., Kim Y. // Exp. Neurobiol. 2022. V. 31.  $\mathbb{N}_2$  2. P. 65–88. doi: 10.5607/en22004.
- 16. Kozin S.A., Kechko O.I., Adzhubei A.A., Makarov A.A., Mitkevich V.A. // Int. J. Mol. Sci. 2024. V. 25. № 1. P. 72. doi: 10.3390/ijms25010072.
- 17. Istrate A.N., Kozin S.A., Zhokhov S.S., Mantsyzov A.B., Kechko O.I., Pastore A., Makarov A.A., Polshakov V.I. // Sci. Rep. 2016. V. 6. № 1. P. 21734. doi: 10.1038/srep21734.
- 18. Istrate A.N., Tsvetkov P.O., Mantsyzov A.B., Kulikova A.A., Kozin S.A., Makarov A.A., Polshakov V.I. // Biophys. J. 2012. V. 102. № 1. P. 136–143. doi: 10.1016/j. bpj.2011.11.4006.
- 19. Kulikova A.A., Tsvetkov P.O., Indeykina M.I., Popov I.A., Zhokhov S.S., Golovin A.V., Polshakov V.I., Kozin S.A., Nudler E., Makarov A.A. // Mol. Biosyst. 2014. V. 10. № 10. P. 2590–2596. doi: 10.1039/c4mb00332b.
- 20. Nisbet R.M., Nuttall S.D., Robert R., Caine J.M., Dolezal O., Hattarki M., Pearce L.A., Davydova N., Masters C.L., Varghese J.N., et al. // Proteins Struct. Funct. Bioinforma. 2013. V. 81. № 10. P. 1748–1758. doi: 10.1002/prot.24312.
- 21. Zirah S., Kozin S.A., Mazur A.K., Blond A., Cheminant M., Ségalas-Milazzo I., Debey P., Rebuffat S. // J. Biol. Chem. 2006. V. 281. № 4. P. 2151–2161. doi: 10.1074/jbc. M504454200.
- 22. Kollmer M., Close W., Funk L., Rasmussen J., Bsoul A., Schierhorn A., Schmidt M., Sigurdson C.J., Jucker M., Fändrich M. // Nat. Commun. 2019. V. 10. № 1. P. 4760. doi: 10.1038/s41467-019-12683-8.
- 23. Barykin E.P., Garifulina A.I., Tolstova A.P., Anashkina A.A., Adzhubei A.A., Mezentsev Y.V., Shelukhina I.V., Kozin S.A., Tsetlin V.I., Makarov A.A. // Int. J. Mol. Sci. 2020. V. 21. № 17. P. 6272. doi: 10.3390/ijms21176272.
- 24. Lawrence J.L.M., Tong M., Alfulaij N., Sherrin T., Contarino M., White M.M., Bellinger F.P., Todorovic C., Nichols R.A. // J. Neurosci. Off. J. Soc. Neurosci. 2014. V. 34. № 43. P. 14210–14218. doi: 10.1523/JNEUROS-CI.0326-14.2014.
- 25. Kozin S.A., Mezentsev Y.V., Kulikova A.A., Indeykina M.I., Golovin A.V., Ivanov A.S., Tsvetkov P.O., Makarov A.A. // Mol. Biosyst. 2011. V. 7. № 4. P. 1053–1055. doi: 10.1039/c0mb00334d.
- 26. Kechko O.I., Adzhubei A.A., Tolstova A.P., Indeykina M.I., Popov I.A., Zhokhov S.S., Gnuchev N.V., Mitkevich V.A., Makarov A.A., Kozin S.A. // Int. J. Mol. Sci. 2023. V. 24. № 14. P. 11241. doi: 10.3390/ijms241411241.
- 27. Khmeleva S.A., Radko S.P., Kozin S.A., Kiseleva Y.Y., Mezentsev Y.V., Mitkevich V.A., Kurbatov L.K., Ivanov A.S., Makarov A.A. // J. Alzheimers Dis. JAD. 2016. V. 54. N2. P. 809–819. doi: 10.3233/JAD-160415.
- 28. Zheng H., Koo E.H. // Mol. Neurodegener. 2006. V. 1. P. 5. doi: 10.1186/1750-1326-1-5.

- Chasseigneaux S., Allinquant B. // J. Neurochem.
   V. 120 Suppl 1. P. 99–108. doi: 10.1111/j.1471-4159.2011.07584.x.
- 30. van Dyck C.H., Swanson C.J., Aisen P., Bateman R.J., Chen C., Gee M., Kanekiyo M., Li D., Reyderman L., Cohen S., et al. // N. Engl. J. Med. 2023. V. 388. № 1. P. 9–21. doi: 10.1056/NEJMoa2212948.
- 31. Kepp K.P., Robakis N.K., Høilund-Carlsen P.F., Sensi S.L., Vissel B. // Brain J. Neurol. 2023. V. 146. № 10. P. 3969–3990. doi: 10.1093/brain/awad159.
- 32. Cummings J., Zhou Y., Lee G., Zhong K., Fonseca J., Cheng F. // Alzheimers Dement. 2023. V. 9. № 2. P. e12385. doi: 10.1002/trc2.12385.
- 33. Ribarič S. // Mol. Basel Switz. 2018. V. 23. № 2. P. 283. doi: 10.3390/molecules23020283.
- 34. Mitkevich V.A., Barykin E.P., Eremina S., Pani B., Katkova-Zhukotskaya O., Polshakov V.I., Adzhubei A.A., Kozin S.A., Mironov A.S., Makarov A.A., et al. // Aging Dis. 2023. V. 14. № 2. P. 309–318. doi: 10.14336/AD.2022.0827.
- 35. Altschul S.F., Gish W., Miller W., Myers E.W., Lipman D.J. // J. Mol. Biol. 1990. V. 215. № 3. P. 403–410. doi: 10.1016/S0022-2836(05)80360-2.
- 36. Zhou J., Liyanage U., Medina M., Ho C., Simmons A.D., Lovett M., Kosik K.S. // Neuroreport. 1997. V. 8. № 8. P. 2085–2090. doi: 10.1097/00001756-199705260-00054.
- 37. Cohen C.J., Shieh J.T.C., Pickles R.J., Okegawa T., Hsieh J.-T., Bergelson J.M. // Proc. Natl. Acad. Sci. USA. 2001. V. 98. № 26. P. 15191–15196. doi: 10.1073/pnas.261452898.
- 38. Luissint A.-C., Artus C., Glacial F., Ganeshamoorthy K., Couraud P.-O. // Fluids Barriers CNS. 2012. V. 9. № 1. P. 23. doi: 10.1186/2045-8118-9-23.
- 39. Nakamura Y., Sakudo A., Saeki K., Kaneko T., Matsumoto Y., Toniolo A., Itohara S., Onodera T. // J. Gen. Virol. 2003. V. 84. № Pt 12. P. 3495–3502. doi: 10.1099/vir.0.19222-0.
- 40. Caruso P., Burla R., Piersanti S., Cherubini G., Remoli C., Martina Y., Saggio I. // Virology. 2009. V. 385. № 2. P. 343–350. doi: 10.1016/j.virol.2008.12.005.
- 41. Miao H., Burnett E., Kinch M., Simon E., Wang B. // Nat. Cell Biol. 2000. V. 2. № 2. P. 62–69. doi: 10.1038/35000008.
- 42. Jakob S., Schroeder P., Lukosz M., Büchner N., Spyridopoulos I., Altschmied J., Haendeler J. // J. Biol. Chem. 2008. V. 283. № 48. P. 33155–33161. doi: 10.1074/jbc. M805138200.
- 43. Noda S., Takahashi A., Hayashi T., Tanuma S., Hatakeyama M. // Biochem. Biophys. Res. Commun. 2016. V. 469. № 4. P. 1133–1139. doi: 10.1016/j.bbrc.2015.12.117.
- 44. Pannone L., Bocchinfuso G., Flex E., Rossi C., Baldassarre G., Lissewski C., Pantaleoni F., Consoli F., Lepri F., Magliozzi M., et al. // Hum. Mutat. 2017. V. 38. № 4. P. 451–459. doi: 10.1002/humu.23175.
- 45. Matthews R.T., Yang L., Browne S., Baik M., Beal M.F. // Proc. Natl. Acad. Sci. USA. 1998. V. 95. № 15. P. 8892–8897. doi: 10.1073/pnas.95.15.8892.
- 46. Yang X., Yang Y., Li G., Wang J., Yang E.S. // J. Mol. Neurosci. MN. 2008. V. 34. № 2. P. 165–171. doi: 10.1007/s12031-007-9033-7.
- 47. Kaufmann P., Thompson J.L.P., Levy G., Buchsbaum R., Shefner J., Krivickas L.S., Katz J., Rollins Y., Barohn R.J., Jackson C.E., et al. // Ann. Neurol. 2009. V. 66. № 2. P. 235–244. doi: 10.1002/ana.21743.
- 48. Cui J., Li Y., Zhu L., Liu D., Songyang Z., Wang H.Y., Wang R.-F. // Nat. Immunol. 2012. V. 13. № 4. P. 387–395. doi: 10.1038/ni.2239.
- 49. Chen Y., Lu P., Wu S., Yang J., Liu W., Zhang Z., Xu Q.

#### RESEARCH ARTICLES

- // Int. J. Mol. Sci. 2024. V. 25.  $\mathbb{N}_{2}$  4. P. 2293. doi: 10.3390/ iims25042293.
- 50. Brown A., Dalpé G., Mathieu M., Kothary R. // Genomics. 1995. V. 29. № 3. P. 777–780. doi: 10.1006/ geno.1995.9936.
- 51. Young K.G., Kothary R. // Cell Motil. Cytoskeleton. 2007. V. 64.  $\mathbb{N}_2$  12. P. 897–905. doi: 10.1002/cm.20235.
- 52. Sanbe A., Osinska H., Saffitz J.E., Glabe C.G., Kayed R., Maloyan A., Robbins J. // Proc. Natl. Acad. Sci. USA. 2004. V. 101. № 27. P. 10132–10136. doi: 10.1073/pnas.0401900101.
- 53. Lutsch G., Vetter R., Offhauss U., Wieske M., Gröne H.J., Klemenz R., Schimke I., Stahl J., Benndorf R. // Circulation. 1997. V. 96. № 10. P. 3466–3476. doi: 10.1161/01. cir.96.10.3466.
- 54. Baumkötter F., Schmidt N., Vargas C., Schilling S., Weber R., Wagner K., Fiedler S., Klug W., Radzimanowski J., Nickolaus S., et al. // J. Neurosci. Off. J. Soc. Neurosci. 2014. V. 34. № 33. P. 11159–11172. doi: 10.1523/JNEUROS-CI.0180-14.2014.

- 55. Ariyoshi M., Katane M., Hamase K., Miyoshi Y., Nakane M., Hoshino A., Okawa Y., Mita Y., Kaimoto S., Uchihashi M., et al. // Sci. Rep. 2017. V. 7. P. 43911. doi: 10.1038/srep43911.
- 56. Mogha A., Benesh A.E., Patra C., Engel F.B., Schöneberg T., Liebscher I., Monk K.R. // J. Neurosci. Off. J. Soc. Neurosci. 2013. V. 33. № 46. P. 17976–17985. doi: 10.1523/JNEUROSCI.1809-13.2013.
- 57. Nakajima H., Tanoue T. // J. Cell Biol. 2011. V. 195. № 2. P. 245–261. doi: 10.1083/jcb.201104118.
- 58. Khurana N., Bhattacharyya S. // Front. Oncol. 2015. V. 5. P. 100. doi: 10.3389/fonc.2015.00100.
- 59. Bu S., Lv Y., Liu Y., Qiao S., Wang H. // Front. Neurosci. 2021. V. 15. P. 760567. doi: 10.3389/fnins.2021.760567.
- 60. Fontán-Baselga T., Cañeque-Rufo H., Rivera-Illades E., Gramage E., Zapico J.M., de Pascual-Teresa B., Ramos-Álvarez M.D.P., Herradón G., Vicente-Rodríguez M. // Front. Pharmacol. 2024. V. 15. P. 1506049. doi: 10.3389/fphar.2024.1506049.

# The Generation and Characterization of a Mouse Embryonic Stem Cell Line with *Psmb9* Immunoproteasome Gene Knockout

D. V. Kriger\*, U. I. Podenkova, A. A. Kuzmin, N. D. Aksenov, A. V. Kropacheva, A. S. Zinovyeva, A. V. Selenina, A. N. Tomilin, A. S. Tsimokha\*\*

Institute of Cytology, Russian Academy of Sciences, St-Petersburg, 194064 Russia

\*E-mail: daryamalikova@gmail.com; \*\*E-mail: atsimokha@incras.ru

Received: December 06, 2024; in final form, May 15, 2025

DOI: 10.32607/actanaturae.27583

Copyright © 2025 National Research University Higher School of Economics. This is an open access article distributed under the Creative Commons Attribution License, which permits unrestricted use, distribution, and reproduction in any medium, provided the original work is properly cited.

ABSTRACT Immunoproteasomes, a unique type of proteasome complex, play a critical role in antigen presentation and cellular homeostasis. Unlike the constitutive 20S proteasome, the catalytic subunits β1, β2, and β5 in the immunoproteasome are replaced by inducible isoforms: β1i (LMP2), β2i (MECL-1), and β5i (LMP7). The expression of the genes encoding these subunits (Psmb9, Psmb10, and Psmb8) is activated by cytokines, primarily interferon-y (IFNy). Although it has been demonstrated more and more convincingly that immunoproteasomes are expressed in embryonic stem cells (ESCs), their involvement in maintaining pluripotency, promoting self-renewal, and regulating differentiation processes remains unexplored. This study implemented CRISPR/Cas9 technology to generate a Psmb9 gene knockout (Psmb9KO) mouse ESC line. The resulting cells exhibited a normal karyotype and morphology, maintained normal proliferation rates, and retained the capacity to form teratomas containing derivatives of all three germ layers. However, the differentiation induced by retinoic acid (RA) and IFNγ caused an accumulation of Mecl-1 precursors in Psmb9KO cells, suggesting modifications in immunoproteasome assembly. Furthermore, an increase in the caspase-like activity of immunoproteasomes was detected, suggesting the integration of a constitutive β1-subunit into the complex in place of Lmp2. The findings underscore the adaptability of the ubiquitin-proteasome system in maintaining cellular proteostasis by compensatory mechanisms that counteract the lack of Lmp2. The Psmb9KO line can serve as a valuable model for examining the function of immunoproteasomes in proteostasis regulation during early mammalian embryogenesis differentiation.

KEYWORDS Psmb9, Lmp2, immunoproteasome, mouse ESCs, differentiation.

ABBREVIATIONS UPS – ubiquitin-proteasome system; ESC – embryonic stem cells; ROS – reactive oxygen species; CL – caspase-like activity; RA – retinoic acid; IFNγ – interferon-γ.

#### **INTRODUCTION**

For the body to function properly and maintain its integrity, proteins must circulate within cells without interruption. The cellular protein equilibrium – known as proteostasis – is maintained through the concerted activity of the *de novo* protein synthesis machinery and the degradation processes responsible for the removal of damaged or superfluous proteins. Cellular protein degradation is mainly mediated by autophagy and the ubiquitin-proteasome system (UPS). At least 80% of intracellular proteins are degraded by the UPS [1]. This particular system identifies and directs ubiquitinated proteins for proteasomal degradation.

The key component of the UPS is the proteasome, a multi-subunit protein complex that breaks down proteins into peptides. The proteasome complexes can be distinguished by the variations in their proteolytic subunits and the regulatory complex that interacts with the core particle [2]. The 26S proteasome is a term that typically refers to proteasome complexes that have a 20S core particle and a 19S regulator. The 20S proteasome, the core particle, is shaped like a barrel due to the arrangement of its four constituent rings. Every ring comprising seven subunits – either alpha ( $\alpha$ ) or beta ( $\beta$ ) – is arranged in a specific  $\alpha\beta\beta\alpha$  sequence. This configuration of rings results in sealed spaces, referred to as "chambers," within the

proteasome [3]. Proteolytic cleavage of protein substrates within the proteasome happens in a "catalytic" chamber, which is formed by two central  $\beta$ -rings. In eukaryotes, three subunits, commonly referred to as  $\beta$ 1,  $\beta$ 2, and  $\beta$ 5, perform proteolytic activity. These catalytic subunits are known to possess differences in their substrate specificity. The  $\beta1$  subunit can cleave peptide bonds following "acidic" amino acid residues, a process referred to as caspase-like activity. The  $\beta2$ subunit exhibits trypsin-like activity and cleaves polypeptide chains subsequent to basic amino acids. As for the β5-subunit, it is characterized by chymotrypsin-like activity, which leads to the hydrolysis of peptide bonds following hydrophobic amino acid residues. The catalytic chamber is completely sealed from the external environment, preventing accidental degradation of proteins and ensuring process specificity. The N-terminal sequences of  $\alpha$ -subunits act as a gate, limiting the access of substrate proteins to the catalytic chamber of the core particle, opening only upon binding to the regulatory particle [4], thereby ensuring stringent regulation of the protein degradation process.

Upon stimulation of mammalian cells with interferon-γ (IFNγ), the expression of alternative catalytic subunits is induced, resulting in the assembly of a modified 20S proteasome, also known as the immunoproteasome [5]. Within the immunoproteasome, the constitutive catalytic  $\beta$ -subunits ( $\beta$ 1,  $\beta$ 2, and  $\beta$ 5) are replaced by their inducible counterparts: Lmp2 (β1i), Mecl-1 (β2i), and Lmp7 (β5i). These substitutions alter the proteolytic activity of the proteasome complex [5, 6], as the Lmp2 ( $\beta$ 1i) and Lmp7 ( $\beta$ 5i) subunits exhibit chymotrypsin-like activity, whereas Mecl-1 ( $\beta$ 2i) is defined by trypsin-like activity. Immunoproteasomes are crucial in the generation of peptide antigens for MHC I presentation [7], by which they play a vital role in antiviral [8] and antitumor defense [9]. In addition to their role in antigen presentation, immunoproteasomes play a crucial role in the regulation of proteostasis by inhibiting the accumulation of damaged or misfolded proteins within the cell [10, 11]. Furthermore, during the differentiation of human embryonic stem cells (ESCs), immunoproteasome activity gradually recedes, suggesting their involvement in adaptive shifts in the cellular state [12]. In addition, immunoproteasomes have been shown to participate in the degradation of oxidized proteins, which plays a crucial role in the maintenance of proteome integrity under conditions of cellular differentiation-induced stress. For example, in mouse ESCs, immunoproteasomes are activated through the accumulation of oxidized proteins, but this activity increases substantially during differentiation, not in the state of pluripotency [13, 14]. According to our research, mouse ESCs activate the expression of all three catalytic subunits of the immunoproteasome when transitioning out of the naïve pluripotency state [15]. Consequently, recent data suggest that the role of immunoproteasomes in pluripotent cells may be associated with preparation for differentiation, thereby facilitating the degradation of damaged proteins and maintaining cellular homeostasis. Nonetheless, the functional role of immunoproteasomes in maintaining pluripotency and self-renewal in ESCs remains for the most part unexplored.

Previously, we generated and characterized a mouse embryonic stem cell line with knockout of the Psmb8 gene, which encodes the immunoproteasome subunit Lmp7 (β5i) [16]. To examine the contributions of individual catalytic subunits of the immunoproteasome during early embryogenesis, we acquired mouse ESCs with Psmb9 gene knockout, which encodes another catalytic subunit of the immunoproteasome: Lmp2 (β1i). The resulting cell lines underwent genotyping, karyotyping, and functional characterization, encompassing the assessment of proliferation rates, analysis of pluripotency marker expression, determination of the Lmp7 and Mecl-1 expression levels, evaluation of proteasome proteolytic activities, and assessment of their capacity for in vivo differentiation.

#### **EXPERIMENTAL PART**

#### Cell culture

This study used mouse ESCs of the E14 Tg2a line. The cells were cultivated at  $-37^{\circ}C$  in a humidified atmosphere with 5% CO $_2$ . Culture dishes were pre-coated with a 0.1% gelatin solution (Sigma, USA). The SL medium based on Knockout DMEM (Thermo Fisher, USA) was supplemented with 15% heat-inactivated fetal bovine serum (HyClone, GE Healthcare Life Sciences, UK), 100 U/mL penicillin and 100 µg/mL streptomycin (Thermo Fisher, USA), 2 mM L-glutamine (Thermo Fisher, USA), a 100 µM non-essential amino acids solution (Thermo Fisher, USA), 100 µM  $\beta$ -mercaptoethanol (Sigma, Germany), and a 500 U/mL leukemia inhibitory factor (LIF, produced in our laboratory).

The protein levels of the immunoproteasome subunits were evaluated after ESCs had been differentiating for 2 days in the SL medium without LIF but supplemented with 0.1  $\mu$ M retinoic acid (RA, Sigma). Subsequently, the cells remained in culture for an additional 24 h within a medium enriched with IFN $\gamma$  (ProSpec, Israel) at a concentration of 150 U/mL.

Table 1. gRNA sequences and possible off-target sites with primers designed for amplifying specific genomic regions

Type	Sequence (5' -> 3')	Score	Cleavage-prone chromosomal region	Primers (5' -> 3')
gRNA	GTTTGACGGGGGTGTCGTGG	100	chr17:-34404735	AACTGCAGATAACACAGTCCATC
				CCAGGACCAGGAAAGACCTGG
Off-target 1	GTGTGAAGGGGGTGTCATGG	0.9	chr7:+15781982	AAGTGCAGGTCCTCTGAAAAGAA
				AGAAATGGAGTAGTGTGCTCCACAA
Off-target 2	AGTAGACGGGGGTGTCGTGC	0.9	chr16:+96466310	CTCTTGTCTTCCTCTCCTGT
				GCTTGGACCCTAGAGTGGAA
Off-target 3	GTCAGACTGGGGTGTCCTGG	0.7	chr6:+28141384	TCGGATCTAGGAAGCAGTCTC
				GCAGTAGATAGCCTGAACCTG
Off-target 4	TTATGACGTGAGTGTCGTGG	0.6	chr14:-118326405	AGTCTGGTCTAGAGCTGTCCTC
				TCCTTTGGGAGTAGGGCTATGT
Off-target 5	GCTGGATGGGGGTGTCTTGG	0.5	chr5:+114566059	ATAAACGGCCAAGGTCAACC
				TGGGAGACACAGATTCCTAAACT

#### Generation of Psmb9 knockout mouse ESCs

The Psmb9 gene was inactivated utilizing CRISPR/Cas9 genome editing technology. The guide RNA (gRNA) sequence (5'-GTTTGACG-GGGGTGTCGTGG-3') was selected using the online Benchling tool (https://www.benchling.com). This sequence was subsequently cloned into the pX330-U6-Chimeric\_BB-CBh-hSpCas9 vector (Addgene, USA), which contains the gene for the green fluorescent protein (GFP). A control ESC line was generated by transfecting the cells with nonspecific gRNA (Scrambled) [17]. Transfection was performed using the FuGene HD reagent (Promega, USA) according to the manufacturer's protocol. Selection of the transfected cells was performed by fluorescence-activated cell sorting (FACS) using an S3e Cell Sorter (Bio-Rad Lab., USA). The cells were prepared according to a previously described procedure [16]. The sorted cells were plated at low density and cultured for 10-14 days. The selected clones were checked by immunoblotting with anti-Lmp2 antibodies and by sequencing.

#### Genomic DNA extraction and sequencing

Genomic DNA was isolated according to a protocol described previously [17]. The regions of the flanks of the gRNA target site were amplified by PCR using the primers 5'-AACTGCAGATAACACAGTCCATC-3' and 5'-CCAGGACCAGGAAAGACCTGG-3'. The products were cloned into the pAL2-T vector (Eurogen, Russia). Subsequent sequencing (Eurogen, Russia) was performed using the universal M13 primer.

Potential off-target sites for the selected gRNA were searched for using the online Benchling tool. The genomic regions encompassing these potential

off-target sites were amplified by PCR with specific primers (*Table 1*) and sequenced (Eurogen, Russia).

#### **Karyotyping**

Metaphase spreads were prepared following a procedure described previously [18]. The microscopic analysis of the preparations was performed using an EVOS FL Auto Imaging System (Applied Biosystems, USA) with immersion oil at  $\times 100$  magnification. The chromosomes were counted using Fiji (ImageJ) software. A cell line was considered normal if the sample contained more than 90% of cells with the standard mouse chromosome number of 40.

#### **Determination of ESC proliferative activity**

The proliferative activity of the control (Scr) and Psmb9 knockout (Psmb9KO) cell lines was assessed on the third day after seeding. The cells were passaged at a concentration of 5  $\times$  10³ live cells/cm². Prior to their counting, the cells were trypsinized with a 0.05% trypsin/EDTA solution (Gibco, USA) and pelleted. The pellet was then resuspended in PBS containing 50 µg/ml propidium iodide (PI). Cell counting was performed on a Coulter EPICS XL Flow Cytometer (Beckman Coulter, USA).

#### Immunocytochemical staining and microscopy

Immunocytochemical staining was performed according to a procedure described previously [19]. Image acquisition and subsequent analysis were performed using a CellVoyager CQ1 high-content screening system (Yokogawa Electric, Japan). The primary antibodies used were Nanog (1:500, Bethyl A300-397), Oct4 (1:300, Santa Cruz sc-5279) and secondary antibodies conjugated to Alexa 488 and

568 fluorophores (a-11008 and a-11004), respectively (Invitrogen, USA).

#### **Immunoblotting**

Cell extracts were obtained using a method described previously [15]. Each sample was separated by electrophoresis on a 13% SDS-polyacrylamide gel, with proteins transferred onto a 0.45 µm PVDF membrane in a Tris-glycine buffer (Bio-Rad, USA). After the transfer, the membrane was incubated in a solution of 5% non-fat dry milk in PBS buffer. For protein visualization, the membrane was incubated overnight at 4°C with specific primary antibodies, followed by a 1 h incubation with the appropriate secondary antibodies. Chemiluminescence was detected using a ChemiDoc imaging system (Bio-Rad, USA). The study employed the following primary antibodies: Lmp2 (1:500, Abclonal A9549), Lmp7 (1:5000, kindly provided by Prof. Dr. Ulrike Seifert, University Medicine Greifswald, Germany), Mecl-1 (1:500, Abcam ab183506), Oct4 (1:500, Santa Cruz sc-5279), Nanog (1:500, Cell Signaling #8822), α7 (1:1000, Enzo Life Sciences PW8110), β2 (1:1000, Enzo Life Sciences PW9300), β5 (1:1000, Bethyl A303-847), Rpn1 (1:1000, ServiceBio GB113525), Rpt2 (1:1000, ServiceBio GB114427), and β-Actin (1:5000, Cell Signaling #3700). Additionally, we used secondary antibodies conjugated to horseradish peroxidase (HRP): against rabbit IgG (1:5000, Jackson ImmunoResearch, 111-035-003) and against mouse IgG (1:5000, Jackson ImmunoResearch, 115-035-062).

#### Determining the proteasomal proteolytic activity

The caspase-like (CL) peptidase activity of the proteasomes in the cell extracts (~6 µg) was measured using the substrate Z-LLE-AMC (carbobenzoxy-Leu-Leu-Glu-7-amido-4-methylcoumarin) (Enzo Life Sciences, Germany) at a concentration of 0.25 mM. The reaction was conducted in a buffer containing 50 mM Tris-HCl (pH 7.5), 5 mM MgCl<sub>2</sub>, 40 mM KCl, 1 mM DTT, and 1 mM ATP, at 37°C for 30 minutes according to a previously described procedure [20]. The reaction was stopped by adding an equal volume of 2% SDS. The proteasomal activity was determined by measuring the fluorescence of free AMC (7-amino-4-methylcoumarin) using a VersaFluor fluorometer (Bio-Rad, USA) at excitation and emission wavelengths of 340-380 nm and 455-465 nm, respectively. The values obtained were normalized by subtracting the background fluorescence and recalculated using an equalization coefficient (determined after measuring the protein concentration in the samples). Finally, the mean values and standard deviations were calculated.

#### Teratoma assay

All the experiments were performed on BALB/c mice obtained from the Lobachevsky University Laboratory Animal Breeding Facility (Nizhny Novgorod, Russia). The animals were housed in individual cages under a 12-hour light/dark cycle in a temperature-controlled room (22°C) with ad libitum access to food and water. All the studies were conducted in accordance with the principles of biomedical ethics outlined in the 1964 Helsinki Declaration and its later amendments and were approved by the Commission on Biological Safety and Bioethics of the Institute of Cytology of the Russian Academy of Sciences (St. Petersburg, Russia), protocol No. 02/24 dated June 6, 2024. The resulting ESCs ( $2 \times 10^6$  cells) were injected subcutaneously into the hind limbs of the mice to assess their pluripotent properties. Four weeks after injection, the mice were euthanized. The resulting teratomas were excised, weighed, fixed in Bouin's solution (75 ml saturated aqueous picric acid solution; 25 ml 40% aqueous formaldehyde solution; 5 ml glacial acetic acid), and embedded in paraffin. Sections 7 µm thick were prepared from the paraffin blocks, deparaffinized, stained with hematoxylin and eosin (BioVitrum, Russia), and examined microscopically using an EVOS FL Auto Imaging System (Applied Biosystems, USA).

#### Statistical analysis

All the immunofluorescence and immunoblotting images presented in this work emanate from at least three independent experiments. Flow cytometry analysis was performed on a minimum of  $1\times 10^4$  cells per sample. The data are presented as the mean value  $\pm$  standard deviation (SD) from a minimum of three replicates. Statistical significance was determined at a level of p<0.05 using a one-way analysis of variance (ANOVA) performed with the GraphPad Prism 8 software.

#### **RESULTS**

ESC lines with knockout of the *Psmb9* gene (Psmb9KO) were obtained using the CRISPR/Cas9 genomic editing system. The gRNA targeting the second exon of the *Psmb9* gene was cloned into the pX330-U6-Chimeric-BB-CBh-hSp-Cas9 plasmid. This plasmid also encodes the green fluorescent protein (GFP). The construct was introduced into the cells through transfection, followed by the selection of GFP-positive cells via fluorescence-activated cell sorting (FACS) (see the Experimental Part). As a result, more than 20 clones lacking the Lmp2 protein were identified using immunoblotting data. Among these, clones containing indels (insertions and/or deletions)

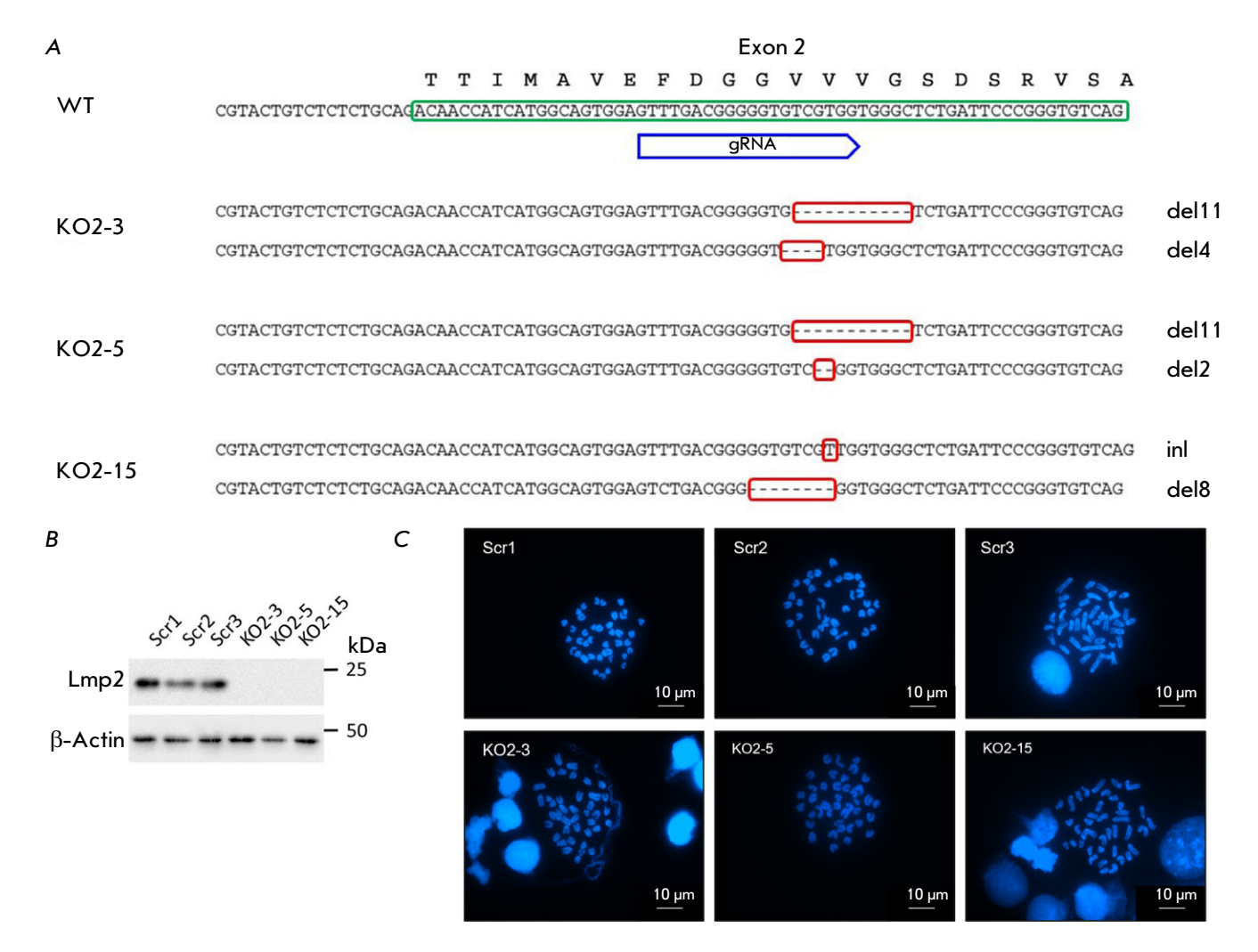


Fig. 1. Validation of Psmb9 gene knockout in mESCs. (A) Genotyping results of three mESC lines with Psmb9 gene knockout (KO2-3, KO2-5, KO2-15). WT – sequence of the second exon of the Psmb9 gene in wild-type mESCs. Indel mutations are highlighted with a red rectangle, del – deletion, in – insertion. (B) Western blot analysis of Lmp2 protein expression levels in the control (left) and Psmb9KO clones (right) following differentiation induced by RA and Psmb9KO clones (right) following differentiation induced by RA and Psmb9KO cells; the chromosomes were stained with DAPI. The scale bar is 10 pmb9KO cells; the chromosomes were stained with DAPI. The scale bar is 10 pmb9KO cells;

in both alleles of the *Psmb9* gene were identified by TA-cloning and sequencing (*Fig. 1A*). As expected, these mutations caused a frameshift, leading to the disruption of functional Lmp2 protein translation (*Fig. 1B*). The five most probable potential off-target sites (*Table 1*) which could have been modified due to nonspecific interaction with the gRNA were assessed in the selected Psmb9KO ESC clones. Furthermore, all selected Psmb9KO ESC clones were confirmed by chromosome counting to contain 40 chromosomes (*Fig. 1C*), corresponding to the normal karyotype of mouse ESCs. The morphology of the KO2-3, KO2-5, and KO2-15 cell lines cultured on gelatin-coated plastic substrates did not exhibit significant differences from that of the control cells (Scr) (*Fig. 2A*).

Additionally, the proliferation and cell death rates *in vitro* for all three lines were comparable to those of the control lines (*Fig. 2B*).

The staining intensity of the pluripotency factors Nanog, Oct4, and Sox2, as determined by immunocytochemical analysis, remained consistent, irrespective of *Psmb9* gene expression levels (*Fig. 3A*). Additionally, the immunoblotting data demonstrated that the levels of the Nanog and Oct4 factors remained unchanged despite the lack of the Lmp2 protein (*Fig. 3B*).

Next, we assessed the ability of Psmb9KO cells to differentiate *in vivo* within teratomas. The sizes of the teratomas formed by Psmb9KO cells were similar to those formed by the control cells (*Table 2*, *Fig. 4A*).

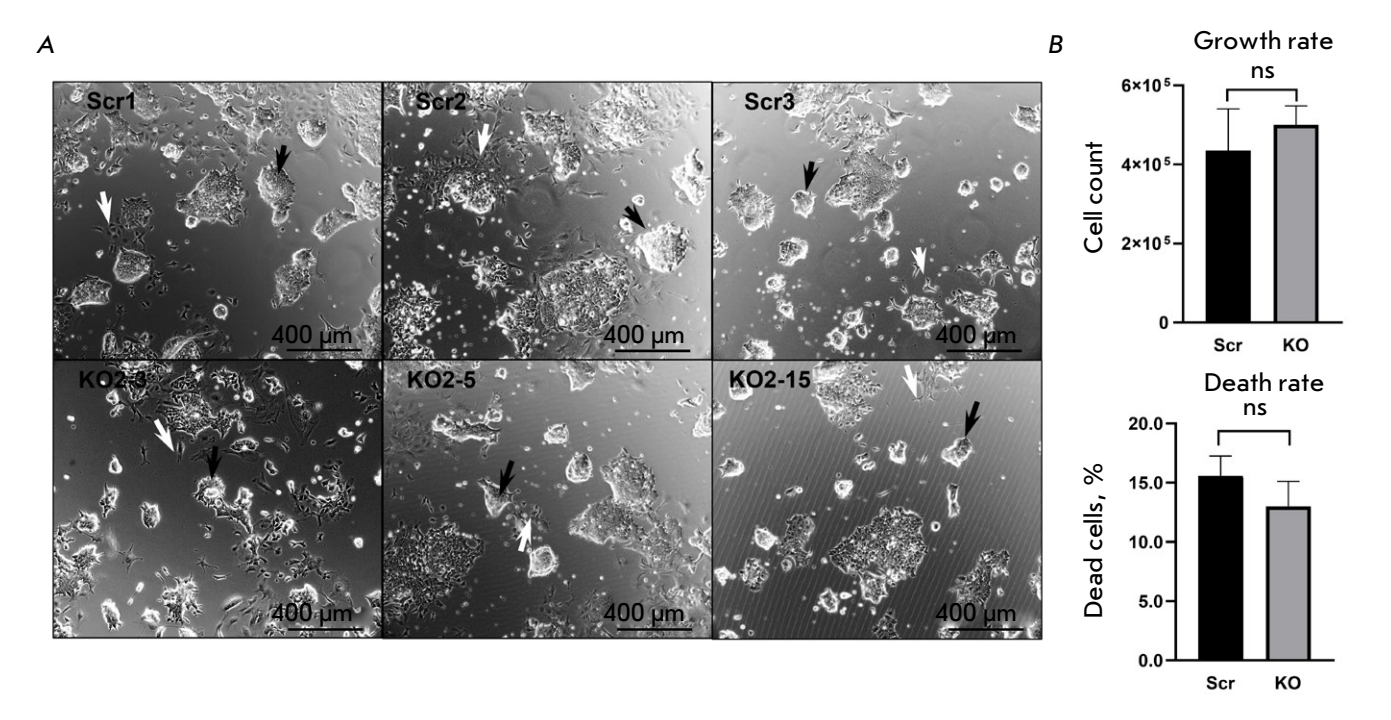
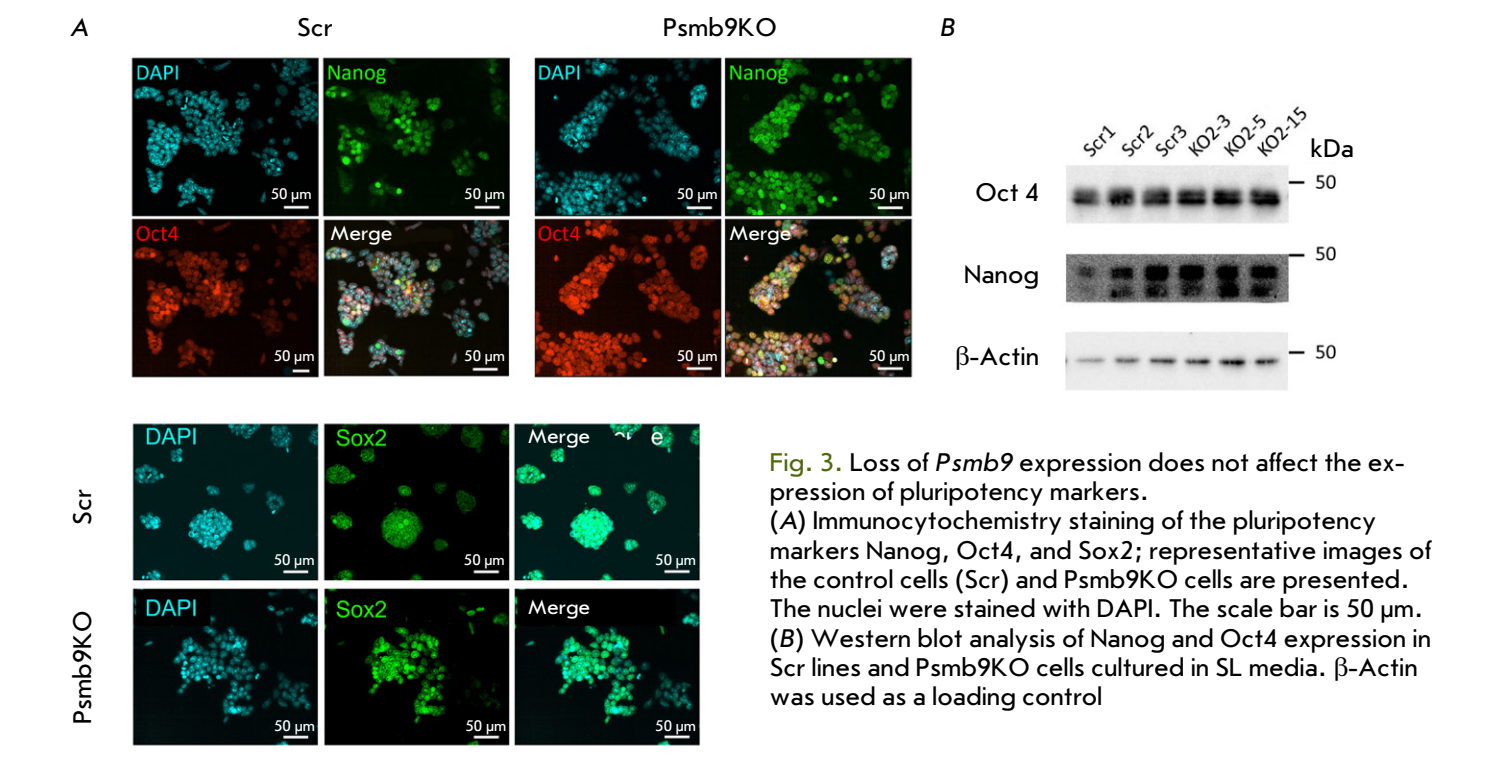


Fig. 2. Psmb9 knockout does not affect the morphological and proliferative characteristics of mESCs. (A) Representative images of Psmb9KO mESCs and control lines (Scr1-3) under standard culture conditions. Colonies with a morphology characteristic of undifferentiated mESCs are marked with black arrows. Cells that undergo spontaneous differentiation are indicated by white arrows. The scale bar is  $400 \, \mu m$ . (B) Comparison of the cellular proliferation rates between Psmb9KO lines and control lines (Scr). Cell death analysis was performed using propidium iodide (Pl) staining. Data are presented as the mean  $\pm$  standard deviation (n=3). ns-not statistically significant (one-way ANOVA)



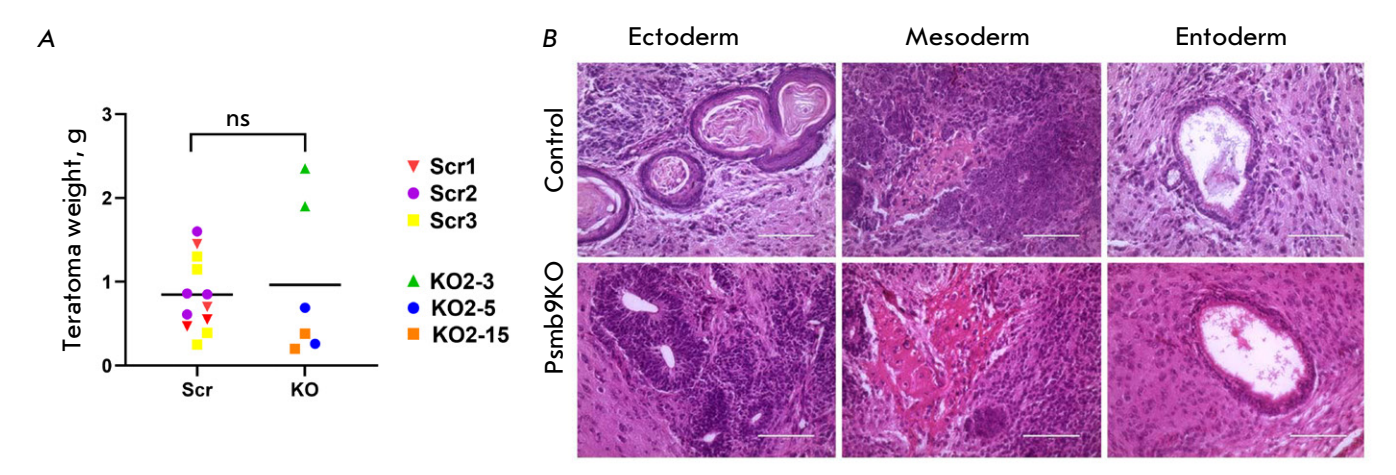


Fig. 4. Psmb9KO ESC lines retain pluripotency, giving rise to derivatives of all three germ layers. (A) Dot plot showing individual teratoma masses derived from the control (Scr) and Psmb9KO mESC lines. Horizontal lines represent the mean teratoma mass for each group. ns – not statistically significant (one-way ANOVA). (B) Histological analysis of teratomas formed by Psmb9KO ESCs. The teratomas contain cell structures representative of all three germ layers: ectoderm (keratinizing epithelium and neuroepithelial rosettes), mesoderm (chondroblasts and chondrocytes in mesenchyme), and endoderm (differentiating enterodermal epithelium). Samples were counterstained with hematoxylin and eosin. The scale bar is 100 µm

Table 2. Teratoma mass values from individual mice transplanted with control (Scrambled) or Psmb9 knockout (Psmb9KO) embryonic stem cells (ESCs)

Group	ESC type	Number of animals (n)	Individual values of teratoma masses, g	
	Scrambled #1	4	1.45, 0.7, 0.55, 0.47	
Control	Scrambled #2	4	0.85, 1.6, 0.86, 0.61	
	Scrambled #3	4	1.3, 1.15, 0.39, 0.25	
Psmb9 KO	KO 2-3	2	1.9, 2.35	
	KO 2-5	2	0.69, 0.26	
	KO 2-15	2	0.38, 0.20	

Both the control and Psmb9KO cells were demonstrated using histological analysis to successfully differentiate into derivatives of all three germ layers: areas of keratinized epithelium and neuroepithelial rosettes (ectoderm), cartilage (mesoderm), and ciliated epithelium (endoderm) (Fig.~4B). Thus, we had successfully generated a panel of mouse ESC lines with Psmb9 knockout. The panel is expected to be invaluable for further research.

In Psmb9KO ESCs, the immunoblot analysis of proteasomal protein expression revealed no significant changes in the levels of the  $\alpha$ 7,  $\beta$ 2, and  $\beta$ 5 subunits of the 20S proteasome (*Fig. 5A,B*). Furthermore, the protein levels of the 19S regulatory subunits (Rpn1 and Rpt2) remained constant, suggesting that the fundamental structure of the proteasome complex remains

undisturbed in the absence of a Psmb9 gene product. No significant change in the expression of the immunoproteasome subunits Lmp7 (β5i) and Mecl-1 (β2i) was recorded between the Psmb9KO and control ESCs. At the same time, retinoic acid (RA)-differentiated and interferon-γ (IFNγ)-treated Psmb9KO cells tended to exhibit a lower content of the mature form of the immunoproteasome subunit Mecl-1 (β2i) while accumulating its non-processed form (pro-Mecl-1) compared to the control ESCs. However, these differences did not attain statistical significance (Fig. 5A,B). That notwithstanding, the ratio of signal levels between the precursor form of pro-Mecl-1 and the mature form of Mecl-1 indicated that the precursor accumulated more significantly in Psmb9-knockout cells than it did in the controls (Fig. 5A,B). The absence of specific antibodies

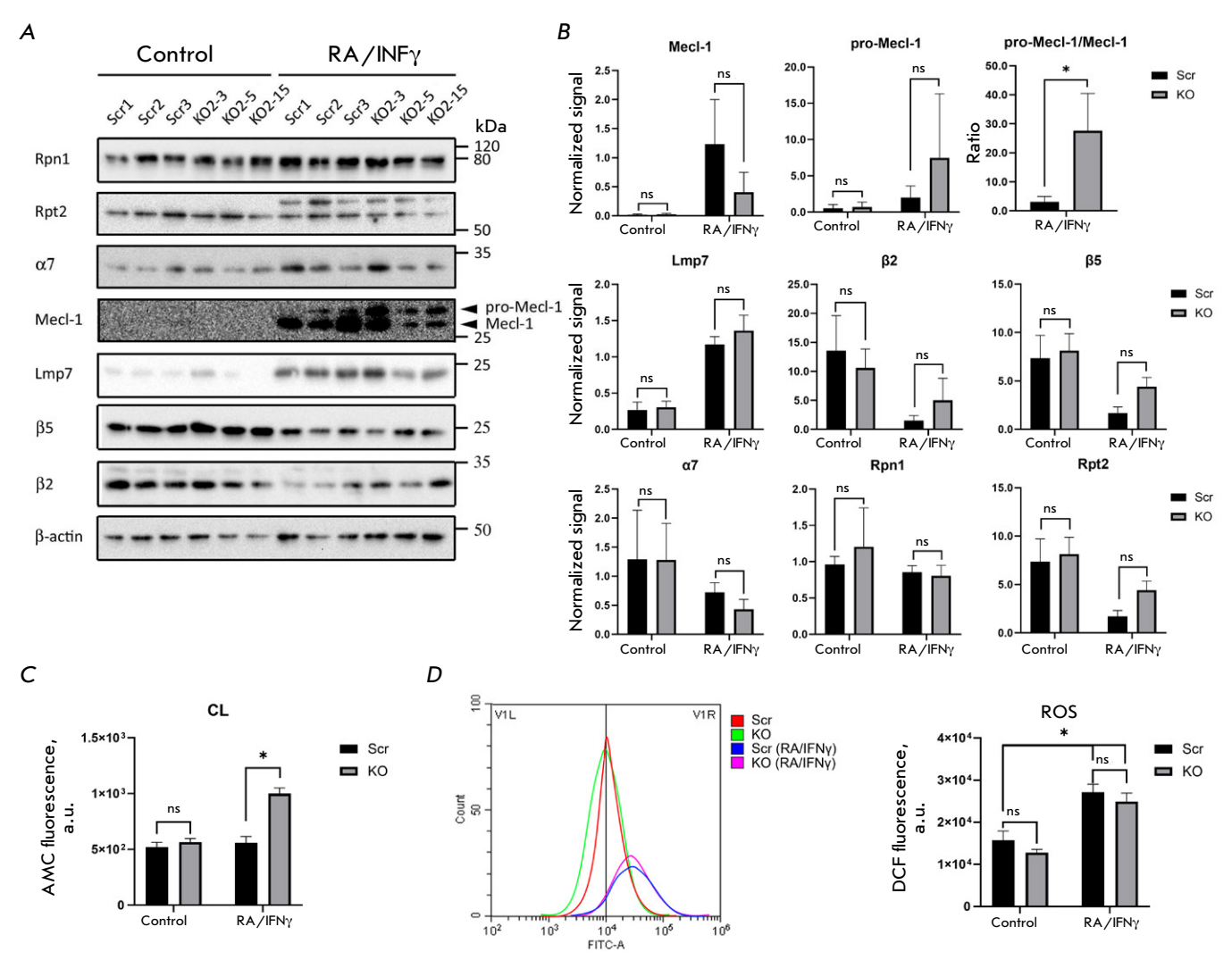


Fig. 5. Analysis of proteasome activity and reactive oxygen species (ROS) production in Psmb9 knockout mESCs. The control cell lines (Scr1-3) and Psmb9KO mESCs (KO2-3, 2-5, and 2-1) were cultured in a SL medium. Differentiation was induced with retinoic acid (RA) for 2 days, followed by IFN $\gamma$  treatment for 1 day. (A) Western blot analysis of constitutive and immunoproteasome subunit expression in Psmb9 knockout mESCs compared to the control cells (Scr).  $\beta$ -Actin was used as a loading control. (B) Integral intensity measurements of the western blot bands shown in (A), normalized to  $\beta$ -actin. (C) Measurement of the caspase-like (CL) activity of the 20S proteasome. (D) Assessment of ROS production. Representative histograms of cell distribution by fluorescence intensity in the FITC channel are shown. The rightward shift of the histogram indicates increased ROS production. Data are presented as mean  $\pm$  standard deviation (n = 3). ns – not statistically significant; \*p < 0.05 (one-way ANOVA)

was an impediment to us evaluating the levels of the  $\beta 1$  catalytic subunit in Psmb9KO cells. For this reason, we examined the peptidase activity of the 20S proteasome in cell extracts employing a fluorogenic substrate specific to this subunit. Following RA-induced differentiation and IFN $\gamma$  treatment, Caspase-like activity was found to be significantly enhanced in Psmb9KO ESCs compared to the control cells, indicating an upregulation of the  $\beta 1$  subunit in Psmb9KO cells and its incorporation into the 20S proteasome instead of Lmp2,  $\beta 1i$  (Fig. 5C).

Competing studies suggest that the absence of Lmp2 in mouse and rat cells can lead to oxidative stress through the accumulation of reactive oxygen species (ROS) [21, 22]. We conducted a comparative analysis of ROS production in the Psmb9 knockout cell versus the control cell lines. Following RA-induced differentiation and IFN $\gamma$  treatment, an increase in ROS levels was detected across all the cells under analysis. However, we found no differences in ROS production associated with Psmb9 expression (Fig. 5D).

#### DISCUSSION

The immunoproteasome subunit Lmp2 (\(\beta1\)i) encoded by the Psmb9 gene has been reported to play a crucial role in numerous processes related to immune defense [23-26], maintenance of cellular homeostasis [10, 21, 27, 28], and tissue development [22, 29]. Furthermore, the expression of Psmb9, along with other immunoproteasome subunits, has been demonstrated to be essential during the early stages of mammalian embryogenesis [12]. Given the diverse functions of Lmp2 in human cells, investigating its mechanisms of action is of significant interest. In the present study, we generated a cell model of mouse ESCs with Psmb9 gene knockout using the CRISPR/Cas9 technology. The resulting lines exhibited no impairments in the growth rate or expression levels of key pluripotency markers compared to the control lines. Moreover, they successfully formed teratomas in immunodeficient mice. The histological analysis of teratomas revealed structures derived from all three embryonic germ layers, thus confirming the retention of the pluripotent potential in Psmb9-deficient ESCs. The absence of Psmb9 expression did not alter the protein levels of the proteasomal subunits  $\alpha$ 7 and the catalytic  $\beta 2$  and  $\beta 5$  or the levels of the other two immunoproteasome subunits, Lmp7 (β5i) and Mecl-1 (β2i). However, RA-differentiated and IFNγ Psmb9KO-treated ESCs were observed to accumulate the precursor form of Mecl-1. The data suggest that in mouse ESCs, immunoproteasomes lacking the Lmp2 subunit can still exist as an intermediate, albeit with less efficient assembly, which aligns with prior studies [23]. Furthermore, the differentiation of Psmb9KO ESCs resulted in an elevation of caspaselike activity in the 20S proteasome. This suggests a possible compensatory integration of the β1-subunit into the immunoproteasome complex, substituting Lmp2. This substitution mechanism may be interpreted as an adaptive response to the absence of Lmp2, which maintains functional UPS activity in IFNyinduced differentiated cells.

The *Psmb9* and *Psmb8* genes, which encode the Lmp2 and Lmp7 subunits, respectively, are located within the major histocompatibility complex class II (MHC II) locus [30]. The part played by these subunits in the regulation of the immune response have been a subject of considerable research since they were first described. Impaired Lmp2 function was reported to disrupt antigen presentation [24], alter the repertoire of CD8+ T lymphocytes [26], and cause an absolute collapse in their numbers in mice [25]. Immunoproteasomes, including Lmp2, are involved in the maintenance of proteostasis and the regulation of cell differentiation. Increased Lmp2 levels are ob-

served under cellular stress conditions, such as mitochondrial dysfunction in human cells, which results in elevated proteasome activity and reduced accumulation of oxidized proteins [27]. Additionally, Lmp2 loss is correlated with the onset of neurodegenerative changes in Alzheimer's disease. For instance, mice with Psmb9 knockout exhibit myelin loss, increased blood-brain barrier permeability, accumulation of amyloid-β, and elevated levels of reactive oxygen species (ROS). Consequently, these factors contribute to chronic oxidative stress, amplified neuroinflammation, and cognitive impairment, thereby stressing the relevance of Lmp2 in preserving optimal brain cell function [28]. The function of Lmp2 in tissue development has been demonstrated in research on neurogenesis. In scenarios with excessive mTORC1 complex activity, the lack of Lmp2 impedes the proliferation of neuronal progenitors, thereby regulating their differentiation [29]. Moreover, the Lmp2 subunit is essential for muscle cell differentiation. Immunoproteasome inhibition in myoblasts causes an increase in oxidized proteins and hinders myoblast differentiation [22].

Given the existing data on the role of Lmp2 in the regulation of cellular proteostasis across different tissue types, it is of particular interest to examine the role played by immunoproteasomes in maintaining ESC pluripotency and differentiation. The distinctive potential of ESCs for self-renewal and differentiation is contingent upon highly regulated processes that underpin genomic stability and proteostasis. The term "pluripotency" denotes the ability of ESCs to selfrenew and differentiate into any cell type within an organism, except for specific extraembryonic tissues, such as the trophoblast and primitive endoderm. Prior to embryo implantation, significant morphological and molecular changes occur in the epiblast, preparing the cells for development. Development of the postimplantation epiblast is preceded by epiblast cell polarization, which is characterized by rosette formation, followed by the formation of the proamniotic cavity through embryo cavitation [31, 32]. During this phase, epiblast cells shift from a state of "naïve" pluripotency to a "primed" state, initiating their differentiation into ecto-, meso-, and endoderm. This transition involves several intermediate states with unique characteristics [33]. To date, at least four distinct types of pluripotent cells with stable in vitro culture analogues have been identified [33].

Our prior research has demonstrated that immunoproteasome expression is initiated at the epiblast-like cell stage [15], reaches its highest level on the third day of mesodermal differentiation (unpublished data), and steadily decreases until it becomes undetectable. Epiblast-like cells and cells from the third

day of mesodermal differentiation in culture correlate with postimplantation epiblast cells and the primitive streak stage in mouse embryo development. According to public single-cell RNA sequencing (scRNA-seq) data, the peak of immunoproteasome expression also coincides with the stage of primitive streak formation [34, 35].

The formation of the primitive streak involves epiblast cells that undergo an epithelial-mesenchymal transition (EMT) marked by modifications in cell shape due to actin cytoskeleton remodeling, the breakdown of intercellular junctions, degradation of the basement membrane, and the activation of cellextracellular matrix interactions [36]. Furthermore, epiblast cell division proceeds at a notably higher rate during this phase. During the transition to gastrulation, mouse epiblast cells experience a reduction in cell cycle duration from 12 to 14 h to 6 to 8 h [37]. Given the substantial changes characteristic of early embryonic development, ensuring rapid cell adaptation to internal and external signals is critical. Immunoproteasomes are characterized by their rapid assembly kinetics and short half-lives [38]. The hypothesis is that immunoproteasomes may degrade damaged and polyubiquitinated proteins more effectively under conditions of stress and pro-inflammatory signaling (refer to review [11]). It seems safe to assume that the role of immunoproteasomes in early embryonic development is to prevent the accumulation of unnecessary and/or damaged proteins. However, it is worth noting that mice with knockout of all three catalytic immunoproteasome subunits do not exhibit critical neonatal developmental anomalies. This phenomenon may be indicative of compensatory mechanisms that can substitute for their functions. The role of the immunoproteasome in maintaining proteostasis and participating in the differentiation of ESCs is expected to be clarified through studies using cells deprived of both individual catalytic subunits of the immunoproteasome and all three.

#### **CONCLUSIONS**

In conclusion, we have succeeded in generating and characterizing a mouse ESC line with knockout of the Psmb9 gene encoding the catalytic subunit of the immunoproteasome Lmp2 ( $\beta$ 1i). The absence of Lmp2 was found to have no effect on the morphology, proliferative activity, and pluripotent status of ESCs. This cell line represents a promising tool for investigating the role of the Psmb9 gene and immunoproteasomes in the subsequent stages of ESC differentiation  $in\ vitro$ .

This study was supported by a grant from the Russian Science Foundation (project No. 22-14-00390). The sequencing experiments were performed with financial support from the Ministry of Science and Higher Education of the Russian Federation (Agreement 075-15-2021-1075, dated September 28, 2021).

#### REFERENCES

- 1. Jang H.H. // J. Cancer Prev. 2018. V. 23. № 4. P. 153–161. doi: 10.15430/JCP.2018.23.4.153.
- 2. Abi Habib J., Lesenfants J., Vigneron N., van den Eynde B.J. // Cells. 2022. V. 11. № 3. P. 421. doi: 10.3390/cells11030421.
- 3. Zhang H., Zhou C., Mohammad Z., Zhao J. // bioRxiv. 2024. doi: 10.1101/2024.08.08.607236.
- 4. Budenholzer L., Cheng C.L., Li Y., Hochstrasser M. // J. Mol. Biol. 2017. V. 429. № 22. P. 3500–3524. doi: 10.1016/j. jmb.2017.05.027.
- 5. Aki M., Shimbara N., Takashina M., Akiyama K., Kagawa S., Tamura T., Tanahashi N., Yoshimura T., Tanaka K., Ichihara A. // J. Biochem. 1994. V. 115. № 2. P. 257–269. doi: 10.1093/oxfordjournals.jbchem.a124327.
- 6. Boes B., Hengel H., Ruppert T., Multhaup G., Koszinowski U.H., Kloetzel P.M. // J. Exp. Med. 1994. V. 179. № 3. P. 901–909. doi: 10.1084/jem.179.3.901.
- 7. Strehl B., Seifert U., Kruger E., Heink S., Kuckelkorn U., Kloetzel P.M. // Immunol. Rev. 2005. V. 207. № 1. P. 19–30. doi: 10.1111/j.0105-2896.2005.00308.x.
- 8. McCarthy M.K., Weinberg J.B. // Front. Microbiol. 2015. V. 6. № 1. P. 21. doi: 10.3389/fmicb.2015.00021.
- 9. Chen B., Zhu H., Yang B., Cao J. // Acta Pharm.

- Sin. B. 2023. V. 13.  $\mathbb{N}_{2}$  5. P. 1976–1989. doi: 10.1016/j. apsb.2022.11.005.
- 10. Seifert U., Bialy L.P., Ebstein F., Bech-Otschir D., Voigt A., Schroter F., Prozorovski T., Lange N., Steffen J., Rieger M., et al. // Cell. 2010. V. 142. № 4. P. 613–624. doi: 10.1016/j.cell.2010.07.036.
- 11. Basler M., Groettrup M. // Cells. 2021. V. 10. № 11. P. 1–18. doi: 10.3390/cells10113216.
- 12. Atkinson S.P., Collin J., Irina N., Anyfantis G., Kyung B.K., Lako M., Armstrong L. // Stem Cells. 2012. V. 30. № 7. P. 1373–1384. doi: 10.1002/stem.1113.
- 13. Hernebring M., Fredriksson A., Liljevald M., Cvijovic M., Norrman K., Wiseman J., Semb H., Nystrom T. // Sci. Rep. 2013. V. 3. № 1. P. 1381. doi: 10.1038/srep01381.
  14. Hernebring M., Brolen G., Aguilaniu H., Semb H., Nystrom T. // Proc. Natl. Acad. Sci. USA. 2006. V. 103. № 20. P. 7700–7705. doi: 10.1073/pnas.0510944103.
- 15. Kriger D., Podenkova U.I., Bakhmet E.I., Potapenko E., Ivanova E., Tomilin A.N., Tsimokha A.S. // Cells. 2024. V. 13. № 16. P. 1–13. doi: 10.3390/cells13161362.
- 16. Podenkova U.I., Kriger D.V., Kuznetsov A.V., Kuzmin A.A., Koltunova L.A., Yevreiskaya A., Aksenov N.D., Fokin N.P., Selenina A.V., Tomilin A.N. // Cell Tissue Biol. 2025. V. 19. № 2. P. 130–140. doi: 10.1134/

#### RESEARCH ARTICLES

#### S1990519X24600741

- 17. Bakhmet E.I., Ponomartsev S.V., Dyban P.A., Nazarov I.B., Kuzmin A.A., Aksenov N.D., Potapenko E., Gordeev M.N., Tomilin A.N. // Cell Tissue Biol. 2020. V. 14. № 6. P. 413–418. doi: 10.1134/S1990519X20060036.
- 18. Gordeev M.N., Zinovyeva A.S., Petrenko E.E., Lomert E.V., Aksenov N.D., Tomilin A.N., Bakhmet E.I. // Acta Naturae. 2024. V. 16. № 4. P. 12–22. doi: 10.32607/actanaturae.27510.
- 19. Kriger D., Novitskaya K., Vasileva G., Lomert E., Aksenov N.D., Barlev N.A., Tentler D. // Biol. Direct. 2022. V. 17. № 1. P. 1–13. doi: 10.1186/s13062-022-00354-6.
- 20. Kulichkova V.A., Artamonova T.O., Zaykova J.J., Ermolaeva J.B., Khodorkovskii M.A., Barlev N.A., Tomilin A.N., Tsimokha A.S. // Mol. Biotechnol. 2015. V. 57. № 1. P. 36–44. doi: 10.1007/s12033-014-9799-0.
- 21. Chen X., Mao Y., Guo Y., Xiao D., Lin Z., Huang Y., Liu Y.C., Zhang X., Wang Y. // J. Transl. Med. 2023. V. 21. № 1. P. 1–16. doi: 10.1186/s12967-023-04071-0.
- 22. Cui Z., Hwang S.M., Gomes A.V. // Mol. Cell. Biol. 2014. V. 34.  $N_2$  1. P. 96–109. doi: 10.1128/MCB.00622-13.
- 23. Hensley S.E., Zanker D., Dolan B.P., David A., Hickman H.D., Embry A.C., Skon C.N., Grebe K.M., Griffin T.A., Chen W., et al. // J. Immunol. 2010. V. 184. № 8. P. 4115–4122. doi: 10.4049/jimmunol.0903003.
- 24. Sibille C., Gould K.G., Willard-Gallo K., Thomson S., Rivett A.J., Powis S., Butcher G.W., De Baetselier P. // Curr. Biol. 1995. V. 5. № 8. P. 923–930. doi: 10.1016/s0960-9822(95)00182-5.
- 25. van Kaer L., Ashton-Rickardt P.G., Eichelberger M., Gaczynska M., Nagashima K., Rock K.L., Goldberg A.L., Doherty P.C., Tonegawa S. // Immunity. 1994. V. 1. № 7. P. 533–541. doi: 10.1016/1074-7613(94)90043-4.
- 26. Chen W., Norbury C.C., Cho Y., Yewdell J.W., Bennink J.R. // J. Exp. Med. 2001. V. 193. № 11. P. 1319–1326. doi: 10.1084/jem.193.11.1319.

- 27. Kim M., Serwa R.A., Samluk L., Suppanz I., Kodron A., Stepkowski T.M., Elancheliyan P., Tsegaye B., Oeljeklaus S., Wasilewski M., et al. // Nat. Commun. 2023. V. 14. № 1. P. 1–23. doi: 10.1038/s41467-023-39642-8.
- 28. Guo Y., Wang S., Li L., Zhang H., Chen X., Huang Z., Liu Y. // Mol. Neurobiol. 2024. V. 61. № 1. P. 28–41. doi: 10.1007/s12035-023-03564-9.
- 29. Choi J.H., Jo H.S., Lim S., Kim H.T., Lee K.W., Moon K.H., Ha T., Kwak S.S., Kim Y., Lee E.J., et al. // Nat. Commun. 2018. V. 9. № 1. P. 1–16. doi: 10.1038/s41467-018-04774-9
- 30. Brown M.G., Driscoll J., Monaco J.J. // Nature. 1991. V. 353.  $\mathbb{N}_2$  6342. P. 355–357. doi: 10.1038/353355a0.
- 31. Bedzhov I., Zernicka-Goetz M. // Cell. 2014. V. 156.  $\mathbb{N}_{2}$  5. P. 1032–1044. doi: 10.1016/j.cell.2014.01.023.
- 32. Shahbazi M.N., Scialdone A., Skorupska N., Weberling A., Recher G., Zhu M., Jedrusik A., Devito L.G., Noli L., Macaulay I.C., et al. // Nature. 2017. V. 552. № 7684. P. 239–243. doi: 10.1038/nature24675.
- 33. Gordeev M.N., Bakhmet E.I., Tomilin A.N. // Rus. J. Devel. Biol. 2021. V. 52. № 6. P. 429–440. doi: 10.31857/s0475145021060057.
- 34. Kim I.S., Wu J., Rahme G.J., Battaglia S., Dixit A., Gaskell E., Chen H., Pinello L., Bernstein B.E. // Cell Rep. 2020. V. 33. № 1. P. 1–15. doi: 10.1016/j.celrep.2020.108222.
- 35. Mohammed H., Hernando-Herraez I., Savino A., Scialdone A., Macaulay I., Mulas C., Chandra T., Voet T., Dean W., Nichols J., et al. // Cell. Rep. 2017. V. 20. № 5. P. 1215–1228. doi: 10.1016/j.celrep.2017.07.009.
- 36. Kojima Y., Tam O.H., Tam P.P. // Semin. Cell. Dev. Biol. 2014. V. 34. № 1. P. 65–75. doi: 10.1016/j.semcdb.2014.06.010. 37. Snow M.H.L. // Development. 1977. V. 42. № 1. P. 293–303. doi: 10.1242/dev.42.1.293.
- 38. Heink S., Ludwig D., Kloetzel P.M., Kruger E. // Proc. Natl. Acad. Sci. USA. 2005. V. 102. № 26. P. 9241–9246. doi: 10.1073/pnas.0501711102.

## Targeted Nanoliposomes for the Delivery of Boronophenylalanine into HER2-Positive Cells

G. M. Proshkina<sup>1\*</sup>, E. I. Shramova<sup>1,2</sup>, A. B. Mirkasymov<sup>1</sup>, I. N. Zavestovskaya<sup>2,3,4</sup>, S. M. Deyev<sup>1,2,3,4,5</sup>

<sup>1</sup>State Research Center "Shemyakin-Ovchinnikov Institute of Bioorganic Chemistry RAS", Moscow, 117997 Russia

<sup>2</sup>Lebedev Physical Institute RAS, Moscow, 119991 Russia

<sup>3</sup>National Research Center "Kurchatov Institute", Moscow, 123098 Russia

<sup>4</sup>Moscow Institute of Engineering Physics, National Research Nuclear University "MEPhl", Moscow, 115409 Russia

<sup>5</sup>Ogarev National Research Mordovia State University, Saransk, 430005 Russia

\*E-mail: gmb@ibch.ru

Received June 17, 2025; in final form, July 17, 2025

DOI: 10.32607/actanaturae.27722

Copyright © 2025 National Research University Higher School of Economics. This is an open access article distributed under the Creative Commons Attribution License, which permits unrestricted use, distribution, and reproduction in any medium, provided the original work is properly cited.

ABSTRACT Boron neutron capture therapy (BNCT) is a rapidly developing field of radiation therapy for cancer that is based on the accumulation of the radiosensitive <sup>10</sup>B isotope in cancer cells, followed by tumor irradiation with thermal neutrons. Widespread use of BNCT in clinical practice remains limited because of the poor accumulation of boron-containing (<sup>10</sup>B) drugs in the tumor or their high toxicity to the body. This study focuses on the engineering of tumor-specific liposomes loaded with 4-L-boronophenylalanine (4-L-<sup>10</sup>BPA) for application in boron neutron capture therapy. According to the spectrophotometry and ICP-mass spectroscopy data, the 4-L-<sup>10</sup>BPA-to-liposome molar ratio is ~ 120,000. Liposomal targeting of human epidermal growth factor receptor 2 (HER2) was determined by HER2-specific designed ankyrin repeat protein (DARPin)\_9-29 on the outer surface of liposomes. DARPin-modified liposomes were found to bind to HER2-overexpressing cells and be effectively internalized into the cytoplasm. The ability of DARPin-functionalized liposomes to precision-deliver large quantities of 4-L-<sup>10</sup>BPA into cancer cells may open up new prospects for BNCT. KEYWORDS boron neutron capture therapy, HER2-specific therapy, liposomes, 4-L-<sup>10</sup>BPA.

ABBREVIATIONS BNRT – boron neutron capture therapy; HER2 – human epidermal growth factor receptor II;  $4-L^{-10}$ BPA –  $^{10}$ B-4-L-boronophenylalanine.

#### INTRODUCTION

Boron neutron capture therapy (BNCT) is a method used to treat malignant tumors by which the radiosensitive <sup>10</sup>B isotope preliminarily accumulated in the tumor is subjected to neutron irradiation. Neutron absorption by 10B is accompanied by a nuclear reaction with a substantial energy release that leads to cell death:  ${}^{10}B + {}^{1}n \rightarrow {}^{4}He(\alpha) + {}^{7}Li + 2.4 \text{ MeV [1]}.$ Hypothetically, only <sup>10</sup>B-loaded cells are expected to die as a result of this reaction, since alpha particles and lithium nuclei experience rapid deceleration and have short penetration ranges in biological tissues  $(5-9 \mu m)$ ; approximately equal to the diameter of a single cell. Hence, the cytotoxic effect is supposed to be confined to the immediate vicinity of the reaction site [2]. BNCT is currently under intensive development, with efforts focused on designing compact accelerator-driven neutron sources and <sup>10</sup>B-containing agents characterized by *in vivo* biocompatibility and stability [3].

Today, a phenylalanine derivative containing a <sup>10</sup>B atom, 4-borono-L-phenylalanine (4-BPA), is the only available drug approved for clinical application in BNCT. Thus, 4-L-<sup>10</sup>BPA has been approved for use under the trade name Borofalan (Steboronine®) as a medication for the treatment of locally recurrent head and neck cancer in Japan since 2020 [4].

The problems limiting the use of 4-L-<sup>10</sup>BPA are related to its low accumulation in cancer cells and poor solubility in water.

4-L-<sup>10</sup>BPA is delivered into cancer cells via the active transport mechanism, through L-type amino acid transporters (mainly LAT-1 [5, 6]), which is independent of both pH and the concentration of Na<sup>+</sup> ions.

LAT-1, a heterodimer transmembrane protein, is involved in the delivery of neutral amino acids with branched side chains (valine, leucine, and isoleucine). as well as aromatic amino acids (tryptophan and tyrosine) into the cell [7–9]. This transporter is likely to be overexpressed in many tumor types [10] and can be regarded as a target for 4-L-10BPA delivery. However, the challenge of 4-L-10BPA accumulation in cancer cells is related to the fact that L-type amino acid transporters function as antiporters: reduction of the extracellular concentration of L-10BPA leads to an efflux of intracellular L-10BPA, accompanied by its replacement with a different extracellular substrate (e.g., tyrosine) [11]. This mechanism impedes attainment of the intratumoral boron concentrations  $(20-50 \mu g^{10}B/g \text{ tumor}, \sim 10^9 \text{ atoms} ^{10}B/\text{cell})$  needed for effective BNCT [12].

The clinical application of 4-L-10BPA is also significantly complicated by its poor solubility (0.6 g/L) in solutions with a neutral pH. Mori et al. proposed to use a complex of 4-L-10BPA with monosaccharides to enhance the solubility of 4-L-10BPA [13]. The usual method in the clinical application of 4-L-10BPA in BNCT involves intravenous administration of a 4-L-10BPA complex with D-fructose or sorbitol. However, this approach is far from ideal: thus, a patient weighing 60 kg systemically receives 1 L of a solution containing 30 g of 4-L-10BPA and 31.5 g of D-sorbitol. Such a high burden causes side effects such as hypoglycemia, hepatic, and renal failure in individuals with hereditary fructose intolerance (as a result of sorbitol metabolism), as well as hematuria resulting from 4-L-10BPA crystallization in urine [4, 14, 15].

Hence, designing novel formulations of boron-containing compounds that would improve drug accumulation in tumors and alleviate side effects is a top priority in fundamental medical research under the development of BNCT.

Liposomes are viewed as effective drug delivery systems owing to their lack of inherent toxicity, capacity to encapsulate large quantities of a drug in both aqueous and hydrophobic phases, as well as the potential for modifying the outer surface with ligands specific to tumor-associated antigens for active targeting [16].

Previously, we had developed a system for engineering nanoliposome (~ 100 nm) whose outer surface is modified with a module specifically targeting the human epidermal growth factor receptor 2 (HER2), while the inner aqueous environment contains a large quantity (up to 10,000 molecules per liposome) of protein toxins [17–19] or peptide nucleic acids [20]. This approach has been used in our

study to engineer HER2-specific liposomes loaded with  $4-L^{-10}BPA$ .

#### **EXPERIMENTAL PART**

### Engineering DARPin-modified liposomes loaded with 4-L-<sup>10</sup>BPA

Accurately weighed samples of 4-L-10BPA (Katchem, Czech Republic), 10 and 15 mg (three replicates used for each weight), were dissolved in 300 µL of Milli-Q water and mixed with a D-fructose solution (Sigma, USA) at a 1:1 molar ratio. Next, 1 M NaOH was added slowly, dropwise (within 10-15 min) until complete dissolution of 4-L-10BPA had been achieved; pH of the solution was 10-10.5. Next, pH was slowly adjusted to 8.0 using concentrated 1 M HCl. A mixture of phospholipids prepared from granules of L-αphosphatidylcholine (40%), phosphatidylethanolamine (16%), and phosphatidylinositol (11%) (Avanti Polar Lipids) was added to the resulting solution to a final concentration of 4 g/L. The mixture was subjected to five quick freeze-thaw cycles and extruded through a filter with a pore diameter of 100 nm. In order to remove the BPA-D-fructose complex not incorporated into the liposomes, the liposome mixture was passed through a NAP-5 column equilibrated with a 100 mM NaPi buffer, pH 8.0. Next, the liposomes were modified with 2-iminothiolane (Merck, Germany) for inserting the SH groups and the SH-containing liposomes were conjugated to DARPin 9-29 modified with a sulfo-EMCS heterobifunctional crosslinker (Thermo Fisher Scientific, USA), according to the protocol described in ref. [17].

The hydrodynamic size and  $\zeta$ -potential of the targeted and non-targeted boron-loaded liposomes were determined on a Zetasizer Nano ZS analyzer (Malvern Instruments, UK). Prior to measurements, the samples in the solution containing 150 mM NaCl and 20 mM NaPi, pH 7.5, were diluted with water 25-fold. The  $\zeta$ -potential values were calculated using the Smoluchowski approximation.

To be used in confocal microscopy and flow cytometry experiments, the DARP-Lip(BPA) samples were conjugated to AF-488 hydroxysuccinimide ester (Lumiprobe, Russia), according to the manufacturer's protocol.

#### Quantification of boron in liposomes

The content of 4-L- $^{10}$ BPA loaded into the targeted liposomes was determined using a NexION 2000 inductively coupled plasma mass spectrometer (PerkinElmer). For this purpose, 50  $\mu$ L of the liposome sample was dissolved in 300  $\mu$ L of aqua regia, incubated at 70°C for 1 h, mixed with 1,200  $\mu$ L of

Milli-Q water, and analyzed by inductively coupled plasma mass spectrometry (ICP-MS). The liposome concentration was determined spectrophotometrically according to the procedure described in ref. [17] by recording the absorption spectrum in a quartz cuvette on an Ultrospec 7000 spectrophotometer (GE) in the wavelength range of 210–800 nm.

#### **Cell cultures**

Human ovarian carcinoma (SKOV-3) and cervical carcinoma (HeLa) cell lines were used in the study. Cells were cultured at 37°C in humidified atmosphere in a RPMI 1640 medium (PanEco, Russia) supplemented with 2 mM L-glutamine (PanEco), 10% fetal bovine serum (Gibco, USA), and antibiotics (10 U/mL penicillin, 10 µg/mL streptomycin, PanEco).

#### Flow cytometry

In order to assess the ability of DARP-Lip(BPA) to bind to HER2, 200,000 SKOV-3 and HeLa cells were incubated in a complete growth medium at 37°C for 10 min in the presence of DARP-Lip(BPA)-AF488 at different concentrations (350 or 150 nM) (concentration calculated on the basis of the dye; the concentration of the DARPin-modified liposomes was 1 nM and 0.5 nM, respectively). After the incubation, the cells were washed thrice with PBS and analyzed using a NovoCyte 3000 flow cytometer. The fluorescence of AF488 was excited using a 488-nm laser; fluorescence was detected in the 530  $\pm$  30 nm channel (the FITC channel).

#### Confocal microscopy

Binding of the targeted module within DARP-Lip(BPA) to HER2 on the surface of SKOV-3 cells typically characterized by overexpression of this receptor was studied by confocal microscopy. Approximately 3,500 SKOV-3 cells were seeded into the wells of a 96-well glass-bottom microplate (Eppendorf) and cultured overnight. The next day, 250 nM of a DARP-Lip(BPA)-AF488 conjugate (concentration calculated on the basis of the dye) was added to the cells and the mixture was incubated for 20 or 120 min. The nuclei were stained with 10 nM Hoechst 33342 (10 min at 37°C). After washing of the cells thrice with PBS and addition of the FluoroBright medium (Gibco), an analysis using an LSM 980 confocal microscope (Carl Zeiss, Germany) with a 63× Plan-Apochromat oil-immersion objective was conducted. The fluorescence of Hoechst 33342 was excited using a 405-nm laser and detected at 410-520 nm; the fluorescence of AF488 was excited with a 488-nm laser and detected at 497-562 nm.

#### **RESULTS AND DISCUSSION**

#### Engineering and characterization of HER2specific liposomes loaded with 4-L-<sup>10</sup>BPA

The poor water solubility of 4-L-<sup>10</sup>BPA, low accumulation in tumor tissue, and rapid clearance are the main obstacles in the application of 4-L-<sup>10</sup>BPA for BNCT. Various 4-L-<sup>10</sup>BPA carriers that would enhance the compatibility of this compound with aqueous media, increase its accumulation in the target tissue, and extend its circulation time in the bloodstream are currently under development in the attempt to solve these problems [21, 22]. Liposomes 100–200 nm in diameter are the most commonly used drug delivery systems, since they penetrate through the fenestrated endothelium of blood vessel walls in tumors and can be accumulated in the underlying tumor tissue [23].

The tumor-associated antigen HER2, whose expression is typically upregulated in many human epithelial cancers [24], was selected as a target in liposomal targeting of cancer cells. In modern medical practice, the HER2 tumor marker is a therapeutic target for monoclonal antibodies (pertuzumab and trastuzumab) and kinase inhibitors (lapatinib) in patients with HER2-positive breast cancer [24].

The scaffold-designed ankyrin repeat protein DARPin\_9-29 was used as a vector molecule to target nanoliposomes to a specific tumor-associated antigen. DARPin\_9-29 is an antibody mimetic capable of highly specifically interacting with HER2 subdomain I ( $K_p$ = 3.8 nM) [25].

4-L-<sup>10</sup>BPA was loaded into liposomes as part of a complex with *D*-fructose at a 1 : 1 molar ratio (*Fig. 1A*). To verify the reproducibility of the procedure of loading 4-L-<sup>10</sup>BPA into liposomes, six samples of liposomes loaded with 4-L-<sup>10</sup>BPA were prepared, starting at the stage of weighing of the 4-L-<sup>10</sup>BPA samples.

The absorption spectra of the samples #1-6 of DARPin-modified liposomes loaded with 4-L-10BPA have a characteristic peak at 270 nm due to the absorption of the incorporated <sup>10</sup>BPA. The absorption spectra of empty liposomes obtained from a suspension of 1.9 mg/mL of phospholipids (the red curve in Fig. 1B) do not contain any peak at 270 nm. Otherwise, the spectra of empty and loaded liposomes are identical. We had previously determined that the molar concentration of a 1 mg/mL suspension of unmodified liposomes is 1.1 nM [17]. DARPin 9-29 is characterized by weak absorption at 280 nm, since the protein molecule has a very low content of aromatic residues (five phenylalanine and no tryptophan residues). Therefore, the presence of DARPin on the liposome surface does not alter the absorption spectrum

of the liposome. Hence, the molar concentration of the liposomes in samples #1–6 is 2.09 nM.

Boron content in the liposomes was quantified by ICP-MS. Boron concentration in the liposome samples proved independent of the initial weighed sample (which might indicate that the degree of filling of the aqueous phase with the BPA–D-fructose complex in the liposome is at its maximum), on average equal to 258  $\pm$  44  $\mu$ M and corresponding to (1.2  $\pm$  0.2)  $\times$  10<sup>5</sup> 4-L-<sup>10</sup>BPA molecules per liposome.

The size and  $\zeta$ -potential of  $4L^{-10}BPA$ -loaded liposomes, modified and non-modified with DARPin\_9-29, were measured by dynamic and electrophoretic light scattering. Conjugation of liposomes and DARPin\_9-29 increases their hydrodynamic diameter from  $125.9 \pm 37.2$  to  $151.80 \pm 52.79$  nm (Fig. 2A) and shifts the  $\zeta$ -potential from -59.1  $\pm$  10.1 to -50.0  $\pm$  6.96 mV (Fig. 2B). The negative  $\zeta$ -potential of the liposomes indicates that the sample is stable and not prone to aggregation.

## Analysis of the interaction specificity of DARP-Lip(BPA) with the HER2 receptor in vitro

The ability of the targeted DARPin 9-29 module residing on the surface of 4L-10BPA-loaded liposomes to interact with HER2 on the cell surface was studied using two independent techniques: flow cytometry and confocal microscopy (Fig. 3). Since DARP-Lip(BPA) does not exhibit autofluorescence, the liposomes were conjugated to AF-488-NH fluorescent dye prior to their application in the aforementioned optical analysis methods. Two human cancer cell lines were used in the experiment: the SKOV-3 ovarian carcinoma cell line, characterized by an elevated HER2 level on the cell surface (10<sup>6</sup> receptors per cell), and the HeLa cervical carcinoma cell line, characterized by the normal (for all epithelial tissues) HER2 level (104 receptors per cell). The SKOV-3 and HeLa cells were incubated with DARP-Lip(BPA)/ AF488 at two concentrations: 150 and 350 nM, as described in the Experimental section. The flow cytometry data demonstrate that the interaction between DARP-Lip(BPA) and the cells was HER2-specific. Hence, for the HER2-overexpressing SKOV-3 cells, a higher DARP-Lip(BPA)/AF488 concentration in the cell suspension increased the shift of the fluorescence intensity with respect to the control (a green curve): ~ 13.6-fold for a DARP-Lip(BPA)/AF488 concentration of 150 nM (the blue curve) and  $\sim$  36.9-fold for a DARP-Lip(BPA)/AF488 concentration of 350 nm (the red curve) (Fig. 3A, upper left pictogram). Meanwhile, the fluorescence intensity of HeLa cells proved to be virtually independent of the DARP-Lip(BPA)/AF488 concentration in the medium and differed from

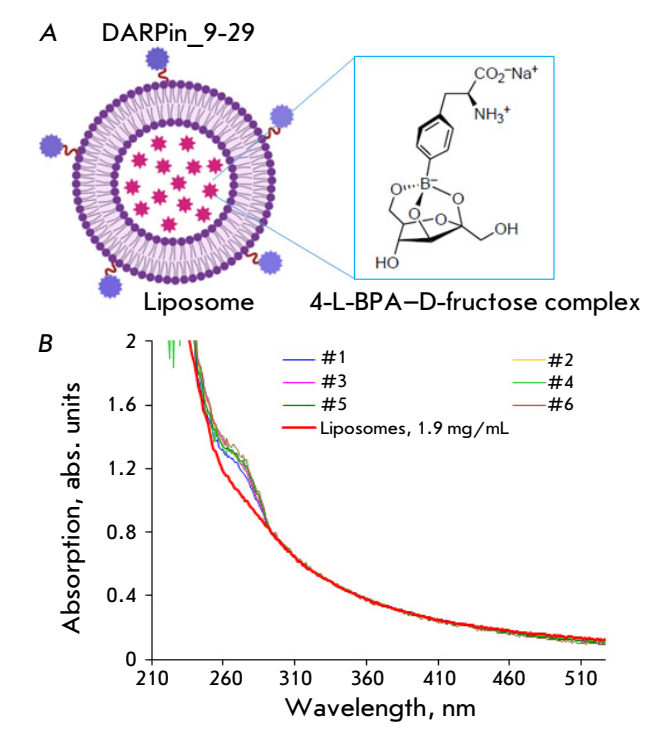


Fig. 1. DARPin-modified liposomes loaded with the 4-L-<sup>10</sup>BPA-D-fructose complex. (A) The schematic representation of DARP-Lip(BPA). The internal environment of liposomes is loaded with the 4-L-<sup>10</sup>BPA-D-fructose complex. The outer surface is modified by the HER2-specific scaffold protein DARPin\_9-29. (B) The absorption spectra of DARPin-modified samples #1-6 containing 4-L-<sup>10</sup>BPA and the absorption spectrum of empty liposomes with a concentration of 1.9 mg/mL (red curve)

the control (the green line) four- and fivefold for 150 nM (the blue curve) and 350 nM (the red curve) DARP-Lip(BPA)/AF488, respectively (*Fig. 3A*, upper right pictogram). The reason behind this is the absence of unbound HER2 receptors accessible for interaction with DARP-Lip(BPA) on the HeLa cell surface. Non-targeting liposomes loaded with 4-L-<sup>10</sup>BPA shift fluorescence intensity in neither SKOV-3 nor HeLa cells, thus attesting to DARPin-mediated interaction between liposomes and cells (*Fig. 3A*, the lower series of pictograms).

The specificity of DARP-Lip(BPA) binding to HER2 on the surface of cancer cells was also confirmed by confocal microscopy. Thus, characteristic staining of the cell membrane was observed after the SKOV-3 cells had been co-incubated with DARP-Lip(BPA)/AF-488 for 20 min (*Fig. 3B*, upper pictogram). Further incubation of cells in the presence of DARP-Lip(BPA) resulted in internalization of liposomes (during 120 min), as indicated by green pixels in the cytoplasm (*Fig. 3B*, lower pictogram).

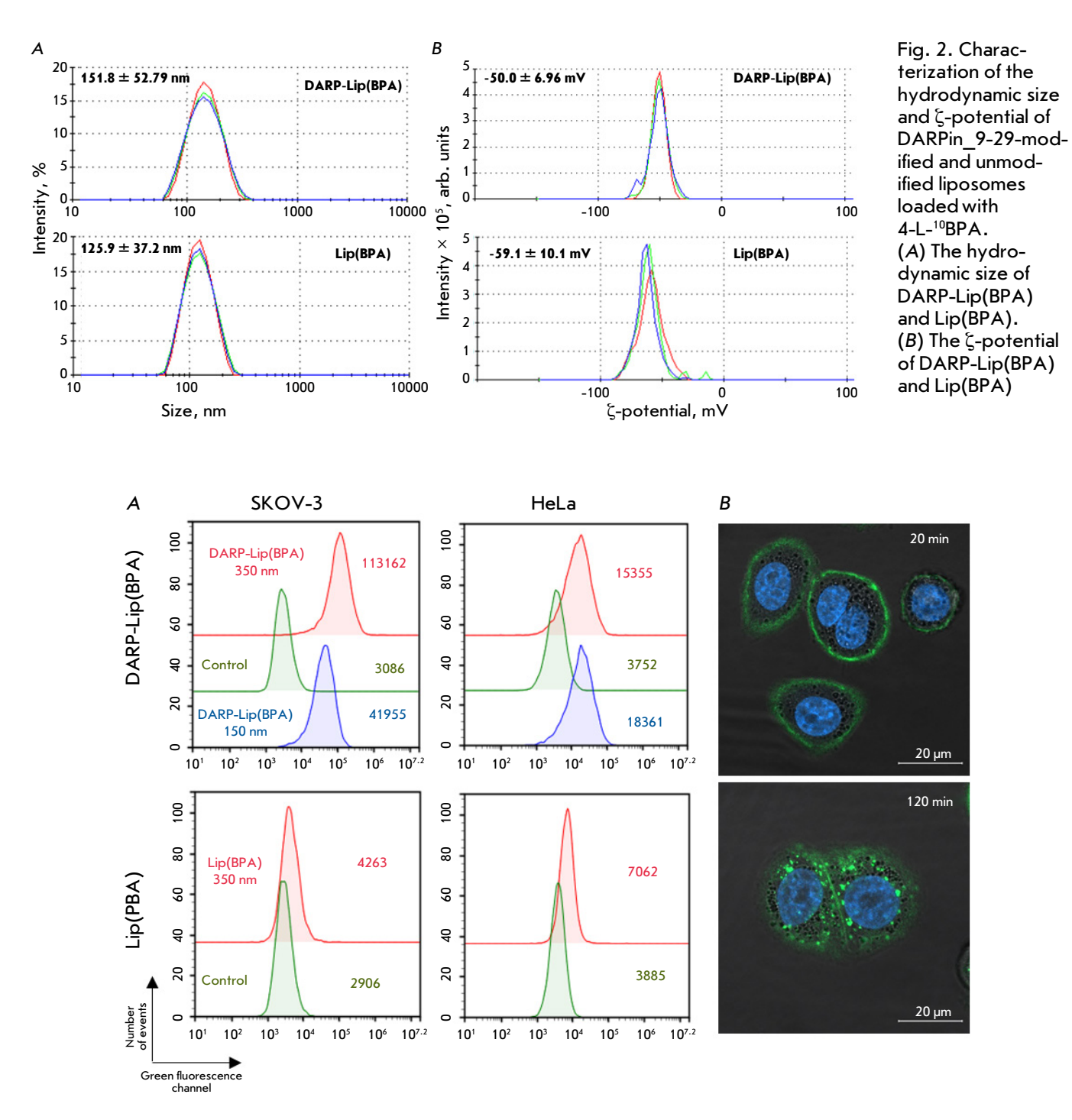


Fig. 3. Interaction of DARP-Lip(BPA) with the HER2 receptor *in vitro*. (A) Evaluation of the specific interaction of DARP-Lip(BPA) (upper pictograms) and Lip(BPA) (lower pictograms) with HER2-positive SKOV-3 cells and HeLa cells with normal HER2 expression levels by flow cytometry. The mean fluorescence intensity in the green channel is indicated on the pictograms. The green curve corresponds to fluorescent-unlabeled cells (control). The blue and red curves correspond to cells treated with 150 nM and 350 nM of DARP-Lip(BPA), respectively. (B) Confocal microscopy study of the interaction between DARP-Lip(BPA) and SKOV-3 cells. The duration of incubation of the cells in the presence of DARP-Lip(BPA) is indicated. Nuclei are stained with Hoechst 33342

#### RESEARCH ARTICLES

#### **CONCLUSIONS**

A total of ~ 10<sup>9</sup> <sup>10</sup>B atoms need to accumulate in a cancer cell in order to ensure effective BNCT [12]. The applicability of 4-L-<sup>10</sup>BPA in BNCT is constrained by its poor water solubility and low accumulation in cells. This study has proposed a method for engineering nanosized HER2-specific liposomes whose inner environment contains large quantities (~120,000 molecules per liposome) of 4-L-<sup>10</sup>BPA. *In vitro* studies demonstrated that the engineered liposomes effectively interacted with the HER2 receptor on the

surface of cancer cells and were efficiently internalized. We believe that the ability of DARPin-modified liposomes to precision-deliver large quantities of  $4-L^{-10}BPA$  into cancer cells will help solve the problem of low  $4-L^{-10}BPA$  accumulation and possibly open up new avenues for BNCT.  $\bullet$ 

This work was supported by the Russian Science Foundation (grant No. 24-62-00018 "Advanced Combined Technologies of Neutron Capture Therapy").

#### REFERENCES

- Nakamura H. // Methods Enzymol. 2009. V. 465. P. 179– 208. doi: 10.1016/S0076-6879(09)65010-2.
- Barth R.F., Vicente M.G., Harling O.K., Kiger W.S., 3rd, Riley K.J., Binns P.J., Wagner F.M., Suzuki M., Aihara T., Kato I., et al. // Radiat. Oncol. 2012. V. 7. P. 146. doi: 10.1186/1748-717X-7-146.
- 3. Dymova M.A., Taskaev S.Y., Richter V.A., Kuligina E.V. // Cancer Commun. (London). 2020. V. 40. № 9. P. 406–421. doi: 10.1002/cac2.12089.
- 4. Kanno H., Nagata H., Ishiguro A., Tsuzuranuki S., Nakano S., Nonaka T., Kiyohara K., Kimura T., Sugawara A., Okazaki Y. et al. // Oncologist. 2021. V. 26. № 7. P. e1250–e1255. doi: 10.1002/onco.13805.
- 5. Wongthai P., Hagiwara K., Miyoshi Y., Wiriyasermkul P., Wei L., Ohgaki R., Kato I., Hamase K., Nagamori S., Kanai Y. // Cancer Sci. 2015. V. 106. № 3. P. 279–286. doi: 10.1111/cas.12602.
- 6. Detta A., Cruickshank G.S. // Cancer Res. 2009. V. 69. № 5. P. 2126–2132. doi: 10.1158/0008-5472.CAN-08-2345.
- 7. Mastroberardino L., Spindler B., Pfeiffer R., Skelly P.J., Loffing J., Shoemaker C.B., Verrey F. // Nature. 1998. V. 395. № 6699. P. 288–291. doi: 10.1038/26246.
- 8. Prasad P.D., Wang H., Huang W., Kekuda R., Rajan D.P., Leibach F.H., Ganapathy V. // Biochem. Biophys. Res. Commun. 1999. V. 255. № 2. P. 283–288. doi: 10.1006/bbrc.1999.0206.
- 9. Kanai Y., Segawa H., Miyamoto K., Uchino H., Takeda E., Endou H. // J. Biol. Chem. 1998. V. 273.  $\mathbb{N}_2$  37. P. 23629–23632. doi: 10.1074/jbc.273.37.23629.
- 10. Yanagida O., Kanai Y., Chairoungdua A., Kim D.K., Segawa H., Nii T., Cha S.H., Matsuo H., Fukushima J., Fukasawa Y. et al. // Biochim. Biophys. Acta. 2001. V. 1514. № 2. P. 291–302. doi: 10.1016/s0005-2736(01)00384-4.
- 11. Nomoto T., Inoue Y., Yao Y., Suzuki M., Kanamori K., Takemoto H., Matsui M., Tomoda K., Nishiyama N. // Sci. Adv. 2020. V. 6. № 4. P. eaaz1722. doi: 10.1126/sciadv. aaz1722.
- 12. Barth R.F., Coderre J.A., Vicente M.G., Blue T.E. // Clin. Cancer Res. 2005. V. 11. № 11. P. 3987–4002. doi: 10.1158/1078-0432.CCR-05-0035.

- 13. Mori Y., Suzuki A., Yoshino K., Kakihana H. // Pigment Cell Res. 1989. V. 2. № 4. P. 273–277. doi: 10.1111/j.1600-0749.1989.tb00203.x.
- 14. Laakso J., Ruokonen I., Lapatto R., Kallio M. // Radiat. Res. 2003. V. 160. № 5. P. 606–609. doi: 10.1667/rr3067.
- 15. Henriksson R., Capala J., Michanek A., Lindahl S.A., Salford L.G., Franzen L., Blomquist E., Westlin J.E., Bergenheim A.T., Swedish Brain Tumour Study G. // Radiother. Oncol. 2008. V. 88. № 2. P. 183–191. doi: 10.1016/j. radonc.2006.04.015.
- 16. Liu P., Chen G., Zhang J. // Molecules. 2022. V. 27.  $\mathbb{N}_2$  4. P. 1372. doi: 10.3390/molecules27041372.
- 17. Deyev S., Proshkina G., Baryshnikova O., Ryabova A., Avishai G., Katrivas L., Giannini C., Levi-Kalisman Y., Kotlyar A. // Eur. J. Pharm. Biopharm. 2018. V. 130. P. 296–305. doi: 10.1016/j.ejpb.2018.06.026.
- 18. Shramova E., Proshkina G., Shipunova V., Ryabova A., Kamyshinsky R., Konevega A., Schulga A., Konovalova E., Telegin G., Deyev S. // Cancers (Basel). 2020. V. 12. № 10. P. 3014. doi: 10.3390/cancers12103014.
- Shipunova V.O., Shramova E.I., Schulga A.A., Shilova M.V., Deyev S.M., Proshkina G.M. // Russ. J. Bioorg. Chem. 2020. V. 46. P. 1156–1161. doi: 10.1134/S1068162020060308.
- 20. Proshkina G., Shramova E., Ryabova A., Katrivas L., Giannini C., Malpicci D., Levi-Kalisman Y., Deyev S., Kotlyar A. // Cancers (Basel). 2022. V. 14. № 19. P. 4806. doi: 10.3390/cancers14194806.
- 21. Dai L., Liu J., Yang T., Yu X., Lu Y., Pan L., Zhou S., Shu D., Liu Y., Mao W., et al. // Nat. Commun. 2025. V. 16. № 1. P. 1329. doi: 10.1038/s41467-025-56507-4.
- 22. Li J., Sun Q., Lu C., Xiao H., Guo Z., Duan D., Zhang Z., Liu T., Liu Z. // Nat. Commun. 2022. V. 13. № 1. P. 2143. doi: 10.1038/s41467-022-29780-w.
- 23. Maruyama K., Ishida O., Takizawa T., Moribe K. // Adv. Drug Deliv. Rev. 1999. V. 40. № 1–2. P. 89–102. doi: 10.1016/s0169-409x(99)00042-3.
- Iqbal N., Iqbal N. // Mol. Biol. Int. 2014. V. 2014.
   P. 852748. doi: 10.1155/2014/852748.
- 25. Steiner D., Forrer P., Pluckthun A. // J. Mol. Biol. 2008. V. 382. № 5. P. 1211–1227. doi: 10.1016/j.jmb.2008.07.085.

## LINE-1 Methylation Status in Multiple Sclerosis Patients Is Associated with Changes in Folate Metabolism

E. A. Tsymbalova<sup>1</sup>, E. A. Chernyavskaya<sup>1</sup>, G. N. Bisaga<sup>2</sup>, A. Y. Polushin<sup>3</sup>, E. I. Lopatina<sup>3</sup>, I. N. Abdurasulova<sup>1</sup>, V. I. Lioudyno<sup>1\*</sup>

<sup>1</sup>FSBSI "Institute of Experimental medicine", Saint Petersburg, 197022 Russia

<sup>2</sup>Almazov National Medical Research Center, Saint Petersburg, 197341 Russia

<sup>3</sup>FSBEI HE "Academician I.P. Pavlov First St. Petersburg State Medical University" of the Ministry of Healthcare of Russian Federation", Saint Petersburg, 197022 Russia

\*E-mail: vlioudyno@mail.ru

Received: November 30, 2024; in final form, April 21, 2025

DOI: 10.32607/actanaturae.27579

Copyright © 2025 National Research University Higher School of Economics. This is an open access article distributed under the Creative Commons Attribution License, which permits unrestricted use, distribution, and reproduction in any medium, provided the original work is properly cited.

ABSTRACT The disruption of epigenetic regulation and the development of abnormal DNA methylation patterns are crucial steps in the pathogenesis of neurodegenerative diseases. Methylation alterations in multiple sclerosis (MS) patients may contribute to the dysregulation of gene expression linked to the regulation of inflammation, myelin production, and the preservation of the integrity of the myelin sheath. The possibility that epigenetic alterations could be reversed provides a rationale for studying their mechanisms. In this study, we evaluated the methylation status of LINE-1 retrotransposons in the peripheral blood cells of patients with MS and healthy controls. In healthy individuals, LINE-1 methylation levels were observed to decrease with advancing age. MS patients exhibited a positive correlation between LINE-1 methylation and MS duration. The study indicates that the level of LINE-1 methylation is notably higher in progressive MS compared to the remitting type. LINE-1 methylation variations in MS patients were observed to be associated with the serum levels of homocysteine and vitamin B9, and dependent on the genotype for the C677T polymorphism of the MTHFR gene as well. The data obtained point to the contribution of the C677T polymorphism to the appearance of epigenetic disorders in MS development and suggest that hypermethylation may be mediated by disruptions in the folate metabolism that accompany MS.

KEYWORDS methylation, LINE-1, multiple sclerosis, homocysteine, folate metabolism, C677T polymorphism. ABBREVIATIONS MS – multiple sclerosis; CIS – clinically isolated syndrome; CNS – central nervous system; LINE1 – Long Interspersed Nuclear Element-1; BBB – blood-brain barrier; SAM – S-adenosylmethionine; SAH – S-adenosylhomocysteine; MTHFR – methylenetetrahydrofolate reductase; MTR – methionine synthase; MTRR – methionine synthase reductase; Hcy – homocysteine; Hcy/B9 – the ratio of homocysteine levels to vitamin B9 levels; PMNC – peripheral blood mononuclear cells; EDTA – ethylenediaminetetraacetic acid; EDSS – Expanded Disability Status Scale; MSSS – Multiple Sclerosis Severity Score; MS-HRM analysis – Methyl-sensitive High-Resolution Melting Assay; PCR – polymerase chain reaction; AUC – Area Under Curve; RR MS – relapsing-remitting multiple sclerosis; PP MS – primary progressive multiple sclerosis; SP MS – secondary progressive multiple sclerosis.

#### **INTRODUCTION**

Multiple sclerosis (MS) is a chronic autoimmune demyelinating disease that is associated with progressive neurological symptoms and patient disability. The etiology of MS is based on both genetic susceptibility and external factors that initiate the pathological process [1, 2]. Progress in the study of genome modifications has revealed a more intricate picture of MS pathogenesis, encompassing epigenetic factors such as alterations in DNA methylation. Alterations in the

susceptibility to external factors and the increased disease development risk may be attributed to irregularities in gene expression that stem from hypo- or hypermethylation of regulatory regions within the genome [3].

A whole-genome analysis indicates notable variations in DNA methylation profiles among individuals with MS compared to the control group [4–6]. In the progressive course of MS, differentially methylated sites are predominantly hypermethylated [7]. The de-

tectable alterations in DNA methylation influence the mechanisms governing blood-brain barrier (BBB) permeability, the regulation of the immune-inflammatory response, the processes of mature myelinating oligodendrocyte formation, and the maintenance of myelin sheath stability [6, 8, 9]. A relationship has been identified between LINE-1 hypermethylation and a greater likelihood of clinical disease activity through the analysis of global genome methylation, assessed by examining LINE-1 retrotransposon methylation in blood cells [10]. Patients who received IFN-β and demonstrated high LINE-1 methylation levels were found to be less likely to respond adequately to immunomodulatory therapy [11]. Hypermethylated LINE-1 fragments were identified in the cell-free circulating DNA of MS patients [12]. A review of DNA methylation studies in MS indicates that LINE-1 methylation shows potential as a diagnostic and prognostic biomarker, correlating with neurological deficit severity and therapeutic response [13].

The one-carbon metabolism is known to be closely associated with the maintenance of appropriate methylation levels [14]. The interplay of two coordinated cycles – the folate cycle and the homocysteine-methionine cycle – results in the production of S-adenosylmethionine (SAM), a universal methyl group donor, and S-adenosylhomocysteine (SAH), an inhibitor of DNA methyltransferase. The equilibrium of these one-carbon metabolism intermediates may be compromised in cases of dietary methionine deficiency and deficiencies in B vitamins, which function as coenzymes in homocysteine remethylation reactions. Variations in the genes for methylenetetrahydrofolate reductase (MTHFR), methionine synthase (MTR),

Table 1. Characteristics of the patients and healthy participants involved in the research

Parameter	Control $(n = 20)$	MS $ (n = 27)$	
Age, years	31.0 [24.5; 39.3]	33.0 [27.5; 42.5]	
Sex (F: M)	16:4	18:9	
EDSS, score	_	3.0 [2.0; 3.9]*	
MSSS, score	-	3.0 [2.1; 4.1]*	
Diagnosis and MS course (CIS/RRMS/ SPMS/PPMS)	-	4/18/3/2	
MS Duration, years	_	6.5 [2.8; 14.0]*	

Note: the Age, EDSS, and MSSS data are presented as median [1st quartile; 3rd quartile].

and methionine synthase reductase (MTRR) may affect the activity of these enzymes, which are critical to the folate cycle. Consequently, changes in genomewide methylation levels can occur because of the slow conversion of homocysteine to methionine. The resultant effects may include an increased accumulation of homocysteine in the blood and variations in the SAM/SAH ratio [15].

The purpose of this study was to evaluate the LINE-1 methylation status in the peripheral blood cells of individuals with multiple sclerosis and to assess laboratory indicators of folate metabolism, specifically serum homocysteine, cyanocobalamin (vitamin B12), and folic acid (vitamin B9). Moreover, we aimed to identify genotypes for significant polymorphisms within folate cycle genes and investigate the relationship between LINE-1 methylation and folate metabolism.

#### **EXPERIMENTAL PART**

Twenty-seven patients were recruited for this study, including twenty-three diagnosed with MS according to the 2005, 2010, and 2017 McDonald criteria [16, 17], and four patients with clinically isolated syndrome (CIS) and probable MS. Eleven patients presented a disease duration of no more than one year, while sixteen patients had had MS for a period ranging from one to twenty-three years. All the patients were under outpatient observation at the clinic of the Almazov National Medical Research Center of the Ministry of Health of the Russian Federation and the clinic of Pavlov First Saint Petersburg State Medical University. The control group comprised twenty individuals with no neurological pathology. Table 1 summarizes the characteristics of the examined groups. Neurological impairment was assessed using the Expanded Disability Status Scale (EDSS). The rate of disease progression was assessed using the Multiple Sclerosis Severity Score (MSSS), which was calculated based on age, disease duration, and level of disability [18]. Voluntary informed written consent was obtained from all patients and healthy volunteers included in the study.

## Preliminary sample preparation for methylation analysis

Peripheral blood mononuclear cells (PBMCs) were obtained by gradient centrifugation with Ficoll from venous blood samples drawn into vacuum tubes with an anticoagulant (EDTA). DNA was extracted from the PBMC suspension using a column method with a nucleic acid isolation reagent kit (Biolabmix, Russia), in accordance with the manufacturer's protocol. To evaluate the quality of the isolated DNA, we measured

<sup>\*</sup>The median and interquartile ranges of EDSS, MSSS, and disease duration were assessed in patients with a disease duration exceeding one year.

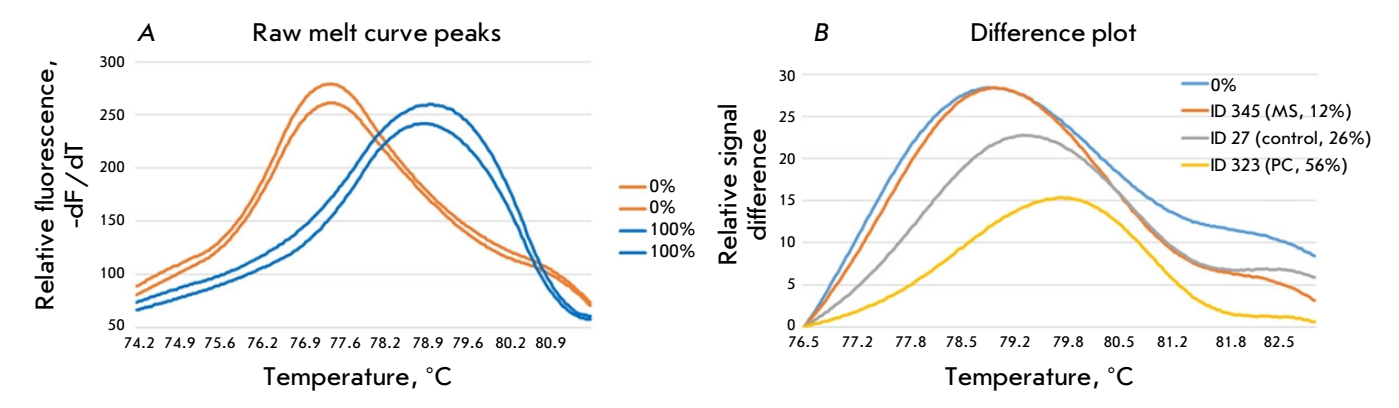


Fig. 1. Assessment of LINE-1 methylation levels via methyl-sensitive high-resolution melting curve analysis (MS-HRM). (A) – raw melting curves and melting peaks of fully methylated (100%) and fully unmethylated (0%) standard samples; (B) – melting curves for the standard sample (0%) and the three tested samples with high (56%), low (12%), and medium (26%) methylation levels, converted to difference plots

its concentration and the A260/280 absorbance ratio using a NanoDrop LITE spectrophotometer (Thermo Fisher Scientific, USA). For bisulfite conversion, the BisQuick reagent kit (Eurogen, Russia) was employed, with a minimum of 100 ng of DNA used in the reaction.

#### LINE-1 methylation level

LINE-1 methylation levels were assessed using methyl-sensitive high-resolution melting curve analysis (MS-HRM assay). PCR was performed following the amplification protocol and oligonucleotide primers as specified in [19]. Amplification, detection of fluorescent signals, and subsequent analysis of melting curves were conducted using a DT-prime detection amplifier (DNA-Technology, Russia). The PCR was performed using a final volume of 25  $\mu L$ , with a prepared reaction mixture that included the SYBER Green intercalating dye (Eurogen), 20 pmol of each primer, and 10 ng of a bisulfite-modified DNA matrix. All the reactions were performed twice.

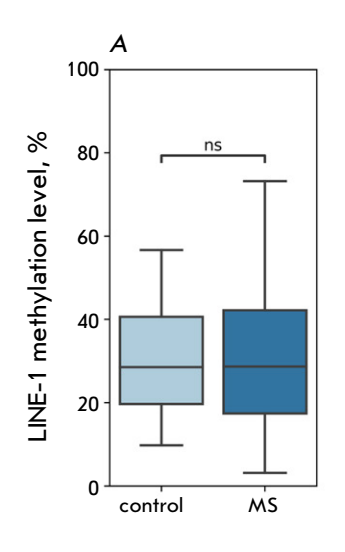
Calibration curves were created using samples that were prepared to contain methylation percentages between 0% and 100%. Fully methylated DNA was prepared using CpG-methylase M.SSI (SibEnzyme, Russia) from the genomic DNA of human cell line L68 (SibEnzyme). Fully unmethylated DNA was represented by a human unmethylated DNA standard (CpGenome Human Non-Methylated DNA Standard Set, Sigma-Aldrich, Sweden). Samples of 100% methylated and unmethylated control DNA underwent bisulfite conversion (along with the tested samples). Next, the target fragment was amplified using the converted standard samples as a matrix. The standards were then concentration-aligned so that the difference in Ct threshold cycle values remained under

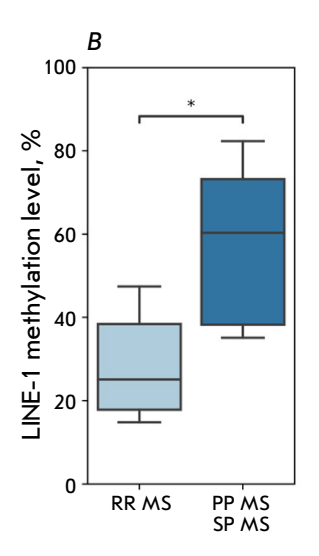
two during real-time fluorescence signal detection. Subsequently, the prepared fully methylated and unmethylated standard samples were combined in specific ratios to generate calibrators with methylation levels of 25%, 50%, and 75%. Following this, all calibration samples underwent amplification at each stage. The disparate melting profiles and temperature differentials for the melting peaks of methylated and unmethylated DNA indicated amplification of the products, which are differ in the cytosine to the thymine ratio (Fig. 1A).

To quantify the methylation levels, the data from fluorescence measurements obtained at each point along the temperature gradient for calibrators and test samples were imported into Excel as a text file. The data were normalized, and, subsequently, a plot of the differences was generated for each normalized melting curve and compared to the baseline melting curve (corresponding to the 100% methylated standard sample). The area under the curve (AUC), representing the derivative of the HRM melting curve, was determined for post-processing MS-HRM data. After normalization on the difference plot, each curve was displayed as it appeared when the AUC value for the baseline was subtracted. Examples of difference plots for samples with different methylation levels are shown in Fig. 1B. The methylation levels of the samples were computed by comparing their AUC values with the calibration curve derived from standard samples with known methylation levels, according to the recommendations outlined in [20].

#### Analysis of folate metabolism parameters

Blood samples were obtained from patients and healthy donors in the morning, under fasting conditions, adhering to established pre-analytical pro-





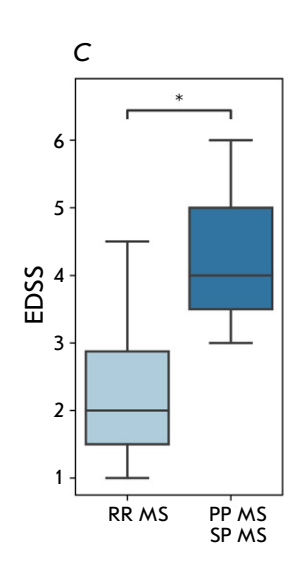


Fig. 2. LINE-1 methylation levels in peripheral blood mononuclear cells. (A) – comparison of indices in the control group and in the group of MS patients; (B) – comparison of indices in patients with RR MS, PP MS, and SP MS; (C) – degree of neurologic deficit in patients with remitting and progressive MS. \* – statistically significant differences between groups; p < 0.05; ns – no significant differences

tocols. The serum levels of homocysteine, folic acid (vitamin B9), and cyanocobalamin (vitamin B12) were assessed immediately following blood collection (the samples were not retained). All studies were conducted in a clinical diagnostic laboratory setting. The folic acid content was measured using an Alisei Q.S. (Next Level S.R.L., Italy) enzyme immunoassay analyzer. Cyanocobalamin was measured via chemiluminescent immunoassay, using the Alinity i analyzer (Abbott Laboratories, USA), with homocysteine determined using the Roche Cobas 6 000 automated modular platform, employing the immunochemical module e601 (Roche Diagnostics, Switzerland).

## Genotyping for polymorphisms C677T and A1298C of the *MTHFR* gene, A2756G of the *MTR* gene, and A66G of the *MTRR* gene

Genotyping was performed by PCR using oligonucleotide primers and fluorescently labeled allele-specific probes (DNA-Synthesis, Russia). The primer and probe sequences are detailed in [21]. Genomic DNA was isolated from whole blood by the standard method using the "DNA-Sorb B" kit (AmpliSens, Russia). Statistical processing of the data was performed using the Statistica (v. 10) program package. The statistical criteria were selected depending on whether the data met the standards of the normal distribution.

#### **RESULTS**

## Methylation of LINE-1 in patients with MS and in control subjects

The study examined the level of global genomic methylation in two groups: control and MS patients. Furthermore, we evaluated how the progression of the disease impacted LINE-1 methylation levels by

comparing individuals with remitting-relapsing MS (RR MS) to those with progressive MS (secondary progressive and primary progressive MS). The comparison of the control group and the MS patient group without accounting for disease duration and course type revealed no significant differences (Kruskal-Wallis test, H = 2.002; p = 0.966) (Fig. 2A). However, patients with progressive forms of MS exhibited a significantly higher methylation level compared to patients with the relapsing-remitting course (Mann-Whitney U test, p = 0.023) (Fig. 2B). In patients with progressive MS, the EDSS scores, which characterize the level of neurological deficit according to the expanded Kurtzke Disability Scale, were notably higher than in patients with remitting MS types. The medians and interquartile ranges for the groups were 4.0 [3.5; 5.0] and 2.0 [1.5; 3.0] points, respectively (Mann-Whitney U test, p = 0.012) (Fig. 2B).

## Effect of age and disease duration on LINE-1 methylation levels

The study groups were similar in age, with a median age and interquartile range of 31.0 [24.5; 39.3] years in the control group and 33.0 [27.5; 42.5] years in the MS group. A significant negative correlation was found between the LINE-1 methylation level and age in the control group (r = -0.61; p = 0.004) (Fig. 3A). In MS patients, the significant relationship between these parameters was maintained at a similar level (r = -0.65; p = 0.032) only in those with a disease duration of less than 1 year. In patients with a longer disease duration, this correlation was absent, indicating a disruption of methylation control mechanisms in MS. Conversely, an increase in disease duration was associated with an elevation in the methylation level, as confirmed by correlation analysis revealing a positive relationship

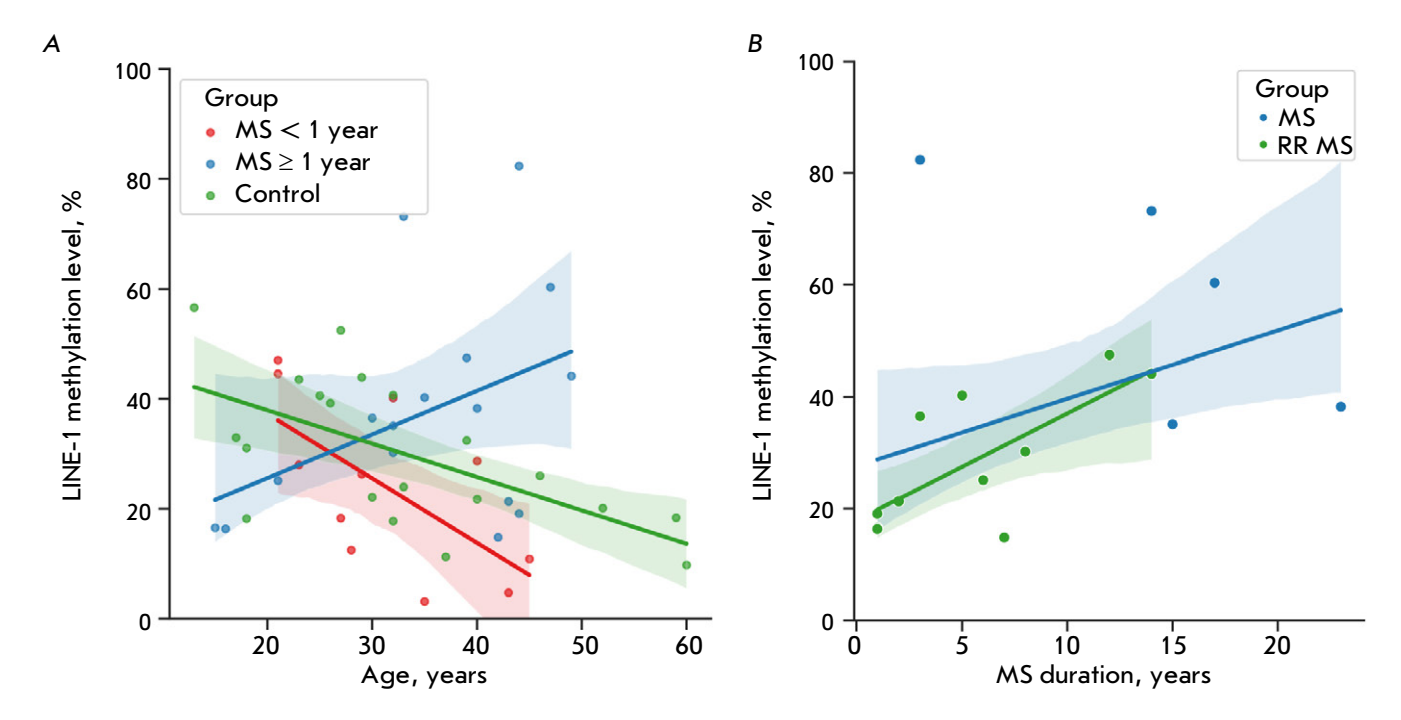


Fig. 3. Correlation analysis data to detect changes in LINE-1 methylation levels. (A) – data from both MS patients and those in the control group; (B) – the blue line shows the correlation between the LINE-1 methylation level and disease duration for the whole group of patients, and the green line shows the results of the analysis of patients with a remitting course (RR MS) and duration of over 1 year

between MS duration and methylation level (r = 0.47; p = 0.014) (Fig. 3B). When the analysis was conducted separately in the group of patients with relapsing-remitting MS (RRMS) and excluded patients with a disease duration of less than 1 year, this trend persisted and manifested itself as a strong positive correlation (r = 0.72; p = 0.013) (Fig. 3B). Due to the limited number of observations (n = 5), a separate analysis could not be performed for patients with progressive MS. Thus, the lowest values of methylation level were observed in patients with MS duration of less than 1 year (patients at the stage of disease onset); as the disease progressed, the methylation level increased. In patients with primary progressive and secondary progressive courses of MS the methylation level was the highest. Interestingly, in patients with RRMS, the increase in methylation with longer disease duration was not associated with a rise in disability as assessed by the EDSS scale (no correlation was found between MS duration and EDSS score: r = -0.27; p = 0.452).

#### LINE-1 methylation levels and folate metabolism

To determine the mechanisms contributing to methylation dysregulation in MS, the levels of homocysteine and B vitamins were measured and the ratios of homocysteine to folic acid (Hcy/B9) and homocysteine to cyanocobalamin (Hcy/B12) were calculated in the groups under investigation. The values for every indicator analyzed are given in Table~2. Additionally, the polymorphisms of folate cycle genes – C677T and A1298C of the MTHFR gene, A2756G of the MTR gene, and A66G of the MTRR gene – were genotyped for all the subjects.

Our earlier work identified the changes in folate metabolism parameters specific to the initial stage of MS (notably, decreased homocysteine levels at adult MS onset) [21]. Hence, in this work, we evaluated folate metabolism parameters across all MS patients, with a separate analysis for those with disease durations of less than and greater than a year. Using this approach, we found that in the group of patients with MS, those with a duration of less than 1 year had predominantly low and medium values of homocysteine levels. In contrast, high and medium values were predominant in the prolonged course (Fig.~4). Homocysteine levels relative to the lower quartile ( $\leq 8.45~\mu$ mol/L) and upper quartile ( $\geq 14.45~\mu$ mol/L) in the control group were taken as low and high levels.

Significant differences in the Hcy/B9 ratio were also identified in patients with different durations of multiple sclerosis (MS). In patients during the initial disease period, the median Hcy/B9 ratio was 0.271,

Table 2. Levels of homocysteine (Hcy), folic acid (vitamin B9), vitamin B12, and the Hcy/B9 ratio in individuals with multiple sclerosis (MS) compared to a control group

Parameter, units	Control $(n = 20)$	All MS patients (n = 27)	MS Duration		Reference interval
	(n-20)		< year $(n = 11)$	$\geqslant$ year $(n=16)$	
Homocysteine, µmol/L	11.1 [8.5; 14.5]	11.7 [8.0; 14.8]	9.9 [6.35; 11.7]	13.5 [10.0; 15.5]	Men: 5.46–16.20 Women: 4.44–13.56
Vitamin B9, nmol/L	14.95 [12.0; 18.5]	12.6 [8.0; 27.0]	26.1 [15.1; 31.7]	8.36 ** [6.1; 11.1]	7.0-46.4
Vitamin B12, pg/mL	277 [211; 392]	363 [264; 551]	300 [233; 500]	375 [277; 553]	197.0-771.0
Hcy/B9	0.693 [0.455; 1.244]	0.981 [0.251; 1.7]	0.271 [0.207; 0.719]	1.724 <sup>#</sup> [1.129; 2.144]	

Note: the data are presented as median [1st quartile; 3rd quartile].

whereas in those with a prolonged disease course, it was 1.724 (p = 0.007). This parameter stood at an intermediate value of 0.693 in the control group (Fig. 5A). The primary factor in the decline of this index during the early stages of the condition (in the group of patients with multiple sclerosis duration of less than 1 year) was the reduction in homocysteine levels. In contrast, folic acid levels remained normal, with all patients in this group exhibiting values within the established reference range (7.0-46.4 nmol/L). Throughout the protracted course of MS, a significant decline in B9 content was observed relative to the control group (Mann–Whitney U test, p = 0.024) and the vitamin B9 concentration was at or below the lower threshold of the reference interval in 10 out of 16 patients. Conversely, the level of homocysteine in patients with chronic MS tended to be high, with three patients presenting hyperhomocysteinemia (homocysteine concentrations exceeding 13.56 µmol/L in women and 16.20 µmol/L in men). Therefore, elevated Hcy/B9 values during the prolonged course of MS stemmed from heightened homocysteine levels and reduced vitamin B9 levels.

Furthermore, a significant positive correlation was found in MS patients but not in the control group between the level of methylation and homocysteine content (r=0.45; p=0.020), as well as between the level of methylation and the Hcy/B9 ratio (r=0.52; p=0.006) (Fig. 5B,C). Regression analysis indicated that the Hcy/B9 ratio could be a predictor of the methylation level (p=0.010).

Regression analysis did not reveal a statistically significant contribution of the studied polymorphic variants of folate cycle genes to changes in LINE-1 methylation levels. Conversely, a notable decrease in vitamin B9 levels, when compared to the control group, was only observed in patients with the CC genotype based on the C677T polymorphism of the MTHFR gene, but not in carriers of the minor T allele (Fig. 6A). This analysis was limited to the patient cohort with MS duration exceeding 1 year. Individuals with the CC genotype also tended to have higher homocysteine concentrations (Fig. 6B) and a notable increase in the Hcy/B9 ratio (Fig. 6C).

The patterns observed suggest the influence of the C677T polymorphism of the *MTHFR* gene on folate metabolism-mediated impairment of methylation control in patients with MS.

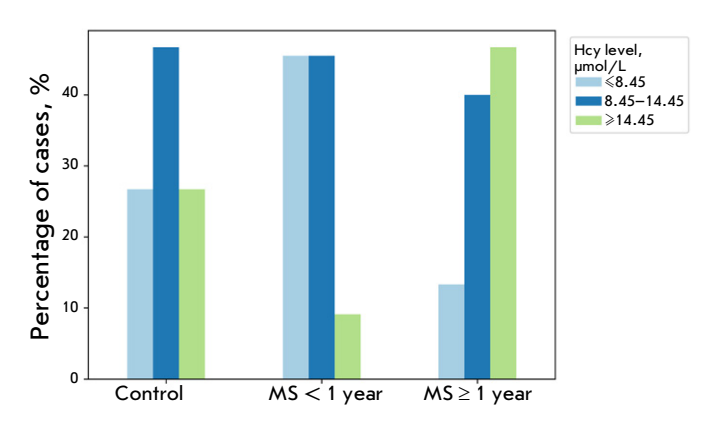


Fig. 4. Homocysteine serum levels in the control subjects and MS patients. The concentration ranges correspond to the quartiles established for the control group. The data for each range are expressed as percentages of the entire cohort within their respective groups

<sup>\*</sup>Significant differences between the MS patient subgroups with different disease durations (Kruskal–Wallis test with subsequent pairwise comparison).

<sup>\*</sup>Significant difference from the control group (Mann-Whitney U test).

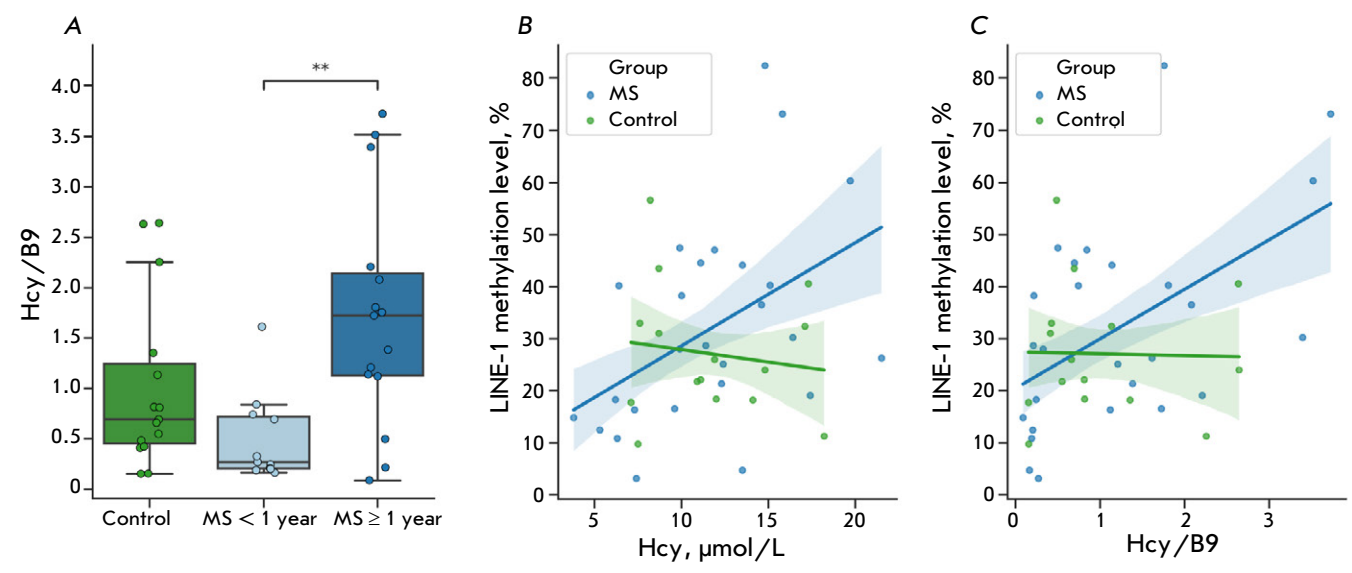


Fig. 5. Alterations in the ratio of serum homocysteine and folic acid concentrations (Hcy/B9) in individuals with MS (A), and the correlation between alterations in homocysteine levels (B) and Hcy/B9 ratios (C) with LINE-1 methylation levels in peripheral blood mononuclear cells. \*\* – statistically significant differences between the groups, p < 0.05 (Kruskal–Wallis test with subsequent pairwise comparisons)

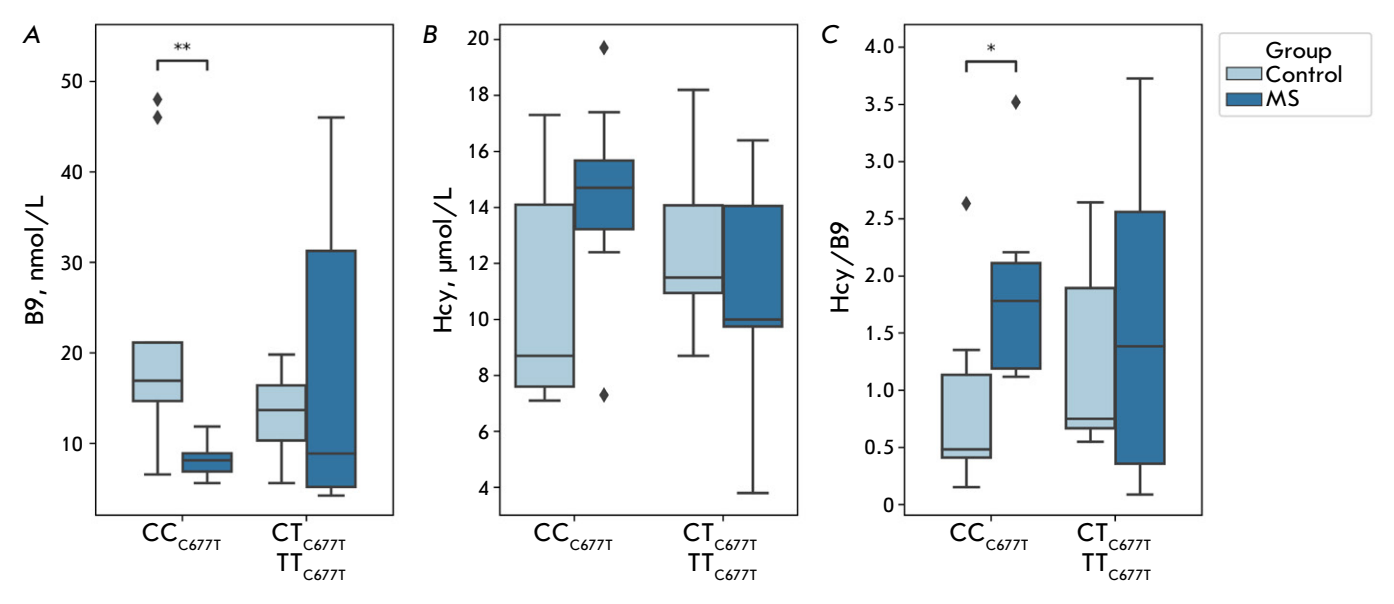


Fig. 6. Concentration of vitamin B9 (A) and homocysteine (B), and the Hcy/B9 ratio (C) in the individuals of the control group and the MS patients depending on the genotype for the C677T polymorphism of the MTHFR gene.  $\blacklozenge$  – values deviating from the median by more than 1.5 interquartile range. \* – statistically significant differences between the groups, p < 0.05; \*\* – statistically significant differences between the groups, p < 0.01

#### **DISCUSSION**

Evaluation of the methylation level of the LINE-1 retrotransposon serves as a surrogate marker of global genomic DNA methylation, as these repetitive genetic elements represent up to 70% of the methylated CpG sites within the genome [22, 23]. Alterations in LINE-1 methylation are also notewor-

thy, given that epigenetic silencing of retrotransposons may contribute to genome instability, chromosomal structural rearrangements, and malignization [24, 25]. In elderly individuals, the activation of LINE-1 retrotransposons results in the induction of interferon synthesis and contributes to the stimulation of inflammatory responses [26].

The present study revealed significant differences in the methylation level of the LINE-1 retrotransposon in PMNCs in patients with remitting and progressive MS, with higher methylation values found in patients with progressive MS.

Furthermore, LINE-1 methylation levels were observed to rise in multiple sclerosis patients, correlating with the length of their disease. In the control group, however, the level of methylation was inversely correlated with age. More precisely, MS alters correlation patterns, such as the loss of the negative correlation between age and global genomic methylation observed in healthy individuals, which is absent in patients.

Altered levels of homocysteine, folic acid, and their ratio in MS patients, coupled with the correlation between these changes and LINE-1 methylation levels, point to potential folate metabolism disruptions as a cause of hypermethylation in MS. One-carbon metabolism is a multi-component metabolic process that occurs in multiple steps. S-adenosylmethionine (SAM) and S-adenosylhomocysteine (SAH), which are intermediaries in the homocysteine-methionine cycle, modulate the activity of DNA methyltransferase, with stimulatory (SAM) and inhibitory (SAH) effects [27, 28]. The imbalance between these metabolites may be attributed to several factors, such as dietary methionine irregularities, deficiency cofactors of folate-metabolizing enzymes, and the presence of gene polymorphisms associated with homocysteine remethylation. Under normal physiological conditions, homocysteine is readily processed, rendering its creation biochemically advantageous. However, the accumulation of homocysteine shifts the equilibrium towards the preferential formation of SAH, a potent inhibitor of methyltransferase activity due to its structural similarity to the SAM molecule [29, 30]. The DNA methyltransferase DNMT1, which is essential for maintaining methylation patterns during cell division, is particularly sensitive to the inhibitory action of SAH. Consequently, an augmentation in blood homocysteine concentration should be correlated with hypomethylation, a phenomenon substantiated in several studies [31-34]. However, in patients with MS, the elevated homocysteine level was associated with increased methylation, suggesting a disruption in the feedback mechanism governing DNMT activity. This suggestion necessitates supplementary research for confirmation.

It is worth noting that only four out of 27 patients exhibited homocysteine levels exceeding the upper limit of the reference range, with a peak value of 21.5  $\mu$ mol/L in one patient, indicating a moderate degree of hyperhomocysteinemia. The elevation in ho-

mocysteine concentration may be insufficient to shift the equilibrium toward SAH formation, thereby failing to inhibit methyltransferase activity.

The observed changes in patients with multiple sclerosis may be attributed to the dysregulation of the MTHFR enzyme, which is responsible for the conversion of 5,10-methylenetetrahydrofolate to 5-methyltetrahydrofolate, the adequate production of which is crucial for the synthesis of SAM and the availability of methyl groups. MTHFR is allosterically inhibited by SAM [35]. The absence of this mechanism results in 5-methyltetrahydrofolate being consistently produced, thereby facilitating increased homocysteine remethylation, methionine biosynthesis independent of its concentration, and SAM synthesis [36]. Our findings may be indicative of the realization of such a mechanism. Thus, throughout the chronic progression of MS, an elevation in the percentage of patients exhibiting high serum homocysteine levels (relative to the average in the control group) was observed, with more frequent indications of folate deficiency and a predictable increase in the Hcy/B9 ratio. An examination of these parameters in relation to the C677T polymorphism of the MTHFR gene genotype revealed a greater propensity for these changes in individuals with the CC genotype. Alterations in folate metabolism demonstrated a correlation with methylation level changes. Therefore, it is reasonable to hypothesize that the influence of the C allele of this polymorphic variant contributes to the manifestation of epigenetic disorders in the development of MS. The hypothesis is supported by the finding that a missense mutation at position 677 of the MTHFR gene causes a decrease in enzyme activity [37]. MTHFR catalyzes the conversion of tetrahydrofolate to 5-methyltetrahydrofolate, providing a substrate for the MTR-mediated remethylation of homocysteine to methionine. The presence of the T allele of the C677T polymorphism in the MTHFR gene lowers enzyme activity by a maximum of 70% in heterozygous and 30% in homozygous carriers. Consequently, a marked reduction in vitamin B9 levels among carriers of the "active" gene variant (genotype CC) might be linked to its increased utilization in the process of converting homocysteine to methionine, maintaining methionine concentrations, facilitating SAM formation, and sustaining a high methylation potential. The idea presented here is congruent with prior findings, which suggest that individuals with the TT genotype of the C677T polymorphism exhibit decreased global methylation in lymphocyte DNA [38]. Additionally, the effect of hyperhomocysteinemia on peripheral mononuclear cell methylation is determined by the C677T polymorphism genotype of the MTHFR gene and fo-

#### RESEARCH ARTICLES

late levels: a reduction in methylcytosine levels was noted in individuals with the TT genotype and diminished blood folate [39].

#### CONCLUSION

The present study is the first to demonstrate a connection between LINE-1 methylation levels in multiple sclerosis and the folate metabolism status. Overall, the obtained results are in good agreement with the current understanding of the influence of metabolic processes on the key epigenetic phenomenon – DNA methylation. One-carbon fragment metabolism disorders can be triggered by inadequate vitamin and nutrient intake or by polymorphic variations in the genes involved in the folic acid and homocysteine remethylation processes. The development of aberrant methylation patterns and persistent alterations in gene expression is attributable to diminished methyl

donor availability and dysregulated methyltransferase activity, both consequences of an impaired folate metabolism. It should be emphasized that epigenetic alterations are regulated and can be reversed. Future research endeavors should prioritize the development of algorithms to correct metabolic disorders and maintain sufficient methylation levels.

Funding. This study was financially supported by the Russian Science Foundation (grant No. 23-25-00312).

Ethical Compliance. The research program received approval from the Local Ethical Committee of the Institute of Experimental Medicine (protocol No. 3/23 20.09.2023).

Before the study, all participants provided written informed consent for the utilization of their data in this publication.

#### REFERENCES

- 1. Oksenberg J.R. // Expert. Rev. Neurother. 2013. V. 13. № 12. Suppl. P. 11–19.
- 2. Jakimovski D., Bittner S., Zivadinov R., Morrow S.A., Benedict R.H., Zipp F., Weinstock-Guttman B. Multiple sclerosis. // Lancet. 2024. V. 403. № 10422. P. 183–202. doi: 10.1016/S0140-6736(23)01473-3.
- 3. Manna I., De Benedittis S., Porro D. // Int. J. Mol. Sci. 2024. V. 25. № 16. P. 8921. doi: 10.3390/ijms25168921.
- 4. Kulakova O.G., Kabilov M.R., Danilova L.V., Popova E.V., Baturina O.A., Tsareva E.Y., Baulina N.M., Kiselev I.S., Boyko A.N., Favorov A.V., et al. // Acta Naturae. 2016. V. 8. № 3. P. 103–110.
- 5. Castro K., Casaccia P. // Mult. Scler. 2018. V. 24.  $\mathbb{N}_2$  1. P. 69–74. doi: 10.1177/1352458517737389.
- 6. Kiselev I.S., Kulakova O.G., Boyko A.N., Favorova O.O. // Acta Naturae. 2021. V. 13. № 2. P. 45–57. doi: 10.32607/actanaturae.11043.
- 7. Kiselev I.S., Kulakova O.G., Danilova L.V., Baturina O.A., Kabilov M.R., Popova E.V., Boyko A.N., Favorova O.O. // Molekulyarnaya biologia. 2022. V. 56. № 3. P. 468–475. doi: 10.31857/S0026898422030089.
- 8. Sokratous M., Dardiotis E., Tsouris Z., Bellou E., Michalopoulou A., Siokas V., Arseniou S., Stamati T., Tsivgoulis G., Bogdanos D., et al. // Auto Immun. Highlights. 2016. V. 7. № 1. P. 12. doi: 10.1007/s13317-016-0084-z.
- 9. Hojati Z. // Adv. Exp. Med. Biol. 2017. V. 958. P. 65–90. doi: 10.1007/978-3-319-47861-6 6.
- Neven K.Y., Piola M., Angelici L., Cortini F., Fenoglio C., Galimberti D., Pesatori A.C., Scarpini E., Bollati V. // BMC Genet. 2016. V. 17. № 1. P. 84. doi: 10.1186/s12863-016-0395-0.
- 11. Pinto-Medel M.J., Oliver-Martos B., Urbaneja-Romero P., Hurtado-Guerrero I., Ortega-Pinazo J., Serrano-Castro P., Fernández Ó., Leyva L. // Sci. Rep. 2017. V. 7. № 1. P. 8727. doi: 10.1038/s41598-017-09301-2.
- 12. Dunaeva M., Derksen M., Pruijn G.J.M. // Mol. Neurobiol. 2018. V. 55.  $\mathbb{N}_2$  6. P. 4681–4688. doi: 10.1007/s12035-017-0679-7
- 13. Kiselev I.S., Kulakova O.G., Boyko A.N., Favorova

- O.O. // Acta Naturae. 2021. T. 13.  $\mathbb{N}_2$  2 (49). C. 45–57. doi: 10.32607/actanaturae.11043.
- 14. Choi S.W., Friso S. // Nutr. Res. Pract. 2023. V. 17. № 4. P. 597–615. doi: 10.4162/nrp.2023.17.4.597.
- 15. Weiner A.S., Boyarskikh U.A., Voronina E.N., Mishukova O.V., Filipenko M.L. // Gene. 2014. V. 533. № 1. P. 168–172. doi: 10.1016/j.gene.2013.09.098.
- 16. Polman C.H., Reingold S.C., Edan G., Filippi M., Hartung H.P., Kappos L., Lublin F.D., Metz L.M., McFarland H.F., O'Connor P.W., et al. // Ann. Neurol. 2005. V. 58. № 6. P. 840–846. doi: 10.1002/ana.20703.
- 17. Thompson A.J., Banwell B.L., Barkhof F., Carroll W. M., Coetzee T., Comi G., Correale J., Fazekas F., Filippi M., Freedman M.S., et al. // Lancet Neurol. 2018. V. 17. № 2. P. 162–173. doi: 10.1016/S1474-4422(17)30470-2.
- 18. Roxburgh R.H., Seaman S.R., Masterman T., Hensiek A.E., Sawcer S.J., Vukusic S., Achiti I., Confavreux C., Coustans M., le Page E., et al. // Neurology. 2005. V. 64. № 7. P. 1144–1151. doi: 10.1212/01.WNL.0000156155.19270. F8.
- Tse M.Y., Ashbury J.E., Zwingerman N., King W.D., Taylor S.A., Pang S.C. // BMC ResNotes. 2011. V. 4. P. 565. doi: 10.1186/1756-0500-4-565.
- 20. Samsø Mathiasen S., Bińkowski J., Kjeldsen T., Wojdacz T.K., Hansen L.L. // PLoS One. 2022. V. 17. № 9. P. e0273058. doi: 10.1371/journal.pone.0273058.
- 21. Lioudyno V.I., Tsymbalova E.A., Chernyavskaya E.A., Scripchenko E.Y., Bisaga G.N., DmitrievA.V., Abdurasulova I.N. // Biochemistry (Moscow). 2024. V. 89. № 3. P. 562–573. doi: 10.1134/S0006297924030143.
- 22. Ponomaryova A.A., Rykova E.Y., Gervas P.A., Cherdyntseva N.V., Mamedov I.Z., Azhikina T.L. // Cells. 2020. V. 9. № 9. P. 2017. doi: 10.3390/cells9092017.
- 23. Alves V.R.G., Micali D., Ota V.K., Bugiga A.V.G., Muniz Carvalho C., Belangero S.I. // Complex Psychiatry. 2023. V. 9. № 1–4. P. 119–129. doi: 10.1159/000530641.
- 24. Jones P.A., Baylin S.B. // Nat. Rev. Genet. 2002. V. 3. № 6. P. 415–428. doi: 10.1038/nrg816.
- 25. Wilson A.S., Power B.E., Molloy P.L. // Biochim. Biophys. Acta. 2007. V. 1775. № 1. P. 138–162. doi: 10.1016/j.

#### RESEARCH ARTICLES

- bbcan.2006.08.007.
- 26. De Cecco M., Ito T., Petrashen A.P., Elias A.E., Skvir N.J., Criscione S.W., Caligiana A., Brocculi G., Adney E.M., Boeke J.D., Le O., et al. // Nature. 2019. V. 566. № 7742. P. 73–78. doi: 10.1038/s41586-018-0784-9. Erratum in: Nature. 2019. V. 572. № 7767. P. E5. doi: 10.1038/s41586-019-1350-9.
- 27. Lu S.C. // Int. J. Biochem. Cell. Biol. 2000. V. 32.  $\mathbb{N}_2$  4. P. 391–395. doi: 10.1016/s1357-2725(99)00139-9.
- 28. Zhang J., Zheng Y.G. // ACS Chem. Biol. 2016. V. 11. № 3. P. 583–597. doi: 10.1021/acschembio.5b00812.
- 29. Perła-Kaján J., Jakubowski H. // Int. J. Mol. Sci. 2019. V. 20. № 13. P. 3140. doi: 10.3390/ijms20133140.
- 30. Caracausi M., Ramacieri G., Catapano F., Cicilloni M., Lajin B., Pelleri M.C., Piovesan A., Vitale L., Locatelli C., Pirazzoli G.L., et al. // Biofactors. 2024. V. 50. № 4. P. 709–724. doi: 10.1002/biof.2044.
- 31. Yi P., Melnyk S., Pogribna M., Pogribny I.P., Hine R.J., James S.J. // J. Biol. Chem. 2000. V. 275. № 38. P. 29318–29323. doi: 10.1074/jbc.M002725200.
- 32. Castro R., Rivera I., Struys E.A., Jansen E.E., Ravasco P., Camilo M.E., Blom H.J., Jakobs C., Tavares de Almeida I. // Clin. Chem. 2003. V. 49. № 8. P. 1292–1296. doi: 10.1373/49.8.1292.

- 33. Fux R., Kloor D., Hermes M., Röck T., Proksch B., Grenz A., Delabar U., Bücheler R., Igel S., Mörike K., et al. // Am. J. Physiol. Renal Physiol. 2005. V. 289. № 4. P. F786–F792. doi: 10.1152/ajprenal.00465.2004.
- 34. Loscalzo J., Handy D.E. // Pulm Circ. 2014. V. 4. № 2. P. 169–174. doi: 10.1086/675979.
- 35. Bhatia M., Thakur J., Suyal S., Oniel R., Chakraborty R., Pradhan S., Sharma M., Sengupta S., Laxman S., Masakapalli S.K., Bachhawat A.K. // J. Biol. Chem. 2020. V. 295. № 47. P. 16037–16057. doi: 10.1074/jbc.RA120.015129.
- 36. Petrova B., Maynard A.G., Wang P., Kanarek N. // J. Biol. Chem. 2023. V. 299. № 12. P. 105457. doi: 10.1016/j. jbc.2023.105457.
- 37. Liew S.C., Gupta E.D. // Eur. J. Med. Genet. 2015. V. 58. № 1. P. 1–10. doi: 10.1016/j.ejmg.2014.10.004.
- 38. Figueiredo J.C., Grau M.V., Wallace K., Levine A.J., Shen L., Hamdan R., Chen X., Bresalier R.S., McKeown-Eyssen G., Haile R.W., et al. // Cancer Epidemiol. Biomarkers Prev. 2009. V. 18. № 4. P. 1041–1049. doi: 10.1158/1055-9965.EPI-08-0926.
- 39. Friso S., Choi S.W., Girelli D., Mason J.B., Dolnikowski G.G., Bagley P.J., Olivieri O., Jacques P.F., Rosenberg I.H., Corrocher R., et al. // Proc. Natl. Acad. Sci. USA. 2002. V. 99. № 8. P. 5606–5611. doi: 10.1073/pnas.062066299.

## The Humoral and Cellular Immune Response to the Administration of OrthopoxVac Vaccine to Volunteers

S. N. Shchelkunov<sup>\*</sup>, E. Yu. Prudnikova, A. A. Shestakova, S. N. Yakubitskiy, S. A. Pyankov, A. E. Nesterov, S. V. Usova, M. P. Bogryantseva, E. A. Nechaeva, T. V. Tregubchak,

A. P. Agafonov

State Research Center of Virology and Biotechnology VECTOR, Rospotrebnadzor, Koltsovo,

Novosibirsk region, 630559 Russia

\*E-mail: snshchel@rambler.ru

Received: March 14, 2025; in final form, May 13, 2025

DOI: 10.32607/actanaturae.27654

Copyright © 2025 National Research University Higher School of Economics. This is an open access article distributed under the Creative Commons Attribution License, which permits unrestricted use, distribution, and reproduction in any medium, provided the original work is properly cited.

ABSTRACT OrthopoxVac, a fourth-generation smallpox vaccine, was the first of its kind registered worldwide in 2022, and it has been shown to be both safe and to induce only a mild reaction. A six-month clinical study confirmed its immunogenicity as compared to the first-generation live smallpox vaccine. Our study aimed to determine the levels of specific humoral and T-cell immune responses in volunteers following intradermal OrthopoxVac vaccine administration either in a single dose of 10<sup>7</sup> PoFU or in two doses of 10<sup>6</sup> PoFU, at 1.5, 3, and 5 years after initial vaccination. Following the immunization of volunteers with the OrthopoxVac vaccine at a dosage of 10<sup>7</sup> PoFU, the T-helper response remained at a relatively high level for three years, before it significantly dropped. Administration of the same vaccine twice at a dose of 10<sup>6</sup> PoFU resulted in a considerable decrease in the level of T-helpers, after 1.5 years. Additionally, some patients exhibited a reduction in viral neutralizing antibody (VNA) titers after 1.5 years of OrthopoxVac vaccine administration. When OrthopoxVac was administered at a dosage of 10<sup>7</sup> PoFU, no substantial differences were noted between groups at the 1.5-, 3-, and 5-year marks. In contrast, in the groups receiving two doses of 10<sup>6</sup> PoFU, VNA titers showed a significant reduction after 1.5 years. These findings indicate that a single intradermal dose of 10<sup>7</sup> PoFU of the OrthopoxVac vaccine elicits a significant and lasting immune response involving both antibodies and T-cells for a minimum of three years.

KEYWORDS smallpox, monkeypox, vaccinia virus, vaccination, antibodies, T-cells.

ABBREVIATIONS VNA – virus neutralizing antibodies; VACV – vaccinia virus; LSV – live smallpox vaccine; WHO – World Health Organization; CS – clinical studies; PFU – plaque forming unit; PoFU – pock forming unit; GMT – geometric mean titer; PBMC – peripheral blood mononuclear cells.

#### **INTRODUCTION**

Smallpox, a highly toxic, deadly, and extremely contagious human infectious disease, is also the only disease eradicated amongst humans through a global vaccination and epidemic surveillance campaign by the World Health Organization (WHO). This achievement remains one of the greatest triumphs of medical science [1].

The smallpox eradication program extensively utilized first-generation vaccines, which were mainly derived from the vaccinia virus (VACV). The virus was propagated on the skin of live animals, predominantly calves, with sheep, buffalo, and rabbits being used to a lesser extent. A major disadvantage of these vaccines has remained the high rate of serious post-vaccination complications, especially in people with immunodeficiencies, atopic dermatitis, and elderly in-

dividuals who have never received the smallpox vaccine [1, 2].

Adverse reactions, with varying degrees of prevalence and intensity, occur in approximately 20–30% of individuals that are vaccinated with the first-generation smallpox vaccine. The most frequently reported adverse reactions are low-grade fever, headache, lymph node swelling, skin inflammation, and fatigue. Significantly fewer individuals who receive the vaccine experience severer conditions, such as eczema, generalized or progressive vaccinia, encephalitis, or myopericarditis. Serious adverse events are observed in only a small fraction of vaccinated individuals, up to several hundreds per million, and fatalities amount to one or two patients per million [1, 3]. Given the severe post-vaccine complications that had accompanied the classical live vaccine and after confirmation of the

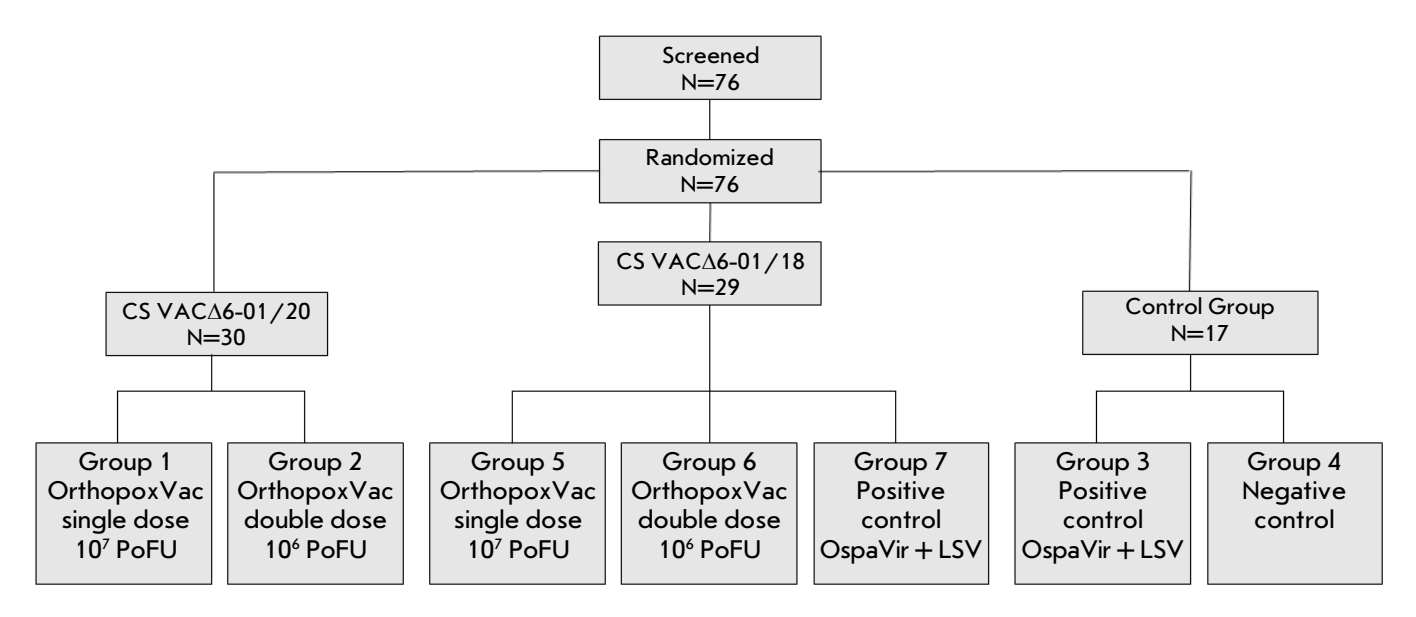


Fig. 1. The scheme to distribute volunteers by groups

eradication of smallpox in 1980, the WHO issued a strong recommendation to all nations that they discontinue vaccination against the infection [1, 2].

It is important to note that natural reservoirs harbor zoonotic orthopoxviruses closely related to the variola virus, including the monkeypox virus, cowpox virus, and other viruses that can infect humans [4]. Due to the cessation of smallpox vaccination, a considerable number of people, mainly those under 45 years of age, are no longer protected against orthopoxvirus infections. In the past few years, multiple outbreaks of zoonotic orthopoxvirus infections have been reported in human populations across geographical regions [2, 4]. Of significant concern has been the incidence of human monkeypox virus infections that resulted in an epidemic of this orthopoxvirus disease that spread across all continents between 2022 and 2023, affecting populations in over 100 countries [5]. At the moment, the primary area of concern regarding human monkeypox transmission is Africa [6]. Thus, renewed and intensified attention should now be focused on the possibility of a resurgence of smallpox or a comparable, dangerous disease that is a result of the natural evolution of zoonotic orthopoxvirus infectious agents [7, 8].

To lower the risk of widespread epidemics that stem from localized outbreaks and the natural evolution of a highly pathogenic human orthopoxvirus, researchers should prioritize the development of safe, new-generation live vaccines based on VACV. These factors highlight the scientific and practical significance of, as well as the urgency for; an updated strategy in the realm of vaccine prophylaxis against infections caused by orthopoxviruses.

Advancements in genetic engineering techniques have enabled the design of modified VACV variants through the targeted insertion of sequences into the viral genome, or by deleting or disrupting specific virulence genes [9, 10], while maintaining the genes essential for viral replication in cell culture. Deactivating virulence genes can markedly diminish the pathogenic attributes of VACV. A particularly promising avenue of research involves the development of highly attenuated variants of VACV through genetic engineering which exhibit an immunogenicity and protective efficacy similar to that of the original smallpox vaccine, but with significantly reduced pathogenicity.

OrthopoxVac, our fourth-generation live vaccine, is a variant designed to protect against smallpox and other orthopoxvirus infections. This vaccine uses the VAC $\Delta$ 6 strain, which harbors six gene disruptions (*C3L*, *N1L*, *J2R*, *A35R*, *A56R*, and *B8R*) and is cultivated in the 4647-cell culture [2, 11].

It is important to study the length of the immune response after vaccination in people who have received the OrthopoxVac vaccine. The results should be compared to the immune response triggered by the live smallpox vaccine (LSV) earlier used in Russia [12]. Such a study will provide insights into the necessity for and timing of revaccination using the new fourth-generation vaccine.

This research aimed to delve into post-registration data from the OrthopoxVac vaccine (a live culture

vaccine for the prevention of smallpox and related orthopoxvirus infections based on the vaccinia virus), focusing on the level and duration of the immune protection provided by both antibodies and T cells.

#### **EXPERIMENTAL PART**

#### Overall study design

A randomized, comparative, parallel-group study was performed, enrolling 76 subjects (male and female) aged between 25 and 40 years, who satisfied the inclusion criteria, met no exclusion criteria, and had prior participated in Phase I (CS VAC $\Delta$ 6-01/18) and Phase II/III (CS VAC $\Delta$ 6-01/20) clinical studies (CS) of OrthopoxVac vaccine (*Fig.* 1).

Group 1 comprised 15 healthy volunteers (7 men and 8 women) enrolled in the VAC $\Delta$ 6-01/20 clinical study who received a single intradermal vaccination with the OrthopoxVac vaccine at a dose of 10<sup>7</sup> PoFU;

Group 2 comprised 15 healthy volunteers (6 men and 9 women) enrolled in the VAC $\Delta$ 6-01/20 clinical study and vaccinated twice intradermally with the OrthopoxVac vaccine at a dose of 10<sup>6</sup> PoFU at intervals of 28 days;

Group 3 (positive control, PC) comprised 7 healthy volunteers (4 men and 3 women) who had worked with viruses of the genus Orthopoxvirus and were vaccinated using a two-stage method with the inactivated smallpox vaccine OspaVir and, after 7 days, again with a live smallpox vaccine based on the strain L-IVP VACV ("Microgen", Russia) as described in the previous paper [13] (OspaVir + LSV, 2020);

Group 4 (negative control, NC) consisted of 10 healthy volunteers (6 men and 4 women) who had never been previously immunized with any smallpox vaccine, had had no contact with patients immunized with a smallpox vaccine, and had never handled viruses belonging to the genus Orthopoxvirus;

Group 5 comprised 9 healthy volunteers (3 men and 6 women) who had participated in the VAC $\Delta$ 6-01/18 clinical study and were administered a single intradermal vaccination of the OrthopoxVac vaccine, at a dosage of  $10^7$  PoFU;

Group 6 comprised 10 healthy volunteers (7 men and 3 women) enrolled in the clinical study VAC $\Delta$ 6-01/18 who had received two intradermal vaccinations of the OrthopoxVac vaccine (10 $^6$  PoFU) at 28-day intervals; and

Group 7 (PC) comprised 10 healthy volunteers (5 men and 5 women) who had participated in the VAC $\Delta$ 6-01/18 clinical study and were vaccinated using the two-stage method of OspaVir + LSV.

Each patient provided written informed consent before inclusion in the study.

#### Viruses, cell culture

The research employed the L-IVP [9] and VACΔ6 VACV [11] strains and the CV-1 African green marmoset kidney cell line, which were sourced from the cell culture collection of the State Research Center of Virology and Biotechnology "Vector", Rospotrebnadzor.

#### Collection of blood samples from the volunteers

Blood sampling was performed from the ulnar vein in the hospital and inoculation room with observance of aseptic and antiseptic rules. A volume of 30–35 mL of blood was drawn during a single collection, using vacuum tubes. This work was performed at the clinical base of the Federal State Budgetary Healthcare Institution, Medical and Sanitary Unit No. 163 of the Federal Medical and Biological Agency of Russia.

The study was approved by the Ethical Committee of the State Research Center of Virology and Biotechnology "Vector", Rospotrebnadzor (Protocol No. 10 of the Ethical Committee meeting, February 14, 2024).

For the assessment of humoral immunity, serum was obtained from blood samples by precipitating the formed elements via centrifugation for 10 minutes at  $1,000 \times g$  and 4°C. The resulting serum samples were heat-inactivated at 56°C for 30 minutes and stored at -20°C.

#### Immunoenzymatic analysis of blood sera

The titers of specific antibodies were determined by ELISA using the "Vector ELISA Pox-IgG reagent kit for the immunoenzymatic detection of class G antibodies to poxvirus antigens" (Registration Certificate No. RZN 2022/15638), in accordance with the manufacturer's instructions [14].

#### Determination of the viralneutralizing antibody titer in sera

A plaque reduction assay of the VACV strain L-IVP in the CV-1 cell culture was used to determine the titer of virus-neutralizing antibodies (VNA). Four serial two-fold dilutions of a volunteer serum samples were prepared for the assay starting from 1:10 up to 1:80. Additional double dilutions, ranging from 1:160 to 1:1,280, were utilized to specify VNA titers for samples that demonstrated serum neutralizing activity beyond 1:80. Subsequently, an equal volume of the VACV dilution, with a titer of approximately 400 PFU/mL (approximately 40 PFU/well), was added to the prepared serum dilutions. The resulting mixtures were incubated at 37°C for 1 h. All the serum and virus dilutions were prepared using a maintenance medium: a DMEM/F-12 nutrient medium (1:1) supplemented with a 2% fetal bovine serum (FBS), 100 IU/mL penicillin, and 100  $\mu g/mL$  streptomycin.

Subsequently, 200  $\mu$ L of each serum-virus mixture was applied onto a 90–100% confluent monolayer of CV-1 cells grown in a 24-well culture plate, using three wells per serum dilution. Viral adsorption was carried out for 1 h at 37°C in a humidified atmosphere containing 5% CO<sub>2</sub>. After the adsorption period, the maintenance medium (1 mL/well) was added and the cells were incubated for an additional 48 h at 37°C and 5% CO<sub>2</sub>. Following the incubation period, the culture medium was removed and the cells were fixed and stained for 15 minutes by applying a solution of 0.2% crystal violet in a 9.6% ethanol aqueous solution containing 2% formaldehyde (approximately 0.2 mL/well). Subsequently, the dye was removed and the culture plate was dried at room temperature.

The number of plaques, representing the foci of cellular monolayer destruction with distinctive white spots on a blue background, was quantified in the CV-1 cell culture monolayer, and the serum dilutions that inhibited 50% PFU formation compared to the number of PFU in the negative control group (non-immune serum wells) were determined. Calculations were performed using the Spearman-Kärber method, and the results were expressed as the 50% plaque-reduction neutralization titer.

#### Peripheral blood mononuclear cell (PBMC) isolation

Venous blood was obtained from volunteers and collected in heparinized tubes (10 U/mL). PBMCs were isolated in a ficoll density gradient of 1.077 g/mL. The collected cell suspension was washed three times with the DMEM/F12 medium supplemented with 5% FBS, and the cells were pelleted via centrifugation at 350 g for 15 minutes at a temperature of (10  $\pm$  2)°C. The cellular sediment was resuspended in the DMEM/F12 medium supplemented with 15% FBS. Following this, a cell suspension at a concentration of 10 million cells/mL was prepared and 100  $\mu$ L of the suspension was added to the wells of a 96-well flat-bottom culture plate (1  $\times$  106 cells/well).

#### Intracellular staining of cells for cytokines

The cell-mediated immune response was evaluated via intracellular cytokine staining following stimulation of PBMC with antigen. Each sample was evaluated using the following conditions: unstimulated cells (background control), cells stimulated with virus-containing material (purified vaccinia virus strain VAC $\Delta$ 6, 4.0  $\mu$ g of total protein), and a positive control comprising cells stimulated with 50 ng/mL phorbol 12-myristate 13-acetate (Sigma-Aldrich, USA) and 0.5  $\mu$ g/mL ionophore (Calcium Ionophore A23187;

Sigma-Aldrich, USA). The cells were incubated at 37°C in a 5.0% CO, atmosphere for 8 h, followed by the addition of GolgiPlug (BD Biosciences, USA) to each well in accordance with the manufacturer's instructions, and followed again by additional overnight incubation at 37°C within a 5.0% CO, atmosphere. After stimulation, the cells underwent washing using a phosphate-buffered saline solution with a 2% casein hydrolysate. Next, the cells were stained for 40 min at 4°C with the Fixable Viability Stain 780 dye and the monoclonal antibodies CD3 (clone SK7, BV786), CD4 (clone RPA-T4, PerCP-Cy 5.5), CD8 (clone RPA-T8, Alexa Fluor 700), and CD45RA (clone HI100, BV510), CCR7 (CD197) (clone 3D12, PE-Cy7) (BD Biosciences). Subsequently, the cells were washed three times using a 2% phosphate-salt buffer solution and incubated for 20 minutes with 100 µl of the Fixation/ Permeabilization solution (BD Biosciences). Following incubation, the samples were washed thrice using 1× wash buffer (BD Perm/Wash™ Buffer, BD Biosciences) and stained for 40 minutes with monoclonal antibodies specific to interleukin-2 (IL-2, clone MQ1 17H12, APC), tumor necrosis factor (TNF, clone MAb11, PE), and interferon-γ (IFN-γ, clone B27, BV421, BD Biosciences). After washing three times with 1× wash buffer, the cells were fixed in 300 µL of 1× buffer (BD CellFix, BD Biosciences). The fixed cells were assessed using an ACEA NOVOCite Quanteon 4025 flow cytometer (Agilent Technologies, USA). Data analysis was performed with the NovoExpress software version 1.5.0.

The cytometric analysis used the following gating strategy (Fig. 2). The lymphocyte population was first identified based on forward and side scatter characteristics (Fig. 2A). Subsequently, singletons (single cells) were isolated: the abscissa represents the integral signal of direct light scattering, and the ordinate represents the peak signal of direct light scattering (Fig. 2B). Next, live cells negative for APC-Cy7 were isolated from single cells (Fig. 2C). BV786-positive T cells were gated according to the CD3 expression level (Fig. 2D). Cytotoxic T lymphocytes (CD3+CD8+ phenotype) were differentiated from helper T lymphocytes (CD3+CD4+ phenotype) using the histogram presented in Fig. 2E. The graph in Fig. 2F depicts cytokine-positive T helper cells, specifically those producing the tumor necrosis factor (TNF) and interferon-gamma (IFN- $\gamma$ ). The graph in Fig. 2F illustrates T-helper cells, identified by their positivity for the TNF and IFN-γ cytokines.

#### Statistical data analysis

Statistical analysis was performed using one-factor analysis of variance (ANOVA) for three or more

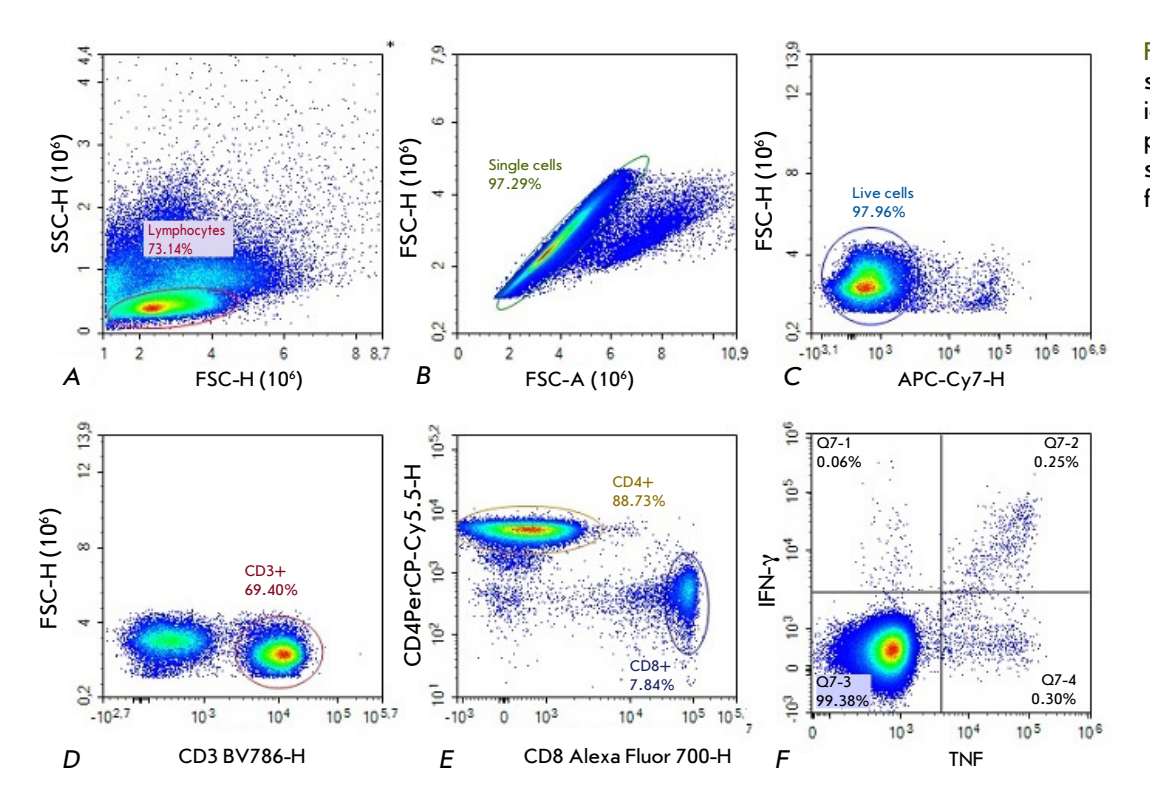


Fig. 2. Gating strategies for the identification of the principal T cell subsets (refer to text for details)

groups. A comparison of the two groups was conducted using the F-criterion. Statistical significance was established for result variations at p < 0.05.

### **RESULTS**

### **Detection of VACV-specific antibodies by ELISA**

A reliable condition of vaccination efficacy is to use the antibody titers in the control group samples as a comparative benchmark: the negative control (NC) group, comprising samples from volunteers who had until then never been vaccinated with smallpox vaccines, had no contact with vaccinated patients, and had had no occupational exposure to orthopoxviruses and the positive control (PC) group, which consists of samples from volunteers vaccinated with a first-generation vaccine, collected 3 and 5 years post-vaccination.

In the experimental groups of phase II/III clinical studies, three years post-vaccination, the percentage of volunteers exhibiting ELISA titers  $\geqslant 1:100$  was 86.7% following a single  $10^7$  PoFU dose of OrthopoxVac, and 92.8% after two administrations of a  $10^6$  PoFU dose. After five years, no serum samples from the phase I clinical study volunteer groups exhibited titers below 1:100.

The geometric mean titer (GMT) of specific IgG detected by ELISA was established to be 46 in the

NC group, with an error range of 36 to 58 for the 95% confidence interval.

The remaining control and experimental groups exhibited significantly different values, with considerably expanded error margins. For example, three years post-vaccination, the GMT values were 212 (121–372), 292 (155–555), and 518 (137–1952) in the  $10^7$  PoFU,  $2 \times 10^6$  PoFU, and PC groups, respectively. Five years post-vaccination, the GMT values in the same groups were 1131 (619–2065), 510 (251–1038), and 379 (204–704), respectively. A logarithmic interpretation of the obtained data is presented in *Fig. 3*.

Statistically significant differences were observed only within the NC group, relative to the other three groups at both the three-year and five-year post-vaccination intervals (*Fig. 3*). In the remaining pairs of groups, the differences are not significant.

## Determination of virus-neutralizing antibody titers in the VACV neutralization assay

The conferring of protective immunity against small-pox and other orthopoxvirus infections is significantly influenced by virus-neutralizing antibodies [15, 16]. The measured VNA titer can depend on the specific virus-cell culture pair and the details of the methodology used. Therefore, a surefire criterion for evaluating vaccination efficacy for this indicator is to use the first-generation vaccine as a control. Its ef-

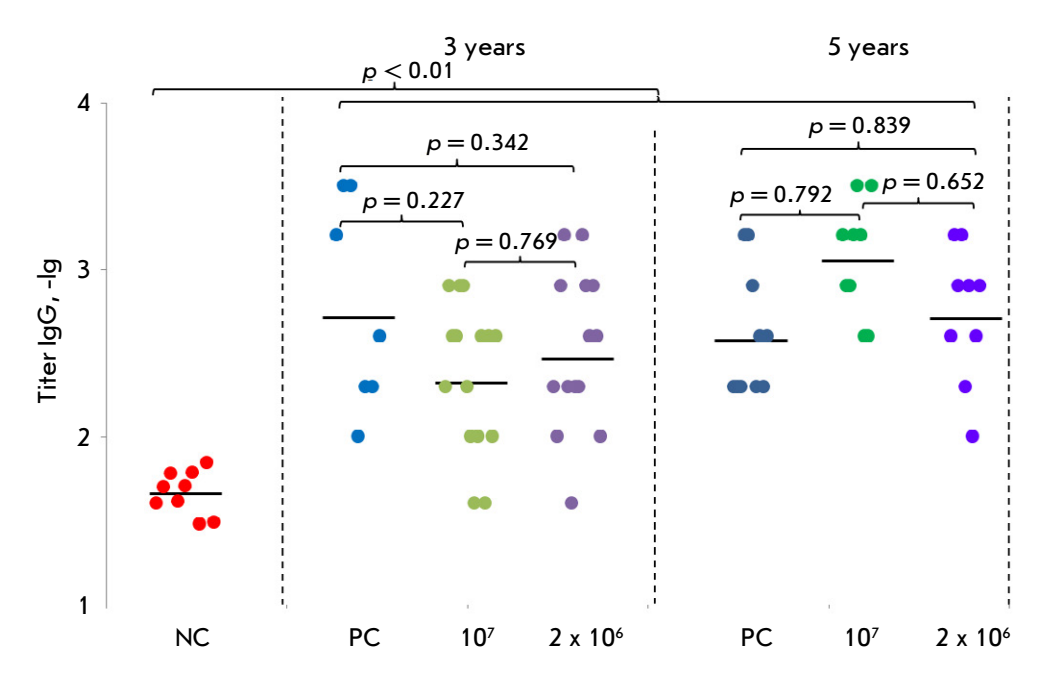


Fig. 3. Logarithms of the ELISA titers of specific IgG to VACV antigens in the blood sera of volunteers from clinical studies of the OrthopoxVac vaccine. NC group (comparison group, negative control) – volunteers who had not been vaccinated with smallpox vaccines, had not been in contact with patients vaccinated with smallpox vaccines, and did not work with viruses of the genus Orthopoxvirus; PC group (positive control) – volunteers vaccinated by the two-stage method with the smallpox inactivated OspaVir vaccine and after 7 days with a live smallpox vaccine based on the L-IVP strain (Microgen); 10<sup>7</sup> group – volunteers vaccinated once intradermally with the OrthopoxVac vaccine at a dose of 10<sup>7</sup> PoFU/0.2 mL; 2 × 10<sup>6</sup> group – volunteers vaccinated twice at 28-day intervals, intradermally at a dose of 10<sup>6</sup> PoFU/0.2 mL. The significance of the differences between the groups was determined by the F criterion. Each point represents a single volunteer. Horizontal lines denote GMT values for each group

ficacy against smallpox has been previously demonstrated.

Our findings (Fig. 4) demonstrate that 1.5 years after vaccination with OrthopoxVac and LSV, the VNA levels were notably higher in all vaccinated volunteer groups than they were in the NC group, with no significant differences observed in VNA titers between the compared vaccinated groups.

Analysis of a NC group patient sera via plaque inhibition reaction yielded a GMT VNA value of 1:7.

In the experimental groups of phase II/III clinical studies 1.5 years after vaccination, the number of volunteers with VNA titers of  $\geq 1:10$  was 60.0% when OrthopoxVac was administered once at a dose of  $10^7$  PoFU and 73.3% when vaccinated twice at a dose of  $10^6$  PoFU. The VNA titers of all volunteers vaccinated with LSV was above 1:10.

Within the same groups, the proportion of volunteers with VNA titers of  $\geq 1:10$  after 3 years was 53.3% following a single OrtopoxVac vaccine immunization at a dosage of  $10^7$  PoFU and 57.1% following a double immunization at a dosage of  $10^6$  PoFU, which

suggests a gradual decrease in VNA titer over time post-vaccination. VNA titers above 1:10 were observed in all LSV-inoculated participants.

The number of volunteers enrolled in phase I clinical studies with VNA titers of  $\geq 1$ : 10 after 5 years was 77.8% when OrthopoxVac was administered once at a dose of  $10^7$  PoFU and 67.7% when vaccinated twice at a dose of  $10^6$  PoFU. The number of volunteers vaccinated by the two-stage method with the first-generation vaccine with VNA titers of 1: 10 or more after 5 years stood at 88.9% (*Fig.* 4).

At 3 years and 5 years after immunization, significant reductions in VNA levels were observed in groups of individuals double-vaccinated with OrthopoxVac at a dose of 10<sup>6</sup> PoFU compared to the levels determined 1.5 years after vaccination (*Fig. 4B*). In groups vaccinated with a single dose of OrtopoxVac at 10<sup>7</sup> PoFU, some decrease in VNA titers was observed after 3 and 5 years, with these not significantly different from the titers at 1.5 years (*Fig. 4A*).

No significant differences in VNA titers were found between the groups of patients vaccinated us-

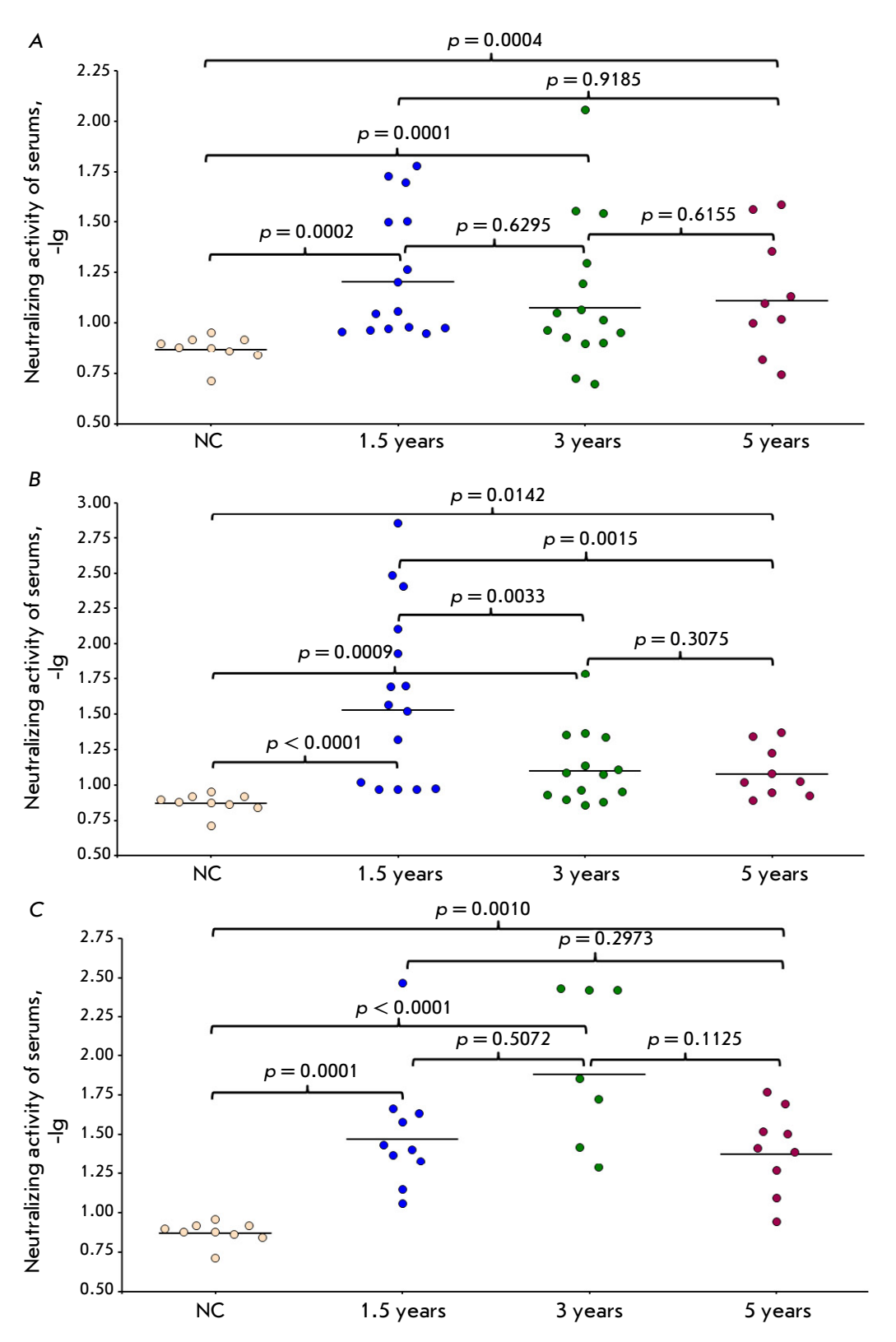


Fig. 4. The neutralizing activity of the blood sera of volunteers vaccinated in phases I and II/III clinical studies of the Orthopox-Vac vaccine. Virus-neutralizing antibody titers were assessed via the plague reduction assay of VACV (strain L-IVP) on CV-1 cell cultures. The data are presented in the form of -lg, with each point representing a single volunteer and horizontal lines indicating the levels of GMT of antibodies in the groups. The significance of the differences between the groups was determined by the F criterion. Presented are data on VNA titers at 1.5, 3, and 5 years post-vaccination for: (A) group - volunteers vaccinated once intradermally with the Orthopox-Vac vaccine at a dose of  $10^7 \text{ PoFU}/0.2 \text{ mL}$ ; (B) group - volunteers vaccinated twice with an interval of 28 days intradermally with the OrthopoxVac vaccine at a dose of 106 PoFU/0.2 mL; (C) group (positive control) - volunteers vaccinated with a two-stage technique: inactivated smallpox vaccine and then Smallpox live vaccine; NC group (comparison group, negative control) – volunteers who were not vaccinated with smallpox vaccines, were not in contact with patients vaccinated with smallpox vaccines, and did not work with viruses of the genus Orthopoxvirus

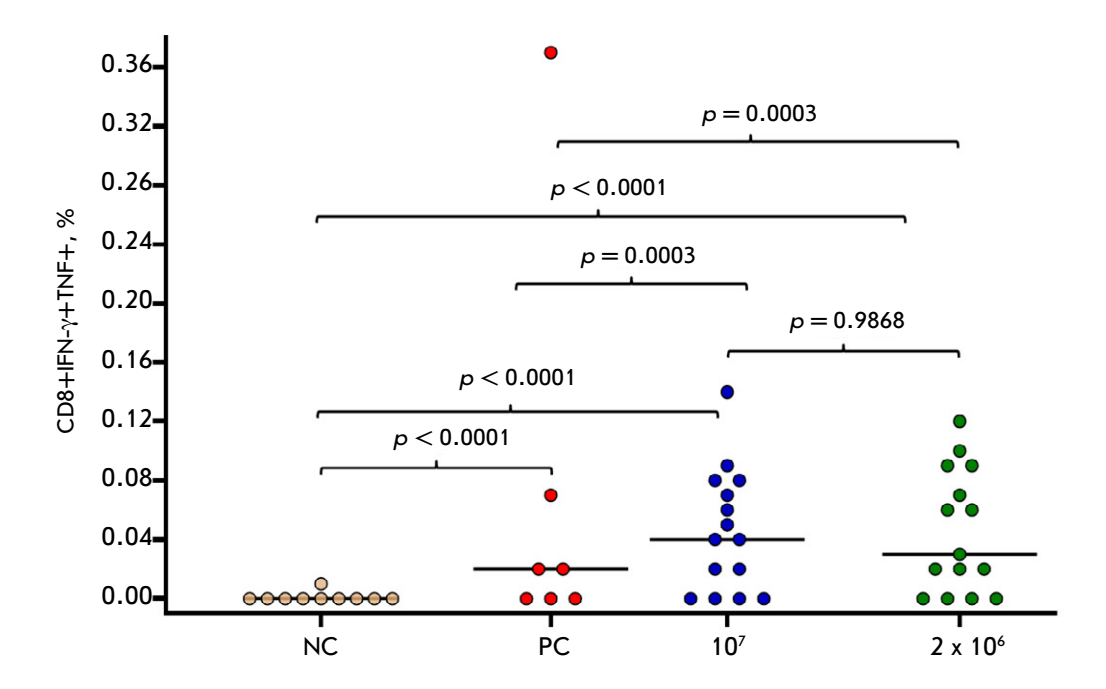


Fig. 5. The percentage of VACV-specific CD8+ T cells producing FN- $\gamma$  and TNF in PBMC samples from volunteers vaccinated with the smallpox vaccine in clinical studies 1.5 years after vaccination. NC group (comparison group, negative control) – volunteers not vaccinated with smallpox vaccines, with no contact with patients vaccinated with smallpox vaccines, and who did not work with viruses of the genus Orthopoxvirus; PC group (positive control) – volunteers vaccinated by the two-stage method with the smallpox-inactivated OspaVir vaccine and after 7 days with the live smallpox vaccine based on the L-IVP strain (Microgen);  $10^7$  group – volunteers vaccinated once intradermally with the OrthopoxVac vaccine at a dose of  $10^7$  PoFU/0.2 mL;  $2 \times 10^6$  group – volunteers vaccinated twice with a 28-day interval, intradermally at a dose of  $10^6$  PoFU/0.2 mL. The significance of the differences between the groups was determined by the F criterion. Each point represents a single volunteer

ing the two-step method (Inactivated smallpox vaccine OspaVir followed by LSV) at 1.5, 3, and 5 years (*Fig. 4C*).

### Evaluation of T cell anti-smallpox immunity

The cell-mediated immune response was determined using an intracellular cytokine staining protocol, which detects specific T cells based on their ability to produce cytokines, including IFN- $\gamma$ , TNF, and IL-2, after costimulation of peripheral blood mononuclear cells (PBMCs)  $ex\ vivo$  with the VAC $\Delta$ 6 strain of VACV (see the Experimental Section).

A cytometric analysis of PBMC samples revealed the presence of VACV-specific T helper (CD4+) and cytotoxic T lymphocytes (CD8+) 1.5 years post-vaccination. After a 20-h stimulation of PBMCs with the VAC $\Delta$ 6 VACV strain, an increase in the number of CD4+IFN- $\gamma$ + and CD8+IFN- $\gamma$ + T-cells was observed. Up to 80–90% of the antigen-specific cells were positive for triple (CD4+IFN- $\gamma$ +TNF+IL-2+) or double (CD8+IFN- $\gamma$ +TNF+) cytokine expression.

VACV-specific CD8+ T-cells were detected in most volunteers from the groups vaccinated with OrtopoxVac (both single dose  $10^7$  PoFU and double dose  $10^6$  PoFU). Up to 90% of the CD8+IFN- $\gamma$ +TNF+cell population was negative for the CD57 marker, indicating that these T-cells had not reached a state of terminal differentiation/exhaustion. In both groups immunized with OrthopoxVac, the level of CD8+IFN- $\gamma$ +TNF+ cells significantly exceeded the corresponding values in the positive control group – volunteers immunized with a first-generation smallpox vaccine (*Fig.* 5).

After 1.5 years, the quantity of CD4+IFN- $\gamma$ +TNF+IL-2+ T-helper cells within both volunteer groups vaccinated with OrthopoxVac presented no statistically significant differences when compared to the group inoculated with the first-generation live smallpox vaccine (LSV) (Fig. 6).

Additionally, the expression of the memory markers CCR7 (CD197) and CD45RA was analyzed in VACV-specific CD4+ and CD8+ T cells. The effec-

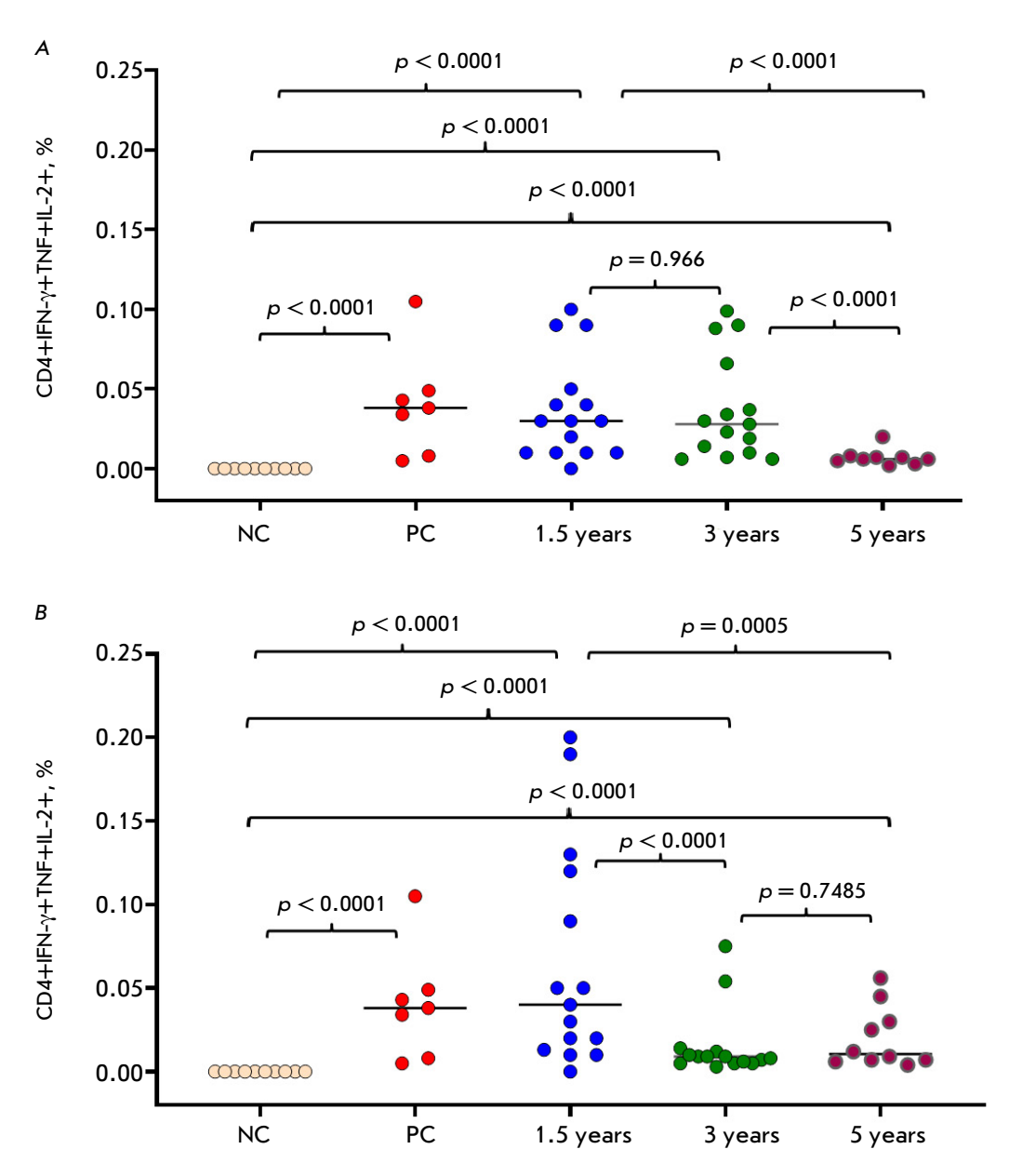


Fig. 6. The percentage of VACV-specific CD4+ T cells producing IFN-γ, TNF, and IL-2 in PBMC samples from volunteers vaccinated with the smallpox vaccine in clinical studies. (A) group – volunteers vaccinated once intradermally with the OrthopoxVac vaccine at a dose of 10<sup>7</sup> PoFU/0.2 mL; (B) group – volunteers vaccinated twice with an interval of 28 days intradermally at a dose of 10<sup>6</sup> PoFU/0.2 mL; NC group (comparison group, negative control) – volunteers not vaccinated with smallpox vaccines, with no contact with patients vaccinated with smallpox vaccines, and did not work with viruses of the genus Orthopoxvirus; PC group (positive control) – volunteers vaccinated by two-stage method with the smallpox inactivated OspaVir vaccine and after 7 days with live smallpox vaccine based on the L-IVP strain (Microgen). The significance of the differences between the groups was determined by the F criterion. Each point represents a single volunteer

tor memory  $\rm T_{\rm EM}$  cells (CCR7-CD45RA-) dominated the VACV-specific CD4+ T-cell population, with a proportion ranging from 80–90%, followed by central memory  $\rm T_{\rm CM}$  cells (CCR7+CD45RA-) at 5–10%, terminally differentiated effector memory  $\rm T_{\rm EMRA}$  cells (CCR7-CD45RA+) at 2–5%, and naïve T cells (CCR7+CD45RA+) representing just 1% (Table 1).

The percentage of  $\rm T_{\rm EM}$  (CCR7-CD45RA-) in the VACV-specific CD8+ T cell population was about 20%, and the percentage of  $\rm T_{\rm EMRA}$  (CCR7-CD45RA+) was up to 80%.

At the three- and five-year point following immunization with LSV and OrthopoxVac, the level of specific CD8+ T cells in the PBMC preparations from

Table 1. Distribution of smallpox virus-specific polyfunctional CD4+ T cells by expression of CCR7 (CD197) and CD45RA markers, 1.5 years after vaccination with smallpox vaccines

Groups	Serum No.	T <sub>CM</sub> central memory T cells CCR7+CD45RA-	Naïve T cells CCR7+CD45RA+	T <sub>EM,</sub> effector memory T cells CCR7-CD45RA-	$T_{\scriptscriptstyle EMRA}$ CCR7-CD45RA+
OrthopoxVac 10 <sup>7</sup> (single dose)	0-4-12	$6.8 \pm 3.6$	ND*	$89.4 \pm 4.1$	$3.8 \pm 0.6$
	0-4-17	$7.5 \pm 0.5$	$1.7\pm0.8$	$28.0 \pm 1.0$	$62.8 \pm 1.8$
	0-4-8	$14.7 \pm 6.4$	ND	$85.3 \pm 6.4$	ND
	0-4-15	$8.2 \pm 0.3$	ND	$87.0 \pm 0.3$	$4.7 \pm 0.6$
	0-4-3	$5.3 \pm 0.2$	$0.6\pm0.8$	$85.2 \pm 3.1$	$8.9 \pm 4.1$
	0-4-16	$7.2\pm0.1$	ND	$92.5 \pm 0.7$	ND
	0-4-10	$5.9 \pm 2.6$	ND	$90.0 \pm 3.3$	$4.2 \pm 5.9$
	0-4-11	$6.0 \pm 2.9$	ND	$92.1 \pm 2.9$	$2.0 \pm 0.1$
	0-4-13	$9.1\pm0.5$	ND	$88.7 \pm 0.1$	$2.2 \pm 0.3$
	0-4-14	$4.2 \pm 5.9$	ND	$92.0\pm0.5$	$3.8 \pm 0.4$
	0-4-1	$6.1 \pm 2.1$	$0.5\pm0.7$	$88.1 \pm 0.3$	$5.3 \pm 1.1$
	0-4-2	$7.8 \pm 4.6$	ND	$89.9 \pm 1.4$	$2.3 \pm 3.2$
	0-4-5	$4.4 \pm 1.2$	ND	$91.2 \pm 4.1$	$4.4 \pm 2.9$
	0-4-9	$13.8 \pm 3.2$	ND	$84.2 \pm 3.2$	$2.0 \pm 0.1$
	0-4-6	$4.9 \pm 1.0$	ND	$93.1 \pm 2.0$	$2.1 \pm 2.9$
	0-5-3	$5.6 \pm 0.9$	ND	$88.8 \pm 1.8$	$5.6 \pm 0.9$
	0-5-16	$4.9 \pm 0.9$	ND	$85.3 \pm 2.2$	$9.8 \pm 1.1$
OrthopoxVac 10 <sup>6</sup> (double dose)	0-5-4	$14.0 \pm 2.2$	ND	$84.9 \pm 3.7$	$1.1 \pm 0.1$
	0-5-5	$8.2 \pm 2.5$	$1.4 \pm 2.0$	$80.8 \pm 17.3$	$8.6 \pm 1.6$
	0-5-6	$3.8 \pm 1.4$	ND	$95.7 \pm 4.7$	ND
	0-5-8	$5.3 \pm 0.8$	$2.9 \pm 4.2$	$81.1 \pm 6.5$	$10.6 \pm 1.1$
	0-5-9	$8.8 \pm 2.3$	$0.3\pm0.4$	$87.3 \pm 2.1$	$3.6 \pm 2.1$
	0-5-11	$6.1 \pm 3.4$	$0.6\pm0.3$	$90.1 \pm 2.0$	$3.2 \pm 0.3$
	0-5-12	$7.6 \pm 6.4$	ND	$90.9 \pm 8.6$	$1.5 \pm 1.1$
	0-5-17	$12.7 \pm 0.8$	$1.3 \pm 1.9$	$84.8 \pm 2.3$	$1.1 \pm 0.1$
	0-5-18	$10.4 \pm 2.0$	$3.3 \pm 0.1$	$75.8 \pm 0.8$	$10.5 \pm 1.1$
	0-5-1	$6.8 \pm 0.8$	ND	$86.2 \pm 3.5$	$7.0 \pm 2.7$
	0-5-2	$7.3\pm0.4$	$1.0 \pm 0.1$	$91.2 \pm 0.4$	$0.5\pm0.7$
	0-5-10	$6.3\pm0.1$	$0.8\pm0.4$	$92.4 \pm 0.3$	$0.5\pm1.1$
	0-5-7	$9.5 \pm 2.1$	$0.4 \pm 2.1$	$86.0 \pm 1.5$	$2.0 \pm 2.8$
Positive control	0-2-34	$6.3 \pm 1.3$	$5.3 \pm 0.9$	$77.1 \pm 3.2$	$11.4 \pm 1.2$
	0-2-32	$1.9 \pm 0.8$	ND	93.1 ± 1.1	$5.1 \pm 2.3$
	0-2-2	$12.2 \pm 0.2$	$1.2 \pm 0.1$	$72.5 \pm 2.8$	$14.1 \pm 2.1$
	0-2-3	$9.0\pm2.7$	$2.2 \pm 0.1$	$59.6 \pm 1.6$	$29.3 \pm 3.3$
	0-2-30	$7.3 \pm 2.8$	ND	$90.9\pm5.4$	$1.9 \pm 0.6$
	0-2-36	$4.2 \pm 1.2$	$1.7\pm0.2$	$79.6 \pm 4.4$	$14.6 \pm 3.1$

<sup>\*</sup>Note: ND – not detected (below the sensitivity level of the method).

Table 2. Distribution of poxvirus-specific polyfunctional CD4+ T cells by expression of CCR7 (CD197) and CD45RA markers, 3 years after vaccination with smallpox vaccines

Groups	Serum No.	T <sub>CM,</sub> central memory T cells CCR7+CD45RA-	Naïve T-cells CCR7+CD45RA+	T <sub>EM,</sub> effector memory T cells CCR7-CD45RA-	T <sub>EMRA</sub> CCR7-CD45RA+
OrthopoxVac 10 <sup>7</sup> (single dose)	155	$6.6 \pm 2.2$	$0.5\pm0.1$	$87.2 \pm 0.9$	$5.8 \pm 0.7$
	158	$5.8 \pm 3.0$	$\mathrm{ND}^*$	$91.6 \pm 6.7$	$2.6 \pm 0.6$
	164	$12.9 \pm 4.1$	ND	$87.1 \pm 4.1$	ND
	166	$7.5 \pm 1.0$	ND	$82.8 \pm 4.7$	$6.7 \pm 1.7$
	199	$7.0 \pm 0.2$	$0.6\pm0.2$	$86.9 \pm 0.1$	$5.6 \pm 0.1$
	206	$11.3 \pm 5.2$	ND	$86.8 \pm 6.1$	$1.9 \pm 0.9$
	209	$10.2\pm0.5$	ND	$86.4 \pm 1.5$	$1.3 \pm 1.8$
	216	$10.9\pm2.7$	$0.7 \pm 0.1$	$85.4 \pm 2.4$	$3.1 \pm 0.4$
	222	$10.8 \pm 2.2$	ND	$86.1 \pm 0.8$	$3.1 \pm 3.0$
	223	$14.2 \pm 1.9$	$1.7 \pm 0.6$	$82.3 \pm 4.0$	$1.8 \pm 2.5$
	229	$7.7 \pm 0.1$	ND	$54.6 \pm 0.5$	$36.7 \pm 0.4$
	246	$8.8 \pm 2.9$	ND	$87.9 \pm 7.5$	$3.3 \pm 1.6$
	249	$7.6 \pm 1.5$	$1.1 \pm 0.3$	$85.7 \pm 0.9$	$5.6 \pm 2.1$
	246	$11.0 \pm 1.0$	$0.8 \pm 1.1$	$85.6 \pm 5.4$	$2.7 \pm 0.5$
	259	$8.0 \pm 0.6$	ND	$89.7 \pm 1.4$	$2.3 \pm 0.7$
OrthopoxVac 10 <sup>6</sup> (double dose)	059	$9.2 \pm 3.1$	$2.2 \pm 1.1$	$82.6 \pm 3.8$	$6.0\pm0.2$
	089	$3.5 \pm 4.9$	ND	$88.8 \pm 3.6$	$7.8 \pm 2.5$
	095	$6.1 \pm 1.2$	$2.6 \pm 0.7$	$89.6 \pm 0.1$	$1.7 \pm 0.3$
	098	$7.1 \pm 0.1$	ND	$92.4 \pm 9.4$	$0.1 \pm 0.1$
	108	$3.8 \pm 1.7$	$0.6\pm0.3$	$85.8 \pm 2.1$	$9.8 \pm 2.1$
	106	$8.0 \pm 0.2$	ND	$88.2 \pm 2.5$	$3.8 \pm 1.2$
	105	$6.0 \pm 1.3$	$1.1 \pm 0.4$	$90.6 \pm 1.2$	$2.3 \pm 0.1$
	104	$7.1 \pm 1.2$	$0.6\pm0.2$	$88.4 \pm 1.2$	$3.9 \pm 0.2$
	103	$9.0 \pm 2.8$	ND	81.2 ± 1.7	$9.8 \pm 2.9$
	178	$4.1 \pm 3.2$	$0.9\pm0.3$	$87.6 \pm 4.9$	$7.4 \pm 2.4$
	177	$9.6 \pm 1.3$	ND	$90.8 \pm 9.3$	$2.6 \pm 0.1$
	109	$6.7 \pm 0.1$	ND	$86.4 \pm 1.8$	$6.8 \pm 1.8$
	255	$6.5\pm0.7$	ND	$90.5\pm0.7$	$3.0 \pm 0.1$
	256	$7.3\pm0.4$	ND	$91.8 \pm 0.4$	$2.0 \pm 0.1$
	257	$6.0 \pm 1.4$	ND	$93.9 \pm 7.1$	$2.5 \pm 1.3$
Positive control	BLV	$7.1 \pm 1.6$	$0.5\pm0.7$	$90.5 \pm 3.9$	$1.9 \pm 0.5$
	DGV	$5.9 \pm 0.8$	$0.7 \pm 0.1$	$75.7 \pm 0.6$	17.7 ± 1.3
	RAS	$5.0 \pm 0.1$	$0.4\pm0.5$	$79.3 \pm 2.9$	$15.3 \pm 2.4$
	GTA	$13.0 \pm 2.6$	$0.3\pm0.4$	$83.6 \pm 3.4$	$3.2 \pm 0.8$
	FEN	$7.7 \pm 2.9$	ND	$68.3 \pm 9.5$	$24.0 \pm 1.4$
	NIN	$9.8 \pm 1.6$	$2.9 \pm 1.2$	$87.2 \pm 1.4$	ND
	LMP	$7.9 \pm 1.7$	$3.7 \pm 0.1$	$67.1 \pm 1.6$	$21.3 \pm 3.4$

<sup>\*</sup>Note: ND – not detected (below the sensitivity level of the method).

volunteers, after VACV costimulation, was undetectable using this method.

In volunteers immunized with the OrtopoxVac at  $10^7$  PoFU, the production of CD4+IFN- $\gamma$ +TNF+IL-2+ T-helpers remained at its initial level at the 3-year point but decreased significantly by the 5-year point (*Fig. 6A*). For volunteers administered two doses of the OrthopoxVac vaccine ( $10^6$  PoFU), a significant reduction in VACV-specific T-helper cell levels was observed by the third year following vaccination, which persisted up to five years post-vaccination (*Fig. 6B*).

Three years post-immunization, the VACV-specific CD4+ T-cell population in all volunteer groups predominantly comprised effector memory  $T_{\rm EM}$  cells (CCR7-CD45RA-) at 80–90%, central memory  $T_{\rm CM}$  cells (CCR7+CD45RA-) at 5–10%,  $T_{\rm EMRA}$  (CCR7-CD45RA+) at 2–10%, and up to 1% of naïve T cells (CCR7+CD45RA+) (*Table 2*). Cell distribution based on the memory markers CCR7 (CD197) and CD45RA was typical of both volunteers vaccinated with the fourth-generation OrthopoxVac vaccine and those vaccinated using the two-stage method involving inactivated smallpox vaccine and first-generation LSV.

### **DISCUSSION**

The primary challenge when creating a novel small-pox vaccine is the necessity to attenuate the virulence of the VACV vaccine strain while ensuring an adequate and durable humoral and cellular immune response. The standards for determining the degree of immunity generated in humans following small-pox vaccination and that confers complete protection against orthopoxvirus infections have yet to be set. Only a limited number of publications have sought to define such criteria.

Historically, the first criterion for assessing the immune response to the Variola virus infection or VACV vaccination has been to determine VNA levels in the patients' sera. In a study by Mack et al. [17], individuals with a VACV VNA titer below 1:32 were found to be more prone to infection upon coming into contact with each other (20% of contacts became ill), in contrast to those with a VNA titer of 1:32 or higher (1% of contacts became ill). It was also observed that during an epidemic, smallpox was contracted by 14% of exposed, unvaccinated patients with VNA to VACV titers of < 1 : 20, whereas patients with VNA titers ≥ 1:20 did not contract the disease [18]. However, it is important to note that no previously vaccinated patients, including those with VNA titers < 1:10, not contracted smallpox by interacting with other patients. The protective power of a single injectable vaccinia immune globulin preparation has led to the conclusion that even low levels of VNA can provide a sufficient degree of protection against smallpox [19].

In addition to VNA, the cellular immune response plays a vital role in the defense against smallpox [15, 19–21]. However, at the time of smallpox eradication, the methodologies for assessing cell-mediated immune responses had not yet advanced that much. Therefore, criteria for a protective level of the T-cell response to smallpox vaccination have yet to be established [16, 22].

T cells are critical in the early stages of identification and suppression of viral infections, as well as in supporting B cells to produce antibodies. Given the crucial role of T cells, they represent a vital target in evaluating immune responses to an infection or vaccination.

Immunization with the smallpox vaccine generates enduring cell-mediated immune responses via CD4+ and CD8+ T cells, with peak numbers observed between two and four weeks following vaccination, followed by a drop, and ultimately a sustained, stable crop of memory T cells [23, 24]. It should be noted that the population of memory CD8+ T cells declines faster than that of memory CD4+ T cells [25]. The need for CD4+ T cells for purposes of protection is demonstrated by the absence of VACV-specific antibodies in animals that lack CD4+ T cells [26, 27]. Additionally, CD4+ T cells are vital for optimal cytotoxic T-lymphocyte functioning and immunologic memory formation [28].

A significant challenge in demonstrating the effectiveness of novel smallpox vaccines lies in the inability to directly prove that newly developed vaccines elicit protective immunity against smallpox in humans. Given the elimination of smallpox, assessing the efficacy of new vaccines against a naturally occurring disease is impossible. Alternatively, new vaccines undergoing clinical studies should be assessed against existing benchmarks and compared to the first-generation smallpox vaccines utilized in the initial eradication drive [16, 23].

On November 11, 2022, the Ministry of Health of the Russian Federation authorized OrthopoxVac, the first fourth-generation attenuated smallpox vaccine (a live culture vaccine for the prevention of smallpox and related orthopoxvirus infections based on the vaccinia virus). This vaccine was designed using the L-IVP VACV strain used in Russia as a first-generation smallpox vaccine (live smallpox vaccine) [2, 11]. A number of the genes in this strain were targeted for inactivation using genetic engineering methods. These included the genes encoding the gamma-interferonbinding protein (B8R), the complement-binding pro-

tein (C3L), the Bcl-2-like inhibitor of apoptosis (N1L), hemagglutinin (A56R), thymidine kinase (J2R) and the A35R gene, whose protein product inhibits the presentation of antigens by major histocompatibility complex class II, the immune priming of T-lymphocytes, and the subsequent synthesis of chemokines and cytokines. The VACV strain thus created was given the name VAC $\Delta6$  [11]. Following a series of preclinical studies [29] and subsequent phases I and II/III clinical studies (CS), the OrthopoxVac vaccine was deemed to be a safe and weakly reactogenic preparation, with immunologic activity comparable to that of the original Russian first generation smallpox vaccine.

At 60, 90, and 180 days after a double 10<sup>6</sup> PoFU dose of OrthopoxVac vaccine immunization, volunteer sera exhibited GMT VNA values of 79.4, 75.9, and 69.2, respectively. Following a single 10<sup>7</sup> PoFU injection of OrthopoxVac, the respective values were 138.0, 31.7, and 31.6. The GMT VNA values in sera from volunteers who had received the two-step vaccination regimen with the first-generation vaccine were 104.7, 52.5, and 63.1 at the specified time periods.

As is clear, a gradual decrease in VNA titers was observed over a 6-month period in all the vaccinated volunteer groups under study.

It should be noted that OrthopoxVac possesses higher immunogenicity compared to the third-generation MVA smallpox vaccine, which has become widespread in recent years [30]. An optimal immune response necessitates a two-dose administration of this non-replicating, attenuated vaccine. A clinical study has indicated that in the sera of two groups of volunteers immunized twice with liquid or lyophilized MVA preparations, the GMT values of VNA first stood at 45.2 and 77.6, respectively, 14 days after the second administration, before falling to 10.2 and 11.7, respectively, by day 180 [31].

According to the current guidelines in Russian "Conducting smallpox vaccination. MU 3.3.1.2044-06," the next revaccination of people from risk groups with the first-generation vaccine, except for those directly working with smallpox and monkeypox viruses, happens after 5 years. Those working with smallpox and monkeypox viruses are revaccinated after 3 years.

Due to the altered genetic program of the VACV strain  $VAC\Delta 6$ , as opposed to the original L-IVP strain, it was imperative to examine the length and strength of the post-vaccination immune response in the individuals who had received the OrthopoxVac vaccine. Previous investigations had only measured the development of the humoral immune response within six months post-vaccination, without assessing the production of VACV-specific CD4+ and CD8+

T-lymphocytes. This study has evaluated the humoral and T-cell responses to intradermal OrthopoxVac injections in phase II/III CS participants at the 1.5- and 3-year time points and in phase I CS participants at the 5-year time point, as well as compared them to those who had received the first-generation smallpox vaccine.

The humoral immune response was assessed using standard methods: ELISA for determining the specific antibody titer and VACV neutralization reaction on the cell culture.

ELISA-based assessment of VACV-specific antibody titers (*Fig. 3*) demonstrated notable inter-individual variability within each cohort, aligning with previously reported findings and potentially attributable to immune system-related genetic polymorphisms [13, 32, 33]. It is of significance that a notable VACV-specific humoral response was recorded both three and five years after immunization with the first-generation vaccine and the created fourthgeneration OrthopoxVac vaccine. At the same time, no significant differences were observed between the compared groups.

Following a period of 1.5 years post-immunization with the OrthopoxVac vaccine, VNA titers exhibited a drop in certain patients (Fig.~4A,B). It is worth noting that, when OrthopoxVac was administered at a dose of  $10^7$  PoFU, no significant differences were observed among the groups at 1.5, 3, and 5 years (Fig.~4A). However, VNA titers had significantly decreased after 1.5 years in the groups that received two immunizations at a dose of  $10^6$  PoFU (Fig.~4B).

Variations in the proportions of volunteers exhibiting VNA titers exceeding 1:10 at the 3- and 5-year post-vaccination intervals can be attributed to the differing volunteer cohorts involved in the phase II/III and phase I clinical studies, respectively.

Cytometric analyses performed on PBMC preparations of vaccinated volunteers 1.5 years after immunization revealed VACV-specific T cells, including both T helper (CD4+) and cytotoxic T lymphocytes (CD8+). The T-helper cells elicited a more significant cell-mediated immune response than the cytotoxic T-lymphocytes. The loads of CD8+ cells in both groups of volunteers inoculated with OrthopoxVac were notably higher than those in the positive control group (Fig. 5), which presumably can be attributed to the differences in the genetic programs of the recombinant VAC $\Delta6$  and initial L-IVP VACV strain.

Regardless of the dosage or administration method, the OrthopoxVac vaccine generated an effective T-helper cell-mediated immune response to orthopox-viruses 1.5 years after vaccination (*Fig.* 6).

Three years post-vaccination, the study of intracellular cytokines in volunteer PBMC preparations, costimulated with the attenuated VAC $\Delta 6$  VACV strain, revealed virus-specific T-cell immune responses exclusively in T-helper cells, regardless of whether first- or fourth-generation vaccines were used. VACV-specific cytotoxic T lymphocytes (CD8+) were detected in only one volunteer after twice administration of OrthopoxVac at a dose of  $10^6$  PoFU.

T-helper cells specific to VACV were found 3 and 5 years following OrthopoxVac vaccination. However, the strength of the immune response differed depending on the dosage and method of administration. In volunteers immunized with OrthopoxVac at a dose of 10<sup>7</sup> PoFU, the T-helper response stayed relatively elevated for three years before it substantial dropped. If patients had received two doses of the vaccine at 10<sup>6</sup> PoFU, a substantial reduction in T-helper cells was observed after 1.5 years (*Fig. 6*). The bulk of the specific T cells displayed the characteristics of memory effector cells (*Tables 1, 2*), suggesting they were in active interaction with the antigen.

Following the administration of the fourth-generation smallpox vaccine OrthopoxVac, all our volunteers, regardless of dosage or method of administration, experienced a cell-mediated immune response to VACV at the three and five-year intervals.

The findings here indicate that a single intradermal injection of the OrthopoxVac vaccine, at a dosage of 10<sup>7</sup> PoFU, triggers a significant and specific immune response, including both humoral and T-cell immunity, that persists for at least three years. Additional clinical studies are warranted to establish the most effective revaccination strategy with the OrthopoxVac vaccine, with the goal of achieving prolonged immunity against orthopoxvirus infections. ●

This work was conducted within the framework of the state assignment GZ-1/24 of State Research Center of Virology and Biotechnology "Vector", Rospotrebnadzor, Koltsovo (number of the state registration of R&D Reg. No. 124030100120-8).

### REFERENCES

- Fenner F., Henderson D.A., Arita I., Jezek Z., Ladnyi I.D. Smallpox and Its Eradication. Geneva: World Health Organization, 1988. 1460 p.
- Shchelkunova G.A., Shchelkunov S.N. // Viruses. 2023.
   V. 15. P. 103. doi: 10.3390/v15010103.
- Simon W.L., Salk H.M., Ovsyannikova I.G., Kennedy R.B., Poland G.A. // Immunotherapy. 2014. V. 6(10).
   P. 1097–1112. doi: 10.2217/imt.14.72.
- Shchelkunov S.N. // PLoS Pathog. 2013. V. 9. P. e1003756. doi: 10.1371/journal.ppat.1003756.
- Zhu M., Ji J., Shi D., Lu X., Wang B., Wu N., Wu J., Yao H., Li L. // Front. Med. 2022. V. 16. P. 507–517. doi: 10.1007/s11684-022-0952-z.
- Kumar S., Guruparan D., Karuppanan K., Kumar K.J.S. // Pathogens. 2024. V. 14. P. 1. doi: 10.3390/pathogens14010001.
- Shchelkunov S.N. // Vaccine. 2011. V. 29 (Suppl. 4).
   P. D49-D53. doi: 10.1016/j.vaccine.2011.05.037.
- 8. Olson V.A., Shchelkunov S.N. // Viruses. 2017. V. 9. P. e242. doi: 10.3390/v9090242.
- 9. Yakubitskiy S.N., Kolosova I.V., Maksyutov R.A., Shchelkunov S.N. // Acta Naturae. 2015. V. 7. P. 113–121.
- 10. Shchelkunov S.N., Yakubitskiy S.N., Titova K.A., Pyankov S.A., Shulgina I.S., Starostina E.V., Borgoyakova M.B., Kisakov D.N., Karpenko L.I., Shchelkunova G.A., Sergeev A.A. // Acta Naturae. 2024. V. 16. P. 82–89. doi: 10.32607/actanaturae.27384.
- 11. Yakubitskiy S.N., Kolosova I.V., Maksyutov R.A., Shchelkunov S.N. // Dokl. Biochem. Biophys. 2016. V. 466. P. 35–38. doi: 10.1134/S1607672916010105.
- 12. Perekrest V.V., Movsesyants A.A., Mukhacheva A.V., Shevtsov V.A., Shvedov D.V., Borisevich I.V. // Biopreparation (Biopharmaceuticals). 2013. № 2. P. 4–13.

- 13. Ermilova O.S., Gin'ko Z.I., Belyavskaya V.A., Kuzubov V.I., Sergeev Ar.A., Gorbatovskaya D.O., Azaev M.Sh., Agafonov A.P., Voevoda M.I., Sergeev A.N. // Problems of Particularly Dangerous Infections. 2015. № 1. P. 75–78. doi: 10.21055/0370-1069-2015-1-75-78.
- 14. Shchelkunov S.N., Yakubitskiy S.N., Sergeev A.A., Kabanov A.S., Bauer T.V., Bulichev L.E., Pyankov S.A. // Viruses. 2020. V. 12(8). P. 795. doi: 10.3390/v12080795.
- 15. Shchelkunov S.N., Shchelkunova G.A. // Acta Naturae. 2020. V. 12(1). P. 33–41. doi: 10.32607/actanaturae.10935.
- 16. Moss B. // Immunol. Rev. 2011. V. 239. P. 8–26. doi: 10.1111/j.1600-065X.2010.00975.x.
- Mack T.M., Noble J.Jr., Thomas D.B. // Am. J. Trop. Med. Hyg. 1972. V. 21(2). P. 214–218. doi: 10.4269/ajt-mh.1972.21.214.
- 18. Sarkar J., Mitra A., Mukherjee M. // Bull. World Health Organ. 1975. V. 52(3). P. 307–311.
- Hammarlund E., Lewis M.W., Hansen S.G., Strelow L.I., Nelson J.A., Sexton G.J., Hanifin J.M., Slifka M.K. // Nat. Med. 2003. V. 9. P. 1131–1137. doi: 10.1038/nm917.
- Hammarlund E., Lewis M.W., Hanifin J.M., Mori M., Koudelka C.W., Slifka M.K. // J. Virol. 2010. V. 84. P. 12754–12760. doi: 10.1128/JVI.01763-10.
- 21. Kunasekaran M.P., Chen X., Costantino V., Chughtai A.A., MacIntyre C.R. // Mil. Med. 2019. V. 184. P. e668. doi: 10.1093/milmed/usz181.
- Francis A. Ennis, John Cruz, Walter E. Demkowicz, Jr.,
   Alan L. Rothman, David J. McClain // J. Infect. Dis. 2002.
   V. 185. P. 1657–1659. doi: 10.1086/340517.
- 23. Jacobs B.L., Langland J.O., Kibler K.V., Denzler K.L., White S.D., Holechek S.A., Wong S., Huynh T., Baskin C.R. // Antiviral Res. 2009. V. 84. P. 1–13. doi: 10.1016/j. antiviral.2009.06.006.
- 24. Amanna I.J., Slifka M.K., Crotty S. // Immu-

- nol. Rev. 2006. V. 211. P. 320–337. doi: 10.1111/j.0105-2896.2006.00392.x.
- Amara R.R., Nigam P., Sharma S., Liu J., Bostik V. // J. Virol. 2004. V. 78. P. 3811–3816. doi: 10.1128/jvi.78.8.3811-3816.2004.
- Xu R., Johnson A.J., Liggitt D., Bevan M.J. // J. Immunol. 2004. V. 172. P. 6265–6271. doi: 10.4049/jimmunol.172.10.6265.
- 27. Edghill-Smith Y., Bray M., Whitehouse C.A., Miller D., Mucker E., Manischewitz J., King L.R., Robert-Guroff M., Hryniewicz A., Venzon D., et al. // J. Infect. Dis. 2005. V. 191. P. 372–381. doi: 10.1086/427265.
- 28. Sun J.C., Bevan M.J. // Science. 2003. V. 300. P. 339–342. doi: 10.1126/science.1083317.
- 29. Shchelkunov S.N., Yakubitskiy S.N., Nesterov A.E., Kolosova I.V., Sergeev A.A., Zaykovskaya A.V., Kabanov A.S., Nechaeva E.A., Bogryantseva M.P., Usova S.V., et al.

- // Epidemiology and Vaccinal Prevention. 2022. V. 21(6). P. 34–47. doi: 10.31631/2073-346-2022-21-6-34-47.
- 30. Volz A., Sutter G. // Adv. Virus Res. 2017. V. 97. P. 187–243. doi: 10.1016/bs.aivir.2016.07.001.
- 31. Frey S.E., Wald A., Edupuganti S., Jackson L.A., Stapleton J.T., El Sahly H., El-Kamary S.S., Edwards K., Keyserling H., Winokur P., et al. // Vaccine. 2015. V. 33. P. 5225–5234. doi: 10.1016/j.vaccine.2015.06.075.
- 32. Benhnia M.R., McCausland M.M., Su H., Singh K., Hoffmann J., Davies D.H., Felgner P.L., Head S., Sette A., Garboczi D.N., et al. // J. Virol. 2008. V. 82. P. 3751–3768. doi: 10.1128/jvi.02244-07.
- 33. Moutaftsi M., Tscharke D.C., Vaughan K., Koelle D.M., Stern L., Calvo-Calle M., Ennis F., Terajima M., Sutter G., Crotty S., et al. // Future Microbiol. 2010. V. 5. P. 221–239. doi: 10.2217/fmb.09.110.

# Test System for Studying Biotin Transport upon *SLC5A6* Gene Inactivation

A. Yu. Rudenko<sup>1,2\*</sup>, P. A. Zotova<sup>1,3</sup>, O. A. Averina<sup>1</sup>, A. V. Priymak<sup>1,2</sup>, M. P. Rubtsova<sup>3,4</sup>, S. S. Mariasina<sup>1,2,3,5</sup>, R. M. Ozhiganov<sup>1,6</sup>, O. A. Dontsova<sup>1,3,4,7</sup>, P. V. Sergiev<sup>1,3,7</sup>

<sup>1</sup>Belozersky Institute of Physico-Chemical Biology, Lomonosov Moscow State University, Moscow, 119192 Russia

<sup>2</sup>Faculty of Fundamental Medicine, Lomonosov Moscow State University, Moscow, 119192 Russia

<sup>3</sup>Department of Chemistry, Lomonosov Moscow State University, Moscow, 119192 Russia

<sup>4</sup>Shemyakin-Ovchinnikov Institute of Bioorganic Chemistry, Russian Academy of Sciences, Moscow, 117997 Russia

<sup>5</sup>Research and Educational Resource Center "Pharmacy", RUDN University, Moscow, 117198 Russia

<sup>6</sup>Higher Chemical College RAS, Mendeleev University of Chemical Technology, Moscow, 125190 Russia

<sup>7</sup>Center for Molecular and Cellular Biology, Skolkovo Institute of Science and Technology, Moscow, 121205 Russia

\*E-mail: RudenkoAY@my.msu.ru

Received: February 27, 2025; in final form, May 21, 2025

DOI: 10.32607/actanaturae.27645

Copyright © 2025 National Research University Higher School of Economics. This is an open access article distributed under the Creative Commons Attribution License, which permits unrestricted use, distribution, and reproduction in any medium, provided the original work is properly cited.

ABSTRACT This paper introduces a test system for the investigation of biotin transport following inactivation of the SLC5A6 gene, which encodes the sodium-dependent multivitamin transporter SLC5A6. The aim was to develop a method for assessing the efficiency of biotin penetration across the cell membrane following inactivation of the SLC5A6 gene and to explore the feasibility of delivering biotin derivatives into cells independent of SLC5A6. The test system is built upon modified HEK293 cell lines with overexpression of the BirA\* biotin ligase, with the first line comprising a functional SLC5A6 gene and the second one involving an inactivated version of this gene mimicking impaired biotin transport. This test system was used to investigate the transport of biotin and its two derivatives, namely the biotin conjugate with p-aminophenylalanine (Bio-1) and biotin methyl ester (Bio-2), through the cell membrane. It has been determined that biotin and its methyl ester (Bio-2) can enter cells independently of the SLC5A6 transporter, which points to the presence of alternative transport pathways. The biotin derivative Bio-1, which contains p-aminophenylalanine, is internalized into cells solely through the hSMVT transporter. The novel test system will serve as a tool for investigating the pathways involved in vitamin entry into cells and for developing therapeutic strategies for individuals with mutations in the SLC5A6 gene, as well as other transport-related genes.

KEYWORDS biotin, SLC5A6, hSMVT, biotin transport, cell membrane, test system, biotin derivatives.

ABBREVIATIONS Strep-HRP – streptavidin conjugated with horseradish peroxidase; SLC5A6 or SMVT – so-dium-dependent multivitamin transporter; BirA\* – mutant biotin ligase from E. coli (BirA R118G); PBS – phosphate-buffered saline; GFP – green fluorescent protein.

### **INTRODUCTION**

The *SLC5A6* gene, located at locus 2p23.3 of human chromosome 2, encodes a membrane-bound sodium-dependent multivitamin transporter (SMVT). The human hSMVT protein is composed of 635 ami-

no acid residues and is essential for the transport of water-soluble compounds such as biotin, pantothenic acid, and alpha-lipoic acid [1]. The SMVT protein demonstrates significant evolutionary conservation and is prevalent throughout the organism. This pro-

tein is most actively expressed in intestinal epithelium and brain capillary endothelial cells [2, 3]. It is also involved in the transport of biotin and pantothenic acid across the blood-brain barrier [4]. SMVT function is crucial for the typical growth and development of mammals, including humans, given that mammalian cells do not synthesize biotin and pantothenic acid, which only enter the body through the intestine [5, 6]. Biotin, a coenzyme for five carboxylases, plays a role in several metabolic functions, specifically fatty acid synthesis, gluconeogenesis, and amino acid catabolism [7]. Biotin also affects gene expression, as well as cell proliferation and survival [8, 9]. Pantothenic acid is essential for coenzyme A biosynthesis and fatty acid synthesis, which are crucial for energy metabolism and hormone synthesis [10].

In vivo investigations in mice indicate that the inactivation of the Slc5a6 gene in intestinal cells results in growth retardation, decreased bone density, and reduced bone length, along with changes in the small intestine (villi shortening, dysplasia) and cecum (chronic inflammation, dysplasia) [6]. Therapy involving elevated dosages of biotin and pantothenic acid forestalls growth retardation and intestinal inflammation [11].

Biallelic mutations in the *SLC5A6* gene have been observed in children with growth and developmental delays, seizures, gastrointestinal, skin, and peripheral nervous system disorders, and immunodeficiency resulting from impaired T- and B-cell function [12–18]. Clinical improvements were noted in these children, who were predisposed to infant death, after they had undergone targeted treatment with vitamins to *SLC5A6* gene mutation carriers [13–15, 18].

For example, whole exome sequencing of a 15-month-old boy with developmental delay, microcephaly, severe immunodeficiency, and severe gastroesophageal reflux disease revealed a mutation in the *SLC5A6* gene. At 19 months of age, the child received vitamin therapy involving high doses of biotin (10 mg/day, then 30 mg/day), pantothenic acid (250 mg/day, then 500 mg/day), and lipoic acid (150 mg/day, then 300 mg/day), with the vitamin dosages subsequently increased at 24 months. Following 14 months of therapy, the immunoglobulin levels were normalized and no bone system abnormalities remained. Comparable clinical improvement was observed in other pediatric patients who were administered high doses of biotin [19, 20].

According to our analysis of published data, studies on vitamins have not assessed the effectiveness of their absorption, distribution, and metabolism. Only a few methods are currently available for the assessment of vitamin permeation efficiency across the

membrane. Typically, tritium or carbon-14 isotopes are used to label biotin for this application [21]. This methodology offers enhanced sensitivity in detecting and quantifying biotin distribution, although it requires specialized equipment for handling radioactive substances. Furthermore, this method does not facilitate the evaluation of membrane permeation of biotin derivatives, which usually do not possess a radioactive label. Biotin quantification can also be achieved using mass spectrometric analysis, which, nonetheless, requires the use of advanced analytical instruments and time-intensive procedures.

This study aimed to create a method for assessing the effectiveness of biotin permeation through the cell membrane following inactivation of the SLC5A6 gene. Further, we examined the possibility of delivering biotin derivatives into cells independently of SLC5A6, which could provide new avenues for patient treatment in cases of SLC5A6 gene mutations.

We have developed a test system to assess the efficacy of biotin penetration through the cell membrane following inactivation of the *SLC5A6* gene. The system relies on the inhibition of biotin-carrying cellular proteins through the utilization of streptavidin and a horseradish peroxidase conjugate. Biotinylation is artificially enhanced through the application of a mutant BirA biotin ligase with reduced specificity.

The test system involves modified HEK293 cell lines that overexpress the BirA\* biotin ligase. One of the lines contains a functional *SLC5A6* gene, while in the other line this gene is inactivated. The *SLC5A6* gene is inactivated to simulate a state where biotin transport via hSMVT is impeded. The ectopic expression of biotin ligase results in the nonspecific biotinylation of proteins within the cell, which can be identified using Western blotting. Assessment of protein biotinylation levels in the cell lines following incubation with biotin or its derivatives facilitates the detection of biotin transport across the cell membrane.

The developed system was used to study the transport mechanism across the cell membrane of biotin and its two derivatives: biotin conjugate with p-aminophenylalanine (Bio-1) and biotin methyl ester (Bio-2).

### **EXPERIMENTAL PART**

### Oligonucleotide synthesis

All oligonucleotides (primers) were synthesized by Lumiprobe RUS LLC (Russia).

### **Cell cultivation**

Wild-type (WT), as well as modified (BirA\*,  $\Delta SLC5A6$ , and BirA\*\_ $\Delta SLC5A6$ ) HEK293, cells were cultured in a DMEM/F12 medium (Gibco, USA) supplement-

ed with 10% (v/v) fetal calf serum (FBS HI, Gibco), 1% (v/v) L-alanine-L-glutamine (2 mM, GlutaMAX, Gibco), a 1% (v/v) antibiotic mixture (100 units/mL penicillin and 100  $\mu$ g/mL streptomycin, Gibco) at 37°C and 5% CO $_2$ . The cells were cultivated in culture vials designed for adherent cells (25 cm²). Once the cells reached 90-100% confluency, they were split at a 1 : 10 ratio, rinsed with PBS, then detached using a trypsin-EDTA solution (1×, Gibco) in PBS, and, finally, resuspended in a fresh medium to achieve the required cell density. For the experiments, the cells were cultured in 24-well plates.

### Introduction of the BirA\* gene

Cells with increased biotinylated protein levels were obtained by introducing the mutant  $E.\ coli$  BirA<sup>R118G</sup> biotin ligase (BirA\*) into the cells. The cell selection process involved the introduction of the BirA\* gene, along with the eGFP gene, which encodes a green fluorescent protein from jellyfish, optimized for mammalian cells. The BirA\* and eGFP genes were inserted using the plasmid pSBbiGN\_BirA\*, which was constructed previously [22] based on the pSBbiGN vector (Addgene #60517) [23].

Wild-type (WT) HEK293 cells were transfected with plasmid pSBbiGN\_BirA\* and plasmid pCMV(CAT)T7-SBX100 [24] that encodes a transposase, using Lipofectamine 3000, following the manufacturer's guidelines. At 24 hours post-incubation, cells producing BirA\* and eGFP were selected using a FACSAria III BD sorter and the signal was recorded at 488/530 nm. The selected cells were seeded into 96-well plates (200  $\mu$ l of medium per well), followed by culturing of individual clones in 24-well plates. The resulting monoclonal cells exhibited a stable BirA\* and GFP expression.

### Inactivation of the SLC5A6 gene

The *SLC5A6* gene in WT and BirA\* cell lines was inactivated using the CRISPR-Cas9 system. The sgRNA sequences were selected for cleavage using the Benchling CRISPR design tool (https://benchling.com). The selection was made of a guide RNA targeting exon 8 of the *SLC5A6* gene (5'-GCGGTACCTCAGTCAGTCCGCA-3').

The pX459-SLC5A6 construct, designed for inactivation, was derived from the pSpCas9(BB)-2A-Puro plasmid (pX459 V2.0, Addgene #62988 [25]), which includes CRISPR/Cas9 system elements and a puromycin resistance gene. The plasmid was pre-cleaved with BpiI endonuclease to generate sticky ends.

The guide RNA-encoding sequence was synthesized from two DNA oligonucleotides (5'-CACCACCGCGGCGGTACCTCAGTTCC-

CGCA-3′ and 5′-AAACTGCGGCGGGAACTGAGGAGGTACCGC-3′) designed to generate complementary sticky ends (4 nucleotides) after hybridization, which would then be compatible with the sticky ends on the pX459 vector. Oligonucleotides were hybridized within a T4-DNA ligase buffer (Thermo Scientific, USA), with each added to a concentration of 1  $\mu$ M, and then incubated at 95°C for 5 minutes, followed by gradual cooling to 30°C in a closed thermostat. The resulting duplex (1  $\mu$ l) was ligated at sticky ends into the pX459 vector using the Rapid DNA Ligation Kit (Thermo Fisher, USA).

Following transfection of competent  $\it E.~coli$  JM109 cells with the ligase mixture, the colonies were cultivated on ampicillin-supplemented plates (50  $\mu g/mL$ ). Plasmid DNA was purified from overnight cultures, using the Plasmid Miniprep kit (Eurogen, Russia). Sanger sequencing, with a primer positioned on the U6 promoter (5'-GACTATCATCATATGCTTACCGT-3'), confirmed the correct insertion.

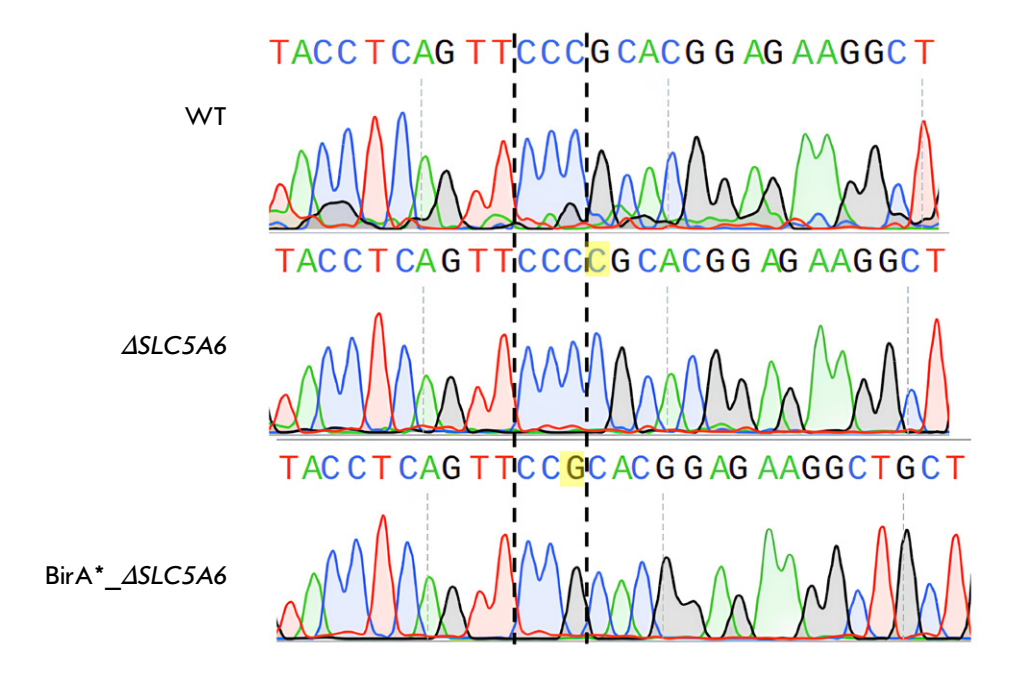
In order to generate cell lines with gene-specific knockouts, the cells were transfected with plasmid pX459-SLC5A6, using the LipofectamineTM 3000 reagent (Invitrogen\*\*: L3000001). The transfection protocol employed 100,000 cells, 1  $\mu g$  of plasmid, and 1.5  $\mu$ l of lipofectamine. After a 24-h incubation, the culture medium was replaced with a fresh medium including puromycin (1  $\mu g/mL$ ). In parallel, wild-type HEK293 control cells were incubated in a medium containing puromycin, and after 48 h, cell death was observed in all the control cells. Cells transfected with the pX459-SLC5A6 plasmid were seeded into 96-well plates (200  $\mu L$  medium per well), followed by individual clone culture in 24-well plates.

Monoclonal lines were genotyped using total DNA extracted from the cells (QuickExtract DNA Extraction Solution, Lucigen). Subsequently, the region within the predicted cleavage site was amplified via PCR (PCR primers: 5'-CTTCTG-GACCTTGGACCTTGGCCTTCGG-3' and 5'-GACCTTGCTCCACTCCACTCCCTTC-3'). Sanger sequencing of amplified fragments confirmed the presence of a mutation that resulted in inactivation of the SLC5A6 gene (Fig. 1). Consequently, cell lines with disrupted SLC5A6 reading frames were chosen for additional investigation, with a 1 bp insertion identified in the  $\Delta SLC5A6$  line and a 1 bp deletion identified in the BirA\*  $\Delta SLC5A6$  line.

### Synthesis of Bio-1

Biotin (1.74 g, 7.13 mmol), HATU (2.71 g, 7.13 mmol), and DIPEA (2.49 mL, 14.27 mmol) were dissolved in 15 mL of anhydrous DMF via sonication. In a sepa-

Fig. 1. Inactivation of the *SLC5A6* gene in HEK293 cells. Sanger sequencing results of the PCR-amplified target locus in the *SLC5A6* gene are shown for wild-type (WT) cells, knockout cells (Δ*SLC5A6*, 1 bp insertion), and cells with the BirA\* construct insertion (BirA\*\_Δ*SLC5A6*, 1 bp deletion)



rate flask, a solution of 4-aminophenylalanine (2 g, 7.13 mmol) in 5 mL DMF was prepared. The biotin solution was introduced into the amino acid solution using a syringe pump with strong stirring for over an hour. Then the DMF was removed under vacuum. Under stirring, 100 mL of water was added to the residue, which was then left for one hour to precipitate. The precipitate was filtered, rinsed with  $\rm H_2O$  (2 × 100 mL), and then air-dried. Thus, Product 2, gray in color (3.1 g, 86%), was obtained.

Bio-1

Scheme 1. Synthesis of the Bio-1 compound

<sup>1</sup>**H-NMR** (600 MHz, DMSO- $d_6$ ) δ = 9.8 (s, 1H), 7.5 (d, J = 8.0, 2H), 7.1 (d, J = 8.0, 2H), 7.0 (d, J = 8.3, 1H), 6.4 (s, 1H), 6.4 (s, 1H), 4.3 (t, J = 6.8, 1H), 4.3–4.1 (m, 1H), 4.1–4.0 (m, 1H), 3.2–3.1 (m, 1H), 3.0–2.9 (m, 1H), 2.9–2.7 (m, 2H), 2.6 (d, J = 12.4, 1H), 2.3 (t, J = 7.1, 2H), 1.7–1.5 (m, 3H), 1.5–1.5 (m, 1H), 1.4–1.3 (m, 1H), 1.3 (s, 9H), 1.3–1.2 (m, 1H). <sup>13</sup>**C-NMR** (151 MHz, DMSO- $d_6$ ) δ = 173.8, 173.6, 171.0, 162.7, 155.4, 137.7, 132.5, 129.3, 118.9, 78.0, 61.1, 59.2, 55.4, 55.3, 36.2, 35.9, 28.2, 28.2, 28.1, 25.2.

Product 2, which was obtained in the preceding reaction (3 g, 5.9 mmol), was dissolved in 4 M HCl/dioxane (60 mL). The stirring of the reaction mixture for 5 h yielded a suspension. Following filtration, the precipitate was washed with  $\rm Et_2O$  (2  $\times$  50 mL) and airdried, producing colorless **Bio-1** hydrochloride (2.6 g, 98%).

<sup>1</sup>**H-NMR** (600 MHz,  $D_2O$ ) δ = 7.4 (d, J=8.1, 2H), 7.3 (d, J = 8.1, 2H), 4.6–4.5 (m, 1H), 4.4 (dd, J = 8.0, 4.5, 1H), 4.3 (t, J = 6.7, 1H), 3.4–3.3 (m, 2H), 3.2 (dd, J = 14.8, 7.7, 1H), 3.0 (dd, J = 13.0, 4.8, 1H), 2.7 (d, J = 13.0, 1H), 2.4 (t, J = 7.3, 2H), 1.7 (tt, J = 14.8, 7.1, 3H), 1.6–1.5 (m, 1H), 1.5–1.4 (m, 2H). <sup>13</sup>**C-NMR** (151 MHz,  $D_2O$ ) δ = 176.4, 171.9, 165.9, 137.1, 131.6, 130.8, 123.2, 62.7, 60.9, 56.0, 54.6, 40.3, 36.8, 35.7, 28.5, 28.3, 25.7.

### Synthesis of Bio-2

Biotin (1 g, 4.1 mmol) was dissolved in 20 mL of methanol, then cooled to 0°C, and thionyl chloride

Scheme 2. Synthesis of the Bio-2 compound

(2 mL, 20 mmol) was subsequently added dropwise. The reaction mixture was stirred at  $20^{\circ}\mathrm{C}$  for 10 h, and the solvent was removed in vacuo. The residue was neutralized using 1 M NaHCO $_{3}$ . The precipitate was filtered off, washed with water, and dried in air, yielding Bio-2 (939 mg, 91%) after recrystallization from acetone.

The Bio-2 spectral data were consistent with those described previously [26].

<sup>1</sup>**H-NMR** (600 MHz, DMSO- $d_6$ ) δ = 6.4 (s, 1H), 6.4 (s, 1H), 4.4–4.3 (m, 1H), 4.2–4.1 (m, 1H), 3.6 (s, 3H), 3.2–3.0 (m, 1H), 2.8 (dd, J=12.4, 5.1, 1H), 2.6 (d, J=12.4, 1H), 2.3 (t, J=7.5, 2H), 1.7–1.4 (m, 4H), 1.4–1.2 (m, 2H). <sup>13</sup>**C-NMR** (151 MHz, DMSO- $d_6$ ) δ = 173.3, 162.7, 61.0, 59.2, 55.3, 51.2, 39.8, 33.1, 28.1, 28.0, 24.5.

### Western blotting

Protein biotinylation efficiency was assessed at varying biotin concentrations using HEK293 WT, BirA\*,  $\Delta SLC5A6$ , and BirA\*\_ $\Delta SLC5A6$  cell lines to determine the optimal concentration. Cells from each cell line were seeded into a 24-well plate and then incubated for 24 h. Subsequently, either an aqueous solution of biotin at the appropriate concentration or a control solution (water) was added to the culture medium. The cells were further incubated with biotin for 24 h. Afterward, the cells were lysed on ice using RIPA buffer containing benzonase (Sigma, USA) for 15 minutes and the enzyme was inactivated by heating at 80°C for 3 minutes.

Western blotting was employed to analyze diluted lysates, with normalization for total protein content. Electrophoretic separation of proteins was performed in a 10% polyacrylamide gel with 0.1% SDS, followed by transfer to a nitrocellulose membrane using wet transfer (1 h at 400 mA). The membrane was blocked using a 5% skim milk powder solution [27] in TBST (1–12 h), followed by incubation for 1 h at room temperature with a streptavidin-peroxidase conjugate solution (1 : 3000 in TBST, "IMTEK", P-S Avs, Russia). Following sequential washes with TBST (3 × 5 min), TBS (3 × 5 min), and distilled water, detection was performed using the Clarity Western ECL substrate (Bio-Rad).

### **RESULTS AND DISCUSSION**

The impact of the functional activity of the multivitamin transporter SLC5A6 on biotin internalization was evaluated using the human embryonic kidney cell line HEK293. The SLC5A6 gene was inactivated in this cell line using the CRISPR/Cas9 system, resulting in the generation of the  $\Delta SLC5A6$  cell line.

## Maintenance of biotinylated biotin-dependent carboxylases in the HEK293 cell line does not require the SLC5A6 transporter

The efficiency of biotin transport across the cell membrane was assessed by comparing the levels of biotinylated proteins in the HEK293 WT and  $\Delta SLC5A6$ cell lines. To this end, cells were incubated with biotin at different concentrations, after which biotinylated proteins were visualized by Western blotting using the streptavidin-peroxidase conjugate (Strep-HRP, Fig. 2). No change in the level of biotinylation was observed following the inactivation of the SLC5A6 gene. We hypothesize that this may be due to transmembrane diffusion or endocytosis of biotin during the 24-h incubation, resulting in its comparatively elevated intracellular concentration. Moreover, other transporters, such as monocarboxylate transporter 1 (MCT1), could be involved in delivering biotin across the cell membrane [28-30]. It should be noted that Subramanian V.S. et al. formulated a hypothesis on vitamin diffusion through the membrane, which provides a rationale for the effectiveness of biotin and pantothenic acid therapy in patients with deficient multivitamin transporters [15].

## Test system for monitoring biotin permeation through the cell membrane

Having determined that the functioning of the multivitamin transporter SLC5A6 was not a factor limiting

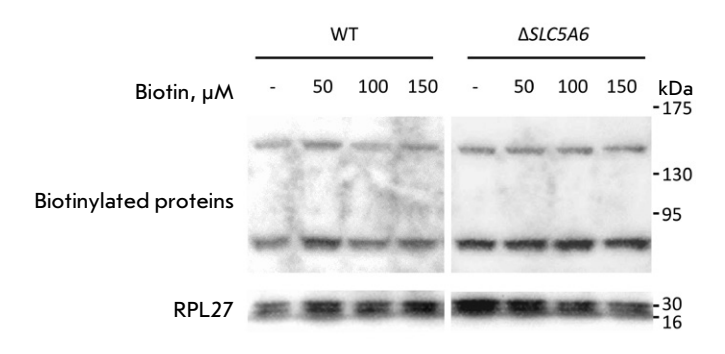


Fig. 2. Western blotting results for HEK293 WT (left) and  $\Delta SLC5A6$  (right) cell lines incubated with different concentrations of biotin (50, 100, and 150  $\mu$ M)

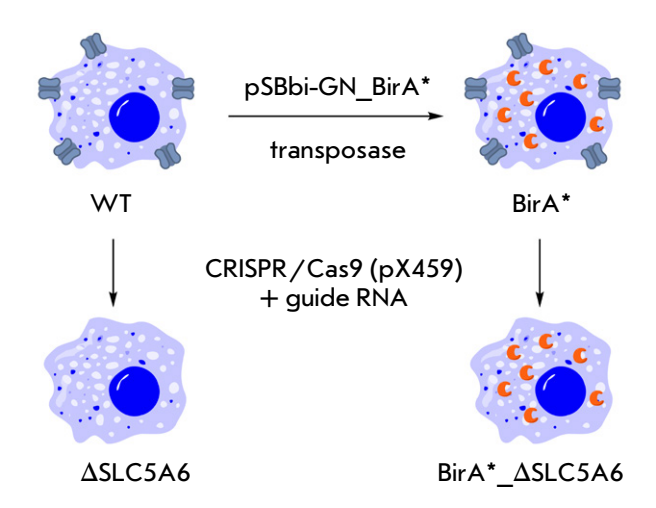


Fig. 3. Generation of HEK293-derived cell lines. Cells with increased levels of biotinylated proteins (BirA\* line) were generated by introducing the mutant biotin ligase BirA\*. The BirA\* gene was integrated into the genome using the pSBbi-GN\_BirA\* plasmid with the aid of a transposase. Inactivation of the SLC5A6 gene in WT and BirA\* cell lines was performed using the CRISPR-Cas9 system with the pX459 vector carrying a guide RNA targeting exon 8 of the gene. As a result, \( \Delta SLC5A6 \) and \( \text{BirA\*} \) \( \Delta SLC5A6 \) lines were obtained

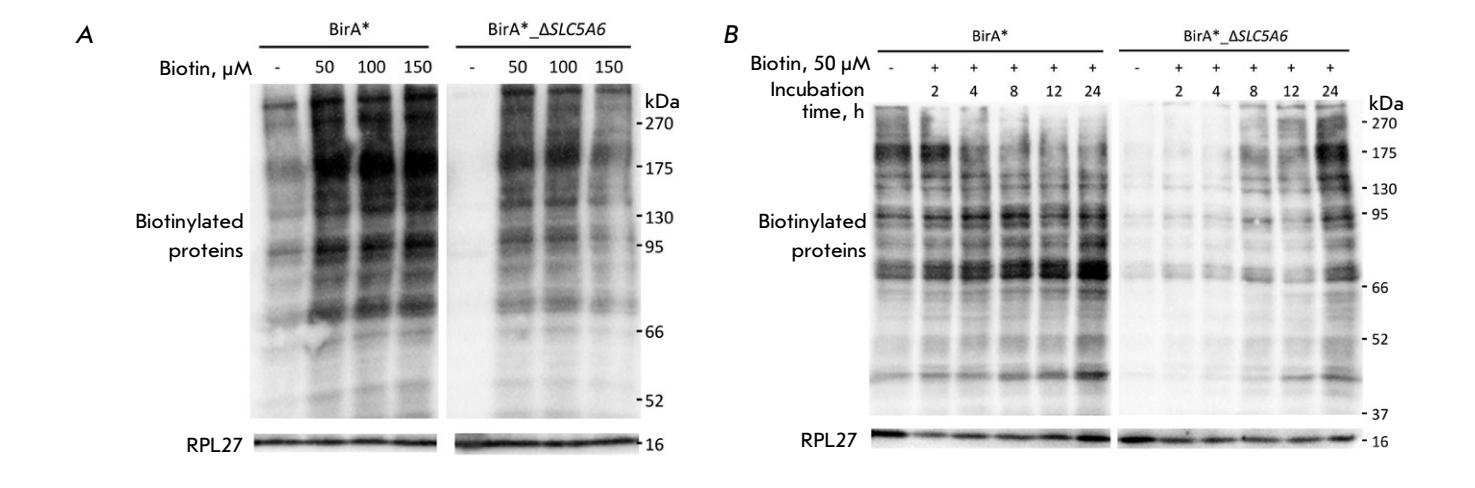


Fig. 4. Assessment of protein biotinylation levels in BirA\* and BirA\*\_\Delta\Lambda\LC5A6 cells. (A) Dependence of the protein biotinylation level on biotin concentration in the medium after 24-h incubation. (B) Dependence of the protein biotinylation level on incubation time

biotin entry into cells in culture at the natural biotinylated protein content, we decided to create cell lines with artificially increased biotinylation levels.

To this end, two additional cell lines were generated from HEK293 cells (Fig. 3).

The *BirA*\* gene, encoding a mutant *E. coli* BirA<sup>R118G</sup> biotin ligase, was introduced into HEK293 cells using a Sleeping beauty transposase-based vector (SB100X) [31, 32]. This enzyme mediates the indiscriminate

binding of biotin to lysine residues found in the protein. Consequently, the biotin that enters the cell is quickly used to biotinylate proteins that do not typically bind biotin. The level of biotinylated proteins in the cell enables one to estimate the rate of biotin penetration through the membrane.

Next, we introduced an inactivating mutation into the *SLC5A6* gene, which encodes the hSMVT protein. This enabled us to compare the biotinylation process

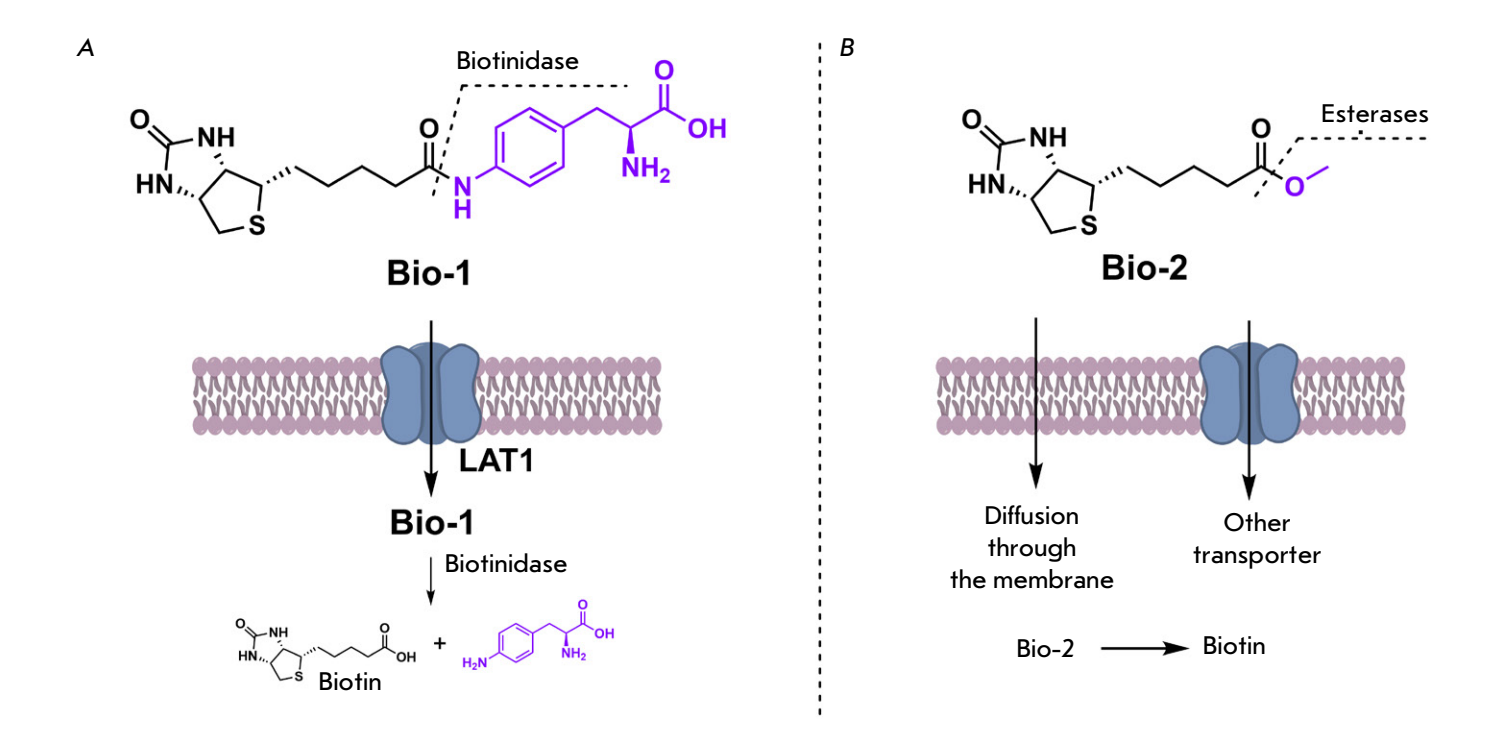


Fig. 5. Synthesized biotin analogs Bio-1 (A) and Bio-2 (B), with the proposed mechanism of membrane transport and subsequent enzymatic cleavage leading to the release of free biotin

in cells with active and inactive hSMVT transporters. The BirA\*\_ $\Delta SLC5A6$  line was created by introducing an inactivating mutation into cells containing the BirA\* gene using CRISPR/Cas9 technology (Fig. 3), which was similar to how the  $\Delta SLC5A6$  line was generated from wild-type cells.

## Assessment of biotin transport efficiency across the cell membrane using the test system

After establishing lines with ectopic expression of the nonspecific biotin ligase BirA\*, we decided to determine the optimal biotin concentration in the medium suitable for detecting the transport of this vitamin. To this end, we incubated BirA\* and BirA\*\_ΔSLC5A6 cell lines with different concentrations of biotin: 0, 50, 100, and 150 µM (Fig. 4A) for 24 h. Both lines exhibited a significant difference in biotinylation levels when biotin was absent and at a concentration of 50 µM, followed by saturation and a further increase in biotin concentration, which did not increase biotinylation levels. Consequently, a concentration of 50 µM is the optimal concentration for the evaluation of biotin transport. Furthermore, even in the absence of specifically added biotin, the level of biotinylation was lower in cells with inactivated hSMVT than in cells with the active transporter.

Extended incubation with biotin correlated with augmented biotinylation (Fig. 4B), and notable disparities were evident relative to the presence of the SLC5A6 gene. In the first few hours of incubation, the maximum level of biotinylation in the BirA\* cell line was already achieved. Concurrently, in BirA\*\_ $\Delta SLC5A6$  cells exhibiting compromised biotin transport, the accumulation of biotinylated proteins was decelerated, achieving a comparable level to the maximum observed in BirA\* cells after a 24-h delay. These data suggest that hSMVT plays a critical role in biotin transport, potentially influencing the development of pathological conditions in patients with mutations in this gene.

### Synthesis of biotin derivatives for cell penetration

The rationale for synthesizing biotin derivatives involved modifying their molecular properties to enable cell entry via alternative pathways that bypass the hSMVT transporter, which could broaden therapeutic options for individuals with SLC5A6 gene mutations. Two approaches were taken into consideration to accomplish this task.

The first approach to delivering the molecule bypassing SLC5A6 is to create hybrid molecules (prodrugs) comprising a therapeutic part and a compo-

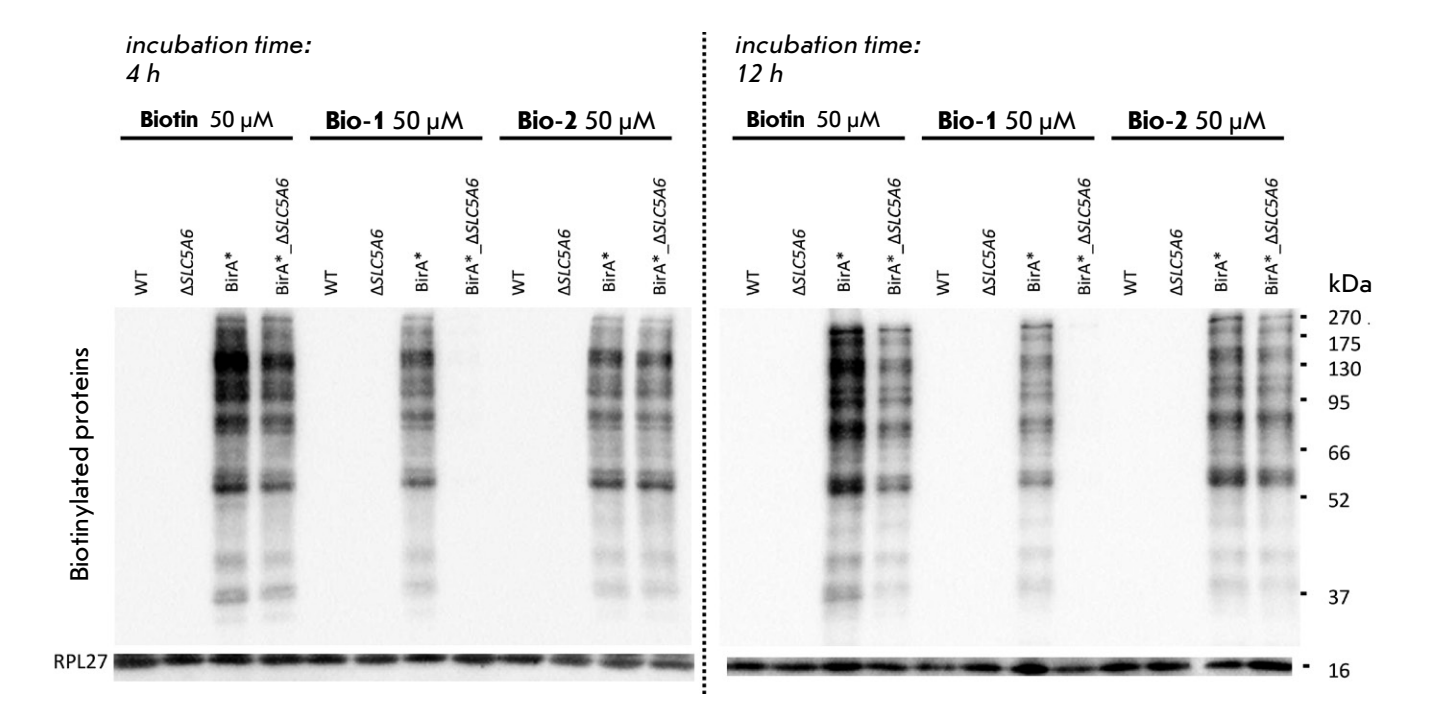


Fig. 6. Comparison of protein biotinylation levels in various cell lines after incubation with biotin, Bio-1, and Bio-2

nent that mimics a useful metabolite capable of being recognized by a specific transporter. For example, the LAT1 (Large Amino Acid Transporter-1) transporter has been successfully used to deliver ketoprofen and ferulic acid to neurons, as well as some drugs to tumor cells [33-35]. This process involves the modification of the therapeutic molecules by conjugating them to amino acids, which are LAT1 substrates. To evaluate the performance of this approach, we synthesized a biotin derivative of p-aminophenylalanine (Bio-1, Fig. 5A, Scheme 1). Our hypothesis was that upon intracellular delivery of this substance, the biotinidase enzyme would promote the release of biotin in its free form (Fig. 5A), as observed when biotinidase cleaves N-biotinyl-4-aminobenzoic acid into biotin and p-aminobenzoic acid [36, 37].

The second approach is to reduce the polarity of the molecule. This could either enable free diffusion of the molecule across the membrane or activate a different transporter, which would render hSMVT unnecessary. We synthesized a biotin methyl ester (**Bio-2**) that exhibits enhanced hydrophobicity. After entering the cell, biotin can be released by the action of esterases (*Fig. 5B, Scheme 2*).

## Transport efficiency of biotin and its derivatives across the cell membrane

Cellular permeability of biotin and its derivatives was assessed by incubating biotin, Bio-1, or Bio-2 with HEK293 (WT),  $\Delta SLC5A6$ , BirA\*, and BirA\*\_ $\Delta SLC5A6$  cell lines. All three molecules were shown to serve as a source of biotin in cells with a functional hSMVT transporter. Hence, no disparities in protein biotinylation levels were apparent in wild-type cells exposed to biotin, Bio-1, and Bio-2 (data not shown).

When cells with ectopic expression of BirA\* biotin ligase were used, the level of protein biotinylation increased manifold. Under these conditions, each of the three molecules can be used to transport biotin into the cell (*Fig.* 6, BirA\* line). A modest reduction in membrane permeation rates was observed for Bio-1 and Bio-2 compared to biotin. In all cases, saturation was observed after 4 h of incubation.

Upon hSMVT inactivation, biotin entry into the cell was reduced. After both 4 h and 12 h of incubation, the level of biotinylated proteins in  $BirA^*\_\Delta SLC5A6$  cells was observed to be lower than in  $BirA^*$  cells.

The cell incubation with Bio-1 yielded surprising outcomes: inactivating hSMVT prevented the

increase of biotinylated proteins in cells even after 12 h of Bio-1 exposure (Fig. 6, BirA\*\_ΔSLC5A6 cells), but biotinylation remained high when a functional transporter was present (Fig. 6, BirA\* line). Based on these findings, it is reasonable to conclude that the transport mechanism of Bio-1 does not involve LAT1, contrary to the initial hypothesis. The molecule in question probably can enter the cell solely through hSMVT participation, accounting for the high biotinylation level in BirA\* cells and the absence thereof when the SLC5A6 gene is inactivated. Therefore, the effect we observed was contrary to our expectations. It was found that biotin can enter cells through several pathways, with the pathway via hSMVT being only one of many. In contrast, the Bio-1 derivative proved unable to use the transport pathway available to biotin and could enter cells only via hSMVT.

Conversely, when cells were incubated with Bio-2, the disparity in protein biotinylation between  $BirA^*\_\Delta SLC5A6$  cells and  $BirA^*$  cells was negligible. These data indicate that the cellular penetration of the Bio-2 compound does not rely on the hSMVT transporter.

These findings suggest that biotin within the Bio-1 molecule is crucial for transporting related fragments via hSMVT. At the same time, p-aminophenylalanine coupled with biotin does not affect transport via hSMVT, but it does interfere with other transport pathways. This property finds application in targeted drug delivery into cells [38, 39] in the form of a biotin conjugate. The hSMVT protein is believed to be essential for the transport of these drugs. However, despite extensive research, several questions regarding the mechanism of transport of these conjugates remain unanswered [30]. For instance, research [40] has shown that an unbound carboxyl group in the biotin compound is necessary for its effective movement through the SMVT. Nevertheless, in studies positing SMVT-mediated prodrug transport, biotin was attached to the conjugate only through the carboxyl group [30]. Our findings also indicate that the free carboxyl group of biotin is not required for the transport of biotin derivatives via hSMVT.

The newly developed test system enabled us to demonstrate that biotin and its methyl ester Bio-2

could be transported into cells without the involvement of hSMVT. We anticipate that our test system will be instrumental in developing biotin-containing prodrugs.

### CONCLUSION

This work introduces a new system for monitoring the cellular transport of biotin and its derivatives. This system offers an alternative to intricate methodologies involving radioactively labeled biotin.

Using this novel test system, we determined that biotin and its methyl ester (Bio-2) can permeate cells independently of the hSMVT transporter, encoded by the *SLC5A6* gene, implying the existence of other methods of transportation. However, as cellular biotin demands increase, hSMVT becomes critical for efficient delivery.

The cellular uptake of the biotin conjugate with p-aminophenylalanine (Bio-1) is mediated solely by hSMVT, rendering it incompatible with alternative delivery pathways. Nevertheless, this specificity enables hSMVT to be used to transport other compounds into cells when conjugated with biotin. The developed test system is an important tool for investigating the process of vitamin uptake by cells, potentially enabling the development of treatment strategies and the assessment of drug efficacy in patients with SLC5A6 gene mutations and other transporter deficiencies.  $\bullet$ 

This study was supported
by the grant No. 24-S04-13
from the Moscow State University Scientific Schools
(Moscow, Russia): "Personalized Mice:
Creation and Study of Accurate Mouse
Models of Genetically Determined Diseases",
as well as by a state assignment from Lomonosov
Moscow State University.

The authors would acknowledge
the Moscow State University Development Program
for granting access to the CelenaX
and SeqStudio instruments, which facilitated
the analysis of transfection, cell growth,
and the sequencing of genetic constructs.

### REFERENCES

- 1. Yee SW, Wang J, Giacomini KM. Rare Diseases linked to mutations in vitamin transporters expressed in the human blood-brain Barrier. *Clin Pharmacol Ther*. 2024;116(6):1513–1520. doi: 10.1002/cpt.3433
- 2. Uchida Y, Ito K, Ohtsuki S, Kubo Y, et al. Major involvement of Na<sup>+</sup>-dependent multivitamin transporter (SLC5A6/SMVT) in uptake of biotin and pantothenic acid by human brain capillary endothelial cells. *J Neurochem*. 2015;134(1):97–112. doi: 10.1111/jnc.13092
- 3. Subramanian VS, Marchant JS, Boulware MJ, et al. Membrane targeting and intracellular trafficking of the human sodium-dependent multivitamin transporter in polarized epithelial cells. *Am J Physiol Cell Physiol*. 2009;296(4):C663–C671. doi: 10.1152/ajpcell.00396.2008
- 4. Neophytou C, Pitsouli C. Biotin controls intestinal stem cell mitosis and host-microbiome interactions. *Cell Rep.* 2022;38(10):110505. doi: 10.1016/j.celrep.2022.110505
- 5. Said HM. Intestinal absorption of water-soluble vitamins in health and disease.  $Biochem\ J.\ 2011;437(3):357-372.$  doi: 10.1042/bj20110326
- Ghosal A, Lambrecht N, Subramanya SB, Kapadia R, Said HM. Conditional knockout of the Slc5a6 gene in mouse intestine impairs biotin absorption. Am J Physiol Gastrointest Liver Physiol. 2013;304(1):G64-G71. doi: 10.1152/ajpgi.00379.2012
- 7. Zempleni J, Wijeratne SSK, Hassan YI. Biotin. *BioFactors*. 2009;35(1):36–46. doi: 10.1002/biof.8
- 8. Karachaliou CE, Livaniou E. Biotin homeostasis and human disorders: recent findings and perspectives. *Int J Mol Sci.* 2024;25(12):6578. doi: 10.3390/ijms25126578
- 9. Atamna H, Newberry J, Erlitzki R, et al. Biotin deficiency inhibits heme synthesis and impairs mitochondria in human lung fibroblasts. *J Nutr.* 2007;137(1):25–30. doi: 10.1093/jn/137.1.25
- Leonardi R, Jackowski S. Biosynthesis of pantothenic acid and coenzyme A. EcoSal Plus. 2007;2(2). doi: 10.1128/ ecosalplus.3.6.3.4
- 11. Sabui S, Kapadia R, Ghosal A, et al. Biotin and pantothenic acid oversupplementation to conditional *SLC5A6* KO mice prevents the development of intestinal mucosal abnormalities and growth defects. *Am J Physiol Cell Physiol.* 2018;315(1):C73–C79. doi: 10.1152/ajpcell.00319.2017
- 12. Hauth I, Waterham H, Wanders RJ, et al. A mild case of SMVT deficiency illustrating the importance of treatment response in variant classification. Cold Spring Harb Mol Case Stud. 2022;8(2):a006185. doi: 10.1101/mcs.a006185
- 13. Byrne AB, Arts P, Polyak SW, et al. Identification and targeted management of a neurodegenerative disorder caused by biallelic mutations in SLC5A6. *NPJ Genom Med.* 2019;4(1):28. doi: 10.1038/s41525-019-0103-x
- 14. Schwantje M, de Sain-van der Velden M, Jans J, et al. Genetic defect of the sodium-dependent multivitamin transporter: A treatable disease, mimicking biotinidase deficiency. *JIMD Rep.* 2019;48(1):11–14. doi: 10.1002/jmd2.12040
- 15. Subramanian VS, Constantinescu AR, Benke PJ, et al. Mutations in SLC5A6 associated with brain, immune, bone, and intestinal dysfunction in a young child. *Hum Genet*. 2017;136(2):253–261. doi: 10.1007/s00439-016-1751-x
- 16. Holling T, Nampoothiri S, Tarhan B, et al. Novel biallelic variants expand the SLC5A6-related phenotypic spectrum. *Eur J Hum Gen.* 2022;30(4):439–449. doi: 10.1038/s41431-021-01033-2

- 17. Montomoli M, Vetro A, Tubili F, et al. A novel SL-C5A6 homozygous variant in a family with multivitamin-dependent neurometabolic disorder: Phenotype expansion and long-term follow-up. *Eur J Med Genet*. 2023;66(8):104808. doi: 10.1016/j.ejmg.2023.104808
- 18. Van Vyve F-X, Mercier N, Papadopoulos J, et al. A new case of sodium-dependent multivitamin transporter defect occurring as a life-threatening condition responsive to early vitamin supplementation and literature review. *Mol Genet Genomic Med.* 2024;12(2). doi: 10.1002/mgg3.2388
- 19. Biotin. Reactions Weekly. 2024;2020(1):104. doi: 10.1007/s40278-024-64469-9
- 20. Arooran T, Fernando PMS, Dayasiri K, et al. Child with holocarboxylase synthetase deficiency. *Clin Chim Acta*. 2024;558:119086. doi: 10.1016/j.cca.2024.119086
- 21. Livaniou E, Costopoulou D, Vassiliadou I, et al. Analytical techniques for determining biotin. *J Chromatogr A*. 2000;881(1–2):331–343. doi: 10.1016/S0021-9673(00)00118-7
- 22. Mariasina SS, Chang CF, Navalayeu TL, et al. Williams-Beuren syndrome related methyltransferase WB-SCR27: From structure to possible function. *Front Mol Biosci.* 2022;9. doi: 10.3389/fmolb.2022.865743
- 23. Kowarz E, Löscher D, Marschalek R. Optimized sleeping beauty transposons rapidly generate stable transgenic cell lines. *Biotechnol J.* 2015;10(4):647–653. doi: 10.1002/biot.201400821
- 24. Mátés L, Chuah MKL, Belay E, et al. Molecular evolution of a novel hyperactive Sleeping Beauty transposase enables robust stable gene transfer in vertebrates. *Nat Genet.* 2009;41(6):753–761. doi: 10.1038/ng.343
- 25. Ran FA, Hsu PD, Wright J, et al. Genome engineering using the CRISPR-Cas9 system. *Nat Protoc.* 2013;8(11):2281–2308. doi: 10.1038/nprot.2013.143
- 26. Karaj E, Sindi SH, Kuganesan N, et al. Tunable cysteine-targeting electrophilic heteroaromatic warheads induce ferroptosis. *J Med Chem.* 2022;65(17):11788–11817. doi: 10.1021/acs.jmedchem.2c00909
- 27. Cui Y, Ma L. Sequential use of milk and bovine serum albumin for streptavidin-probed western blot. *Biotechniques*. 2018;65(3):125–126. doi: 10.2144/btn-2018-0006
- 28. Daberkow RL, White BR, Cederberg RA, et al. Monocarboxylate transporter 1 mediates biotin uptake in human peripheral blood mononuclear cells. *J Nutr.* 2003;133(9):2703–2706. doi: 10.1093/jn/133.9.2703
- 29. Zempleni J, Hassan YI, Wijeratne SS. Biotin and biotinidase deficiency. Expert Rev Endocrinol Metab. 2008;3(6):715–724. doi: 10.1586/17446651.3.6.715
- 30. Tripathi R, Guglani A, Ghorpade R, et al. Biotin conjugates in targeted drug delivery: Is it mediated by a biotin transporter, a yet to be identified receptor, or (an)other unknown mechanism(s)? *J Enzyme Inhib Med Chem*. 2023;38(1):2276663. doi: 10.1080/14756366.2023.2276663
- 31. Roux KJ, Kim DI, Burke B, et al. BioID: A screen for protein-protein interactions. *Curr Protoc Protein Sci.* 2018;91:19.23.1–19.23.15. doi: 10.1002/cpps.51
- 32. Choi-Rhee E, Schulman H, Cronan JE. Promiscuous protein biotinylation by *Escherichia coli* biotin protein ligase. *Protein Science*. 2004;13(11):3043–3050. doi: 10.1110/ps.04911804
- 33. Peura L, Malmioja K, Laine K, et al. Large amino acid transporter 1 (LAT1) prodrugs of valproic acid: new prodrug design ideas for central nervous system delivery. *Mol Pharm.* 2011;8(5):1857–1866. doi: 10.1021/mp2001878

- 34. Puris E, Gynther M, Huttunen J, et al. L-type amino acid transporter 1 utilizing prodrugs: How to achieve effective brain delivery and low systemic exposure of drugs. *J Control Release*. 2017;261:93–104. doi: 10.1016/j. jconrel.2017.06.023
- 35. Huttunen J, Peltokangas S, Gynther M, et al. l-Type amino acid transporter 1 (LAT1/Lat1)-utilizing prodrugs can improve the delivery of drugs into neurons, Astrocytes and microglia. *Sci Rep.* 2019;9(1):12860. doi: 10.1038/s41598-019-49009-z
- 36. Szabó E, Szatmári I, Szőnyi L, et al. Quantitative analytical method for the determination of biotinidase activity in dried blood spot samples. *Anal Chem.* 2015;87(20):10573–10578. doi: 10.1021/acs.analchem.5b02996
- 37. Kobza KA, Chaiseeda K, Sarath G, et al. Biotinyl-methyl 4-(amidomethyl)benzoate is a competitive inhibitor of human biotinidase. *J Nutr Biochem.* 2008;19(12):826–832. doi: 10.1016/j.jnutbio.2007.11.002
- 38. Maiti S, Paira P. Biotin conjugated organic molecules and proteins for cancer therapy: A review. Eur J Med Chem. 2018;145:206–223. doi: 10.1016/j.ejmech.2018.01.001
- 39. Park S, Kim E, Kim WY, et al. Biotin-guided anticancer drug delivery with acidity-triggered drug release. *Chem Commun.* 2015;51(45):9343-9345. doi: 10.1039/C5CC03003J
- 40. Said HM. Cell and molecular aspects of human intestinal biotin absorption. *J Nutr.* 2009;139(1):158–162. doi: 10.3945/jn.108.092023

### GUIDELINES FOR AUTHORS 2025

### **GENERAL RULES**

Acta Naturae publishes experimental articles and reviews, as well as articles on topical issues, short reviews, and reports on the subjects of basic and applied life sciences and biotechnology.

The journal *Acta Naturae* is on the list of the leading periodicals of the Higher Attestation Commission of the Russian Ministry of Education and Science. The journal Acta Naturae is indexed in PubMed, Web of Science, Scopus and RCSI databases.

The editors of *Acta Naturae* ask of the authors that they follow certain guidelines listed below. Articles which fail to conform to these guidelines will be rejected without review. The editors will not consider articles whose results have already been published or are being considered by other publications.

The maximum length of a review, together with tables and references, cannot exceed 50 000 characters with spaces (approximately 30 pages, A4 format, 1.5 spacing, Times New Roman font, size 12) and cannot contain more than 16 figures.

Experimental articles should not exceed 30 000 symbols (approximately 15 pages in A4 format, including tables and references). They should contain no more than ten figures.

A short report must include the study's rationale, experimental material, and conclusions. A short report should not exceed 12 000 symbols (5–6 pages in A4 format including no more than 12 references). It should contain no more than three figures.

The manuscript and all necessary files should be uploaded to www.actanaturae.ru:

- 1) text in Word 2003 for Windows format;
- 2) the figures in TIFF format;
- 3) the text of the article and figures in one pdf file;
- 4) the article's title, the names and initials of the authors, the full name of the organizations, the abstract, keywords, abbreviations, figure captions, and Russian references should be translated to English;
- 5) the cover letter stating that the submitted manuscript has not been published elsewhere and is not under consideration for publication;
- 6) the license agreement (the agreement form can be downloaded from the website www.actanaturae.ru).

### MANUSCRIPT FORMATTING

The manuscript should be formatted in the following manner:

- Article title. Bold font. The title should not be too long or too short and must be informative. The title should not exceed 100 characters. It should reflect the major result, the essence, and uniqueness of the work, names and initials of the authors.
- The corresponding author, who will also be working with the proofs, should be marked with a footnote \*.
- · Full name of the scientific organization and its departmental affiliation. If there are two or more scientific

organizations involved, they should be linked by digital superscripts with the authors' names. Abstract. The structure of the abstract should be very clear and must reflect the following: it should introduce the reader to the main issue and describe the experimental approach, the possibility of practical use, and the possibility of further research in the field. The average length of an abstract is 20 lines (1 500 characters).

- · Keywords (3 6). These should include the field of research, methods, experimental subject, and the specifics of the work. List of abbreviations.
- · INTRODUCTION
- · EXPERIMENTAL PROCEDURES
- · RESULTS AND DISCUSSION
- · CONCLUSION

The organizations that funded the work should be listed at the end of this section with grant numbers in parenthesis.

· REFERENCES

The in-text references should be in brackets, such as [1].

### RECOMMENDATIONS ON THE TYPING AND FORMATTING OF THE TEXT

- · We recommend the use of Microsoft Word 2003 for Windows text editing software.
- The Times New Roman font should be used. Standard font size is 12.
- · The space between the lines is 1.5.
- · Using more than one whole space between words is not recommended.
- · We do not accept articles with automatic referencing; automatic word hyphenation; or automatic prohibition of hyphenation, listing, automatic indentation, etc.
- We recommend that tables be created using Word software options (Table → Insert Table) or MS Excel.
   Tables that were created manually (using lots of spaces without boxes) cannot be accepted.
- · Initials and last names should always be separated by a whole space; for example, A. A. Ivanov.
- Throughout the text, all dates should appear in the "day.month.year" format, for example 02.05.1991, 26.12.1874, etc.
- There should be no periods after the title of the article, the authors' names, headings and subheadings, figure captions, units (s second, g gram, min minute, h hour, d day, deg degree).
- · Periods should be used after footnotes (including those in tables), table comments, abstracts, and abbreviations (mon. months, y. years, m. temp. melting temperature); however, they should not be used in subscripted indexes ( $T_{\rm m}$  melting temperature;  $T_{\rm p.t}$  temperature of phase transition). One exception is mln million, which should be used without a period.
- · Decimal numbers should always contain a period and not a comma (0.25 and not 0,25).
- The hyphen ("-") is surrounded by two whole spaces, while the "minus," "interval," or "chemical bond" symbols do not require a space.

### GUIDELINES FOR AUTHORS 2025

- The only symbol used for multiplication is "x"; the "x" symbol can only be used if it has a number to its right. The "." symbol is used for denoting complex compounds in chemical formulas and also noncovalent complexes (such as DNA·RNA, etc.).
- · Formulas must use the letter of the Latin and Greek alphabets.
- Latin genera and species' names should be in italics, while the taxa of higher orders should be in regular font.
- Gene names (except for yeast genes) should be italicized, while names of proteins should be in regular font.
- · Names of nucleotides (A, T, G, C, U), amino acids (Arg, Ile, Val, etc.), and phosphonucleotides (ATP, AMP, etc.) should be written with Latin letters in regular font.
- · Numeration of bases in nucleic acids and amino acid residues should not be hyphenated (T34, Ala89).
- · When choosing units of measurement, SI units are to be used.
- · Molecular mass should be in Daltons (Da, KDa, MDa).
- The number of nucleotide pairs should be abbreviated (bp, kbp).
- · The number of amino acids should be abbreviated to aa.
- Biochemical terms, such as the names of enzymes, should conform to IUPAC standards.
- The number of term and name abbreviations in the text should be kept to a minimum.
- · Repeating the same data in the text, tables, and graphs is not allowed.

### **GUIDENESS FOR ILLUSTRATIONS**

- Figures should be supplied in separate files. Only TIFF is accepted.
- · Figures should have a resolution of no less than 300 dpi for color and half-tone images and no less than 600 dpi.
- · Files should not have any additional layers.

## REVIEW AND PREPARATION OF THE MANUSCRIPT FOR PRINT AND PUBLICATION

Articles are published on a first-come, first-served basis. The members of the editorial board have the right to recommend the expedited publishing of articles which are deemed to be a priority and have received good reviews.

Articles which have been received by the editorial board are assessed by the board members and then sent for external review, if needed. The choice of reviewers is up to the editorial board. The manuscript is sent on to reviewers who are experts in this field of research, and the editorial board makes its decisions based on the reviews of these experts. The article may be accepted as is, sent back for improvements, or rejected.

The editorial board can decide to reject an article if it does not conform to the guidelines set above.

The return of an article to the authors for improvement does not mean that the article has been accepted for publication. After the revised text has been received, a decision is made by the editorial board. The author must return the improved text, together with the responses to all comments. The date of acceptance is the day on which the final version of the article was received by the publisher.

A revised manuscript must be sent back to the publisher a week after the authors have received the comments; if not, the article is considered a resubmission.

E-mail is used at all the stages of communication between the author, editors, publishers, and reviewers, so it is of vital importance that the authors monitor the address that they list in the article and inform the publisher of any changes in due time.

After the layout for the relevant issue of the journal is ready, the publisher sends out PDF files to the authors for a final review.

Changes other than simple corrections in the text, figures, or tables are not allowed at the final review stage. If this is necessary, the issue is resolved by the editorial board.

### **FORMAT OF REFERENCES**

The journal uses a numeric reference system, which means that references are denoted as numbers in the text (in brackets) which refer to the number in the reference list.

Bibliographic descriptions of cited sources in the reference list should be formatted according to the requirements of the International Committee of Medical Journal Editors (ICMJE) and the AMA Manual of Style: A Guide for Authors and Editors (11th Edition).

Detailed formatting rules are available at: https://actanaturae.ru/2075-8251/pages/view/references

For users of specialized reference management software, the editorial board recommends the following resources:

- EndNote download the Acta Naturae.ens style file; use the reference style JAMA: Journal of the American Medical Association (AMA 11th edition);
- · Zotero use the reference style American Medical Association 11th edition (brackets);
- $\cdot$  Mendeley use the reference style American Medical Association.

Examples of reference formatting:

- 1. Hisakata R, Nishida S, Johnston A. An adaptable metric shapes perceptual space. *Curr Biol.* 2016;26(14):1911-1915. doi: 10.1016/j.cub.2016.05.047
- 2. Sambrook J, Russell DW. Molecular Cloning: A Laboratory Manual. 3rd ed. CSHL Press; 2001.
- 3. Hogue CWV. Structure databases. In: Baxevanis AD, Ouellette BFF, eds. *Bioinformatics*. 2nd ed. Life Sciences Series. Wiley-Interscience; 2001:83-109.

The following e-mail addresses can be used to contact the editorial staff: actanaturae@gmail.com, tel.: (495) 727-38-60.